Development of geo-electrical methods to characterize dissolution and precipitation processes in a carbonate context

Flore Rembert

Sorbonne Université

École doctorale Géosciences, Ressources Naturelles et Environnement (ED 398)

UMR 7619 METIS

Development of geo-electrical methods to characterize dissolution and precipitation processes in a carbonate context

Par Flore REMBERT

Thèse de doctorat de Géophysique expérimentale

Dirigée par Damien JOUGNOT

Soutenue le 25 mars 2021

Devant le jury composé de :

M. Andreas KEMNA	Professeur, Université de Bonn, Allemagne	Rapporteur
Mme Catherine NOIRIEL	Maître de conférences, Université Paul Sabatier, Toulouse	Rapportrice
M. Jean-François GIRARD	Professeur des Universités, Université de Strasbourg	Examinateur
M. Roger GUÉRIN	Professeur des Universités, Sorbonne Université	Examinateur
M. Niklas LINDE	Professeur, Université de Lausanne, Suisse	Examinateur
Mme Linda LUQUOT	Chargée de recherche CNRS, Université de Montpellier	Examinatrice
M. Alexis MAINEULT	Chargé de recherche CNRS, Sorbonne Université, Paris	Examinateur
M. Damien JOUGNOT	Chargé de recherche CNRS, Sorbonne Université, Paris	Directeur de thèse

À mes parents

À Quentin

À cœur vaillant, rien
d'impossible.

Jacques Cœur

Non mais laissez-moi
manger ma banane.

Philippe Katerine

Remerciements

Il est certain que la thèse est une aventure en solitaire par bien des aspects. Néanmoins, je voudrais remercier ici, toutes les personnes, qui ont, de près ou de loin, permis à cette thèse d'aboutir.

Je voudrais en premier lieu, remercier Damien Jougnot, mon directeur de thèse, qui a su être à la fois le piano soutenant le soliste et le chef d'orchestre de notre duo pendant ces trois années de travail. Je souhaite également saluer la bienveillance de Roger Guérin, qui a assumé le rôle de directeur de thèse pendant deux annnées et demi avant de passer le flambeau à Damien. Je pense également à Pierpaolo Zuddas, qui a su *pimenter* cette direction de thèse.

Je remercie Andreas Kemna et Catherine Noiriel pour avoir bien voulu être rapporteur et rapportrice de ce travail de thèse, malgré les contraintes temporelles. Les commentaires et suggestions présents dans ces rapports ont permis de mûrir d'avantage certains résultats fraîchement interprétés. Je remercie également Jean-François Girard pour avoir présidé ce jury de thèse avec bienveillance à travers l'écran. Je remercie bien sûr les examinateurs et examinatrice de ce jury, en commençant par Niklas Linde et ses questions épineuses. J'ai une pensée particulière pour Roger Guérin, Linda Luquot et Alexis Maineult, qui ont vu l'évolution de mon travail au cours de ces trois ans de thèse en acceptant d'être membres de mon comité de suivi. Je salue leur indulgence et leur compréhension face à un début de thèse hésitant, qu'ils ont aidé à aiguiller.

Je souhaite remercier le laboratoire METIS pour m'avoir accueillie. Trouver un lieu adéquat pour les expériences n'a pas toujours été une tâche simple, mais je remercie l'équipe du couloir 56-66 pour m'avoir hébergée. Je pense notamment à Emmanuel Aubry, pour toutes les analyses des concentrations et son aide pour l'utilisation du matériel de paillasse. Je

remercie égelement l'équipe de choc formée par Bénédicte Sabatier et Valérie Girard : elles ont réponse à tout! Je souhaite aussi remercier les différents collègues géophysiciens pour leur soutien régulier en passant discuter et nous encourager dans le bureau des doctorants, je pense en particulier au philosophe Julien Thiesson et à Ludovic Bodet.

Je souhaite également remercier Loïc Labrousse, directeur de l'école doctorale GRNE, pour sa confiance et son soutien lorsque le navire était balloté.

J'aimerais également remercier différents collègues, rencontrés pendant cette thèse. Je salue d'abord Emmanuel Laurent, qui n'a cessé de m'encourager lors de nos trajets vers le terrain de golf dans le cadre de mon monitorat. Je remercie le projet Startrek avec Linda, Marie et Delphine pour m'avoir fait découvrir Montpellier, ses bars, son Soleil et ses cours de salsa. Je n'oublie pas non plus les cours de zumba de Linda, qui ont rythmé une partie de mon confinement en fin de thèse.

Je me dois bien sûr de remercier Philippe Katerine pour sa chanson sur la banane, qui a donnée naissance au Banana Group, ce cercle d'amateurs de crêpes et de pandas roux, aux discussions parfois surréalistes dans les bars de la Contrescarpe. Merci à Aìda, Cécile, Karim, Angie, Kawtar, Lara et Julio pour cette belle entente et nos fous rires!

Je remercie chaleureusement ma famille ; ma soeur Luce, mon frère Arthur et sa jolie famille, mes grand-mères, Christiane et Maud, mes oncles, tantes, cousines et cousins. Je remercie tout particulièrement mes parents, Franck et Véronique, qui m'ont offert gîte et couverts pendant ces trois ans de retour à la maison. La cohabitation a parfois été mouvementée, mais on s'en est bien sorti. Bien sûr, je remercie Quentin, mon poussin rêveur, mais révolté. Nous avons passé trois ans entre Vincennes et Strasbourg, heureusement que WhatsApp et le TGV fonctionnent. Nous avons mis quelques projets entre parenthèses, mais cela ne nous a pas empêché de nous balader à pied, à cheval ou à bicyclette, en France, en Europe et même en Californie! Je remercie également Martine et Pascal, les parents de Quentin, pour leur soutien au cours de mes quelques visites à Magny-Fouchard.

Pour finir, je remercie bien fort tous les copains et copines, qui m'ont épaulée à un moment ou un autre de cette thèse. Dans un ordre chaotique, je remercie Manon, Hélène, Tiphaine, Aude, Alex, Hans, Benji, Marine, Damian et Marta, Matthias et Lorène, Paul, Prunelle, Diane et Guillaume, Béatrice, Antonin et certainement bien d'autres que je n'ai pas cités.

Résumé

Parmi les différents minéraux constituant les roches carbonatées, la précipitation et la dissolution de la calcite sont des processus primordiaux pour l'étude des roches carbonatées et leur surveillance *in situ* est un enjeu majeur de leur utilisation pour la gestion des risques (e.g., cavités), des ressources (e.g., H_2O) ou déchets (e.g., CO_2). Les méthodes hydrogéophysiques sont fondées sur le développement de techniques géophysiques appropriées pour le suivi des processus hydrologiques et biogéochimiques de manière non-intrusive et à faible coût. En outre, parmi les techniques existantes, les méthodes électriques ont déjà prouvé leur capacité à surveiller les processus hydrologiques et la réactivité géochimique. Pour cette raison, les méthodes du potentiel spontané (PS) et de la polarisation provoquée spectrale (PPS) ont été choisies pour investiguer les processus de dissolution et de précipitation de la calcite. La PS est une technique passive consistant à mesurer le champ électrique naturel généré par les flux d'eau et les gradients de concentration, respectivement par les couplages électrocinétique et électrochimique, tandis que la PPS est une méthode active mesurant la conductivité électrique complexe aux basses fréquences (du mHz au kHz). La conductivité électrique complexe est une propriété géophysique dont les composantes réelle et imaginaire peuvent être reliées respectivement aux propriétés microstructurales du milieu poreux et à l'état de surface des minéraux le constituant. Cependant, pour les études biogéochimiques, les données de PS et de PPS sont encore complexes à interpréter, en raison de la superposition des mécanismes sources. De ce fait, en l'absence de relations pétrophysiques, ces méthodes font rarement l'objet de modélisation quantitative. Cette thèse présente des recherches expérimentales et des développements théoriques connexes visant à améliorer l'interprétation des méthodes PS et PPS. Tout d'abord, un nouveau modèle de conductivité électrique est développé et montre un bon ajustement avec les résultats numériques de dissolution et de précipitation. Deuxièmement, des données PS remarquables ont été obtenues et ont pu être

reliées aux gradients de concentration ionique grâce à une modélisation de transport réactif, conduisant à l'interprétation quantitative du couplage électrodiffusif de la PS. Par la suite, les expériences menées ont conduit à la conception et à l'amélioration d'un banc expérimental permettant une étude complète combinant l'acquisition géo-électrique multiméthodes et les analyses géochimiques. Enfin, les résultats obtenus par la PPS nourrissent la réflexion sur les mécanismes invoqués par d'autres études comme sources des variations de polarisation électrique résultant des processus de précipitation et de dissolution de la calcite.

Mots clés

suivi temporel de la réactivité de la calcite, processus de dissolution et de précipitation, potentiel spontané, polarisation provoquée spectrale, transport réactif, pétrophysique.

Abstract

Calcite precipitation and dissolution are prime processes in carbonate rocks and being able to monitor them *in situ* is a major deal of reservoir exploitation for geo-resources (water, gas) or geological storage (CO2, H2, waste). Hydrogeophysical methods are based on the development of suitable geophysical techniques to monitor hydrological and biogeochemical processes non-intrusively and at low cost. Furthermore, among the existing techniques, electrical methods have already proven their ability to monitor hydrological processes and chemical reactivity. For this reason, self-potential (SP) and spectral induced polarization (SIP) methods are chosen for the study of calcite dissolution and precipitation processes. SP is a passive technique consisting in the measurement of the natural electric field generated by water fluxes and concentration gradients, through electrokinetic and electrochemical couplings, respectively, while, SIP is an active method measuring the electrical complex conductivity at low frequencies (from mHz to kHz).The electrical complex conductivity is a geophysical property whose real and imaginary components can be related to the microstructural properties of the porous medium and to the surface state of the minerals of which it is composed, respectively. However, for biogeochemical studies, SP and SIP data are still complex to interpret, due to the superposition of source mechanisms. Therefore, due to the lack of petrophysical relationships, these methods are rarely quantitatively modeled. This thesis presents experimental investigations and related theoretical developments to improve the interpretation of these methods. First, a new model of electrical conductivity is developed and show successful fitting with dissolution and precipitation numerical results. Secondly, remarkable SP data were obtained and are related to ionic concentration gradients through reactive transport modeling, leading to the quantitative interpretation of the SP electro-diffusive coupling. Then, the conducted experiments led to the design and the improvement of a laboratory setup enabling a complete study combining geo-electrical

acquisition and geochemical analyses. Finally, SIP results nourish the reflection concerning the mechanisms, invoked by other studies, responsible for the electrical polarization variations resulting from calcite precipitation and dissolution processes.

Key-words

calcite reactivity monitoring, dissolution and precipitation processes, self-potential, spectral induced polarization, reactive transport, petrophysics.

Contents

Table of symbols

Symbol	Definition
a	constriction factor (-)
Alk	alkalinity (mol L^{-1})
A_p	REV section area (m^2)
α^*	coupling coefficient (V)
β	mobility (m^2 s^{-1} V^{-1})
β_+	mobility on the cation (m^2 s^{-1} V^{-1})
β_-	mobility on the anion (m^2 s^{-1} V^{-1})
β_{X_i}	mobility on ion X_i (m^2 s^{-1} V^{-1})
C	ionic concentration of the solution (mol L^{-1})
C^{EK}	electrokinetic coupling coefficient (V Pa^{-1})
$C^{\ominus}$	standard concentration (mol L^{-1})
C_{X_i}	ionic concentration of ion X_i (mol L^{-1})
C_1	first electrode of current injection
C_2	second electrode of current injection
d	pore diameter (m)
d_c	column diameter (m)
d_g	grain diameter (m)
$< d_g >$	mean grain diameter (m)
D	diffusion coefficient (m^2 s^{-1})
$\mathscr{D}$	dielectric displacement field (C m^{-2})
D_b	surface diffucion coefficient in the Stern layer (m^2 s^{-1})
D_{eff}	effective diffusion coefficient (m^2 s^{-1})
D_p	fractal dimension of pore size (-)
D_w	diffusion coefficient of water (m^2 s^{-1})
D_{X_i}	diffusion cofficient of ion X_i (m^2 s^{-1})

Symbol	Definition
Da	Damköhler number (-)
Δc	solute concentration differences (mol m^{-3})
Δh	hydraulic charge across the REV (m)
ΔV	electric voltage (V)
E	electric field (V m^{-1}]
EC	electrical conductivity
ϵ	mean absolute percentage error (%)
η	fluid dynamic viscosity (Pa s)
η_w	water dynamic viscosity (Pa s)
f	constrictivity (-)
f	frequency (Hz)
f_b	critical frequency of the Stern layer (Hz)
f_g	geometric factor (m)
F	formation factor (-)
$\mathscr{F}$	Faraday constant (C mol^{-1})
g	standard gravity (m s^{-2})
G	geometrical factor (-)
γ_{X_i}	activity coefficient of ion X_i (-)
i	imaginary unit(-)
$i(\bar{r})$	electric current flowing through a single pore (A)
I	REV electric current (A)
$\|I\|$	electric current amplitude (A)
j_s	source current density (A m^{-2})
j_s^{diff}	electrochemical coupling current density from ionic concentration gradients (A m^{-2})
j_s^{EK}	electrokinetic coupling current density (A m^{-2})
j_s^{redox}	electrochemical coupling current density from oxydation-reduction reactions (A m^{-2})
J_c	conduction electric current density (A m^{-2})
J_C	flux of transported solute concentration (mol m^{-2} s^{-1})
J_d	dielectric displacement current density (A m^{-2})
J_t	diffusive solute mass flow rate (mol s^{-1})
J_{tot}	total electric current density (A m^{-2})
k_g	geometric factor (m)
k^{REV}	REV permeability (m^2)
K_0	Henry's law constant (-)
K_A	acidity constant of acetic acid (-)
K_{A_1}	acidity constant of hydrogencarbonate ion (-)

Symbol	Definition
K_{A_2}	acidity constant of carbonate ion (-)
K_h	hydratation constant (-)
K_{sp}	solubility product of calcite (-)
l	tortuous length (m)
l_{cc}	distance between the electrodes of current injection (m)
l_{cp}	distance between the electrode of current injection and the electrode of potential measurement (m)
l_{pp}	distance between the electrodes of potential measurement (m)
l_0	straight path (m)
L	REV length (m)
λ	wavelength (m)
Λ	Johnson length (m)
Λ_m	molar conductivity (S m^{-2} mol^{-1})
Λ_{X_i}	molar conductivity of ion X_i (S m^{-2} mol^{-1})
m	cementation exponent (-)
M	parameter characterizing the influence of the diffuse layer on the Stern layer (-)
μ	water viscosity (Pa s)
$N(\bar{r})$	number of pores of radius equal or larger than $\bar{r}$ (-)
N_{tot}	total number of pores (-)
N^d	number of data (-)
ω	angular frequency (rad s^{-1})
Ω	saturation index (-)
p	purity coefficient (-)
p_e	empirical parameter for temperature compensation (-)
pH_1	first pH electrode located in Column 2
pH_2	second pH electrode located in Column 2
P_{CO_2}	CO_2 partial pressure (Pa)
P_j	one of the measurement electrodes
P_i^d	electrical property from the data (-)
P_i^m	electrical property from the model (-)
P_a	coefficient to define $a(\phi)$ (-)
P_τ	coefficient to define $\tau(\phi)$ (-)
Pe	Péclet number (-)
P_1	first electrode of electric potential measurement
P_2	second electrode of electric potential measurement
P_3	third electrode of electric potential measurement

Symbol	Definition
P_4	fourth electrode of electric potential measurement
ϕ	porosity (-)
ϕ_{end}	final porosity (-)
ϕ_{init}	initial porosity (-)
φ	complex EC phase shift (rad)
φ_I	electric current phase shift (rad)
φ_V	electric potential phase shift (rad)
q	concentration of the solid phase (mol $kg^{-1}{}_w$)
Q	flow rate (m^3 s^{-1})
$Q_p(\bar{r})$	flow rate of a single pore (m^3 s^{-1})
Q^{REV}	total volumetric flow rate (m^3 s^{-1})
$\hat{Q}_v$	volumetric excess charge (C m^{-3})
r	pore radius (m)
$\bar{r}$	average pore radius (m)
$\bar{r}_{max}$	maximum average pore radius (m)
$\bar{r}_{min}$	minimum average pore radius (m)
R	REV radius (m)
$\mathscr{R}$	molar gas constant (J mol^{-1} K^{-1})
Re	number of Reynolds (-)
REV	Representative elementary volume
ρ	density of water (kg m^{-3})
r'	amplitude of the radius size fluctuation (m)
SIP	spectral induced polarization
SP	self potential
S	section area of the REV (^{2}m)
S1	solution of hydrochloric acid at pH=3
S2	calcite over-saturated solution with $\Omega = 14$
S3	solution of hydrochloric acid at pH=4.5
S4	concentrated buffered solution of acetic acid at pH=4.5
S5	diluted buffered solution of acetic acid at pH=4.5
S6	solution of calcium chloride at 26.2 mmol L^{-1}
S7	solution of sodium carbonate at 29.0 mmol L^{-1}
σ	rock sample EC when neglecting σ_s (S m^{-1})
σ^*	complex EC (S m^{-1})
$\lvert\sigma^*\rvert$	complex EC amplitude (S m^{-1})
σ'	real part of the complex EC (S m^{-1})

Symbol	Definition
σ''	imaginary part of the complex EC (S m^{-1})
σ_{in}	inlet pore water EC (µS cm^{-1})
$\sigma_p(\bar{r})$	contribution to the porous medium conductivity from a single pore (S m^{-1})
σ_{out}	outlet pore water EC (µS cm^{-1})
σ^{REV}	REV electrical conductivity (S m^{-1})
σ_s	surface conductivity (S m^{-1})
σ^*_{surf}	real part of the complex surface conductivity (S m^{-1})
σ'_{surf}	imaginary part of the complex surface conductivity (S m^{-1})
σ''_{surf}	complex surface conductivity (S m^{-1})
σ_w	pore water electrical conductivity (S m^{-1})
$\Sigma_{pore}(\bar{r})$	electrical conductance of a single pore (S)
t	time (sor hor d)
T	temperature (K)
t_{X_i}	transference number (-)
T_+	macroscopic Hittorf number of the cation (-)
T_-	macroscopic Hittorf number of the anion (-)
τ_h	hydraulic tortuosity (-)
τ_e	electrical tortuosity (-)
τ	tortuosity (-)
τ_e	electrical tortuosity (-)
τ_g	geometrical tortuosity (-)
θ	temperature (°C)
u	averaged pore fluid velocity (m s^{-1})
U	Darcy's velocity (m s^{-1})
v	velocity (m s^{-1})
V	electric potential (A)
$\|V\|$	electric potential amplitude (A)
$V_p(\bar{r})$	volume of a single pore (m^3)
V_{pores}	pore volume (m^3)
V_{sol}	volume of the solution (L)
V_{tot}	total rock volume (m^3)
ϑ	reaction rate (s^{-1})
(X_i)	ionic activity of ion X_i (-)
z_{X_i}	valence of ion X_i (-)
Z	impedance (Ω)
$\|Z\|$	impedance amplitude (Ω)

Symbol	Definition
Z_1	first criterion from Zimmermann et al. (2008)
Z_2	second criterion from Zimmermann et al. (2008)
Z_3	third criterion from Zimmermann et al. (2008)

List of Figures

List of Tables

Introduction

Background and problematic

Carbonate rocks cover a large area of the continental surface all over the globe (Chen et al. 2017). From fields to big cities, carbonate rocks are in our close environment and are bounded to many environmental and societal issues due to their exploitation and their proper characteristics.

Carbonate rocks constitute reservoirs for key resources. Indeed, carbonate reservoirs are known to hold 60 % of the world's hydrocarbon reserves (e.g., Burchette 2012; Singh and Joshi 2020) and have been exploited for centuries as a valuable natural resource (Drew et al. 2017). The study of carbonate rocks is also very active because of their potential to serve as geologic repository especially in case of carbon dioxide (CO_2) geological storage (e.g., Luquot and Gouze 2009; Cherubini et al. 2019) and their active use for geothermal energy (e.g., Montanari et al. 2017). Carbonate rocks are also famous for the beautiful coastal landscapes with their immaculate cliffs that are not always that peaceful due to erosion (e.g., Neumann 1966). Carbonate rocks are also a great deal of civil engineering due to the risk of underground cavity formation, landsliding, and collapsing (Figure 0.1). However, the resource of greatest concern in recent years, due to human activities, is drinking water, which is available in the form of underground water in karst terrain (e.g., Kačaroğlu 1999; Bakalowicz and Dörfliger

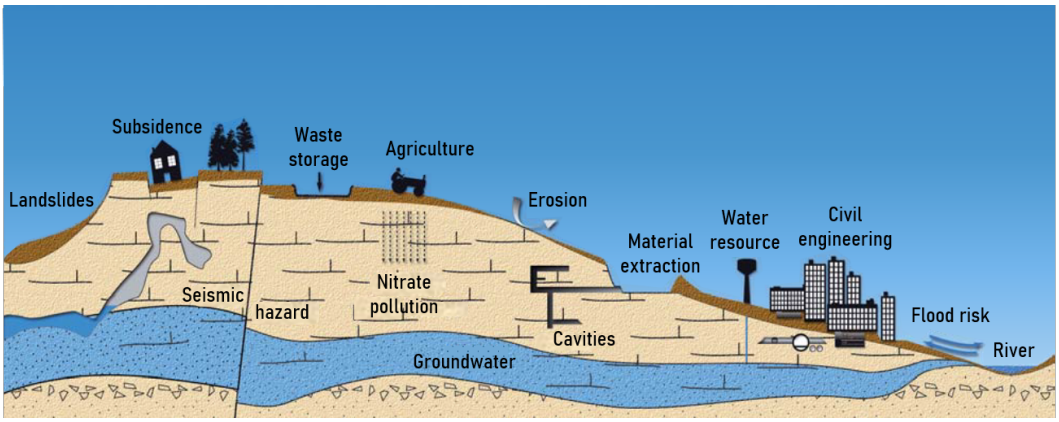

Figure 0.1: Limestone reservoir uses and issues regarding the society needs and environmental consequences, this illustration comes from Varet et al. (2009).

2005). Although karstic terrains cover 7-12 % of the Earth's land surface, karstic regions provide water supplies up to a quarter of the world's population (e.g., Drew et al. 2017). Unfortunately, this resource is threatened by pollution, especially from agricultural activities (e.g., Buckerfield et al. 2020). Hence, karsts constitute potential transit zone of pollution from the surface to the aquifer and the interactions and transfers between water, gas, and pollutants still require a better characterization.

However, studying carbonate reservoirs is a crucial challenge due to the multi-scale heterogeneity of rock properties and it is made even more difficult by the strong chemical reactivity of the minerals with the pore water and its chemistry (e.g., Meyerhoff et al. 2014). These features are responsible for specific processes occurring in carbonate rocks over a wide size range (nm to km), such as ionic transport in a reactive porous medium subjected to dissolution and precipitation due to groundwater circulations. Dissolution and precipitation of carbonate samples have already been well studied in the laboratory to characterize their impact on the porous sample microstructural and hydrodynamic properties (e.g., Hoefner and Fogler 1988; Daccord et al. 1993; Golfier et al. 2002; Luquot and Gouze 2009; Rötting et al. 2015; Noiriel et al. 2012, 2016; Bouissonnié et al. 2018). However, these experiments, which include image analysis (e.g., Teng et al. 2000; Noiriel 2015; Noiriel et al. 2020), are well designed for laboratory investigations, but cannot be used on the field.

To comprehend carbonate reservoirs behavior during dissolution and precipitation, we need to be able to monitor their properties. In a subsurface context, chemical analysis of the pore water can be rather intrusive, only provide restricted and spatially limited information (Goldscheider et al. 2008). On the other hand, among the geophysical techniques, geo-electrical methods are non-intrusive and present a high sensitivity to physical and chemical properties of rocks and of pore fluids, therefore being quite suitable for such monitoring (e.g., Hubbard and Linde 2011; Reynolds 2011; Glover 2015; Lowrie and Fichtner 2020). An increasing amount of work has shown the interest and the effectiveness of geo-electrical methods for laboratory or *in situ* monitoring of hydrological processes and reactive transport related to the critical zone complexity (e.g., Revil et al. 2012; Vialle et al. 2014). Nevertheless, geophysical methods are indirect and thus, require appropriate models and inversion techniques to give a quantitative interpretation (e.g., Oldenburg and Li 2005; Tarantola 2005). Therefore, this thesis focuses on the development of experimental and numerical study of calcite dissolution and precipitation using two geo-electrical methods that are spectral induced polarization (SIP) and self-potential (SP) in addition with the monitoring of pore water electrical conductivity (EC).

Brief overview of the studied geo-electrical techniques

Pore water conducts electric current due to the presence of ionic species, behaving as electric charge carriers. Thus, the pore water EC depends on the ionic concentrations and on the nature of the ions in solution, as not all ions have identical mobility. The pore water conductivity is thus stronlgy related to its chemical composition (e.g., McCleskey et al. 2012).

The rock sample EC of a water saturated porous medium is very sensitive to pore water EC and to geometrical rock properties, such as the porosity. The most widely used relationship to link the rock conductivity to its porosity is an empirical relationship developed by Archie (1942). Since then, many petrophysical models (i.e.,

based on physical principles) have been developed and allow to use EC measurement to describe the geometry of the pore space (e.g., Rembert et al. 2020). Furthermore, sample EC petrophysical modeling serves also to characterize ionic transport (e.g., Maineult et al. 2016; Jougnot et al. 2018) and reactive-transport (e.g., Vialle et al. 2014; Ghosh et al. 2018).

The SIP method, by injecting an alternating current, measures both the sample electrical conductivity and the ability of the porous rock to polarize. This method was originally developed to detect metallic particles (e.g., Schlumberger 1920a; Kemna et al. 2012). Its use on sedimentary rocks is quite recent because the measured signal shows a much lower amplitude particularly in the case of carbonate rocks (e.g., Hupfer et al. 2017; Norbisrath et al. 2017; Johansson et al. 2020), requiring the development of high-precision acquisition instruments (e.g., Zimmermann et al. 2008). Last decade has seen the emergence of the use of SIP to characterize chemical and biological processes (e.g., Kessouri et al. 2019). Indeed, the first experiment using SIP to measure the electrical signature of precipitation has been conducted by Wu et al. (2010). While calcite particles were known to show low polarization, Wu et al. (2010) observed an important increase of SIP signal that they associated to calcite precipitation. Since then, Leroy et al. (2017) proposed a mechanistic model relating polarization amplitude to the size of the growing calcite grains. Even more recently, new experimental studies on both calcite dissolution and precipitation have been performed (e.g., Halisch et al. 2018; Izumoto et al. 2020a; Saneiyan et al. 2019, 2021), but they present contrasting results that lack physical-based modelisation to be properly interpreted.

SP method is based on the measurement of electrical current generated by natural contributions. This method, simple to set up, is however complex to interpret as it involves the superposition of different possible sources of current. Among the contributions, reactive-transport can be linked to two possible couplings (e.g., Jouniaux et al. 2009; Revil and Jardani 2013). Firstly, the electrokinetic coupling generates streaming potential from pore water circulation that carries an excess charge that compensates for the electric surface charge of the minerals (e.g., Quincke 1859; Revil and Leroy 2004). Secondly, the electrochemical coupling, called the electro-diffusive potential, is associated to ionic concentration gradients that generate separation charge due to the difference of mobilities between migrating dissolved ionic species (e.g., Revil 1999; Revil and Linde 2006; Linde et al. 2011). Therefore, the interest of the SP method is that it allows to study mixing and reaction zones between fluids as saline intrusions (e.g., Maineult et al. 2005; MacAllister et al. 2018; Graham et al. 2018) or water intrusion into hydrocarbon reservoir (e.g., Murtaza et al. 2011). A recent study from Cherubini et al. (2019), based on SP and conductivity measurements on limestone samples submitted to calcite dissolution from CO_2 drainage, demonstrated that the streaming potential coupling coefficient obtained from SP measurements could be a tool to estimate dissolution rates. However, Cherubini et al. (2019) did not take into account the contribution of ionic gradients that can be generated by calcite dissolution in their sample. To the best of our knowledge, there is no study of calcite precipitation using SP monitoring.

Outline of this thesis

This thesis is divided into three parts.

The first part comprises three chapters. The first and the second chapters introduce geochemical and geophysical backgrounds related to the study of dissolution and precipitation of calcite. The third chapter presents a published paper on a new petrophysical model that I developed to link EC to porous media microstructure characteristics and evolution due to calcite dissolution and precipitation processes.

The second part presents in two chapters the laboratory developments and tests to design experimental benches suitable for the monitoring of calcite dissolution and precipitation processes combining geo-electrical measurements (SIP and SP methods) and chemical analyses. This parts also summarizes the characteristics of different experimental protocols set up during this thesis.

The third part is dedicated to the presentation of the experimental results of different laboratory experiments conducted during this thesis. This part is divided into three chapters that highlight different studied issues. The first chapter presents the results of the first experiment conducted during this thesis that studied both calcite dissolution and precipitation. Clear SP signatures of both processes were monitored, thus this chapter also presents a new theoretical framework to interpret these data with the combination of reactive transport modeling and petrophysical development of electro-diffusive potential for a multi-species reactive context. In light of the results obtained from this first experiment, the second and third chapters of this part explore more specific questions. The second chapter focuses on SP signature of calcite dissolution depending on the reactive zone location and on the injected reactive solution injected. The third chapter is dedicated to the SIP signal characterization during calcite precipitation under different flow regimes. SIP phase shift spectra are interpreted in light of the results from the literature.

Part I

Theory and petrophysical models

CHAPTER

1 Introduction to the carbonate system and to hydrological and geochemical processes

1.1 Carbonate rocks and carbonate minerals

Carbonate rocks are sedimentary rocks composed of at least 50 % of carbonate minerals, which composition is associated with the carbonate ion CO_3^{2-}. Among the carbonate minerals, the three more abundant on Earth: aragonite , calcite, and dolomite. Aragonite and calcite are polymorphs of calcium carbonate $CaCO_3$ mineral, but these two minerals are distinguished by their different crystal lattice. Dolomite is a solid solution of calcium and magnesium carbonate. Thus dolomite is known as $(Ca,Mg)(CO_3)_2$ which in contrast with calcite does not effervesce with diluted acids at normal temperature (25 °C).

Carbonate rocks are divided into two groups: limestones and dolostones. Limestones are composed of at least 50 % of calcite while dolostones are composed of at least 50 % of dolomite (Foucault et al. 2014). Of course, all the compositional intermediates in calcite and dolomite exist and give rise to a finer classification (see Figure 1.1). There is no carbonate rock associated with majority aragonite due to the fact that aragonite is metastable and transforms into calcite in atmosphere conditions.

Limestones mainly originate from the accumulation of skeletons, shells, or calcareous tests. Several types of limestone rocks are distinguished depending on the medium of deposition (e.g., lacustrine, fluvial, marine

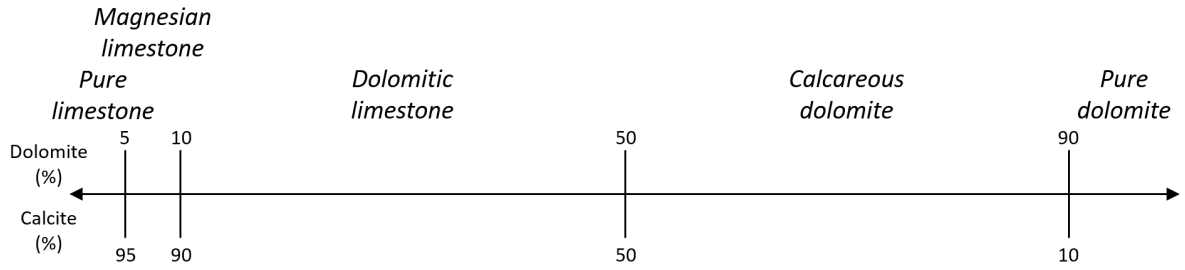

Figure 1.1: Carbonate sedimentary rocks ranging from pure limestone to pure dolostone according to the proportions of calcite and dolomite minerals in their compositions.

pelagic or marine netritic), the size of the calcite crystals (e.g., micritic with crystals of 20 μm, microgranular with crystals of 100 μm to 250 μm, saccharoid with crystals of 1 mm to 2 mm), or the importance and the nature of the fossils. Some of the limestones come from chemical precipitation (e.g., travertine). Limestones can also contain terrigenous material, especially clayey limestones, which form marly banks.

Limestones and dolomites can undergo metamorphism and form marbles. Marbles are characterized as rocks with visible crystals, which in the case of limestone marbles are also called crystalline limestones (Foucault et al. 2014), with calcite crystals over 0.1 mm in diameter and having a translucent saccharoid grain break (see Figure 4.1).

In a near surface context, carbonate rocks can produce a characteristic type of relief known as karstic modeling. Karsts are mainly formed by the dissolution of carbonate rocks under the action of meteoric water (i.e., rain), surface water (e.g., rivers, runoff water, Jozja et al. 2010) and groundwater circulation connecting to the aquifer. Karsts are complex systems comprising a great diversity of morphologies (e.g., Bakalowicz 1979; Plagnes 1997; Chalikakis 2006). Karstification brings together a set of processes involving the geochemical reactivity of carbonate minerals and water flows.

1.2 Calcite reactive system

1.2.1 Carbonate chemistry

As seen in previous section, calcite mineral is composed of calcium carbonate, which can dissociate in water as follows

$$CaCO_3 \rightleftharpoons Ca^{2+} + CO_3^{2-}. \tag{1.1}$$

This dissociation is controlled by the solubility product of calcite K_{sp} defined as

$$K_{sp} = (Ca^{2+})(CO_3^{2-}). \tag{1.2}$$

At 25 °C, the solubility product of calcite is $K_{sp} = 10^{-8.42}$ (Plummer and Busenberg 1982). (Ca^{2+}) and (CO_3^{2-}) (-) are the calcium and carbonate ions activities. Activity (X_i), of ion X_i, is linked to its ionic concentration C_{X_i} through the activity coefficient γ_{X_i} (-) as follows (e.g., Cohen et al. 2007)

$$(X_i) = \gamma_{X_i} \frac{C_{X_i}}{C^{\ominus}}, \tag{1.3}$$

where $C^{\ominus}$ is the standard concentration ($C^{\ominus} = 1$ mol L^{-1}). For an ideal solutions (i.e., at low concentrations), the activity coefficient is close to one ($\gamma_{X_i} \approx 1$), thus the ionic activity can be approximate with the ionic concentration. However, for more concentrated solutions, this approximation is not valid and the activity coefficient must be computed. First, one must compute the ionic force of the solution IF (mol L^{-1}), defined by

$$IF = \frac{1}{2} \sum_{X_i} C_{X_i} z_{X_i}^2, \tag{1.4}$$

where z_{X_i} (-) is the valence of ion X_i. Then, for the case of a low ionic force ($IF < 0.1$), the activity coefficient can be computed following the Debye-Hückel theory. In this thesis work, I used the approximation from

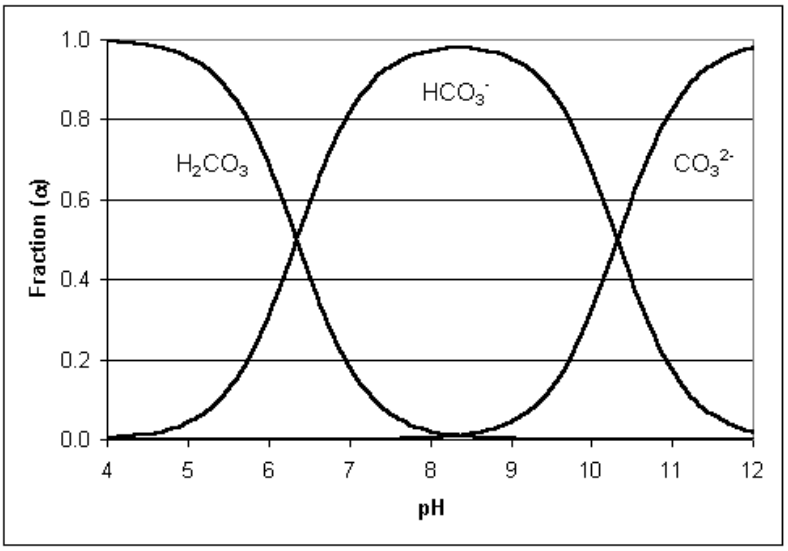

Figure 1.2: The distribution of carbonate species as a fraction of total dissolved carbonate in relation to solution pH.

Güntelberg, which establishes

$$\log(\gamma_{X_i}) = -0.509\, z_{X_i}^2 \left(\frac{\sqrt{IF}}{1+\sqrt{IF}} \right). \tag{1.5}$$

For solutions with higher ionic forces, other models exist, but they are not in the scope of the present work.

Carbonate ion CO_3^{2-} is a weak base. This means that depending of the solution pH, it will be present through different species as shown in Figure 1.2. Thus, the equations of the carbonate system are

$$H_2CO_3 \rightleftharpoons H^+ + HCO_3^- \tag{1.6}$$

and

$$HCO_3^- \rightleftharpoons H^+ + CO_3^{2-}. \tag{1.7}$$

The above expressions from Equations (1.6) and (1.7) are equations of acid dissociation. Their related acidity constants are thus

$$K_{A_1} = \frac{(HCO_3^-)(H^+)}{(H_2CO_3)} \tag{1.8}$$

and

$$K_{A_2} = \frac{(CO_3^{2-})(H^+)}{(HCO_3^-)}. \tag{1.9}$$

Their related acidity constants are $K_{A_1} = 10^{-6.35}$ and $K_{A_2} = 10^{-10.33}$ at 25 °C.

Carbonic acid H_2CO_3 is linked to carbon dioxide CO_2 through its hydration, which is expressed as

$$H_2CO_3^- \rightleftharpoons H_2O + CO_{2\,(aq)}. \tag{1.10}$$

The hydratation constant K_h (-) is thus

$$K_h = \frac{(H_2CO_3)}{C_{CO_{2\,(aq)}}} \tag{1.11}$$

and in pure water $K_h = 1.7\times10^{-3}$. The concentration of dissolved carbon dioxide is linked to CO_2 partial pressure P_{CO_2} through Henry's law which establishes

$$C_{CO_{2\,(aq)}} = K_0\, P_{CO_2}, \tag{1.12}$$

where K_0 (-) is the Henry's law constant, which depends on temperature and pressure conditions and on the solution salinity.

1.2.2 Alkalinity

The alkalinity of a solution can be defined as its acid neutralizing capacity (ANC) and is measured by titration with strong acid. The electroneutrality implies that the sum of cations concentrations is equivalent to the sum of the concentrations of the anions:

$$C_{cations} - C_{anions} = 0. \tag{1.13}$$

For the carbonate system, ions such as sodium (Na^+) or chloride (Cl^-), are defined as conservative ions. This implies that their concentrations are unaffected by changes of pH (e.g., Barker 2016) and thus, Alkalinity Alk (mol L^{-1}) is a constant defined as the difference between the conservative ions,

$$Alk = C_{conservativecations} - C_{conservativeanions}. \tag{1.14}$$

Combining Equations (1.13)and (1.14), alkalinity is also expressed as

$$Alk = C_{non-conservativecations} - C_{non-conservativeanions}. \tag{1.15}$$

In the carbonate system it leads to

$$Alk = C_{HCO_3^-} + 2C_{CO_3^{2-}} - C_{H^+} + C_{HO^-}, \tag{1.16}$$

where the three main ions HCO_3^-, CO_3^{2-}, and HO^- consume the protons H^+.

For most natural waters their pH falls between 6 and 8.5, a region in which the equilibrium between hydrogencarbonate and carbonate ions is strongly in favor of hydrogencarbonate. In addition, in most cases the hydrogencarbonate concentration is far greater than the hydroxyl or hydrogen proton concentrations. Thus for most situations the alkalinity is approximately equal to hydrogencarbonate concentration (e.g., Schroeder 2003).

1.2.3 Saturation index

Calcite dissolution or precipitation occurs when the pore water is not at the chemical equilibrium with calcite. Thus, the saturation index Ω (-) is defined as

$$\Omega = \frac{(Ca^{2+})(CO_3^{2-})}{K_{sp}}. \tag{1.17}$$

When $\Omega < 1$, the system is undersaturated with respect to calcite, thus calcite may dissolve to reach the equilibrium ($\Omega = 1$). On the contrary, $\Omega > 1$ indicates an oversaturated solution with respect to calcite may lead to calcite precipitation.

As seen previously, alkalinity can be approximated by the concentration of the hydrogencarbonate ion ($C_{HCO_3^-}$) and hydrogencarbonate concentration is related to carbonate concentration with Equation (1.9). The saturation index, defined by Equation 1.17, can thus be rewritten as

$$\Omega = \frac{\gamma_{Ca^{2+}} C_{Ca^{2+}} \gamma_{HCO_3^-} Alk K_{A_2}}{K_{sp} 10^{-\mathrm{pH}}}. \tag{1.18}$$

Hydrogen proton activity has been replaced by pH since $\mathrm{pH} = -\log(H^+)$.

1.3 Microstructural parameters of the porous medium

1.3.1 Porous medium and representative elementary volume

Most carbonate rocks can be considered as porous media, which are defined as solid structures with sufficient open space to let a passage for the fluid to flow through (e.g., Rubenstein et al. 2015). In the case of this thesis, we will only consider a water-saturated porous medium.

Porous media can be characterized at the microscopic or at the macroscopic scales (e.g., Chhabra and Richardson 2008). The microscopic scale tends to give a statistical description of the pore distribution and is necessary to understand surface phenomena. However, for natural porous media, the microstructure is complex and heterogeneous, including an irregular pore size and shape distribution. Thus, the microscopic description of the porous medium is adapted for the precise characterization of small samples, but is not suitable for a field-scale description. Therefore, it is preferable to use the macroscopic approach, since the macroscopic scale intends to define effective parameters to describe the averaged properties of the porous medium (e.g., Bachmat Y. 1987). The accuracy of these averaged parameters to describe the porous medium depends on the definition of the representative volume to be investigated. Therefore, the theory of the representative elementary volume (REV) is developed to theorized this notion (e.g., Yio et al. 2017). According to this theory, the porous medium is no longer considered as a discrete distribution of pores, but as a continuum where its physical properties can be described as time and space functions. The REV is thus large in relation to the grain size since it describes average properties independent of the fluctuations from one pore to another, but the REV shall also be small in relation to the characteristic length over which the quantities considered vary in order to be able to describe their local variations related to the characterization of key processes affecting the porous medium. Thus, porous media can be described through different geometrical parameters whose values can vary depending on if one considers unconsolidated medium (e.g., pack of glass beads) or consolidated rock samples.

The aim of this chapter is to summarize the different effective geometrical parameters of the porous medium REV.

1.3.2 Porosity

Porosity ϕ (-) is defined as the ratio of the pore volume V_{pores} (m^3) over the total rock volume V_{tot} (m^3):

$$\phi = \frac{V_{pores}}{V_{tot}}. \tag{1.19}$$

Porosity is thus defined between 0 and 1, but is often expressed in percents.

However, due to the pore space distribution, some pores may be isolated from the rest of the pore network due to the absence of connections or due to nano-pores that are too small to let the water flows. Therefore, porosity measurements techniques provide an estimation of the porosity. For unconsolidated samples, this approximation can be really close to the reality, but for other types of rocks (e.g., clays, recrystallization), the difference can be more important.

1.3.3 Tortuosity

Tortuosity is one of the parameters that accounts for the complexity of the paths through the pore space. Tortuosity can be defined through different techniques and thus has different expressions (see Ghanbarian et al. 2013, for a review).

Among the tortuosity definitions, the geometrical tortuosity $\tau_g = \frac{l}{l_0}$, corresponds to the ratio between the length of the tortuous flow path l (m) and the length in a straight line l_0 (m) in the direction of flow (see Figure 1.3a, Adler 1992).

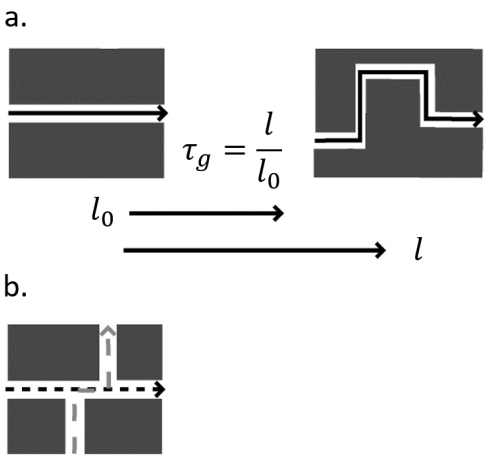

Figure 1.3: Schematic illustrations from Adler (1992) of (a) the geometrical tortuosity (b) the anisotropy effect on the tortuosity value.

There is also the electrical tortuosity τ_e (-) defined by Pirson (1983) as (e.g., Ziarani and Aguilera 2012)

$$\tau_e^2 = \phi F, \tag{1.20}$$

where F (-) is the formation factor, a property of the porous medium computed from geo-electrical measurement (see Section 2.2.5.2). However, this definition of the tortuosity leads for some complex microstructures to very high values of τ_e that are not comparable with the geometrical tortuosity (e.g., Niu and Zhang 2019).

Contrary to porosity which depends of volumes, tortuosity relies on flow path. Thus, in case of an anisotropic sample, which is not that rare due to geologic processes, tortuosity will also be anisotropic (see Figure 1.3b).

Model	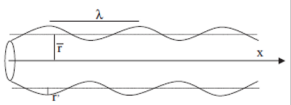	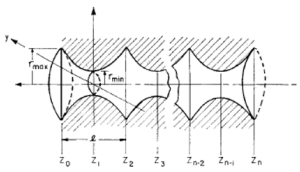	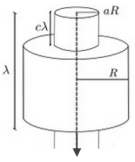
Reference	Guarracino et al., 2014	Petersen, 1958	Soldi et al., 2020
Model geometry and constriction factor a (-)	$a = \frac{r'}{2\bar{r}}$ $a \in [0\,;0.5[$	$a = \frac{r_{max}}{r_{min}}$ $a > 1$	$c \in [0;1]$ $a \in [0;1]$
Constrictivity f (-)	$f \propto \frac{(1-4a^2)^{3/2}}{1+2a^2}$	$f = \frac{\sin\left(0.3\pi a^2 + 0.7\pi a + \frac{\pi}{2}\right)+1}{2}$	$f = a^2c + 1 - c$

Figure 1.4: Description of the geometry, the formation factor, and the constrictivity for the models from Guarracino et al. (2014), Petersen (1958), and Soldi et al. (2020).

1.3.4 Constrictivity

Another parameter describing the porous medium microstructure is the constrictivity. This parameter is related to the size of the pore throats connecting the pore bodies and thus characterizes what is called the bottleneck effect (Holzer et al. 2013). The constrictivity can hence be introduced as an additional parameter f (-) which is geometrically characterized from the constriction factor, a parameter directly linked to the ratio of the maximal over the minimal pore aperture for a conceptualized porous medium geometry (e.g., Petersen 1958; Holzer et al. 2013). For example, this constriction factor has been defined for cylindrical segments (e.g., Soldi et al. 2020), sinusoidal segments (e.g., Currie 1960; Guarracino et al. 2014) or hyperbolas of revolution (e.g., Petersen 1958; Holzer et al. 2013). The model geometries, constriction factors, and constrictivities of these models are summarized in Figure 1.4.

Thus, based on geometrical description of the porous medium, van Brakel and Heertjes (1974) proposed the following expression for the formation factor

$$F = \frac{\tau_g^2}{\phi f}. \tag{1.21}$$

Given the definition of the electrical tortuosity τ_e from Equation (1.20), it appears that the use of the constrictivity term enable to use the geometrical tortuosity τ_g instead of τ_e, which combines the effects of tortuosity and constrictivity.

1.4 Flow and transport in porous medium

1.4.1 Permeability and Darcy's law

Permeability is the ability of the porous medium to let the fluid flow through it. Permeability is an intrinsic property of the porous medium defined at the macroscopic scale and is thus a constant of the REV. Even if the permeability is related to the porous medium microstructure, it corresponds more to a flow property.

Permeability k (m^2) of an incompressible Newtonian fluid can be defined as an effective parameter using

Darcy's law (1856)

$$Q = \frac{k}{\eta} S \frac{\Delta p}{L}, \tag{1.22}$$

where Q ($m^3\ s^{-1}$) is the flow rate, η (Pa s = kg $m^{-1}\ s^{-1}$) is the fluid dynamic viscosity (for water at 25 °C, $\eta_w = 8.9 \times 10^{-3}$ Pa s), S (m^2) is the section of the porous medium, Δp (Pa) is the pressure gradient, and L (m) is the length of the porous medium.

One can define Darcy's velocity U ($m\ s^{-1}$) as

$$U = \frac{Q}{S}. \tag{1.23}$$

Darcy's velocity is a fictive velocity since it proposes an average flow velocity of the entire porous medium section, including the solid structure of the porous matrix. Nevertheless, the true averaged fluid velocity can be deduced from Darcy's velocity as

$$u = \frac{U}{\phi}, \tag{1.24}$$

where u ($m\ s^{-1}$) is the averaged pore fluid velocity.

1.4.2 Number of Reynolds

When the fluid flows in the porous medium capillaries, depending on its inertial and viscous properties, it can be smooth and creates straight fluid laminations parallel to the pore walls or the flow can cause eddies and turbulence.

In order to characterize the type of flow, the dimensionless Reynolds number is used and defined as (e.g., Shashi Menon 2015)

$$Re = \frac{\rho L u}{\eta}, \tag{1.25}$$

where ρ (10^{-3} kg m^{-3}) is the fluid volumic mass (for water, ρ_w = kg m^{-3}). Laminar flow is defined for $Re < 2000$ and is thus interpreted as a viscous flow where the fluid viscosity plays a dominant role in the fluid flow. For very low Reynolds number, inertia effects are even negligible and the fluid flow corresponds to a viscous creeping motion.

1.4.3 Transport

1.4.3.1 Ionic diffusion

Diffusion is generally defined as the spontaneous spreading of heat, matter, or momentum from higher to lower concentration (e.g., Marion 2008). For the study of calcite dissolution and precipitation processes, we focus on the solute concentration distributions in the porous medium and thus on ionic diffusion.

Ionic diffusion only occurs in case of concentration variations in the medium. Thus, the flux of transported solute concentration J_C (mol $m^{-2}\ s^{-1}$) is expressed as the product of the solute concentration gradient with a physical property known as the diffusion coefficient D ($m^2\ s^{-1}$). In a 1D problem this gives

$$J_C = -D \frac{\partial C}{\partial x}. \tag{1.26}$$

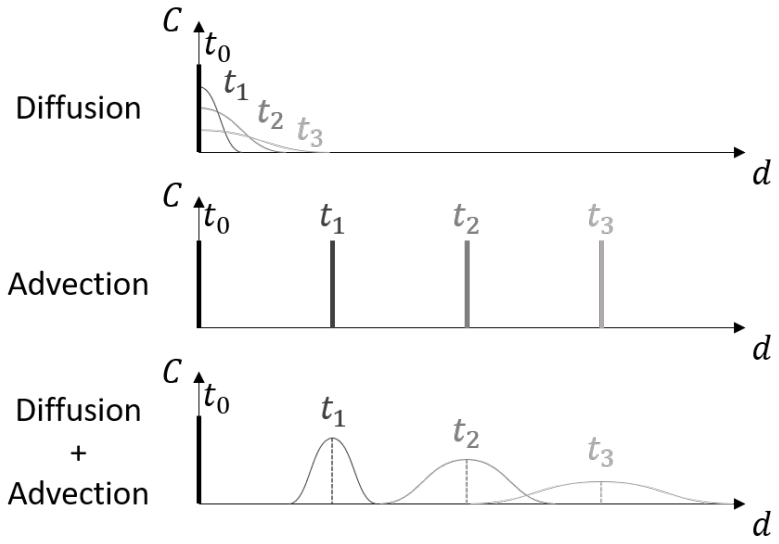

Figure 1.5: Illustrations of diffusion, advection, and advection-diffusion on the transport of solute concentration.

This expression of the diffusive flux leads to the Fick's law (1855), describing the time evolution of solute concentration in case of transport by diffusion only. In 1D, it is defined as

$$\begin{aligned} \frac{\partial C}{\partial t} &= -\frac{\partial J_C}{\partial x} \\ &= D\frac{\partial^2 C}{\partial x^2}. \end{aligned} \tag{1.27}$$

The time evolution of solute concentration is illustrated in Figure 1.5. Diffusion is microscopically described by the small displacement of molecules from their position. This microscopic process is known as the Brownian motion and is relatively slow.

1.4.3.2 Advection

Advection is defined as the transport of a conserved scalar quantity in a vector field (e.g., Marion 2008; Fitts 2013). In the scope of this thesis, it corresponds to the transport of the solute concentration by pore water flow. For steady conditions of a 1D flow, this transport corresponds to a simple translation of the solute concentration through the pore space (see Figure 1.5). Thus, advection follows

$$\frac{\partial C}{\partial t} = -u\frac{\partial C}{\partial x}. \tag{1.28}$$

However, advection never exists alone. It is always associated to molecular diffusion in the case of laminar flow. Thus, the transport of solution concentration in porous medium is of the advection-diffusion type and leads to the spreading of the solution concentration (see Figure 1.5).

1.4.3.3 Péclet number

In case of advection-diffusion transport, the two modes of transport compete. In order to express the relative importance of one in relation to the other, the dimensionless Péclet number is defined as

$$Pe = \frac{t_{\text{diffusion}}}{t_{\text{advection}}} = \frac{L/U}{L^2/D} = \frac{UL}{D}. \tag{1.29}$$

When the Péclet number tends toward zero, this means that transport is in majority driven by diffusion. On the contrary, when the Péclet number tends toward the infinite, diffusion is negligible compared to advection. For a Péclet number close to one, both advection and diffusion compete (see Figure 1.5).

1.4.4 Reactive transport

Reactive transport corresponds to the joint study of transport and chemical reactivity with the porous matrix. This approach is relevant for the study of dissolution and precipitation. For example, depending on the combination of the flow regime and the dissolution rate, preferential paths can form in the porous medium (e.g., Noiriel and Deng 2018). On the contrary, calcite precipitation can locally reduce the permeability and drastically affect the hydrodynamic properties of the porous medium.

The purpose of this section is to briefly present the issues of reactive transport and the parameters used to determine how the geometric and hydrodynamic properties of the porous medium are affected by solute transport, resulting in calcite dissolution and precipitation processes.

1.4.4.1 Reactive transport equation

Reactive transport description combines the transport of the reactive species through the porous medium and the chemical reaction with the porous matrix. Thus, for one considered element of the reactive system, its reactive transport study is based on the temporal and spatial evolution of its concentration, which is conservative. In case of a system with advection, diffusion, and chemical reaction, the 1D mass conservation equation is thus

$$\frac{\partial C}{\partial t} = D\frac{\partial^2 C}{\partial x^2} - u\frac{\partial C}{\partial x} - \frac{\partial q}{\partial t}, \tag{1.30}$$

where q (mol kg_w^{-1}, i.e., in mole per kilogram of water) is the concentration of the solid phase of the considered solute (i.e., calcium or carbonate here).

1.4.4.2 Reactive specific surface area

When a solute flows through the porous medium and reacts with the porous matrix, one can define the reactive specific surface area as the ratio of the reactive surface that will meet the reacting pore fluid over the total bulk volume. Thus, the reactive specific surface s_r is expressed in m^{-1}. This parameter must be distinguished from the specific surface area, which is a geometrical parameter corresponding to the total area of the porous matrix in contact with pore water over the bulk volume.

The reactive specific surface area is a parameter difficult to quantify. It is however an important input of reactive transport numerical simulations (e.g., Noiriel et al. 2009). Indeed, a small reactive specific surface area

indicates that only a very local part of the porous medium is affected by the reacting solute. On the contrary, if the reactive specific surface area has a value close to the specific surface area, this means that almost all of the porous matrix is affected by the chemical processes.

1.4.4.3 Damköhler number

For the study of transport coupled with chemistry, a dimensionless parameter called the Damköhler number Da is used and represents the ratio of the reaction speed with which a reactant specie is consumed over the flux of this reactant (e.g., Palciaukas and Domenico 1976). Thus, the Damköhler number determines whether the reaction will be controlled by mass transfer (high Da) or the surface reaction (low Da). In case of an advection-diffusion transport, the Damköhler number is expressed depending on the dominant mode of transport. Thus, if advection dominates, the Damköhler number follows

$$Da = \frac{\vartheta L}{u}, \tag{1.31}$$

where ϑ (s^{-1}) is the reaction rate (i.e., of calcite dissolution or precipitation) and d (m) is the pore diameter. In case of dominant diffusion, the Damköhler number is defined as

$$Da = \frac{\vartheta L^2}{D}. \tag{1.32}$$

It appears that different system behaviors can be described from the combination of Péclet and Damköhler numbers (e.g., Adler and Thovert 1998).

1.5 Importance of petrophysical relations

Petrophysics is a discipline of rock studies which tends to link geophysical properties to parameters of interest based on theoretical developments. Since geophysics only provide indirect measurements of the properties of interest for hydrological and geochemical studies. This makes clear the need for petrophysical models (e.g., Guéguen and Palciauskas 1994; Rubin and Hubbard 2006).

First phenomenological relationships were determined from measured data (e.g., Archie 1942; Pelton et al. 1978; Ghanbarian et al. 2013), but their disadvantage is that it is difficult to relate them to physical parameters of the porous medium since these empirical relationships are based on empirical coefficients that are not defined in relation to the microstructure of the medium. Therefore, mechanistic approaches are proposed to give physical-based relationships. These models are based on the development of equations linking different properties of the medium in order to describe its characteristics. The mechanistic approach is therefore based on a simplified representation of the porous medium. It thus appears that the accuracy of a mechanistic model is based on the acuity of the pore geometry defined in the model. Moreover, most mechanistic models are only relevant in relation to certain types of media. For example, specific models are developed for the study of granular or fractured media.

In the case of geoelectric methods, mechanistic models aim to relate measured electrical properties, such as electrical conductivity (EC) and electrical potential differences (see Chapter 2), to the parameters of the porous

medium described in Section 1.3. Chapters 3 and 6 of this thesis intend to present some advances in this domain related to calcite dissolution and precipitation processes and to experiments conducted for this thesis work.

Chapter 3 focuses on the theoretical development of a new model describing the electrical conductivity of a water-saturated fractal porous medium through the two microstructural parameters, tortuosity and constrictivity. Thus, the electrical conductivity is related to parameters of interest that are porosity and permeability. This model is applied to various datasets from the literature comprising unconsolidated samples, consolidated sedimentary rock samples, and simulation results of dissolution and precipitation from digital images.

Chapter 6 presents a new theoretical framework to interpret self-potential measurements of calcite dissolution and precipitation obtained from an experiment conducted during this thesis. This framework associates reactive-transport simulation parametrized from the experiment chemical analyses, to a new petrophysical development of electro-diffusive potential relating ionic concentration distributions to self-potential signals for a multi-species context.

CHAPTER

2 Geo-electrical methods applied to hydrogeophysics: an overview

2.1 Geo-electrical prospection for hydrogeophysical study

Geophysical methods measure space and time variations of physical properties in the ground. The four main properties measured with geophysical methods are the density, elastic waves propagation velocity, magnetic susceptibility, and electrical conductivity (e.g., Hubbard and Linde 2011). Each of these properties is associated to a group of methods which are: seismic, gravimetry, magnetic, and electric. Given the strong interaction between electric and magnetic fields (Maxwell 1861), another family of geophysical methods has been introduced: the electromagnetic methods.

Using geophysical techniques, geophysicists intend to map contrasts and anomalies (e.g., Reynolds 2011; Lowrie and Fichtner 2020). Then, they attempt to characterize the responsible structures and processes through hypotheses and modeling. This task can be really challenging since the solution is non-unique. Indeed, different models can reproduce the same dataset (e.g., Oldenburg and Li 2005; Tarantola 2005; Menke 2012). Fortunately, ambiguities can be overcome combining different complementary methods and using geological or hydrological knowledge.

All geophysical methods are not sensitive to water presence, and not all the techniques are suitable to define the hydrogeological parameters related to groundwater resources. Hence, new techniques have been developed to fit with this problematic. Thus, a new domain of geophysical investigation for hydrological studies has emerged and is called hydrogeophysics (e.g., Rubin and Hubbard 2006; Vereecken et al. 2006; Binley et al. 2015).

Electric and electromagnetic methods are the most commonly used techniques for hydrogeophysical studies, since the electrical conductivity is directly influenced by rock nature and water content and chemistry (e.g., Revil et al. 2012; Glover 2015).

2.2 Spectral induced polarization (SIP)

The purpose of this section is to summarize the SIP method. First, a brief historical background based on Collett (1990) and Kemna et al. (2012) is drawn. Then the subsequent parts present the physical fundamental equations governing SIP, how SIP is implemented, and the mechanical processes generating SIP response.

2.2.1 Brief history of SIP

SIP history begins with the discovery of electrical relaxation after interrupting current injection in the early 1910's by Conrad Shlumberger. He described these phenomena of slow electrical potential decrease in a chapter of Schlumberger (1920a), where he associated this relaxation to a discharge following soil electrical polarization. He observed that this polarization was caused by direct current injection in the presence of metallic mass or conductive ore having a distinct behavior from the surrounding rocks. Schlumberger has, thus, developed a new prospection method of metallic conductors detection called induced polarization (IP) and since, it has been tested for oil exploration, associated with disseminated mineralization, but the recorded signals lacked of accuracy due to the technology equipment of this time.

During the late 1950's, the use of IP technique started to evolve. Vaquier et al. (1957) applied IP method for groundwater investigation and several laboratory research have been conducted by Madden and Marshall. They also established the theoretical basis of nonmetallic induced polarization (Marshall and Madden 1959). However, it is only since the 1960's that IP research started to focus on spectral investigations (i.e., over a frequency range) and leading to a new technique: the spectral induced polarization (SIP). To be able to measure over large frequency range, there was an improvement of the of wide-band frequency devices during the 1970's and the 1980's, but SIP remained focused on oil exploration during this period.

The 1990's have seen the beginning of environmental applications of SIP and the apparition of new high-precision instruments. Vanhala (1997) conducted laboratory study on polluted samples and mapped contamination, showing that SIP method is sensitive to organic contaminants influencing grain surface properties.

From long ago IP was known to be dependent of pore-space geometry (e.g., Marshall and Madden 1959). Thus, SIP measurement contains information about rock permeability and fluid properties. However, it is only more recently, that laboratory studies have been conducted to link SIP data to the hydraulic conductivity at various degrees of water saturation (e.g., Börner and Schön 1991; Ulrich and Slater 2004; Binley and Kemna 2005b). More generally, SIP is one of the hydrogeophysical methods increasingly used for environmental studies and the investigation of hydrological (e.g., Kemna et al. 2012; Revil et al. 2012), geochemical (e.g., Zhang et al. 2012), and biogeophysical (see Kessouri et al. 2019, for a review) of the critical zone. These new study issues therefore see the emergence of studies on sedimentary rocks such as carbonates (e.g., Hupfer et al. 2017; Norbisrath et al. 2017; Johansson et al. 2020) and their associated chemical processes.

2.2.2 Summary of studies on calcite dissolution and precipitation SIP signature

SIP signature of calcite precipitation was first studied by Wu et al. (2010). They showed that SIP method is sensitive to calcite precipitation induced by the mixing of calcium dichloride $CaCl_2$ and sodium carbonate Na_2CO_3 in a matrix of glass beads. However, Wu et al. (2010) only used an empirical relation to interpret SIP time variations. Thus, they could not give a mechanistic description of their SIP data (Wong 1979), while the results do not present an univocal response over the twelve days of experiment. Indeed, during the first nine days, Wu et al. (2010) measured a constant increase of SIP signal during the calcite precipitation experiment. Then, while the experimental conditions remained unchanged, the signal decreased day by day until the end

of the experiment. Based on scanning electron microscopy (SEM) images of slices of the sample at the end of the experiment, the authors concluded that the size of the precipitated calcite grains must play a key role in the amplitude of the measured SIP signal.

Leroy et al. (2017) proposed a physical-based model to interpret the SIP results of Wu et al. (2010). Their model relates the SIP response with particle size distribution of the calcite precipitated grains. For simplicity, grains are assumed to be spheres. The authors explain that during the first part of the experiment conducted by Wu et al. (2010), the observed polarization increase can be associated to the nucleation of new small particles of calcite. The grains nucleate as suspended solids and individually deposit at the surface of glass beads, thus contributing to SIP signal by adding new polarizable surfaces. Then, after a few days of experiment, Leroy et al. (2017) explain the SIP decrease by the formation of aggregates formed by the growth and the coalescence of precipitated calcite grains that start to coat the glass beads and to clog the pore space. In these conditions, the surface area of calcite grains decreases and thus, the SIP response, which is only generated by the few amount of new nucleated particules. This model proposes an interesting explanation but is based on many simplifications, such as the sphericity of grains or a homogeneous solute concentration inside the cell. This model must therefore be considered with a lot of caution, as it provides an interpretation subject to discussion.

Nevertheless, calcite precipitation influence on SIP response remains difficult to characterize. Indeed, since the study of Wu et al. (2010), other experiments of SIP measurements during calcite precipitation have been conducted. Izumoto et al. (2020a) induced calcite precipitation in a sand matrix by mixing $CaCl_2$ with Na_2CO_3 and observed an SIP response sensitive to the concentration of the dissolved reactive species, rather than on the amount or the shape of precipitated calcite as conceptualized in the model of Leroy et al. (2017). Zhang et al. (2012) conducted an experiment of urea hydrolysis (by injecting urea in a water saturated sample, producing hydrogencarbonate HCO_3^-, hydroxyde HO^- and ammonium NH_4^+ ions) followed by calcite precipitation (by injecting dissolved calcium reacting with the hydrogencarbonate resulting from urea hydrolysis) in a silica gel column. They observed SIP variations, but they found that SIP was much more sensitive to pH variations (due to HO^- ions producted by urea hydrolysis) than by calcite precipitation. In light of these experimental results of Zhang et al. (2012), the results presented in Saneiyan et al. (2019) and in Saneiyan et al. (2021) must be carefully considered. In these field and laboratory studies, calcite precipitation is induced from ureolytic bacteria activity. Therefore, although pH changes are not mentioned in these studies, the bacterial activity stimulated to precipitate calcite involves the hydrolysis of urea, impacting the SIP measurement as shown by Zhang et al. (2012). Moreover, Saneiyan et al. (2021) unsuccessfully tried to use the model developed by Leroy et al. (2017). Thus, the observed SIP variations should not be attributed solely to calcite precipitation.

To the best of our knowledge, only Halisch et al. (2018) studied carbonate dissolution with SIP method, but in contrast to studies on precipitation, they did not observe a clear signature. Indeed, Halisch et al. (2018) conducted SIP measurements on a carbonate sample saturated with brine after several steps of dissolution with an acid activated when heating the sample (Kjoller et al. 2016). They measured a specific response but it remained constant with time, while the petrophysical measurements showed clear patterns in favor of strong dissolution. A first hypothesis to explain this absence of variations could be that, contrary to calcite precipitation, calcite dissolution does not generate variations on the SIP signal. A second hypothesis that we propose to examine in

this study, is that the experimental protocol proposed by Halisch et al. (2018) does not allow the observation of SIP variations, because they did not perform the measurements when the sample is undergoing the chemical imbalance.

2.2.3 Constitutive equations

In the following, fundamental constitutive equations are summarized to establish the basics for the induced polarization definition summarized in this work.

For a medium under electrical voltage, the Ampere's law defines the total electrical current density J_{tot} (A m^{-2}) as follows

$$J_{tot} = J_c + J_d, \tag{2.1}$$

where J_c (A m^{-2}) is the conduction current density and J_d (A.m^{-2}) is the dielectric displacement current density.

Conduction is carried through the migration of electrical free charges and is, thus, controlled by the Ohm's law with

$$J_c = \sigma E, \tag{2.2}$$

where σ (S m^{-1}) and E (V m^{-1}) are the conductivity and the electric field, respectively. For sedimentary rocks, the free charges are the dissolved ionic species present in the electrolyte filling the pores.

Dielectric displacement current is related to the separation of bounded charges, creating electric dipoles as in a capacitor. The dielectric displacement current density is defined as the time derivative of the dielectric displacement field $\mathscr{D}$ (C m^{-2}),

$$J_d = \frac{\partial \mathscr{D}}{\partial t}. \tag{2.3}$$

In frequency domain, this gives

$$J_d = i\omega\mathscr{D}, \tag{2.4}$$

where i is the imaginary unit ($i^2 = -1$) and ω (rad s^{-1}) is the angular frequency defined by $\omega = 2\pi$f, with f (Hz) the frequency. The dielectrical displacement field is related to the electric field through the dielectric permittivity ϵ (F m^{-1}) as follows

$$\mathscr{D} = \epsilon E. \tag{2.5}$$

Combining Equations (2.2), (2.4), and (2.5) in Equation (2.1) yields to

$$J_{tot} = (\sigma + i\omega\epsilon)E. \tag{2.6}$$

Here, σ and ϵ are complex frequency-dependent values and Equation (2.6) can be rewritten as

$$J_{tot} = \sigma^* E, \tag{2.7}$$

where σ^* is the electrical complex conductivity, describing conduction and polarization mechanisms. This last expression has the advantage to express $(\sigma + i\omega\epsilon)$ into a generalized complex term and not to choose between

the ambiguous conventions attributing real and imaginary parts to conductivity or permittivity. Furthermore, below 10 kHz, the delay in response to the electrical excitation is attributed to conductive rather than dielectric phenomena. This comes from the work of Pelton et al. (1983) who relate the movement amplitude of charges carriers to migration of *free* charges rather than the reorientation of *bound* charges.

2.2.4 Principles of SIP measurements

SIP method is based on the measurement of the soil conductivity by injecting an electric current and measuring the resulting electrical potential. Its implementation requires four electrodes also called a quadripole (e.g., Binley and Kemna 2005b). The first pair of electrodes generates the electric field in the medium, while the electrical voltage is measured with the second pair. For SIP measurements, the injected electrical current $I(\omega)$ (A) is alternating in time (known as alternating current AC), following sinusoidal variations at various frequencies and is thus defined as

$$I = |I|e^{i(\omega t - \varphi_I)}, \tag{2.8}$$

where $|I|$ and φ_I are the electric current amplitude (A), and the electric current phase (rad), respectively. Consequently, the imposed voltage V (V) is also given by

$$V = |V|e^{i(\omega t - \varphi_V)}, \tag{2.9}$$

where $|V|$, and φ_V are the voltage amplitude (V), and the voltage phase (rad), respectively. Then, the generalized Ohm's law gives the following definition of the measured impedance

$$Z = \frac{V}{I} = \frac{|V|}{|I|}e^{i(\varphi_V - \varphi_I)} = |Z|e^{i\varphi}. \tag{2.10}$$

Impedance Z (Ω) is thus a complex value invariable with time.

Geophysicists prefer to use the complex conductivity σ^* rather than the impedance, since for a homogeneous water-saturated sample, it does not depend of the investigated volume. Impedance and complex conductivity are related by a geometrical factor k_g (m), which value is determined by the acquisition geometry. The complex conductivity is hence defined by

$$\sigma^* = \frac{1}{k_g Z} = \frac{1}{k_g|Z|}e^{-i\varphi} = |\sigma^*|e^{-i\varphi}. \tag{2.11}$$

The complex conductivity presents an amplitude $|\sigma^*|$ and phase shift $-\varphi$ which are frequency dependent. The SIP method covers a range of frequencies to measure these two spectra. The shape and amplitude of these spectra are controlled by different mechanisms presented in the next section. For a four electrodes measurement system, complex conductivity is typically measured from 10^{-3} Hz to 10^4 Hz.

2.2.5 Petrophysical understanding of the complex electrical conductivity

The electrical conductivity of a material is defined as its ability to conduct electric current. Thus, high conductivity indicates that the medium readily allows electric current. Electrical conductivity SI unit is S m^{-1}, but it is often expressed in µS cm^{-1}(1 µS cm^{-1} = 10^{-4} S m^{-1}). The electrical conductivity of the porous medium is related to several components that originate from the superposition of different contributions related to two mechanisms corresponding to conduction and polarization. This section intends to summarize these contributions in the context of studying carbonate rocks using the SIP method.

2.2.5.1 Pore water electrical conductivity

Metal bodies are known to conduct electric current through the displacement of electrons. However, electrolytic conduction is caused by the electrolytic dissociation of anions and cations from dissolved salts composing the electrolyte (Arrhenius 1903). Thus, the pore water electrical conductivity σ_w (S m^{-1}) depends on the type of ions in solution and their concentrations through the molar conductivity Λ_m (S m^2 mol^{-1}). Λ_m is defined as the conductivity of an aqueous solution of one molar solute concentration ($C = 10^{-3}$ mol m^{-3}), measured in a conductimetry cell with electrodes spaced 1 cm apart. Thus, the molar conductivity is described as

$$\Lambda_m = \frac{\sigma_w}{C}. \tag{2.12}$$

For an electrolyte composed of multiple solutes, the molar conductivity can be decomposed in the sum of ionic molar conductivity Λ_{X_i}. Hence, the pore water conductivity can be written as

$$\sigma_w = \sum_{X_i} \Lambda_{X_i} C_{X_i} \tag{2.13}$$

For a porous medium subjected to an electric field, charged particles of the electrolyte (i.e., cations and anions) will move through the pores in response. The ability of the particle to reach certain velocity v (m s^{-1}) is called the mobility β (m^2 s^{-1} V^{-1}): $v = \beta E$. The mobility depends on the electrical charge and on the particle Stokes radius (e.g., Atkins and de Paula 2006). Each ionic specie has hence, a specific mobility value β_{X_i}, which is proportional to the molar conductivity

$$\Lambda_{X_i} = z_{X_i} \beta_{X_i} \mathrm{f}, \tag{2.14}$$

where z_{X_i} (-) is the valence of ion X_i and f is the Faraday constant (f $\approx 9.649 \times 10^4$ C mol^{-1}). Thus, the pore water electrical conductivity becomes

$$\sigma_w = \mathrm{f} \sum_{X_i} z_{X_i} \beta_{X_i} C_{X_i}. \tag{2.15}$$

Table 2.1 summarizes the values of molar conductivity and mobility of ionic species considered in this thesis.

One can note that protons H^+ and hydroxyde anion HO^- have mobilities of one order higher than the rest of the considered ions. Thus, their concentrations and their variations associated to acid-base reactions must have a major impact on the electrical conductivity.

2.2.5.2 Electrical conductivity

The bulk electrical conductivity of a non-metallic porous medium comes from the contribution of the pore water electrolytic conduction. In absence of surface conductivity, the porous medium electrical conductivity σ (S.m^{-1}) has thus an amplitude proportional to the pore water electrical conductivity σ_w. The ratio of these two terms is known as the formation factor $F = \sigma_w / \sigma$ (-). This term is a useful parameter which is widely used to link the electrical conductivity to other porous medium properties, when neglecting the surface conductivity. The most known empirical relationship comes from Archie (1942) and relates the formation factor to porosity ϕ (-) as

$$F = \phi^{-m}, \tag{2.16}$$

Table 2.1: Values of molar conductivity and mobility of the ionic species considered in this thesis. These values are taken from the literature at 25 °C (Robinson and Chia 1952; Gregory et al. 1991; Parkhurst and Appelo 2013).

Ionic specie	Molar conductivity Λ_{X_i} (S cm^2 mol^{-1})	Mobility β_{X_i} (10^{-3} m^2 s^{-1} V^{-1})
Ca^{2+}	119.1	0.62
H^+	349.6	3.62
Na^+	50.0	0.52
$CaCl^+$	50.9	0.53
$CaHCO_3^+$	19.0	0.20
$CaOH^+$	39.1	0.41
Cl^-	76.2	0.79
HCO_3^-	44.3	0.46
CO_3^{2-}	143.5	0.74
$NaCO_3^-$	22.0	0.23
HO^-	197.9	2.05

where m (-) is an empirical constant usually referred as the cementation exponent. The cementation exponent is defined between 1.3 and 4.4 for unconsolidated samples and for most of well-connected sedimentary rocks (e.g., Friedman 2005). It does not correspond to an exact geometrical parameter of the pore space, but its value is implicitly controlled by such microstructural features known as the tortuosity and the constrictivity. Tortuosity is already a well-known parameter describing how pores do not present straight paths through the medium. There are many tortuosity-based models proposed in the literature to interpret the electrical conductivity (e.g., Pfannkuch 1972; Revil et al. 1998; Niu and Zhang 2018; Thanh et al. 2019). On the contrary, even if constrictivity is a known parameter associated to the so-called bottleneck effect (e.g., Petersen 1958) that takes into account the pore size variation (i.e., the coexistence of pore bodies and pore throats), there is no model of the electrical conductivity based on this parameter description. Only Kennedy and Herrick (2012) have conceptualized the pore space description using a geometrical factor G (-) gathering both tortuosity and constrictivity effects and expressed as

$$\sigma = G\sigma_w\phi. \tag{2.17}$$

However, this geometrical factor is not based on a real description of the pore space. Thus, the paper presented in chapter 3 is about the development of a new model of the electrical conductivity based on a porous medium geometry considering tortuosity and constrictivity parameters in its microstructural description.

2.2.5.3 Surface conductivity

Most minerals have a surface charge due to substitution and defaults of crystallization. When grain surfaces are in contact with the electrolyte, in absence of electric field, chemical and electrostatic forces cause the agglom-

eration around the grains of ions of opposite sign of the grain surface charge to maintain the electroneutrality. This area is the so-called electrical double layer (EDL), since it is divided into two parts according to the concentration of charge carriers (e.g., Hunter 1981; Chelidze and Gueguen 1999; Leroy and Revil 2004). The first one is called the Stern layer and corresponds to a compact layer surrounding the grain and characterized by a high concentration of adsorbed ions. The second layer is called the diffuse layer. It is characterized by the presence of mobile charges in a decreasing exponential concentration laying between the concentrations of the Stern layer and the free electrolyte.

The previous section established that in our context, the porous medium electrical conductivity is controlled by ions migration in the pore volume. As the ionic concentrations are higher in the EDL, there is also a contribution to the electrical conductivity coming from the surface of the grains. This contribution is especially measurable for low ionic concentrations (e.g., Bolève et al. 2007; Cherubini et al. 2019; Soueid Ahmed et al. 2020).

The surface conductivity can be considered as a parallel conductivity σ_s (S m^{-1}) with an adjustable value (e.g., Waxman and Smits 1968; Weller et al. 2013; Revil et al. 2014):

$$\sigma = \frac{1}{F}\sigma_w + \sigma_s. \tag{2.18}$$

This expression is only valid for low surface conductivity value. This hypothesis is often verified in the case of the study of clay-poor carbonate rocks (e.g., Soueid Ahmed et al. 2020). Moreover, for measurement of water-saturated carbonate rocks at standard values of σ_w (e.g., Liñán Baena et al. 2009; Meyerhoff et al. 2014; Jeannin et al. 2016), the surface conductivity can be neglected (e.g., Cherubini et al. 2019).

In equation (2.18), surface conductivity is considered as a simple term that can be adjusted to the data. However, for the study of rocks, where this parameter plays a role as important as the pore water conductivity on the sample conductivity measurement, this term is expressed through different models and is thus related to parameters characterizing the behavior of ions close to the surface of the mineral. Ruffet et al. (1995) and more recently Glover (2015) propose a review of these models. It can be noted that the main parameters of these models (e.g., Bussian 1983; Revil and Glover 1997; Revil 2013) are the pore water electrical conductivity, the formation factor, the ion mobility at the surface, the surface charge, the ratio of surface conductance over Johnson's length (e.g., Johnson et al. 1986; Johnson and Sen 1988), the fraction of counter-ions present at the surface (e.g., Revil and Florsch 2010), and to the cation exchange capacity (e.g., Ketterings et al. 2007; Revil 2012b).

2.2.5.4 Interfacial conductivity controlled by the electrical double layer polarization

The previous paragraphs of this section relates the electrical conductivity to the conduction phenomena occurring in the electrolyte and at the surface of the minerals. However, when injecting a sinusoidal electrical current at various frequencies, other effects of relaxation occur. In light of the frequency range explored with the SIP method (1 mHz $< f <$ 10 kHz), higher frequencies mechanisms are not considered. Furthermore, as this thesis focuses on carbonate rocks, only their related effects are considered. The only origin of the interfacial

conductivity, hence, lays in the electrical double layer formed at the interface between the electrolyte and the surface of the particles.

Electrical double layer polarization In absence of source of current, the EDL structure is maintained by electrostatic forces. However, when subjected to an electric field, ions of the double layer move tangentially to the surface grain. This movement polarizes the double layer since anions and cations of the double layer migrate in opposite directions but stay close to the grain surface (e.g., Leroy and Revil 2009; Revil et al. 2012). When the injection current is interrupted, ions of the EDL return to their initial configuration due to retro-diffusion forces. Both Stern and diffuse layers contribute to this polarization, but since the Stern layer is more concentrated in ions, its contribution is considered to be the most important (e.g., Lesmes and Morgan 2001; Bücker et al. 2019).

It appears that the displacement of the charges on the surface of the grains is dependent on the frequency of the injected electric current (e.g., Lesmes and Frye 2001). The SIP method thus allows to relate the relaxation time as a function of the characteristic lengths of the medium (i.e., grain size) and the diffusion coefficient of the charges in the electric double layer and especially in the Stern layer (e.g., Schwarz 1962; Revil and Florsch 2010).

Membrane polarization Depending on compaction, pore throats can also act as charges filters because electrical double layers of close grains overlap and reduce counter-ions mobility (e.g., Bucker and Hördt 2013; Okay et al. 2014; Bücker et al. 2019). Under the effect of an electric current, concentration gradients are thus generated on both sides of these selective zones, since counter-ions cannot cross the pore throat as free charges. This mechanism is usually attributed to the presence of clays, but Titov et al. (2002) demonstrated that it could be observed in other conditions.

2.2.6 Writing the complex electrical conductivity

In order to separate the complex conductivity contributions from the pore space filled with the electrolyte and from the electrical double layer, the complex conductivity can be written based on a parallel addition of two contribution terms (e.,g., Vinegar and Waxman 1984; Weller et al. 2013)

$$\sigma^* = \frac{\sigma_w}{F} + \sigma^*_{surf}. \tag{2.19}$$

Note that this above expression is only valid at low frequencies (e.g., less than 100 Hz) and that at this frequency range, covered with SIP method, $\frac{\sigma_w}{F}$ is a real value, while the star on σ^*_{surf} indicates that it is complex. As for all complex values, the complex conductivity σ^* can then be described by its real and imaginary parts, $\sigma^{'}$ and $\sigma^{''}$, respectively. Consequently, they can be defined as

$$\begin{aligned} \sigma^{'} &= \frac{\sigma_w}{F} + \sigma^{'}_{surf} \\ \sigma^{''} &= \sigma^{''}_{surf} \end{aligned}$$

One can note that this writing is a bit artificial but has the advantage to attribute the polarization to the electrical double layer behavior. Thus, the real and imaginary components of the complex conductivity represent the

ohmic conduction and the polarization mechanisms, respectively. These properties are directly determined from SIP measurement. Indeed, the amplitude $|\sigma|$ and the phase shift φ are related to $\sigma^{'}$ and $\sigma^{''}$ as follows

$$|\sigma^*| = \sqrt{\sigma^{'2} + \sigma^{''2}}$$
$$\varphi = \arctan\left(\frac{\sigma^{''}}{\sigma^{'}}\right).$$

2.3 Self-potential (SP)

SP is a really old geophysical method based on the measurement of natural electrical voltage using a pair of electrodes. However, it is still rarely used due to the complexity of its interpretation, since many contributions can be source of signal. This section intends to introduce the constitutive equations of SP method, then to briefly summarize SP history through its different associated sources apart from electrothermic and sismoelectric couplings which are not source of strong electrical anomalies in the context of this thesis.The SP chronological developments described in the following sections are taken from Revil and Jardani (2013).

2.3.1 Constitutive equations of SP

Since SP method is a passive geophysical technique based on measuring the natural electric field. The measured current is generated by a physical coupling with other forces impacting the geological media. Thus, based on the developments of Sill (1983), the total electric current density J_{tot} (A m^2) follows

$$J_{tot} = -\sigma \nabla V + j_s, \tag{2.20}$$

where ∇V (V m^{-1}) is the gradient of the electric potential ($E = -\nabla V$) and j_s (A m^2) is the cross coupling current density also called the source current density. In the case of SP acquisition, no electrical source is imposed, then for an homogeneous medium, the total electric current density is divergenceless ($\nabla \cdot J_{tot} = 0$). This leads to (Sill 1983)

$$\nabla \cdot j_s = \nabla \cdot (\sigma \nabla V). \tag{2.21}$$

The main contributions to SP signal are related to electrokinetic (superscript EK) and electrochemical couplings (e.g., Linde et al. 2011; Revil and Jardani 2013). The electrochemical coupling can be related to two mechanisms: oxydation-reduction reactions (superscript $redox$) and ionic concentration gradients (superscript $diff$). Thus, the total source current density can be expressed as the sum of all of these contributions

$$j_s = j_s^{EK} + j_s^{diff} + j_s^{redox}. \tag{2.22}$$

Note that the measured SP signal can be the superposition of these contributions, therefore some models integrating these three sources of current are developed (e.g., Revil 1999; Revil and Linde 2006).

2.3.2 Self-potential discovery from redox potential

SP method was first used in the nineteenth century by Fox and Gilbert (1830) in ore exploration, where they observed 'electrical action' in the vicinity of sulfide veins. Other studies highlighted this phenomenon of SP anomaly around a conducting body as metallic or graphitic bodies (e.g., Schlumberger 1920b; Rust Jr 1938).

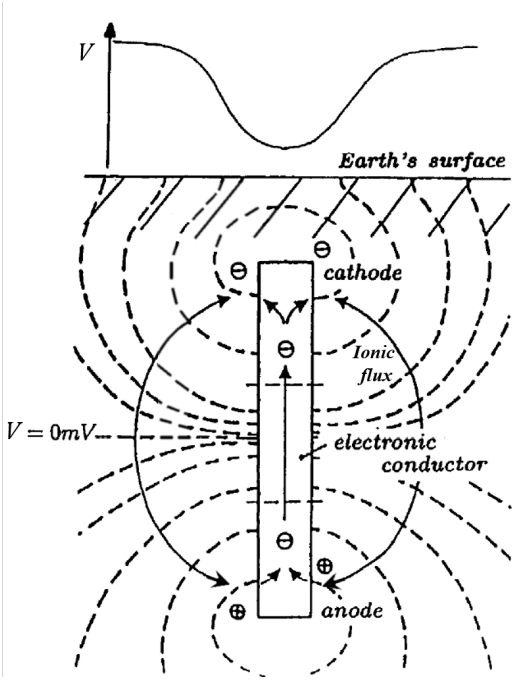

Figure 2.1: Schematic representation of the geo-battery model modified from Bigalke and Grabner (1997). The electronic conductor undergoes electron transfer generated by the oxydation and reduction reactions that take place at the anode (positive pole) and cathode (negative pole), respectively. The electrical circuit is completed by ion exchanges between these two poles (anions from the cathode exchanged against cations from the anode).

Sato and Mooney (1960) developed the geobattery theory, explaining that a conducting ore, relating areas in the soil with differing redox potentials, could be considered as an electrical battery. According to this theory, the oxydized zone corresponds to the most superficial area, richer in dioxygene, and for which reductive reactions occur in the vicinity of the conducting body (i.e., the conducting body yields electrons to the oxydized species in order to reduce them). In parrallel, the reductive zone is located beneath and its reduced species are oxydized by the conducting body (i.e., electrons of the reduced species are yielded to the conducting body). These oxydation-reduction reactions, occuring at the edges of the conducting body, generate transfers of electrons through the conducting body from the reductive to the oxydized zone. This electric circuit is closed by ionic exchanges between the reductive and the oxydized zones. Given the direction of flow of the electrons (i.e., from below to above), the potential measured at the surface thus presents a negative anomaly above the conductive body. This redox coupling can reach 400 mV (Sato and Mooney 1960), which makes it the most powerful source of SP signal.

The conducting body responsible for this source of current can also be a polluted plume (e.g., Arora et al. 2007; Linde and Revil 2007). In this case, the reductive zone is located upstream to the plume and the potential anomalies could be produced by bacterial activity and the presence of biofilms (e.g., Naudet et al. 2003, 2004; Naudet and Revil 2005; Revil et al. 2010).

2.3.3 Electrokinetic coupling

Since redox coupling was the biggest source of signal, SP early use was primarily focused on ore and hydrocarbon exploration. However, as early as 1859, the proportionality between SP amplitude and the flow rate was experimentally established by Quincke (1859). Furthermore, to remarkably explain his observation of the changing sign of the electrical potential with the change of flow direction, he intuited the EDL existence at grains surface, which was first theorized two decades later by von Helmholtz (1879).

Electrokinetism is defined as the generation of an electrical current by pore water fluxes in a porous medium composed of minerals electrically charged at their surface. The SP signal that originates from the electrokinetic coupling is called the streaming potential.

In absence of flow, the surface charge of the mineral is counterbalanced by an excess of ionic charges located in the EDL. Based on the EDL description, the counterions are distributed in the Stern Layer and in the diffuse layer. Ions from the Stern layer are sorbed onto the mineral surface. Thus, they cannot slip easily on the mineral surface. On the contrary, ions in the diffuse layer, as its name suggests, can diffuse more freely because they are less affected by the surface charges. Therefore, when the pore water flows, it drags a volumetric excess of charge $\hat{Q}_v$ (C m^{-3}) from the diffuse layer, creating an advective flow of electrical charges. This net electrical charge advection is therefore a net source of current density, which is thus the electrokinetic source current density and is defined by

$$j_s^{EK} = \hat{Q}_v u, \tag{2.23}$$

where u (m s^{-1}) is the water flux (e.g., Kormiltsev et al. 1998; Jougnot et al. 2020). Therefore, one can note that, in case of low surface charge or for a small water flow, the displaced excess of charge will be low, leading to a small streaming potential contribution.

Revil and Leroy (2004) developed a theoretical framework for the electrokinetic coupling among other sources. Hence, they relate the coupling coefficient C^{EK} (V Pa^{-1}) to this volumetric excess charge displacement writing

$$C^{EK} = -\frac{\hat{Q}_v k}{\eta_w \sigma}, \tag{2.24}$$

where η_w (Pa s) is the dynamic viscosity of water, σ (S m^{-1}) is the medium electrical conductivity, and k (m^2) is the medium permeability.

This expression shows that permeability or conductivity variations will directly affect the streaming potential coefficient. Thus, dissolution and precipitation processes affecting the porous matrix properties can influence the streaming potential amplitude.

Cherubini et al. (2019) conducted SP and conductivity measurements on limestone samples submitted to drainage with a non-wetting phase composed of CO_2. They found that calcite dissolution, induced by CO_2 injection, caused an increase of Ca^{2+} and HCO_3^- concentrations in the pore water during drainage, explaining the change of pore fluid conductivity, and thus the increase of the measured sample conductivity. Cherubini et al. (2019) also observed a decrease of the magnitude of the streaming potential coupling coefficient. In agreement with their development of the electrokinetic coupling coefficient based on the excess of surface

charge displacement in unsaturated conditions due to CO_2 injection, they established that the ionic strength increase due to calcite dissolution is responsible of the streaming potential coupling coefficient decrease. They conclude that the streaming potential coupling coefficient obtained from SP measurements can be a tool to estimate dissolution rates.

2.3.4 The electro-diffusive potential

An other contribution to the SP signal is related to concentration gradients of dissolved ionic species in the pore water. When there is a gradient of ionic concentrations, ions tend to migrate from the most concentrated area towards the diluted area. However, ions tend not to migrate at the same velocity due to their differences of mobility (see Table 2.1 and Section 1.4.3.1). In that case, the charge separation between ions is neutralized by an electrical current (J_{diff}), which orientation depends on the electric charge of ions with the highest mobilities. Consequently the electroneutrality of the system is maintained and all the charges migrate at the same speed. This source of current is called the electro-diffusive potential or the fluid junction potential (e.g., Jouniaux et al. 2009) or the exclusion-diffusion potential (e.g., MacAllister et al. 2018) or the membrane potential in the presence of clays (e.g., Revil and Leroy 2004).

2.3.4.1 The diffusion potential of a single salt

For a system composed of a simple salt, typically sodium-chloride (NaCl) or potassium chloride (KCl), this coupling has been measured by Maineult et al. (2004, 2005, 2006) during laboratory experiments in a sand matrix and is successfully modeled using the Henderson formula (Henderson 1907; Guggenheim 1930; Revil 1999), initially developed for cells with liquid-liquid junctions, but adapted by Maineult et al. (2005) for porous media, by introducing the porosity ϕ in the coupling coefficient α^*. Thus, the electrical potential difference ΔV (V) can be written as follows,

$$\Delta V = \alpha^* \frac{\nabla C}{C} = \phi \frac{\mathscr{R} T}{\mathrm{f}} \frac{\beta_+ - \beta_-}{\beta_+ + \beta_-} \frac{\nabla C}{C}, \tag{2.25}$$

where $\mathscr{R}$ is the molar gas constant ($\mathscr{R} \approx 8.314$ J mol^{-1} K^{-1}) and T (K) is the absolute temperature. β_+ and β_- refer to the mobilities of the cation and the anion, respectively.

Diffusion potential can also be related to ionic exclusion because of the presence of pore throats acting as selective zones. These zones act as membranes and are particularly abundant in shales and clays (e.g., Leroy et al. 2006; Jougnot et al. 2009), leading to slower diffusion from the counterions in these zones. Thus, to model the diffusion coefficient of the counterions in these selective zone Revil and Leroy (2004) have reformulated Eq. (2.25) by introducing macroscopic Hittorf numbers $T_{(+)}$ and $T_{(-)}$, which represent the fraction of electrical current transported by the cations and anions in the pore water and is defined as

$$T_{(\pm)} = \frac{\sigma_{(\pm)}}{\sigma}, \tag{2.26}$$

where $\sigma_{(\pm)}$ is the contribution of the cations or the anions to the electrical conductivity. In absence of surface conductivity, the electrical conductivity of the sample is related to the pore water electrical conductivity through the formation factor F. Thus, Equation (2.26) becomes

$$T_{(\pm)} = \frac{\sigma_{w,(\pm)}}{\sigma_w}. \tag{2.27}$$

Given the description of the pore water conductivity (see Section 2.2.5.1), the macroscopic Hittorf number can be related to ions mobilities as

$$T_{(\pm)} = \frac{\mathrm{f}C\beta_{(\pm)}z_{(\pm)}}{\mathrm{f}Cz_{(\pm)}(\beta_{(+)}+\beta_{(-)})}$$
$$T_{(\pm)} = \frac{\beta_{(\pm)}}{\beta_{(+)}+\beta_{(-)}}. \tag{2.28}$$

The macroscopic Hittorf number expressed above is thus only dependent of the ionic mobilities. This definition is normally applied to the microscopic Hittorf number $t_{\pm}$ (e.g., MacInnes 1939). Nevertheless, as explained by Revil and Leroy (2004), in absence of surface conductivity, microscopic and macroscopic Hittorf numbers are equivalent ($T_{\pm} = t_{\pm}$). Thus, using the macroscopic Hittorf numbers instead of the mobilities, Eq. (2.25) is simplified as (e.g., Revil 1999; Graham et al. 2018)

$$\Delta V = \phi\frac{\mathscr{R}T}{\mathrm{f}}(2T_{+}-1)\frac{\nabla C}{C}. \tag{2.29}$$

Revil and Jougnot (2008) extended this formulation for unsaturated conditions.

On the field, the electro-diffusive coupling is often neglected due to its low amplitude compare to the electrokinetic potential. Nevertheless, MacAllister et al. (2016; 2018) monitored SP signal related to saline intrusion in boreholes of a coastal aquifer. They found that their SP signal cannot be modeled by the electrokinetic coupling generated by the ocean tidal, but that it is dominated by the diffusion potential of the saline sea water toward the coast and that the SP time variations are related to the tidal movement of the saline front. Graham et al. (2018) rely on a precursor decrease of these SP data to model local variations in ionic exclusion efficiency in a fracture zone. They intend to use these results to forecast saline intrusion. MacAllister et al. (2019) confirmed these interpretations through laboratory measurements.

2.3.4.2 The diffusion potential in a multi-species context

The expression of the diffusion potential defined in Eq. (2.29) has proven to be useful to model the diffusion of ionic tracers that comprise multi-species. In this case, the solution salinity is considered instead of the ionic concentration in the diffusion potential expression (e.g., Revil 1999; Revil and Leroy 2004). However, when considering chemical reactions involving changes in the pore water composition, the salinity is not suitable. Revil and Linde (2006) proposed an expression of the electro-diffusive potential in a multi-ionic context, which is synthesized by Linde et al. (2011) following

$$j_s^{diff} = \frac{\mathscr{R}T}{e}\sum_{X_i}\frac{t_{X_i}\sigma}{z_{X_i}}\frac{\nabla C_{X_i}}{C_{X_i}} \tag{2.30}$$

where X_i of the sum describes the different ions present in solution. Then, t_{X_i} and z_{X_i} correspond to the microscopic Hittorf number (-) and the valence (-) of ion X_i, respectively. t_{X_i} is also called the transference number by Strathmann (2004) and is defined as

$$t_{X_i} = \frac{C_{X_i}\,\beta_{X_i}}{\sum_{X_j} C_{X_j}\,\beta_{X_j}}. \tag{2.31}$$

Strathmann (2004) relates t_{X_i} to the macroscopic Hittorf number T_{X_i} by

$$t_{X_i} = \frac{T_{X_i}}{z_{X_i}}, \tag{2.32}$$

where the macroscopic Hittorf number of ion X_i is rather called the transport number T_{X_i} by Strathmann (2004).

Given the definition of the transference number t_{X_i}, the abrupt variations in ionic concentrations generated by the processes of calcite dissolution and precipitation create large variations in the distributions of the different ion transference numbers, which will greatly impact the amplitude of the current density defined in Eq. (2.30). Therefore, the expression of the diffusion potential derived from the formulation of Linde et al. (2011) is not adapted to these reactive conditions.

In the absence of a diffusion potential model suitable for the study of multi-species reactive transport, I developed a new model that is compared to SP measurements I obtained during this thesis. This experimental and numerical study is presented in Chapter 6.

2.4 Conclusion of the chapter

Geophysical methods have a long history made of experimentation and modeling. Both of these components are necessary to obtain high quality results and to be able to interpret them as parameters of interest for the hole community of geoscientists, and especially for the critical zone study, which is at a nexus of many disciplines. Thus, hydrogeophysical studies hold for characterising key processes of the subsurface.

The study of calcite dissolution and precipitation processes is a topic of research that intersects between disciplines. It is therefore of great interest to combine geochemical investigation methods, traditionally used to deal with this theme, with geophysical methods and hydrogeological parameters. Indeed, the integration of geophysical monitoring with direct geochemical measurements can provide a minimally invasive approach to characterize calcite processes.

Regarding SIP and SP methods, it appears that they are strongly related by geometrical and geochemical conditions, which are key parameters for the monitoring of dissolution and precipitation in carbonate rocks. As these methods are not related to the same mechanisms, they will give complementary information.

CHAPTER

3 Electrical conductivity petrophysical modeling

3.1 Introduction to the paper

The paper presented in this section is about a new model that describes the evolution of the electrical conductivity (Section 2.2) when a porous material is subjected to dissolution and precipitation processes. These processes are described through the evolution of two geometrical properties of the pore space: tortuosity and constrictivity. Tortuosity describes how pores do not follow straight paths through the medium. Constrictivity is linked to the so-called bottleneck effect. It takes into account the pore size variation and the existence of pore bodies connected with pore throats. Tortuosity is already known and used in models from the literature (sometimes abusively), but it is the first time that constrictivity is explicitly considered to describe the electrical conductivity.

As the electrical conductivity is a parameter of interest to describe transport processes (e.g., Jougnot et al. 2009), the model is also developed to link the electrical conductivity to the permeability and to the diffusion coefficient obtained from the Fick's law.

This model is tested on a bunch of datasets found in the literature and covering a large scope of porosity types from simple synthetic and homogeneous porous media, to natural sedimentary rock samples. To fit the data, the Monte-Carlo approach, based on random draws, is used to find the best set of parameters. Finally, the model is successfully used on dissolution and precipitation simulations of digital representations of carbonate samples.

3.2 Paper

The paper is presented in this thesis with an adapted layout. It is referenced as Rembert F., Jougnot D., & Guarracino, L. (2020). A fractal model for the electrical conductivity of water-saturated porous media during mineral precipitation-dissolution processes. *Advances in Water Resources, 145*, 103742, DOI: https://doi.org/10.1016/j.advwatres.2020.103742.

A fractal model for the electrical conductivity of water-saturated porous media during mineral precipitation-dissolution processes

Flore Rembert[1], *Damien Jougnot*[1], *Luis Guarracino*[2]

[1] *Sorbonne Université, CNRS, UMR 7619 METIS, FR-75005 Paris, France*
[2] *CONICET, Faculdad de Ciencias Astronómicas y Geofísicas, Universidad Nacional de La Plata, Paseo del Bosque s/n, 1900 La Plata, Argentina*

Highlights

- A new electrical conductivity model is obtained from a fractal upscaling procedure
- The formation factor is obtained from microscale properties of the porous medium
- Transport properties are predicted from the electrical conductivity
- The model can reproduce dissolution and precipitation processes in carbonates

Abstract Precipitation and dissolution are prime processes in carbonate rocks and being able to monitor them is of major importance for aquifer and reservoir exploitation or environmental studies. Electrical conductivity is a physical property sensitive both to transport phenomena of porous media and to dissolution and precipitation processes. However, its quantitative use depends on the effectiveness of the petrophysical relationship to relate the electrical conductivity to hydrological properties of interest. In this work, we develop a new physically-based model to estimate the electrical conductivity by upscaling a microstructural description of water-saturated fractal porous media. This model is successfully compared to published data from both unconsolidated and consolidated samples, or during precipitation and dissolution numerical experiments. For the latter, we show that the permeability can be linked to the predicted electrical conductivity.

Keywords Electrical conductivity; Fractal model; Dissolution and precipitation processes; Carbonate rocks; Permeability

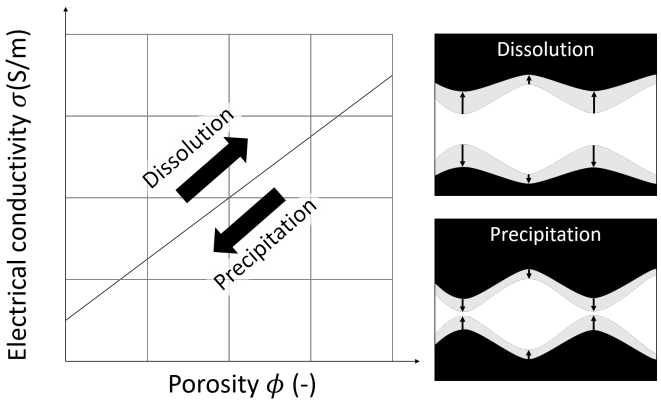

Graphical abstract: a new electrical conductivity model taking into account the effect of dissolution and precipitation on the pore shape at the REV scale through a fractal-based upscaling procedure.

1 Introduction

Carbonates represent a large part of the sedimentary rocks covering the Earth and carbonate aquifers store a large part of fresh water, which is a key resource for society needs. Karst aquifers are extremely complex systems because of the important chemical interactions between rock matrix and water, leading to strong chemical processes such as dissolution and precipitation. Studying these environments can benefit from the use of non-invasive tools such as the ones propose in hydrogeophysics to monitor flow and transport quantitatively (e.g., Hubbard et al. 2011; Binley et al. 2015).

Among the geophysical methods used for hydrological purposes in carbonate formations, electrical and electromagnetic methods have already shown their usefulness and are increasingly used (e.g., Chalikakis et al. 2011; Revil et al. 2012; Binley et al. 2015). Electrical methods, such as direct current (DC) resistivity and induced polarization (IP), involve acquisitions with flexible configurations of electrodes in galvanic or capacitive contact with the subsurface (Hubbard et al. 2011). These methods are increasingly used in different approaches to cover a larger field of applications: from samples measurements in the lab (e.g., Wu et al. 2010), to measurements in one or between several boreholes (e.g., Daily et al. 1992) and 3D or 4D monitoring with time-lapse imaging or with permanent surveys (e.g., Watlet et al. 2018; Saneiyan et al. 2019; Mary et al. 2020). Geophysical methods based on electromagnetic induction (EMI) consist in the deployment of electromagnetic coils in which an electric current of varying frequency is injected. Depending on the frequency range, the distance, and size of the coils for injection and reception, the depth of investigation can be highly variable (Reynolds 1998). As for the electrical methods, EMI based methods can be deployed from the ground surface, in boreholes, and in an airborne manner (e.g., Paine 2003).

These methods enable to determine the spatial distribution of the electrical conductivity in the subsurface. They are, hence, very useful in karst-system to detect the emergence of a sinkhole, to identify infiltration area, or to map ghost-rock features (e.g., Jardani et al. 2006; Chalikakis et al. 2011; Kaufmann et al. 2014; Watlet et al. 2018). The electrical conductivity can then be related to properties of interest for hydrogeological characterization through the use of accurate petrophysical relationships (Binley et al. 2005). In recent works, electrical conductivity models are used to characterize chemical processes between rock matrix and pore water such as dissolution and precipitation (e.g., Leroy et al. 2017; Niu et al. 2019). Indeed, geoelectrical measurements are an efficient proxy to describe pore space geometry (e.g., Garing et al. 2014; Jougnot et al. 2018) and transport properties (e.g., Jougnot et al. 2009; Jougnot et al. 2010; Hamamoto et al. 2010; Maineult et al. 2018).

The electrical conductivity σ (S/m) of a water saturated porous medium (e.g., carbonate rocks) is a petrophysical property related to electrical conduction in the electrolyte through the transport of charges by ions. Then, σ is linked to pore fluid electrical conductivity σ_w (S/m) and to porous medium microstructural properties such as porosity ϕ (-), pore geometry, and surface roughness. Archie (1942) proposed a widely used empirical relationship for clean (clay-free) porous media that links σ and σ_w to ϕ as follows

$$\sigma = \sigma_w \phi^m, \tag{1}$$

where m (-) is the cementation exponent, defined between 1.3 and 4.4 for unconsolidated samples and for most of well-connected sedimentary rocks (e.g., Friedman 2005). For low pore water conductivity, porous medium electrical conductivity can also depend on a second mechanism, which can be described by the surface conductivity term σ_s (S/m). This contribution to the overall rock electrical conductivity is caused by the presence of charged surface sites on the minerals. This causes the development of the so-called electrical double layer (EDL) with counterions (i.e., ions of the opposite charges) distributed in the Stern layer and the diffuse layer (Hunter 1981; Chelidze et al. 1999; Leroy et al. 2004). Groundwater in carbonate reservoirs typically presents a conductivity comprised between 3.0×10^{-2} S/m and 8.0×10^{-2} S/m (e.g., Liñán Baena et al. 2009; Meyerhoff

et al. 2014; Jeannin et al. 2016), while carbonate rich rocks surface conductivity can range from 2.9×10^{-4} S/m to 1.7×10^{-2} S/m depending on the amount of clay (Guichet et al. 2006; Li et al. 2016; Soueid Ahmed et al. 2020). Thus, for the study of dissolution and precipitation of water saturated carbonate rocks at standard values of σ_w, the surface conductivity is generally low and can be neglected (e.g., Cherubini et al. 2019). The small surface conductivity can nevertheless be considered as a parallel conductivity with an adjustable value (e.g., Waxman et al. 1968; Weller et al. 1958; Revil et al. 2014):

$$\sigma = \frac{1}{F}\sigma_w + \sigma_s. \tag{2}$$

The formation factor F (-) is thus assessed using a petrophysical law. Besides, since the late 1950's many models linking σ to σ_w were developed. Most of these relationships have been obtained from the effective medium theory (e.g., Pride 1994; Bussian 1983; Revil et al. 1998; Ellis et al. 2010), volume averaging (e.g., Linde et al. 2006; Revil et al. 2006), the percolation theory (e.g., Broadbent et al. 1957; Hunt et al. 2014), or the cylindrical tube model (e.g., Pfannkuch 1972; Kennedy et al. 2012). More recently, the use of fractal theory (e.g., Yu et al. 2001; Mandelbrot 2004) of pore size has shown good results to describe petrophysical properties among which the electrical conductivity (e.g., Guarracino et al. 2018; Thanh et al. 2019). Meanwhile, several models have been developed to study macroscopic transport properties and chemical reactions by describing the porous matrix microscale geometry (e.g., Reis et al. 1994; Guarracino et al. 2014; Niu et al. 2019) and theoretical petrophysical models of electrical conductivity have been derived to relate the pore structure to transport parameters (e.g., Johnson et al. 1986; Revil et al. 1999; Glover et al. 2006).

Permeability prediction from electrical measurements is the subject of various research studies and these models often rely on petrophysical parameters such as the tortuosity (e.g., Revil et al. 1998; Niu et al. 2019). Moreover, the use of models such as Archie (1942) and Carman (1939) to relate the formation factor, the porosity, and the permeability is reasonable for simple porous media such as unconsolidated packs with spherical grains, but it is less reliable for real rock samples or to study the effect of dissolution and precipitation processes. The aim of the present study is to develop a petrophysical model based on micro structural parameters, such as the tortuosity, the constrictivity (i.e., parameter which is related to bottleneck effect in pores, described by Holzer et al. 2013), and the Johnson length (e.g., Johnson et al. 1986; Bernabé et al. 2015), to express the electrical conductivity and to evaluate the role of pore structure.

The present manuscript is divided into three parts. We first develop equations to describe the electrical conductivity of a porous medium with pores defined as tortuous capillaries that follow a fractal size distribution and presenting sinusoidal variations of their aperture. Then, the model is linked to other transport parameters such as permeability and ionic diffusion coefficient. In the second part, we test the model sensitivity and we compare its performance with Thanh et al. (2019) fractal model. In the third part, we confront the model to datasets presenting an increasing complexity: first data come from synthetic unconsolidated samples, then they are taken from natural rock samples with a growing pore space intricacy. Finally, we analyze the model response to numerical simulations of dissolution and precipitation, highlighting its interest as a monitoring tool for such critical processes.

2 Theoretical developments

Based on the approach of Guarracino et al. (2014), we propose a model assuming a porous medium represented as a fractal distribution of equivalent tortuous capillaries in a cylindrical representative elementary volume (REV) with a radius R (m) and a length L (m) (Fig. 1a). In this model, the surface conductivity σ_s is neglected ($\sigma_s \to 0$).

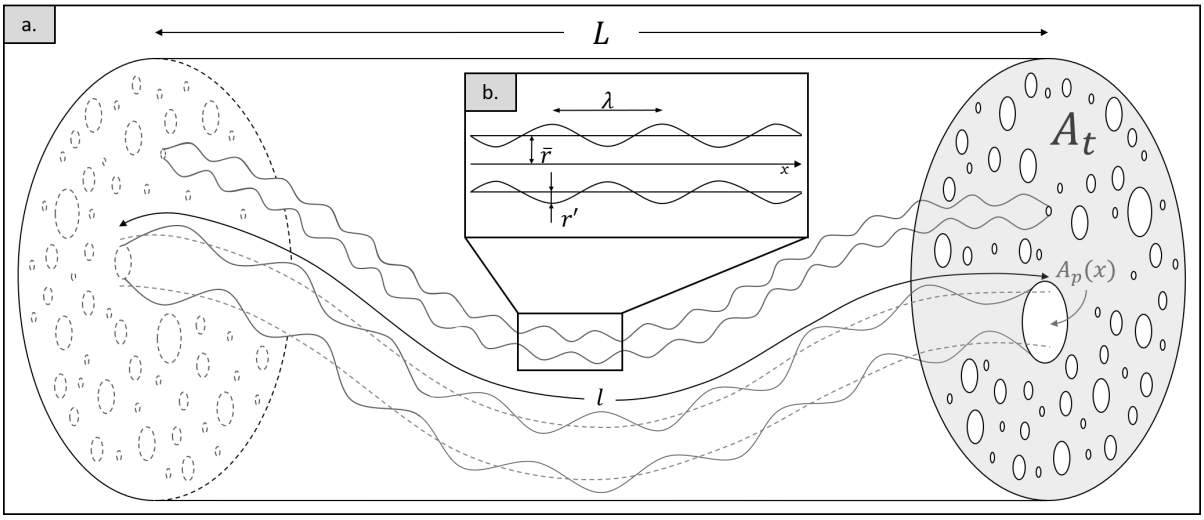

Figure 1: (a) The porous rock model is composed of a large number of sinusoidal and tortuous capillaries in the cylindrical representative elementary volume (REV). All the capillaries have the same tortuous length l (m) and their radii follow a fractal distribution. (b) The considered pore geometry corresponds to the one from Guarracino et al. (2014): $\bar{r}$ is the average pore radius (m) while r' is the amplitude of the sinusoidal fluctuation (m), and λ is the wavelength (m).

2.1 Pore scale

2.1.1 Pore geometry

The porous medium is conceptualized as an equivalent bundle of capillaries. As presented in Fig. 1b, each tortuous pore present a varying radius $r(x)$ (m) defined with the following sinusoidal expression,

$$r(x) = \bar{r} + r' sin\left(\frac{2\pi}{\lambda}x\right) = \bar{r}\left(1 + 2a\, sin\left(\frac{2\pi}{\lambda}x\right)\right), \tag{3}$$

where $\bar{r}$ is the average pore radius (m), r' the amplitude of the radius size fluctuation (m), and λ is the wavelength (m). The parameter a is the pore radius fluctuation ratio (-) defined by $a = r'/2\bar{r}$, which values range from 0 to 0.5. Note that $a = 0$ corresponds to cylindrical pores ($r(x) = \bar{r}$), while $a = 0.5$ corresponds to periodically closed pores. For each pore we define the section area $A_p(x) = \pi r(x)^2$ (m^2).

Most of the models found in the literature, and describing the porous medium with a fractal distribution, define a pore length scaling with pore radius (e.g., Yu et al. 2002; Yu et al. 2003; Guarracino et al. 2014; Thanh et al. 2019). However, in this study we consider a constant tortuous length l (m) for all the pores because it reduces the number of adjustable parameters while maintaining the model accuracy. This constant tortuosity value should be interpreted as an effective macroscopic value for all tube lengths. l is the length taken at the center of the capillary. Thus, the tortuosity τ (-) is also a constant for all pores and is defined as

$$\tau = \frac{l}{L}. \tag{4}$$

In this case, the volume of a single pore $V_p(\bar{r})$ (m^3) can be computed by integrating its section area $A_p(x)$ over the tortuous length l:

$$V_p(\bar{r}) = \int_0^l \pi r(x)^2 dx. \tag{5}$$

According to Eqs. (3) and (4), and assuming that $\lambda \ll l$, volume V_p defined in Eq. (5) becomes

$$V_p(\bar{r}) = \pi \bar{r}^2 (1 + 2a^2)\tau L. \tag{6}$$

2.1.2 Pore electrical conductivity

We express electrical properties at pore scale before obtaining them for the porous medium by upscaling, because the REV can be considered as an equivalent circuit of parallel conductances, when σ_s is neglected. The electrical conductance $\Sigma_{pore}(\bar{r})$ (S) of a single sinusoidal pore is defined by

$$\Sigma_{pore}(\bar{r}) = \left(\int_0^l \frac{1}{\sigma_w \pi r(x)^2} dx \right)^{-1}, \tag{7}$$

where σ_w (S/m) is the pore-water conductivity. Replacing Eq. (3) in Eq. (7) and assuming $\lambda \ll l$, the electrical conductance of a single pore can be expressed as

$$\Sigma_{pore}(\bar{r}) = \frac{\sigma_w \pi \bar{r}^2 (1-4a^2)^{3/2}}{\tau L}. \tag{8}$$

Following Ohm's law, the electric voltage ΔV (V) between the edges of the capillary (0 and l) is defined as

$$\Delta V = -\frac{i(\bar{r})}{\Sigma_{pore} i(\bar{r})}, \tag{9}$$

where $i(\bar{r})$ (A) is the electric current flowing through the pore that can be expressed as follows

$$i(\bar{r}) = \frac{-\pi\, \sigma_w\, \bar{r}^2\, (1-4a^2)^{3/2}}{\tau\, L}\, \Delta V. \tag{10}$$

We, thus, define the contribution to the porous medium conductivity from a single pore $\sigma_p(\bar{r})$ (S/m) by multiplying the pore conductance with a geometric factor $f_g = \pi\, R^2/L$ (m)

$$\sigma_p(\bar{r}) = \frac{\Sigma_{pore}(\bar{r})}{f_g} = \frac{\bar{r}^2 (1-4a^2)^{3/2} \sigma_w}{\tau R^2}. \tag{11}$$

When $a = 0$, the expression of $\sigma_p(\bar{r})$ simplifies itself as in the case of cylindrical tortuous pores developed by Pfannkuch (1972).

2.2 Upscaling procedure using a fractal distribution

To obtain the electrical conductivity of the porous medium at the REV scale, we need a pore size distribution. We conceptualize the porous medium by a fractal distribution of capillaries according to the notations of Guarracino et al. (2014) and Thanh et al. (2019), based on the fractal theory for porous media (Tyler et al. 1990; Yu et al. 2002)

$$N(\bar{r}) = \left(\frac{\bar{r}_{max}}{\bar{r}} \right)^{D_p}, \tag{12}$$

where N (-) is the number of capillaries whose average radius are equal or larger than $\bar{r}$, D_p (-) is the fractal dimension of pore size and $\bar{r}_{max}$ (m) is the maximum average radius of pores in the REV. Fractal distributions can be used to describe objects of different Euclidean dimensions (e.g., 1 dimension for a line, 2 dimensions for a surface, and 3 dimensions for a volume). In this study, the pore size distribution is considered as a fractal distribution of capillary sections on a plane (i.e., in 2 dimensions). Therefore, the fractal dimension D_p is defined from 1 to 2 (among many other papers, see Yu et al. 2002; Yu et al. 2003). Nevertheless, D_p is a unique parameter for each porous medium as it strongly depends on the pore size distribution. Its impact has been quantified by Tyler et al. (1990) with a porous medium defined as a Sierpinski carpet. From the pore size distribution defined in Equation (12), the total number of capillaries equals to

$$N_{tot} = \left(\frac{\bar{r}_{max}}{\bar{r}_{min}} \right)^{D_p}, \tag{13}$$

with $\bar{r}_{min}$ (m) the minimum average radius. From Eq. (12), the number of radii lying between $\bar{r}$ and $\bar{r} + d\bar{r}$ is

$$-dN = D_p \, \bar{r}_{max}^{D_p} \, \bar{r}^{\,-D_p-1} \, d\bar{r}, \tag{14}$$

where $-dN$ (-) is the number of pores with an average radius comprised in the infinitesimal range between $\bar{r}$ and $\bar{r} + d\bar{r}$. The minus sign implies that the number of pores decreases when the average radius increases (Yu et al. 2003; Soldi et al. 2017; Thanh et al. 2019).

2.3 REV scale

In the present section, we present the macroscopic properties at the REV scale obtained from the upscaling procedure.

2.3.1 Porosity

We can express the porosity ϕ (-) of the REV by integrating the pore volume over the fractal distribution as follows

$$\phi = \frac{\int_{\bar{r}_{min}}^{\bar{r}_{max}} V_p(\bar{r})(-dN)}{\pi R^2 L}. \tag{15}$$

Then, by replacing Eqs. (14) and (6) into Eq. (15), it yields to

$$\phi = \frac{(1+2a^2)\tau D_p \bar{r}_{max}^{D_p}}{R^2(2-D_p)}(\bar{r}_{max}^{2-D_p} - \bar{r}_{min}^{2-D_p}). \tag{16}$$

This expression requires $2 - D_p > 0$, which is always true (see Yu et al. 2001). Note that this expression corresponds to the model of Guarracino et al. (2014) when the tortuosity is the same for all the capillary sizes.

2.3.2 Electrical conductivity

As defined in the Kirchhoff's current law, the electric current of the REV, I (A), is the sum of the electric currents of all the capillaries when the surface conductivity is neglected. It can be obtained by integrating the electric current of each pore:

$$I = \int_{\bar{r}_{min}}^{\bar{r}_{max}} i(\bar{r})(-dN). \tag{17}$$

According to Eqs. (4), (10), and (14), I can be expressed as follows,

$$I = \frac{-\sigma_w \pi (1-4a^2)^{3/2} D_p \bar{r}_{max}^{D_p}}{(2-D_p)\tau L} \Delta V (\bar{r}_{max}^{2-D_p} - \bar{r}_{min}^{2-D_p}). \tag{18}$$

The Ohm's law at the REV scale yields to

$$I = -\sigma^{REV} \pi R^2 \frac{\Delta V}{L}, \tag{19}$$

where σ^{REV} is the electrical conductivity of the REV (S/m). By combining Eqs. (18) and (19), σ^{REV} is expressed as

$$\sigma^{REV} = \frac{\sigma_w D_p \bar{r}_{max}^{D_p} (1-4a^2)^{3/2}}{R^2 \tau (2-D_p)} (\bar{r}_{max}^{2-D_p} - \bar{r}_{min}^{2-D_p}). \tag{20}$$

Finally, substituting Eq. (16) into Eq. (20) yields to

$$\sigma^{REV} = \frac{\sigma_w \phi (1-4a^2)^{3/2}}{\tau^2 (1+2a^2)}. \tag{21}$$

Note that if $a = 0$ and $\tau = 1$, Eq. (21) becomes $\sigma^{REV} = \sigma_w \phi$, which is the expression of Archie's law for $m = 1$ where the porous medium is composed of a bundle of straight capillaries with no tortuosity (see Clennell 1997).

The electrical conductivity can be rewritten depending on the tortuosity τ and on the constrictivity f (-) as

$$\sigma^{REV} = \frac{\sigma_w \phi f}{\tau^2}. \tag{22}$$

The constrictivity f is thus defined as

$$f = \frac{(1-4a^2)^{3/2}}{(1+2a^2)}. \tag{23}$$

The above equation highlights that the pore fluctuation ratio a plays the role of the constriction factor defined by Petersen (1958). Constrictivity f ranges between 0 (e.g., for trapped pores) and 1 (e.g., for cylindrical pores with constant radius). As for the tortuosity τ, there is no suitable method to determine constrictivity value directly from core samples, but only some mathematical expressions for ideal simplified geometries (see Holzer et al. 2013, for a review). Therefore, very high tortuosity values (e.g., Niu et al. 2019) must be due to that in most studies the bottleneck effect is not considered.

2.3.3 Formation factor

The model from Archie (1942) links the rock electrical conductivity to the pore water conductivity and the porosity with the cementation exponent, which is an empirical parameter. Kennedy et al. (2012) propose to analyze electrical conductivity data using a physics-based model, which conceptualizes the porous medium with pore throats and pore bodies as in this study and defines the electrical conductivity as follows,

$$\sigma^{REV} = G\sigma_w \phi, \tag{24}$$

where G (-) is an explicit geometrical factor defined between 0 and 1. According to our models G can be expressed by

$$G = \frac{(1-4a^2)^{3/2}}{\tau^2(1+2a^2)} = \frac{f}{\tau^2}. \tag{25}$$

This geometrical factor can be called the connectedness (Glover 2015), while the formation factor F (-) is defined by

$$F = \frac{\sigma_w}{\sigma^{REV}}. \tag{26}$$

Substituting Eq. (21) into Eq. (26) yields to

$$F = \frac{\tau^2(1+2a^2)}{\phi(1-4a^2)^{3/2}} = \frac{\tau^2}{\phi f}. \tag{27}$$

The formation factor F can also be related to the connectedness G as $F = 1/\phi G$.

2.4 Evolution of the petrophysical parameters

The formation factor defined by Eq. (27) depends linearly with the inverse of porosity ($1/\phi$). However, the petrophysical parameters a and τ may be dependent on porosity for certain types of rocks or during dissolution or precipitation processes. In these cases, the formation factor will show a non-linear dependence with $1/\phi$ and can be expressed in general as

$$F(\phi) = \frac{\tau(\phi)^2(1+2a(\phi)^2)}{\phi(1-4a(\phi)^2)^{3/2}}. \tag{28}$$

In section 4.2, we test our model against different datasets from literature using logarithmic laws for the dependence of petrophysical parameters $a(\phi)$ and $\tau(\phi)$ with porosity following existing models from the literature (see Ghanbarian et al. 2013, for a review about the tortuosity). Thus, we define $a(\phi)$ and $\tau(\phi)$ as

$$a(\phi) = -P_a \log(\phi) \tag{29}$$

and

$$\tau(\phi) = 1 - P_\tau \log(\phi), \tag{30}$$

where P_a and P_τ are empirical parameters. Note that 0 and 1 (i.e., first terms in Eqs. (29) and (30), respectively) correspond to the minimum values reached by $a(\phi)$ and $\tau(\phi)$ when $\phi = 1$. Expressing tortuosity as a logarithmic function of porosity has already proven its effectiveness in the literature (Comiti et al. 1989; Ghanbarian et al. 2013; Zhang et al. 2020). However, this is, to the best of our knowledge, the first attempt to propose a constrictivity model as a function of porosity. Then, by replacing Eqs. (29) and (30) in Eq. (28), the expression of the proposed model for the formation factor F becomes

$$F(\phi) = \frac{\left[1 - P_\tau \log(\phi)\right]^2 \left(1 + 2\left[P_a \log(\phi)\right]^2\right)}{\phi\left(1 - 4\left[P_a \log(\phi)\right]^2\right)^{3/2}}. \tag{31}$$

Note that the model parameters from Thanh et al. (2019), another porous medium description following a fractal distribution of pores, also present logarithmic dependencies with the porosity ϕ.

2.5 Electrical conductivity and transport parameters

2.5.1 From electrical conductivity to permeability

The electrical conductivity is a useful geophysical property to describe the pore space geometry. Here we propose to express the permeability as a function of the electrical conductivity using our model.

At pore scale, Sisavath et al. (2001) propose the following expression for the flow rate $Q_p(\bar{r})$ (m^3/s) in a single capillary:

$$Q_p(\bar{r}) = \frac{\pi}{8} \frac{\rho g}{\mu} \frac{\Delta h}{l} \left[\int_0^l \frac{1}{r^4(x)} dx\right]^{-1}. \tag{32}$$

where ρ is the water density (kg/m^3), g is the standard gravity acceleration (m/s^2), μ is the water viscosity (Pa.s) and Δh is the hydraulic head across the REV (m). Substituting Eq. (3) in Eq. (32) and assuming $\lambda \ll l$, it yields:

$$Q_p(\bar{r}) = \frac{\pi}{8} \frac{\rho g}{\mu} \frac{\Delta h}{\tau L} \bar{r}^4 (1 - 4a^2)^{3/2}. \tag{33}$$

Then, the total volumetric flow rate Q^{REV} (m^3/s) is obtained by integrating Eq. (33) over all capillaries (i.e., at the REV scale)

$$\begin{aligned} Q^{REV} &= \int_{\bar{r}_{min}}^{\bar{r}_{max}} Q_p(\bar{r})(-dN) \\ &= \frac{\rho g (1-4a^2)^{3/2} D_p \bar{r}_{max}^{D_p} \pi \Delta h}{8\mu(4-D_p)\tau L} (\bar{r}_{max}^{4-D_p} - \bar{r}_{min}^{4-D_p}). \end{aligned} \tag{34}$$

Based on Darcy's law for saturated porous media, the total volumetric flow rate can be expressed as

$$Q^{REV} = \pi R^2 \frac{\rho g}{\mu} k^{REV} \frac{\Delta h}{L}, \tag{35}$$

where k^{REV} is the REV permeability (m^2). Then, combining Eqs. (34) and (35) it yields to

$$k^{REV} = \frac{(1-4a^2)^{3/2} D_p \bar{r}_{max}^{D_p}}{8R^2(4-D_p)\tau} (\bar{r}_{max}^{4-D_p} - \bar{r}_{min}^{4-D_p}). \tag{36}$$

Considering $\bar{r}_{min} \ll \bar{r}_{max}$, Eq. (36) can be simplified as

$$k^{REV} = \frac{(1-4a^2)^{3/2} D_p \bar{r}_{max}^4}{8R^2(4-D_p)\tau}. \tag{37}$$

Using the same simplification on Eq. (16), the expression of porosity becomes

$$\phi = \frac{(1+2a^2)\tau D_p \bar{r}_{max}^2}{R^2(2-D_p)}. \tag{38}$$

Then, combining Eqs. (37) and (38) yields to

$$k^{REV} = \frac{2-D_p}{4-D_p} \frac{(1-4a^2)^{3/2}}{1+2a^2} \frac{\bar{r}_{max}^2}{8\tau^2}\phi. \tag{39}$$

Finally, the combination of Eqs. (27) and (39) leads to

$$k^{REV} = \frac{2-D_p}{4-D_p} \frac{\bar{r}_{max}^2}{8F}. \tag{40}$$

Note that Eq. (40) relates permeability to electrical conductivity through the formation factor (see Eq. (26)).

This expression can be linked to the model of Johnson et al. (1986)

$$k^{REV} = \frac{\Lambda^2}{8F}, \tag{41}$$

where Λ (also known as the Johnson length) is a characteristic pore size (m) of dynamically connected pores (Banavar et al. 1987b; Ghanbarian 2020). Some authors proposed theoretical relationships to determine this characteristic length Λ. While Revil et al. (1999) or Glover et al. (2006) link it to the average grain diameter, some other publications work on the determination of Λ assuming a porous medium composed of cylindrical pores (e.g., Banavar et al. 1987a; Niu et al. 2019). Considering the proposed model, Λ can therefore be written as follows

$$\Lambda = \sqrt{\frac{2-D_p}{4-D_p}}\, \bar{r}_{max}. \tag{42}$$

2.5.2 From electrical conductivity to ionic diffusion coefficient

Ionic diffusion can be described at REV scale by the Fick's law (Fick 1995)

$$J_t = D_{eff}\pi R^2 \frac{\Delta c}{L}, \tag{43}$$

where J_t (mol/s) is the diffusive mass flow rate, D_{eff} (m^2/s) is the effective diffusion coefficient, and Δc (mol/m^3) is the solute concentration difference between the REV edges. Guarracino et al. (2014) propose to express D_{eff} as a function of the tortuosity, which, in their model, depends on the capillary size. In our model, we consider that the tortuosity is constant, thus by reproducing the same development proposed by Guarracino et al. (2014) we obtain

$$D_{eff} = D_w \frac{(1-4a^2)^{3/2}\phi}{(1-2a^2)\tau^2}, \tag{44}$$

which can be simplified as

$$D_{eff} = D_w \frac{f\phi}{\tau^2}. \tag{45}$$

This last expression of D_{eff} as a function of the tortuosity τ and the constrictivity f, allows to retrieve the same equation as Van Brakel et al. (1974) with both the effect of the tortuosity and the constrictivity. Replacing Eq. (27) in Eq. (45) yields to

$$D_{eff} = \frac{D_w}{F}, \tag{46}$$

which implies

$$F = \frac{\sigma_w}{\sigma^{REV}} = \frac{D_w}{D_{eff}}. \tag{47}$$

This result has already been demonstrated by Kyi et al. (1994) and Jougnot et al. (2009), among others. It means that the formation factor can be used for both electrical conductivity or diffuse properties. This point is consistent with the fact that Ohm and Fick laws are diffusion equations, where the transport of ions take place in the same pore space. The difference lies in the fact that ionic conduction and ionic diffusion consider the electric potential gradient and the ionic concentration gradient, respectively.

3 Model analysis and evaluation

Our model expresses the evolution of the formation factor F as a function of the porosity ϕ, the tortuosity τ and the constrictivity through the pore radius fluctuation ratio a (Eq. (27)). Here we explore wide ranges of values for a and τ to quantify their influence on the formation factor F (Fig. 2) and compare our model with the model from Thanh et al. (2019), for the fractal dimension of the tortuosity $D_\tau = 1$, to appreciate the contribution of the constrictivity to the porous medium description. Figs. 2a and 2b show variations of F as a function of the porosity ϕ when only a or τ varies. On Fig. 2a, parameter a varies from 0 to 0.49 and tortuosity $\tau = 5.0$. We test the case of a constant pore aperture when $a = 0$, but we do not reach $a = 0.5$ because this means that the pores are periodically closed (see the definition of a in section 2.1.1), and this corresponds to an infinitely resistive rock only made of non-connected porosity. On Fig. 2b tortuosity τ varies from 1 to 20 and parameter $a = 0.1$. $\tau = 1$ implies straight pores (i.e., $l = L$). Fig. 2c present variations of F as a function of the tortuosity τ for different values of a and a fixed porosity $\phi = 0.4$. Fig. 2d is the density plot of $\log_{10}(F)$ for a range of values of a and τ and with a fixed porosity value $\phi = 0.4$.

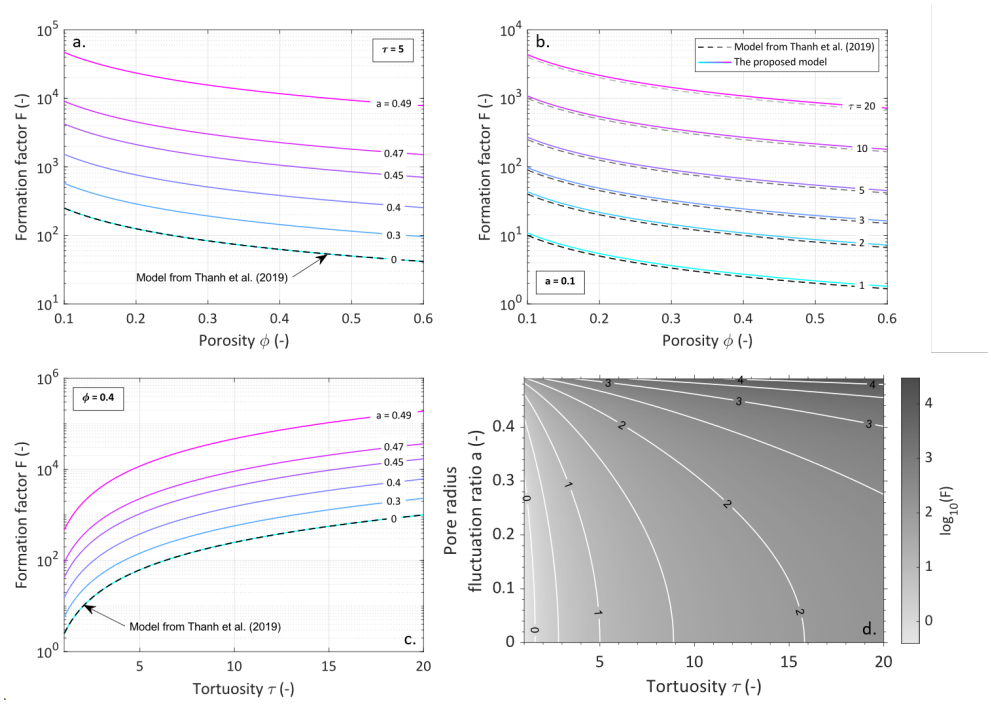

Figure 2: (a) Effect of the pore radius fluctuation ratio a on the formation factor F, represented as a function of the porosity ϕ. a varies from 0 to 0.49, while the tortuosity $\tau = 5$. (b) Effect of the tortuosity τ on the formation factor F, represented as a function of the porosity ϕ. τ varies from 1 to 20, while the pore radius fluctuation ratio $a = 0.1$. (c) Effect of the pore radius fluctuation ratio a on the formation factor F, represented as a function of the tortuosity τ. a varies from 0 to 0.49, while the porosity $\phi = 0.4$. (d) Comparison of the effect of parameters a and τ on the formation factor F for a constant porosity $\phi = 0.4$.

From the analysis of Figs. 2a and 2b, one can note that the formation factor decreases when porosity increases. This was expected because more the water saturated medium is porous, more its electrical conductiv-

ity is close to pore water electrical conductivity. Furthermore, we observe that both parameters a and τ have a strong effect on formation factor variation ranges. Indeed, $F(\phi)$ curve can be shifted by more than 3 orders of magnitude with variations of a or τ and, as expected, the formation factor increases when τ or a increases. Indeed, when these parameters increase, the porous medium becomes more complex: the increase of parameter a means that periodical aperture of capillaries decreases (i.e., more constrictivity), while the increase of τ means that pores become more tortuous (i.e., more tortuosity). Besides, for a close to 0 (i.e., without aperture variation), curves from Thanh et al. (2019) model are similar with the curves from our model. This is consistent with the fact that Thanh et al. (2019) also conceptualize the porous media as a fractal distribution of capillaries. However, when a increases, the curves explore very different ranges of F values (Figs. 2a and 2c). The density plot presented on Fig. 2d compares the effect of a and τ variations for a constant porosity ($\phi = 0.4$). It appears that for a fixed value of τ, variations of a have a low effect on log of F values. On the contrary, variations of τ for one value of a have stronger effect on log of F ranges. However it should be noted that this representation can be biased because value ranges of a and τ are very different. Thus, it is difficult to asses if the tortuosity τ has really much more effect on formation factor than parameter a. Nevertheless, it has the advantage to represent the combined effect of a and τ on the formation factor.

4 Results and discussion

To assess the performance of the proposed model, we compare predicted values to datasets from the literature. References are listed in Table 1 and ordered with a growing complexity. Indeed, data from Friedman et al. (2002) and Bolève et al. (2007) are taken from experiments made on unconsolidated medium. Then, Garing et al. (2014), Revil et al. (2014), and Cherubini et al. (2019) studied natural consolidated samples from carbonate rocks and sandstone samples. Finally, Niu et al. (2019) present numerical but dynamic data under dissolution and precipitation conditions.

For each dataset, the adjusted parameters of the proposed model are listed in Table 1. Values have been determined using a Monte-Carlo inversion of Eqs. (21) and (27) which express the porous medium electrical conductivity σ^{REV} as a function of the pore water conductivity σ_w and the formation factor F as a function of the porosity ϕ, respectively. An additional term σ_s for the surface conductivity (S/m) is used to fit the data out of the application range of the proposed model. That is for low values of pore-water conductivity, when the surface conductivity cannot be neglected. As the proposed model is intended to be mostly used on carbonate rocks, which are known to have low surface conductivity, this physical parameter has not been taken into account in the theoretical development of the expression of the electrical conductivity of the porous medium. However, it can be added considering a parallel model (e.g., Waxman et al. 1968; Börner et al. 1991):

$$\sigma^{REV} = \frac{1}{F}\sigma_w + \sigma_s. \tag{48}$$

A more advanced approach of parallel model is proposed by Thanh et al. (2019) including the contribution of the surface conductance in the overall capillary bundle electrical conductivity.

Table 1 lists also the computed error ϵ of the adjusted model. In statistics ϵ is called the mean absolute percentage error (MAPE). It is expressed in percent and defined as follow:

$$\epsilon = \frac{1}{N^d}\left(\sum_{i=1}^{N^d}\left|\frac{P_i^m - P_i^d}{P_i^d}\right|\right) \times 100, \tag{49}$$

where N^d, P^d, and P^m refer to the number of data, the electrical property from data, and the electrical property from the model, respectively. This type of error has been chosen to compare the ability of the model to

Table 1: Parameters of the proposed model compared to several datasets from different sources. σ_s is the surface conductivity (S/m) used for several comparisons out of our model application range, that is when the surface conductivity cannot be neglected, using Eq. (2). The model parameters are adjusted with a Monte-Carlo approach, except for a in Niu et al. (2019) dataset, where a is adjusted with the least square method. ϵ is the cumulative error computed in percentage, called the mean absolute percentage error (MAPE).

Sample	a	τ	σ_s (S/m)	ϵ (%)	Studied function	Source
S1a	0.004	1.035	2.25×10^{-4}	7.78	$\sigma(\sigma_w)$	Bolève et al. (2007)
S2	0.008	1.062	1.45×10^{-4}	7.47		
S3	0.006	1.050	0.80×10^{-4}	7.09		
S4	0.006	1.051	0.50×10^{-4}	9.21		
S5	0.012	1.093	0.25×10^{-4}	10.22		
S6	0.008	1.062	0.60×10^{-4}	9.21		
Glass	0.022	1.174	-	0.32	$F(\phi)$	Friedman et al. (2002)
Sand	0.026	1.212	-	0.60		
Tuff	0.020	1.159	-	1.63		
FS [a]	0.146 - 0.309	1.365 - 1.773	-	22.62	$F(\phi)$	Revil et al. (2014)
L1, L2	0.113	1.901	7.24×10^{-4}	9.24	$\sigma(\sigma_w)$	Cherubini et al. (2019)
Inter	0.077 - 0.217	1.846 - 3.399	-	26.67	$F(\phi)$	Garing et al. (2014)
Multi	0.172 - 0.345	1.915 - 2.839	-	9.64		
Vuggy	0.068 - 0.109	5.632 - 8.411	-	19.68		
D.T.lim [b]	0.078 - 0.393	1.786	-	0.05	$F(\phi)$	Niu et al. (2019)
D.R.lim [c]	0.315 - 0.393	1.786	-	0.08		
P.T.lim [d]	0.167 - 0.466	1.335	-	0.12		
P.R.lim [e]	0.160 - 0.309	1.320	-	0.04		

[a] FS: Fontainebleau sandstones

[b] D.T.lim: Dissolution transport-limited

[c] D.R.lim: Dissolution reaction-limited

[d] P.T.lim: Precipitation transport-limited

[e] P.R.lim: Precipitation reaction-limited

reproduce the experimental values for all the datasets even if they are expressed as $\sigma^{REV}(\sigma_w)$ or as $F(\phi)$.

4.1 Testing the model on unconsolidated media

The proposed model is first confronted to datasets from Friedman et al. (2002) and Bolève et al. (2007) obtained for unconsolidated samples. In these tests, only one set of parameters a, τ, and σ_s (when needed) is adjusted to fit with each dataset.

Bolève et al. (2007) measured the electrical conductivity of glass beads samples for different values of the pore water conductivity σ_w from 10^{-4} S/m to 10^{-1} S/m on S1a, S2, S3, S4, S5, and S6 (see Fig. 3). For all samples, Bolève et al. (2007) reported a constant porosity of 40 % while grain diameters are comprised between 56 µm for S1a and 3000 µm for S6 (see Fig. 3 for more details).

Table 1 shows that the adjusted model parameters a and τ have rather similar values for all the samples from Bolève et al. (2007). This can be explained by the fact that all samples have the same pore geometry but scaled at different size. Indeed, for homogeneous samples of glass beads, the beads space arrangement is quite

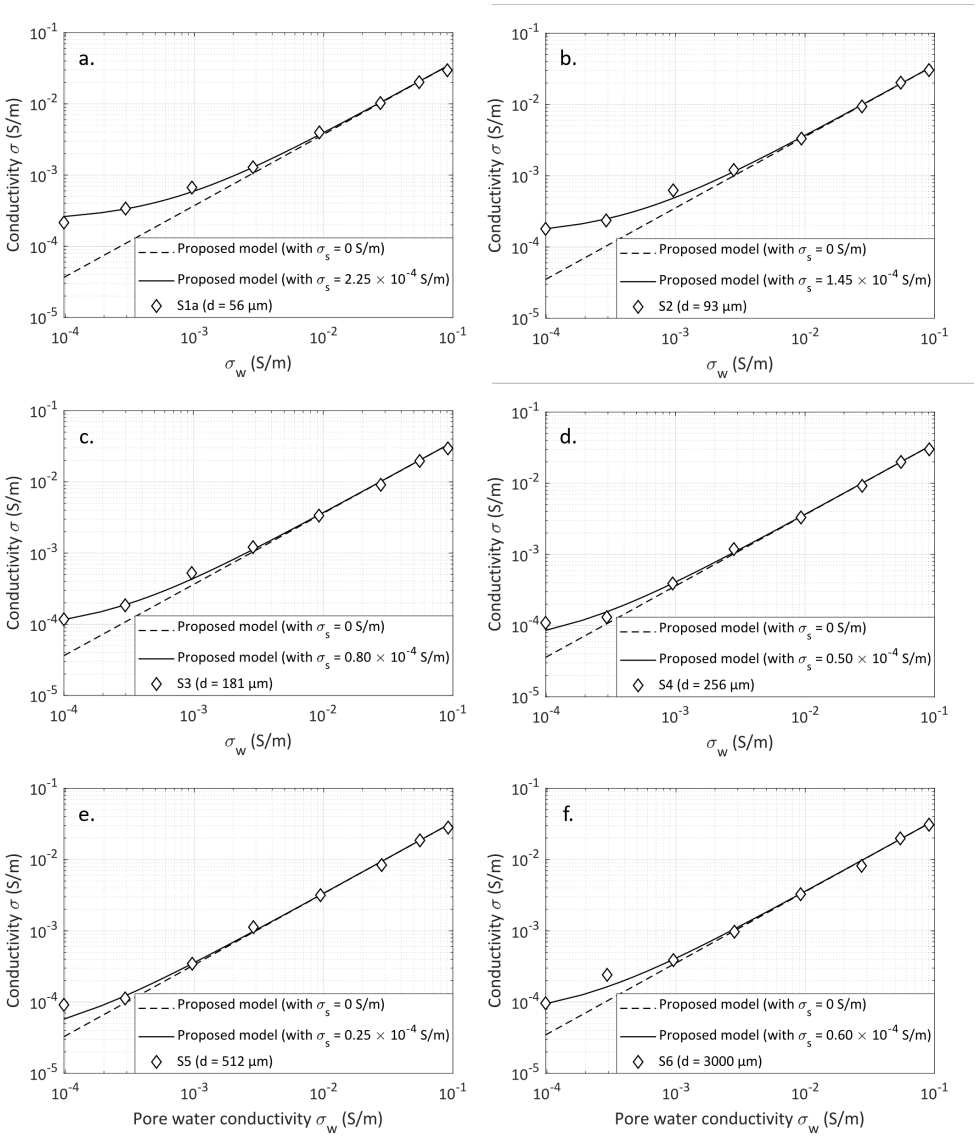

Figure 3: Electrical conductivity of different samples of glass beads (grains sizes are 56, 93, 181, 256, 512, and 3000 µm for samples S1a, S2, S3, S4, S5, and S6, respectively) versus the fluid electrical conductivity for a constant porosity $\phi = 40$ %. The datasets are from Bolève et al. (2007) and best fit parameters are given in Table 1.

independent of the spheres size. Therefore the pore network of all samples presents similar properties such as tortuosity (see also the discussion in Guarracino et al. 2018) and constrictivity, which directly depends on parameters a and τ. Moreover, a and τ are close to their minimum limits (i.e., $a = 0$ and $\tau = 1$). This is due to the simple pore space geometry created by samples made of homogeneous glass spheres. This explains the model good fit for straight capillaries (i.e., Thanh et al. 2019). However, it can be noticed that surface conductivity decreases while grain diameter increases. This is not a surprise considering that for the same volume, samples of smaller beads have a larger specific surface than samples of bigger beads (see, for example, the discussion in Glover et al. 2010).

Friedman et al. (2002) determined the formation factor F for samples of glass beads, sand, and tuff grains with different values of porosity ϕ (see Fig. 4). As the model best fit is determined with a Monte Carlo approach, accepted models are also plotted on Fig. 4. The acceptance criterion is defined individually for each dataset and corresponds to a certain value of the MAPE ϵ. For samples from Friedman et al. (2002), this criterion is fixed at $\epsilon < 1$ or 2 %. These are low values, meaning a really good fit from the model.

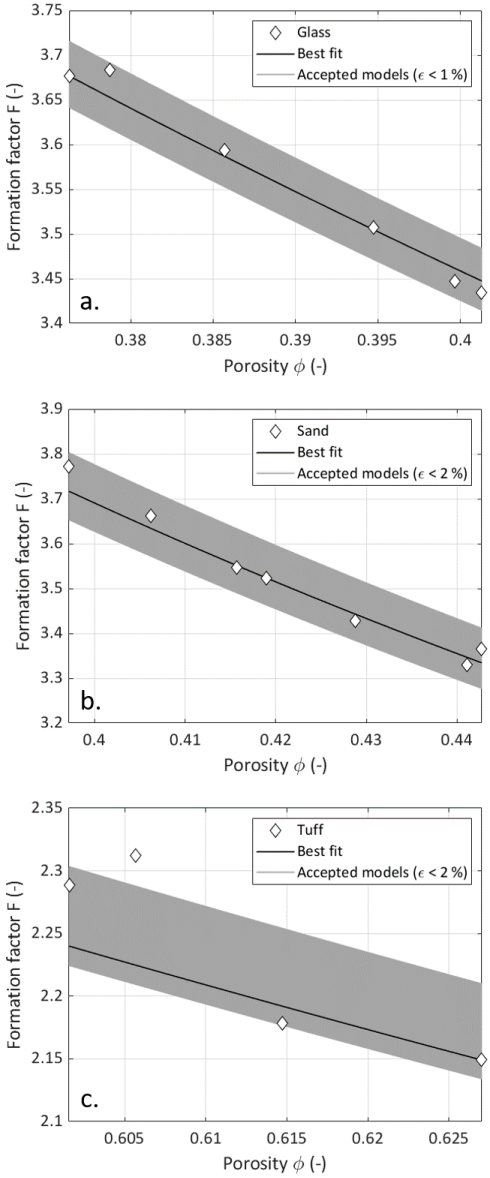

Figure 4: Formation factor of samples with different porosity values: (a) glass beads, (b) sand, and (c) tuff grains (Friedman et al. 2002). The sets of adjusted model parameters a and τ are given in Table 1.

We observe from Table 1 that a and τ values are close to each other for all samples from Friedman et al. (2002). However, these parameters have higher values than for Bolève et al. (2007) dataset. This comes from the fact that some complexity is added in the dataset from Friedman et al. (2002). Indeed, the samples of Friedman et al. (2002) combine particles of different sizes. In this case, smaller grains can fill the voids left by bigger grains. This grains arrangement decreases the medium porosity but increases its tortuosity and constrictivity. Furthermore, sand and tuff grains have rougher surface and are less spherical than glass beads. This explains the misfit increase between data and model for glass, sand, and tuff samples (Friedman et al. 2002). Nevertheless, even for tuff grains, the misfit between data and model is still very low compared to the computed MAPE from Bolève et al. (2007) samples. This is due to that for Bolève et al. (2007), a wide range of pore water conductivity values is explored and thus electrical properties vary much more (over 3 orders of magnitude) than in the case of Friedman et al. (2002).

4.2 Testing the model on consolidated rock samples

In this section, we test our model against datasets of Garing et al. (2014), Revil et al. (2014), and Cherubini et al. (2019). They study carbonate samples from the reef unit of Ses Sitjoles site (from Mallorca), Fontainebleau sandstones, and two Estaillades limestones (rodolith packstones), respectively.

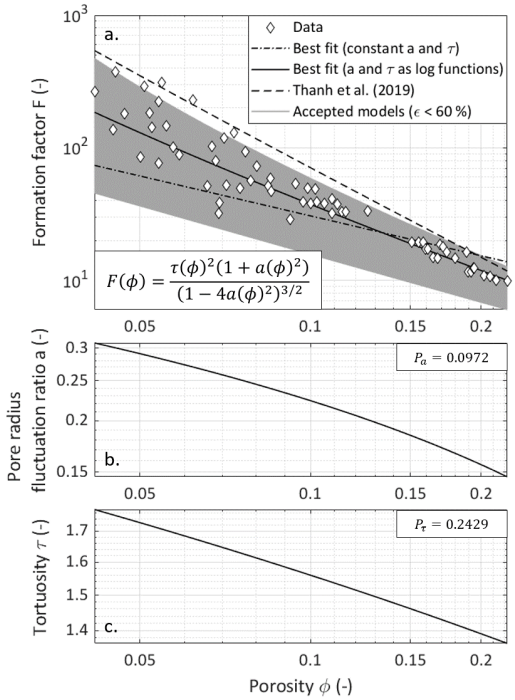

Figure 5: (a) Formation factors of a set of Fontainebleau sandstones versus porosity (the dataset is from Revil et al. 2014). Model parameters are given in Table 1. (b) and (c) a and τ are defined as logarithmic functions of the porosity ϕ.

Revil et al. (2014) obtained a wide range of formation factor values for a large set of Fontainebleau sandstone core samples over a large range of porosity. We first test our model with constant values of a and τ, but we observed that the model could not fit data (see Fig. 5a). This can be explained by the fact that this dataset is composed of numerous sandstone samples presenting a wide range of porosity values (from 0.045 to 0.22). Therefore, we consider that the samples have distinct pore geometry which is describable by $a(\phi)$ and $\tau(\phi)$ distributions, presented in section 2.4 and plotted on Figs. 5b and 5c. We observe that parameters a and τ logarithmic evolution with the porosity ϕ are physically plausible as lower porosity can reflect more complex medium geometries (i.e., more constrictive and more tortuous), described with higher values of a and τ. On Fig. 5a, we also plot the model from Thanh et al. (2019). Even if the curve presents a slope similar to dataset, it overestimates the formation factor.

Despite a quite wide dispersion of the formation factor data for the lowest porosities, it appears that the proposed model is well adjusted to the dataset. Indeed, the proposed model MAPE $\epsilon = 22.62$ % (see Table 1), while $\epsilon = 89.63$ % for the model from Thanh et al. (2019). Note that the relatively high MAPE value comes from the large spread of the formation factor values. Thus, it seems that taking into account the constrictivity of the porous medium in addition to the tortuosity highly improves modeling.

Fig. 6 shows the dependence of electrical conductivity with pore-water electrical conductivity for two limestone samples (named L1 and L2) from Cherubini et al. (2019). Table 1 shows that model parameters and surface conductivity values are larger than for the unconsolidated samples from Bolève et al. (2007) and Fried-

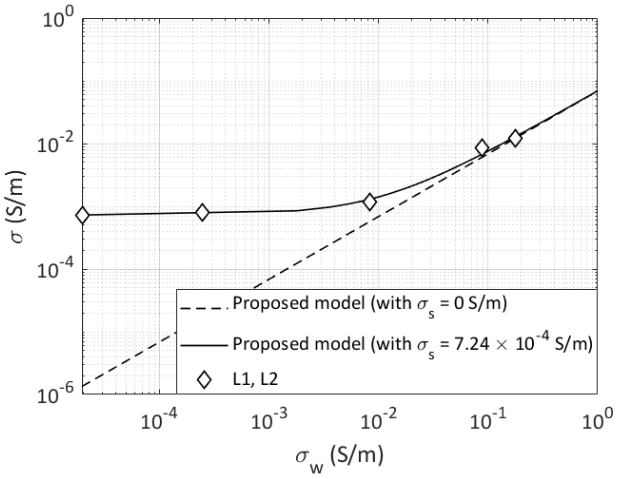

Figure 6: Electrical conductivity of two limestones (L_1 and L_2) versus water electrical conductivity. The dataset is from Cherubini et al. (2019) and model parameters are given in Table 1.

man et al. (2002). This is explained by the fact that natural rock samples can present a more complex geometry and larger specific surface area than glass beads samples. Cherubini et al. (2019) predict the surface electrical conductivity with the model from Revil et al. (2014). They obtain $\sigma_s = 7.0 \times 10^{-4}$ S/m, which is very close to the value obtained in this study. Furthermore, the computed errors for the dataset of Bolève et al. (2007) and for these limestones are close to each other. This test illustrates that even for more complex porous media, the proposed model has still a good data resolution.

Garing et al. (2014) conducted X-ray microtomography measurements on carbonate samples to classify them by pore types and thus they highlight three groups:

1. "Inter" samples present intergranular pores. This pore shape is quite comparable with sandstones porosity type.

2. "Multi" samples hold multiple porosity types: intergranular, moldic, and vugular. Microtomograms of "multi" samples show small but well connected pores. The analyze conducted by Garing et al. (2014) revealed that for samples with smaller porosity, pores are smaller on average, but still numerous and well connected, even for a reduced microporosity.

3. "Vuggy" samples possess vugular porosity. Microtomography highlights the presence of few vugs badly connected, which are less numerous for samples of lower porosity.

Fig. 7 presents the results of formation factor computation versus porosity. As for the dataset from Revil et al. (2014), the proposed model is adjusted using Eq. (31), which considers that model parameters are logarithmic functions of porosity. Despite some dispersion for "inter" and "vuggy" samples (i.e., the acceptance criterion $\epsilon < 40$ %), the model explains well the data for all porosity types and present low MAPE values (Table 1).

The analysis of parameters P_a and P_τ reveals that they present consistent values for the different porosity types. Indeed, for "vuggy" samples, P_a is small while P_τ is high (Fig. 7c). According to Eqs. (29) and (30), these values lead to low and high values for a and τ, respectively (Table 1), and this is consistent with the microtomography analysis from Garing et al. (2014). Indeed, since these samples present large vugs badly connected (i.e., few microporosity), the microstructure is very tortuous but pores are not constricted. Furthermore, for samples with lower porosity, vugs are still present in "vuggy" samples, but they are less numerous, which leads to a microstructure even more tortuous, but nearly as constrictive as for the more porous samples. Moreover,

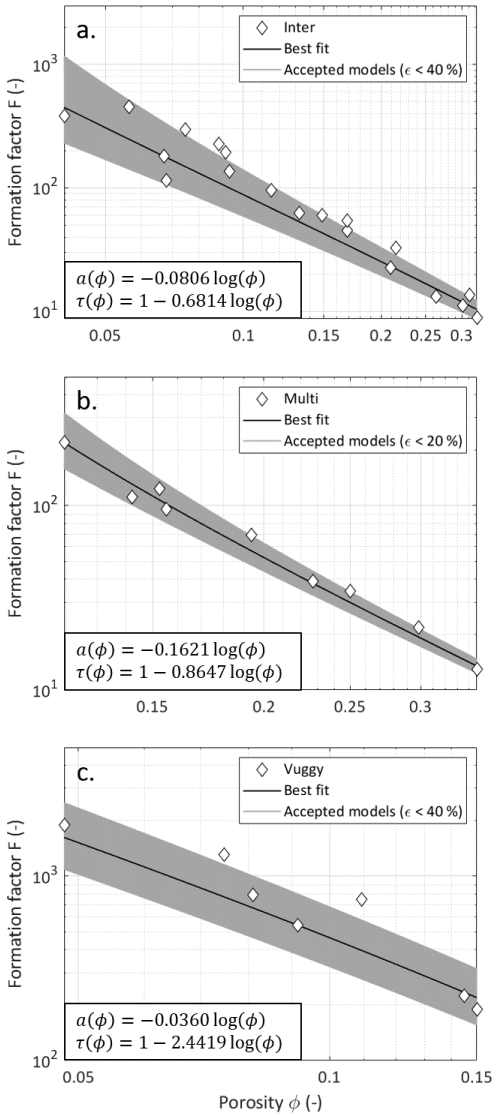

Figure 7: Formation factors of a set of carbonate rocks classified by pore types versus porosity. The dataset is from Garing et al. (2014). The model parameters are given in Table 1. The proposed model parameters are considered to be logarithmic functions of ϕ. (a) "inter" stands for samples with intergranular pores (b) "multi" gathers samples with multiple porosity types: intergranular, moldic, and vuggy. (c) "vuggy" represents samples with vugular porosity.

for "inter" and "multi" samples (Figs. 7a and 7b), P_a and P_τ are closer in value to the parameters of the sandstone samples from Revil et al. (2014) than to the parameters of "vuggy" samples because they have, among other types for the "multi" samples, intergranular porosity. Note that higher P_τ value can be attributed to the more complex structure of carbonate minerals compared to sandstone samples. Furthermore, the high value of P_a for the "multi" samples can be explained with the microtomography observations from Garing et al. (2014). Indeed, constrictivity increases a lot for samples with lower porosity because microporosity is reduced while there are less molds and vugs. Consequently, we conclude that this detailed analysis of model parameters help us to retrieve some characteristic features of the pore space from electrical conductivity measurement.

4.3 Electrical conductivity monitoring of precipitation and dissolution processes

In this section, we consider the numerical datasets from Niu et al. (2019). These authors conduct numerical simulations of dissolution and precipitation reactions on digital representations of microstructural images. They simulate the dissolution of a carbonate mudstone sample and the precipitation of a sample of loosely

packed ooids. For the carbonate mudstone sample, the pore space image is obtained from a microtomography scan while the ooids sample is a synthetic compression of sparsely distributed spherical particles (Niu et al. 2018). The carbonate mudstone sample has an initial porosity of 13 % and the ooids sample has an initial porosity of 30.2 %.

In numerical simulations, the main hypothesis of Niu et al. (2019) is that fluid transport is advection dominated. Then, under this condition, they studied two limiting cases for both dissolution and precipitation: the transport-limited case and the reaction-limited case (Nunes et al. 2016). In the transport-limited case, the reaction at the solid-liquid interface is limited by the diffusion of reactants to and from the solid surface. In the reaction-limited case, the reaction is limited by the reaction rate at the solid-liquid interface.

Their results are presented in Figs. 8a, b, and 9a, b. It appears that for both precipitation and dissolution, the transport-limited case influences the most electrical and fluid flow properties. Indeed, it can be seen in Fig. 8a that for reaction-limited precipitation, a 10 % decrease in porosity leads to an increase in the formation factor from 7.5 to 20, while for transport-limited precipitation, the formation factor reaches 140 for a porosity decrease of less than 2 %. In case of dissolution (Fig. 8b), for a similar decrease of the formation factor, porosity increases only by 3 % in the transport-limited case, while it has to increase by 15 % in the reaction-limited case. The same observations can be made on Figs. 9a and 9b. The variations of permeability are much greater in the transport-limited case than in the reaction-limited case for a lower porosity variation.

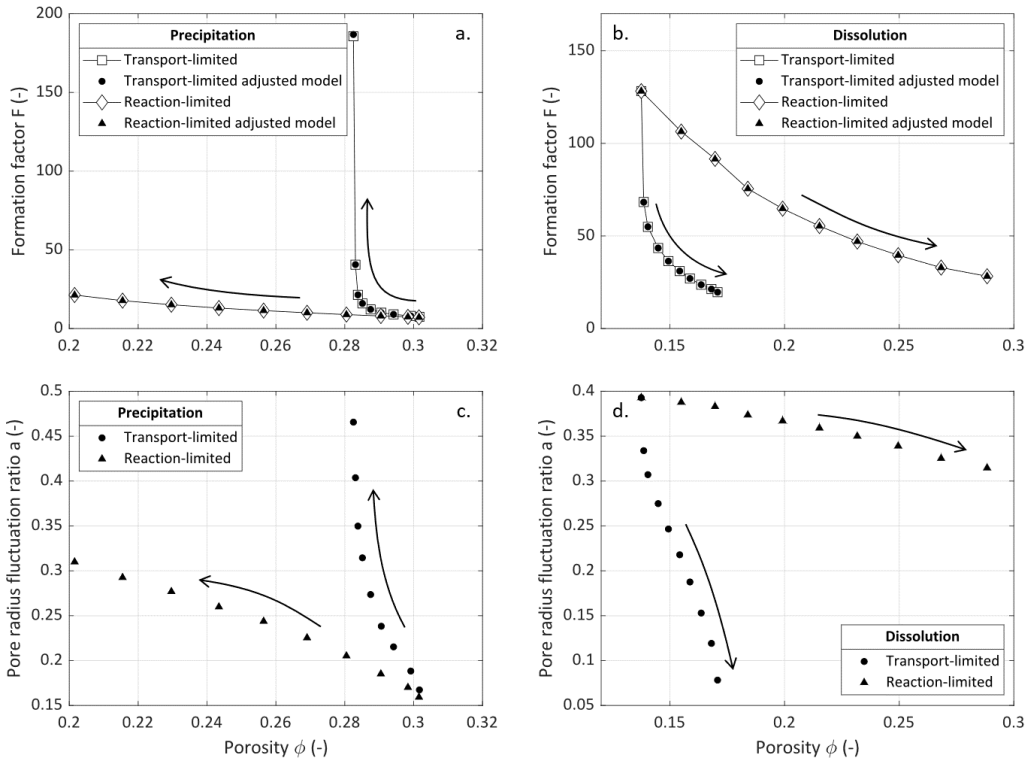

Figure 8: Electrical simulation results for two limiting cases (tansport-limited and reaction-limited) of calcite precipitation and dissolution from Niu et al. (2019). Arrows indicate the direction of dissolution or precipitation process evolution. (a) and (b) Formation factor versus porosity obtained by Niu et al. (2019) simulations and compared with the adjusted model for precipitation and dissolution, respectively. Model parameters are given in Table 1: the tortuosity τ is considered to be constant while the pore radius fluctuation ratio a is the only adjustable parameter of the model. (c) and (d) Evolution of the parameter a which increases when the porosity decreases.

The authors of this study justify the shapes of F and k^{REV} curves with their observations on the digital representations of the microstructural evolution. In the reaction-limited case they observe that precipitated or dissolved minerals are uniformly distributed over grain surfaces. This consequently barely affects electrical and fluid flow properties. On the contrary, in the transport-limited case, dissolution and precipitation mainly occur in some specific areas where fluid velocity is high. This significantly modifies electrical and fluid flow patterns. In the case of transport-limited precipitation, new particles accumulate in pore throats while minerals are preferentially dissolved in the already well opened channels.

To adjust the proposed model to the data, a first set of parameters a and τ has been determined at the initial state with the Monte-Carlo approach. Then, only parameter a is adjusted with the model to each new data point using the least square method. We consider that only a is affected by dissolution and precipitation because these processes mostly affect the pore shape. Indeed, the results of the pore network modeling developed by Steinwinder et al. (2019) to simulate the impact of pore-scale alterations by dissolution and precipitation on permeability, show that pore throats are important parameters to take into account. However, for the proposed model of this study, the assumption that only a varies requires slow processes of dissolution and precipitation in order to keep the cylindrical shape of pores (Guarracino et al. 2014). Besides, we fit parameter a at each time step rather than using the logarithmic law since it lacks physical meaning to explain this parameter time evolution.

Niu et al. (2019) computed the hydraulic tortuosity τ_h (-) from the simulated fluid velocity field for all of their data. They found nearly constant values defined between 1 and 2. As we computed τ = 1.3 and τ = 1.8 in pre-

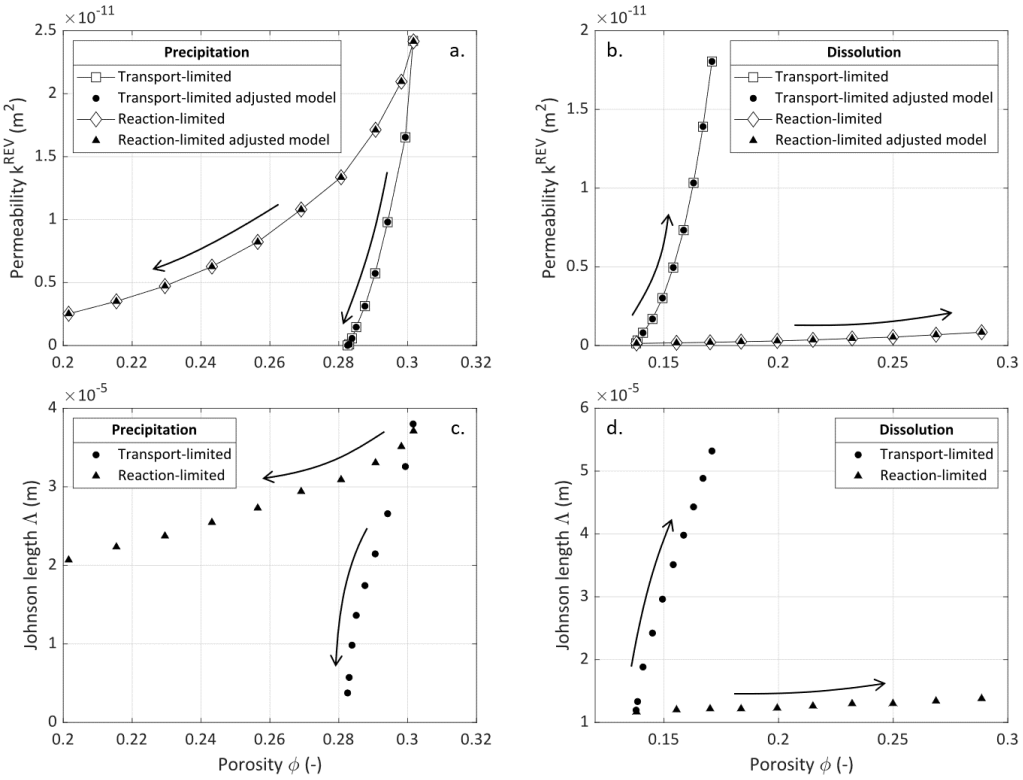

Figure 9: Fluid flow properties simulation results of two limiting cases (tansport-limited and reaction-limited) of calcite precipitation and dissolution from Niu et al. (2019). Arrows indicate the direction of dissolution or precipitation process evolution. (a) and (b) Permeability versus porosity obtained by Niu et al. (2019) simulations and compared with the proposed model for precipitation and dissolution, respectively. The model parameters are given in Tables 1 and 2: as values of the tortuosity τ and the pore radius fluctuation ratio a are reused from the formation factor modeling, the Johnson length Λ is the only adjustable parameter of the model. (c) and (d) Evolution of the parameter Λ which increases with porosity.

cipitation and dissolution, respectively, these results are within the predicted range of the simulated data from Niu et al. (2019) and confirm our hypothesis that constrictivity is the pore feature most impacted by dissolution and precipitation processes. However, to interpret the evolution of the formation factor during dissolution (F decreases) and precipitation (F increases), Niu et al. (2019) computed the electrical tortuosity ($\tau_e = F\phi$, no unit) of their porous medium and obtained high values (from 2 to 200), varying over 1 to 2 decades for the transport-limited cases. These overestimated values of the medium tortuosity highlight that constrictivity and the bottleneck effect should not be neglected to evaluate how dissolution and precipitation processes affect the pore structure.

Figs. 8a and 8b show that in each case the proposed model accurately fits the data with computed errors lower than 1 % (see Table 1). As presented on Figs. 8c and 8d, parameter a follows monotonous variations: it decreases when the porosity increases. We define a as the ratio of the sinusoidal pore aperture r' over the mean pore radius $\bar{r}$ (see the definition of a in section 2.1.1). When a increases, it can be caused by the increase of r', which involves a stronger periodical constriction of the pore aperture, and/or by the decrease of the mean pore radius $\bar{r}$. On the contrary, when a decreases, it implies the increase of $\bar{r}$ and/or the decrease of r', which lead to thicker pores with smoother pore walls, respectively. These variations are consistent with the fact that precipitation and dissolution affect the pore geometry through the sample. In case of precipitation pore throats shrink while they are enlarged with dissolution. It can also be observed on Figs. 8c and 8d that a shows stronger variations in the transport-limited case than in the reaction-limited case. This is consistent with the fact that transport-limited reactions occur in localized areas which will strongly affect the pore properties.

The relation between the permeability k^{REV} and the Johnson length Λ is obtained by combining Eqs. (39) and (42):

$$k^{REV} = \Lambda^2 \frac{(1-4a^2)^{3/2}}{1+2a^2} \frac{\phi}{8\tau^2} \tag{50}$$

The values of parameters a and τ are taken from the adjusted models of the formation factor. Thus, the Johnson length Λ is the only adjustable parameter to fit the data and is fitted with the least square method. Values are given in Tables 1 and 2.

Table 2: Values of the Johnson length Λ and of the MAPE ϵ (defined in Eq. (49)) for the modeling of permeability versus porosity for the samples from Niu et al. (2019). Λ is adjusted with the least square method. Sample names are defined in Table 1.

Sample	Λ (10^{-5} m)	ϵ (%)
Dissolution transport-limited	1.196 - 5.320	0.10
Dissolution reaction-limited	1.167 - 1.380	0.03
Precipitation transport-limited	0.376 - 3.800	0.24
Precipitation reaction-limited	2.069 - 3.711	0.06

On Figs. 9a and 9b, one can observe that for each case the model accurately fits the data with computed errors lower than 1 % (see Table 2). As presented on Figs. 9c and 9d, parameter Λ follows monotonous variations: it increases with porosity. It can also be observed that Λ varies more in the transport-limited case than in the reaction-limited case. For the reaction-limited dissolution it is even nearly constant. Niu et al. (2019) found Johnson lengths with the same order of magnitude and with similar variations except in the case of transport-limited precipitation where their values do not follow a monotonous behavior for low porosity values. Either way, Niu et al. (2019) interpret the Jonhson length as an effective radius of their porous medium which shows monotonous variations during precipitation (Λ decreases) and dissolution (Λ increases). In the

proposed model, the parameter a describes how dissolution and precipitation processes affect the shape of the pore radius (i.e., its constrictivity) while Λ is linked to the fractal distribution of pore size D_p and to the maximum average radius $\bar{r}_{max}$. As we suppose dissolution and precipitation slow enough not to interfere with the pore size distribution, D_p remains constant for each sample. On the contrary, when dissolution or precipitations occurs, it is expected for the pores to grow or to shrink, respectively. Therefore, The monotonous variations of Λ highlight the increase or decrease of $\bar{r}_{max}$ during dissolution or precipitation, respectively. This result is in accordance with the variations of a which can impact $\bar{r}$. Consequently, we describe the pore space evolution during dissolution and precipitation as illustrated in Fig. 10. Indeed, the decrease of a is caused by dissolution, which enlarges the pore and flattens its pore walls. On the contrary, precipitation affects the pores by increasing a, which means that pores shrink and become more periodically constricted because of r' increase. We thus believe that this interpretation of the electrical conductivity measurement is an important issue for future research on the impact of dissolution and precipitation on the pore shape.

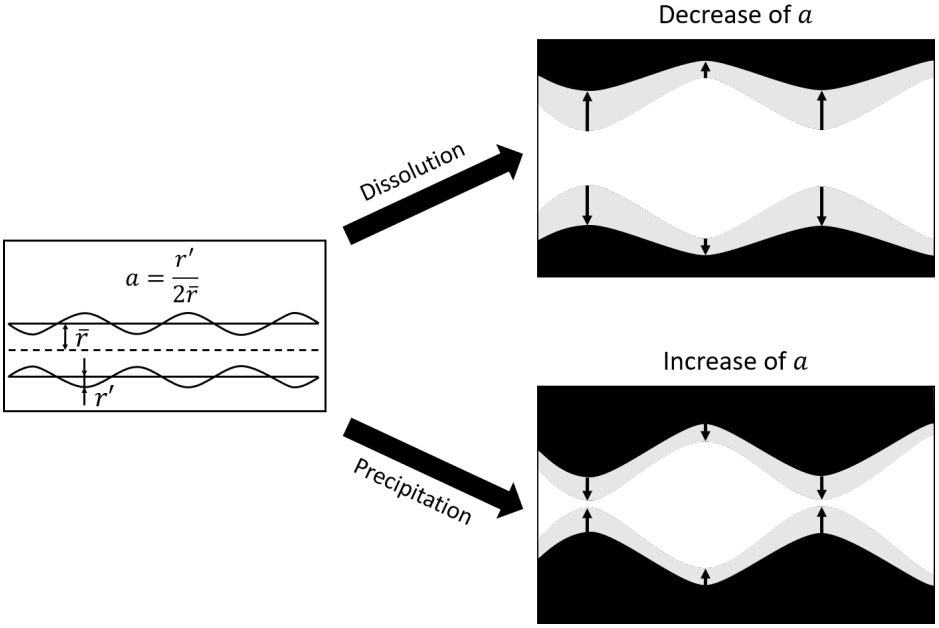

Figure 10: The pore radius fluctuation ratio a is the model parameter which is updated during dissolution and precipitation reactions. Under precipitation a increases, hence the pore aperture varies more. On the contrary a decreases under dissolution and hence the pore becomes smoother.

5 Conclusion

In the present work we express the electrical conductivity and the formation factor of the porous medium in terms of effective petrophysical parameters such as the tortuosity and the constrictivity. The model is based on the conceptualization of the pore space as a fractal cumulative distribution of tortuous capillaries with a sinusoidal variation of their radius (i.e., periodical pore throats). By means of an upscaling procedure, we link the electrical conductivity to transport parameters such as permeability and ionic diffusion coefficient.

The proposed model successfully predicts electrical conductivity and formation factor of unconsolidated samples and natural consolidated rock samples. For datasets of sandstones or carbonates with large range of porosity values, we set that a and τ follow logarithmic functions of ϕ. These empirical relations allow the model to accurately fit the datasets. On one hand, for the sandstone samples, the prediction fits much better than previously published models, while on the other hand, the model parameter analysis shows strong agreement with the porosity types description thanks to X-ray microtomography investigations on carbonate samples.

Even if our model is designed for porous media in which the surface conductivity can be neglected, it is possible to take it into account at very low salinity. We do not express it as a function of the pore structure parameters, but determine its value empirically. The comparison of its value with the one found for other models on the same datasets shows that this approach is consistent and reasonable for the purpose of this model.

The model is finally compared to a numerical dataset from simulations of dissolution and precipitation reactions on digital representations of microstructural images. The model can reproduce structural changes linked to these processes by only adjusting a single parameter related to the medium constrictivity: the pore radius fluctuation ratio a. We observe that this parameter follows monotonous variations under dissolution or precipitation conditions that makes it a good witness of these chemical processes effect on the pore structure.

We believe that the present study contributes to a better understanding of the links between the electrical conductivity measurement, the pore space characteristics and the evolution of the microstructural properties of the porous medium subjected to dissolution and precipitation processes, therefore enhancing the possibility of using hydrogeophysical tools for the study of carbonate hydrosystems. In the future, we will extend this approach to partially saturated conditions and include these new petrophysical models in an integrated hydrogeophysical approach to better understand hydrosystems in the critical zone.

6 Acknowledgments

The authors warmly thank Qifei Niu and the other anonymous reviewer for the constructive comments that helped to greatly improve the manuscript quality. The authors wish to thank the editor for the effective editing process. The authors strongly thank the financial support of the CNRS INSU EC2CO program for funding the STARTREK (Système péTrophysique de cAractéRisation du Transport Réactif en miliEu Karstique) project. The authors are also very thankful for the wise comments of Roger Guérin.

3.3 Conclusion to the paper

The main result of this paper is that constrictivity is a petrophysical parameter which is of major importance to describe the effects of the pore space on the electrical conductivity. This is especially true for complex rock samples, presenting various microstructural shapes for wide porosity ranges. Furthermore, dissolution and precipitation processes mostly impact constrictivity evolution. This result goes against usual representations, which consider exaggerated tortuosity evolution instead. Taking into account constrictivity allow to consider that dissolution and precipitation processes do not affect pore walls homogeneously. Indeed, these chemical reactions take place at the pore throats. Thus, precipitation tends to reduce the connectivity between the pores by closing the pore throats. This corresponds to an increase of the constriction effect. On the contrary, dissolution effect is to smoother the pore walls and enlarge the pore throats, which corresponds to a constrictivity decrease.

Part II

Material and method

CHAPTER

4 Design and tests of the laboratory set-up

4.1 Introduction of the chapter

The water flow can interact with the porous medium and induce calcite dissolution or precipitation, depending on its pore water chemical composition, the temperature, and the pressure conditions. These chemical processes occur at the pore scale and affect the physico-chemical properties of the entire porous rock. These structural modifications can be monitored at the core scale (from mm to m, Baker et al. 2015) using geo-electrical methods thanks to their sensitivity to hydrological parameters, such as porosity and permeability, but also to the minerals surface state.

Since the study of the dissolution and precipitation of calcite by geo-electric methods is scarce and that the results reported in the literature present contradictions, it appears important to conduct a joint study of these processes by comparing the results of several geo-electric methods. This chapter intends to describe the design of the laboratory set-up that I developed for this thesis.

As the subject of this thesis is related to the study of the critical zone processes, the experimental conditions tend to reproduce near-surface conditions by conducting all the experiments at ambient temperature and pressure in a carbonate matrix.

4.2 The studied carbonate material

Carbonate rocks present a wide microstructural diversity and the aim of this thesis is to focus on calcite dissolution and precipitation geo-electrical signatures, rather than studying a specific type of carbonate sample. Therefore, I chose to use a non-consolidated sample of pure calcite. This synthetic sample is thus composed of loose calcite grains obtained from a pure crushed marble with more than 99 % calcium carbonate minerals. These grains are referenced as *Durcal 130*, a product from the Omya company.

The crushed calcite contains a wide variety of grains size. Thus, it is sieved to extract a fine range of grain diameters between 125 µm and 250 µm (see Figure 4.1). This range is chosen so that the polarization of the initial calcite matrix takes place on a lower frequency range than those monitored by Wu et al. (2010) and Izumoto et al. (2020a), which are associated to polarization induced by calcite precipitation. This frequency

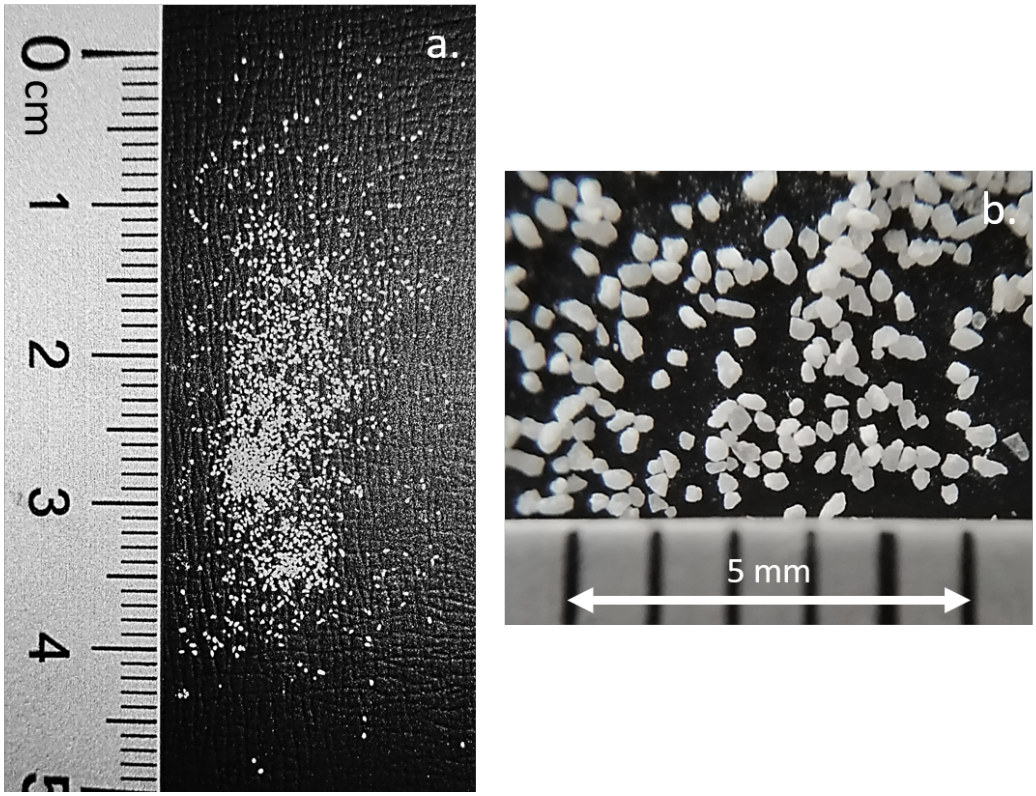

Figure 4.1: Calcite grains with grain diameters comprised between 125 µm and 250 µm. (a) photography of the grains. (b) photography of the grains using a macro lens allowing a x6 magnification.

range is determined using the Stern layer polarization model from Leroy et al. (2017), which states

$$f_b = \frac{4\, D_b\, M}{\pi\, d_g^2}, \tag{4.1}$$

where f_b (Hz) is the critical frequency of the Stern layer, $D_b = 1.5 \times 10^{-10}$ m^2 s^{-1} is the surface diffusion coefficient of the counter-ions in the Stern layer (the counter-ions are Na^+ and Ca^{2+}, D_b value was determined by Leroy et al. 2017), $M = 30.7$ is a dimensionless parameter characterizing the effect of the diffuse layer on the Stern layer, and d_g (m) is the grain diameter. Using Equation (4.1) and the values of the parameters determined by Leroy et al. (2017), the critical frequency ranges from 0.094 Hz and 0.38 Hz.

4.3 The electrodes

4.3.1 Ag-AgCl non-polarizable electrode principles

For electrical potential measurements, Petiau and Dupis (1980) recommend to use silver-silver chloride (Ag-AgCl) electrodes given their low noise and their short stabilization time (e.g., Jougnot and Linde 2013). Other types of electrodes, such as Cu-$CuSO_4$ and Pb-$PbCl_2$, are tested in the literature (e.g., Petiau and Dupis 1980; Abdulsamad et al. 2016) and enable high quality acquisitions. However, the advantage of the Ag-AgCl type is that chloride anions Cl^- are the only ions that diffuses from the electrode to the porous medium. Furthermore, Cl^- is a bystander ion for the calcite system (see Section 1.2.1). It has thus a limited impact compared to copper

Cu^{2+} or lead Pb^{2+}, which are metal ions that can easily react with carbonate ions[1]. Other studies have shown that metallic electrodes placed outside the sample to ensure a zero electric field at the electrode location and connected to the sample through an electrolyte could be a good alternative (e.g., Zimmermann et al. 2008; Izumoto et al. 2020a). However, this type of electrodes that I designed using stainless steel or brass were not a success and lead me to choose Ag-AgCl electrodes instead.

As shown on Figure 4.2, Ag-AgCl electrodes correspond to a solid wire in silver $Ag_{(s)}$ coated with solid sodium-chloride salt $AgCl_{(s)}$ (the AgCl coating is obtained by bleaching the silver wire during 45 min) and immersed in a tube filled with a solution, called the chamber fluid, containing soluble chloride ions $Cl^-_{(aq)}$, which is here a solution of sodium chloride NaCl.

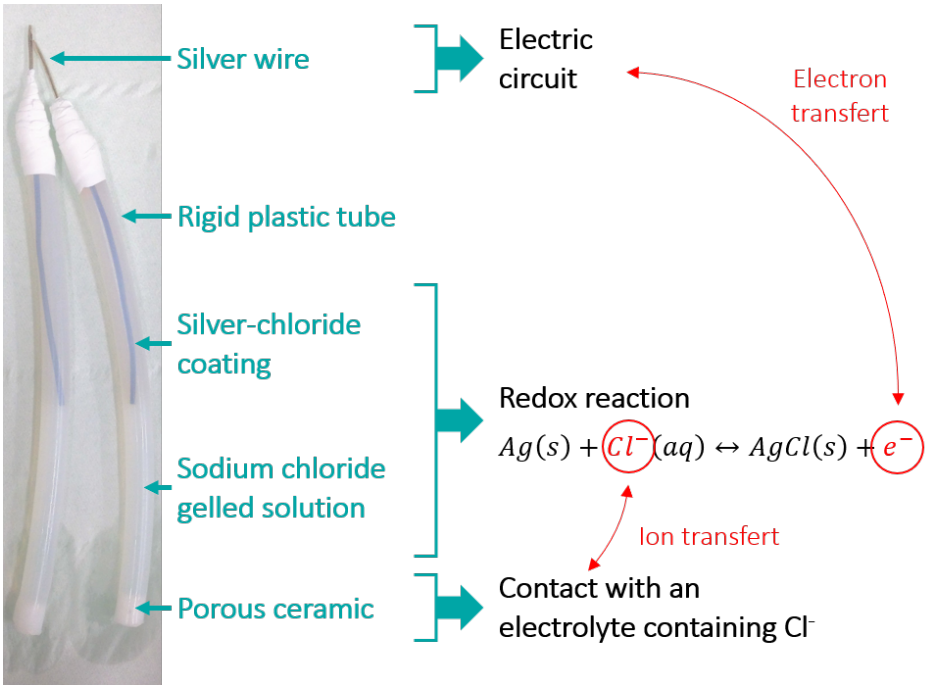

Figure 4.2: Photography of a pair of Ag-AgCl electrodes and their different compartments involved in the contact between the electric circuit and the porous medium.

If the silver wire was directly immersed in the NaCl solution, it would directly dissolved into silver ions $Ag^+_{(aq)}$ to ensure the electrical contact between the electric part and the nonmetallic part of the circuit through ionic and electronic transfers

$$Ag_{(s)} \rightleftharpoons Ag^+_{(aq)} + e^-, \tag{4.2}$$

where e^- represents an electron. Thus, the interest of the AgCl coating is that it can compensate this loss of solid silver by dissolving itself instead following

$$Ag^+_{(aq)} + Cl^-_{(aq)} \rightleftharpoons AgCl_{(s)}. \tag{4.3}$$

[1] $PbCO_3$ corresponds to cerusite, a mineral present in lead-bearing veins. Copper can form two different minerals: $Cu_2(OH)_3CO_3$ corresponding to green malachite and $Cu_3(OH)_2(CO_3)_2$ corresponding to blue azurite. Malachite and azurite are often associated, they are oxydized minerals of copper that can be found in chalcopyrite deposits (Foucault et al. 2014).

The above partial equations yield to an equilibrium between the silver atoms and the chloride anions described by

$$Ag_{(s)} + Cl^-_{(aq)} \rightleftharpoons AgCl_{(s)} + e^-. \tag{4.4}$$

These chemical equilibria show that some silver ions will be dissolved from the AgCl coating into the chamber fluid. However, since the solubility constant of AgCl salt is low ($K_{AgCl} = 1.8 \times 10^{-10}$ at 25 °C), the intrinsic electrical potential of the electrode will be mainly determined by the Cl^- anions concentration (Janata 2009; Jougnot and Linde 2013).

4.3.2 Electrode design for long-term acquisition

4.3.2.1 Electrode features to reduce the chamber fluid leakage

For long-term laboratory measurements, the Ag-AgCl intrinsic potential can change over time due to leakage of the chamber fluid into the investigated medium (e.g., Petiau and Dupis 1980). Nevertheless, this electrode effect is very limited for short periods and it seems to follow a linear drift that can be removed (e.g., Mboh et al. 2012). In order to minimize this aging effect, two elements of the electrode were used in its design: (1) the use of a micro-porous plugging at the end of the electrode (Maineult et al. 2004), (2) the addition of a gelling agent to the chamber fluid to increase its viscosity (Pichot 1932). The micro-porous plugging is a polyethylene frit with a pore size of 20 µm. However, agar agar powder and gelatin were tested to determine the better gelling agent. Figure 4.3 shows the stability test by measuring the SIP phase spectrum in a water tank filled with a solution of NaCl (C =0.05 mol L^{-1}).

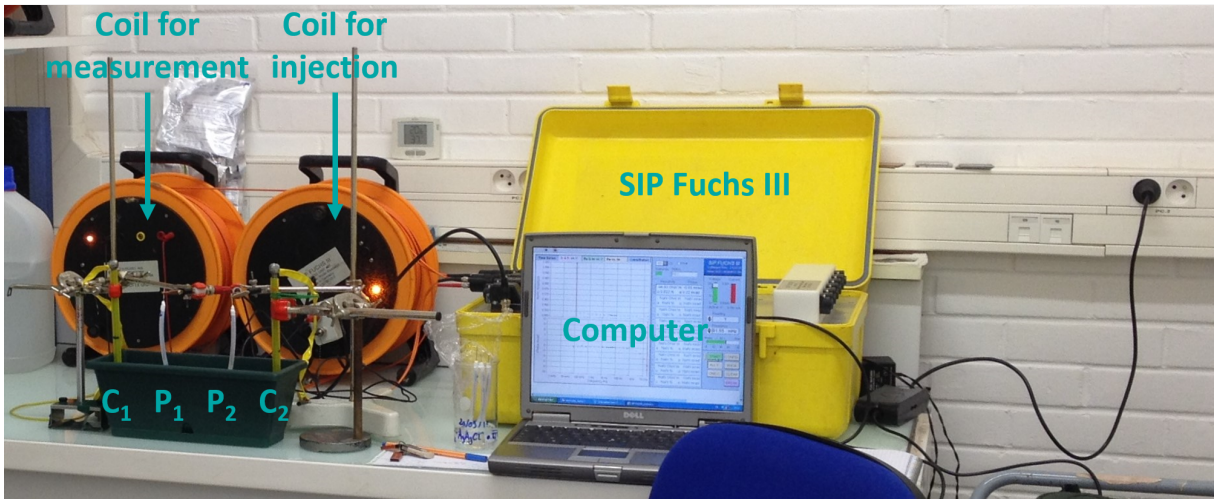

Figure 4.3: Photography of the SIP Fuchs III measuring the complex conductivity of a water tank filled with a solution of NaCl (C =0.05 mol L^{-1}) using a pair of stainless steel electrodes for the injection (referred as C_1 and C_2) and a pair of measuring Ag-AgCl electrodes (referred as P_1 and P_2). The current and potential electrodes are connected to the SIP Fuchs III via fiber optic coils.

The NaCl solution filling the water tank (Figure 4.3) is a free electrolyte, which is thus non-polarizable. Therefore, the measured phase spectrum should remain flat. Figure 4.4 presents the results of this test. For most frequencies the phase remains close to 0 mrad for all pairs of electrodes, but at frequencies above 1 kHz it in-

creases due to the influence of the electrodes (Abdulsamad et al. 2016; Huisman et al. 2016). Therefore, the pair of electrodes with the best design must show the smallest increase of its SIP phase at high frequencies.

On Figure 4.4, three kinds of Ag-AgCl electrodes are compared ; they are made with different NaCl gelled solutions: one with agar agar powder and the two others with gelatin but with a chamber fluid at two different concentrations of NaCl. To assess the effect of the gelling agent, the solution with agar agar powder and one of the solutions with gelatin (light purple curve on Figure 4.2) were prepared with the same NaCl concentration C_1 =0.068 mol L^{-1}. It appears that the polarization of the pair of electrodes made with the agar agar powder is much higher, reaching 100 mrad at 20 kHz, than the polarization of the pair made with gelatin, reaching 28 mrad at 20 kHz. Consequently, gelatin sheets are the selected gelling agent for the chamber fluid.

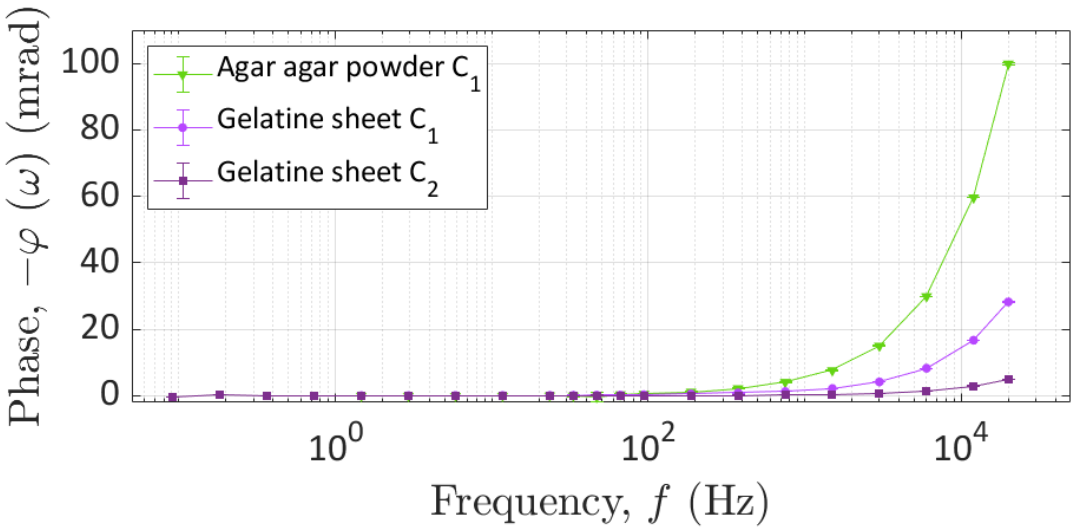

Figure 4.4: SIP phase spectra of the Ag-AgCl electrodes acquired with the SIP Fuchs III for three different NaCl gelled solutions filling the electrode: the first solution is gelled using agar agar powder and the ionic concentration is C_1 =0.068 mol L^{-1}, the second solution is gelled using gelatin with the identical ionic concentration C_1, and the third solution is gelled using gelatin and the ionic concentration is $C_2 = 10C_1$.

4.3.2.2 Reduction of the high-frequency polarization

Abdulsamad et al. (2016) have shown that increasing the NaCl concentration of the chamber fluid reduces the high-frequency polarization of the electrodes. Thus, a pair of Ag-AgCl electrodes with a chamber fluid gelled with gelatine and with a higher NaCl concentration C_2 = 10 C_1 is compared to the pair with the concentration C_1 on Figure 4.4. The increase of NaCl concentration induces a significant decrease of the high-frequency polarization, reaching 5 mrad at 20 kHz. Compared to the results obtained by Abdulsamad et al. (2016), this phase spectrum presents a close high-frequency behavior. Thus, this chamber fluid concentration C_2 =0.68 mol L^{-1} is selected. In addition, one can note that Tallgren et al. (2005) recommend to use Ag-AgCl electrodes immersed in a chamber fluid having a Cl^- concentration of at least 0.7 mol L^{-1}.

4.3.2.3 Reliability test for long-term measurements

These electrodes are designed for long-term laboratory experiments. Thus I performed two tests to measure their reliability despite: (1) Cl^- diffusion, (2) aging during several weeks.

To control the impact of Cl^- diffusion, the test presented by Jougnot and Linde (2013) was reproduced, with the difference that in Jougnot and Linde (2013), the test is conducted for one electrode, whereas here two electrodes have been used, doubling the diffusion. The test consists in the immersion of the electrodes in a beaker filled with deionized water having an initial conductivity σ_w =0.9 µS cm^{-1}. Then, the pore water was measured during 700 h (≈ 29 d).

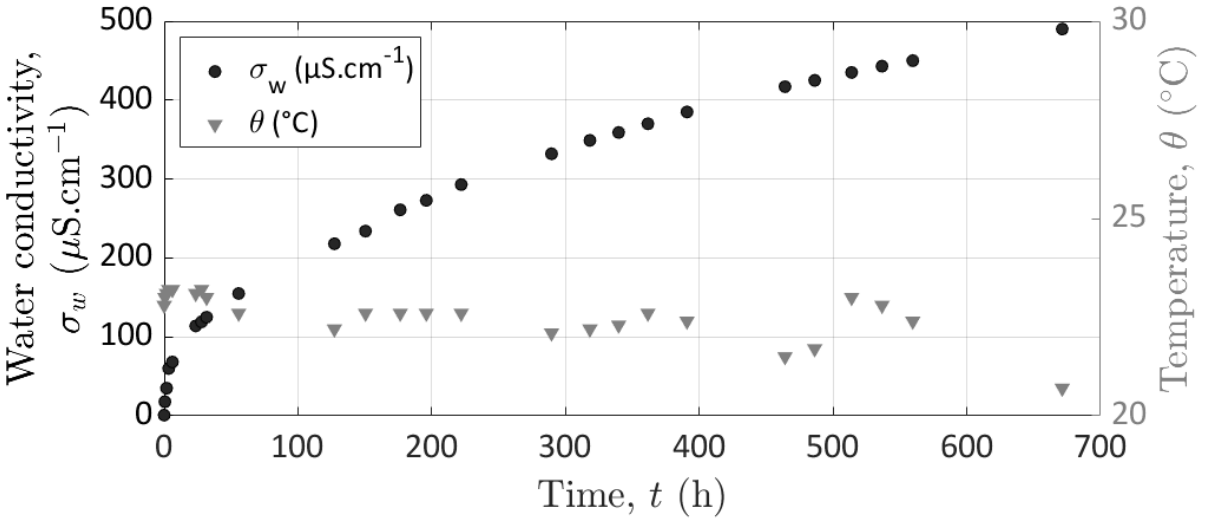

Figure 4.5: Water conductivity and temperature measurements to monitor Cl^- diffusion from the chamber fluid to the water in which the pair of electrodes is immersed.

From Figure 4.5, the water conductivity reaches nearly σ_w = 500 µS cm^{-1} after 700 h and the slope seems always increasing, indicating that they were still leaking due to persistent concentration gradient between the electrode chamber and the beaker. Thus, the impact of Cl^- diffusion cannot be ignored for such initial gradients, but the pore water of the laboratory experiment is much conductive than deionized water, which decreases the diffusion coefficient and thus, the leakage rate (e.g., Revil and Jougnot 2008).

The non-polarizable electrode potential is known to drift with aging. This effect is troublesome for SP investigation, but can be corrected in case of an accurate monitoring. However, this effect has to be tested for SIP acquisition to verify the stability of the electrode behavior. Figure 4.6 presents the SIP phase spectra of the same pair of electrodes at two separate times of acquisition. The first spectrum was acquired 3 d after the conception of the electrodes (July 30th) and the second spectrum was acquired 8 weeks later (September 21st). The two spectra present similar values, except that after 8 weeks, the electrodes polarize a slightly more at high-frequencies (at 20 kHz the phase has increased of 1 mrad) and the error bars increase at low frequencies (below 3 Hz). Thus, aging slightly decreases the electrode accuracy at low frequencies, but has a small impact on the electrodes high-frequency behavior. East and del Valle (2000) attest that Ag-AgCl can at least work for 2 months and explain that the electrode has to be rebuilt if the chamber has to be refilled or if the silver wire coating has

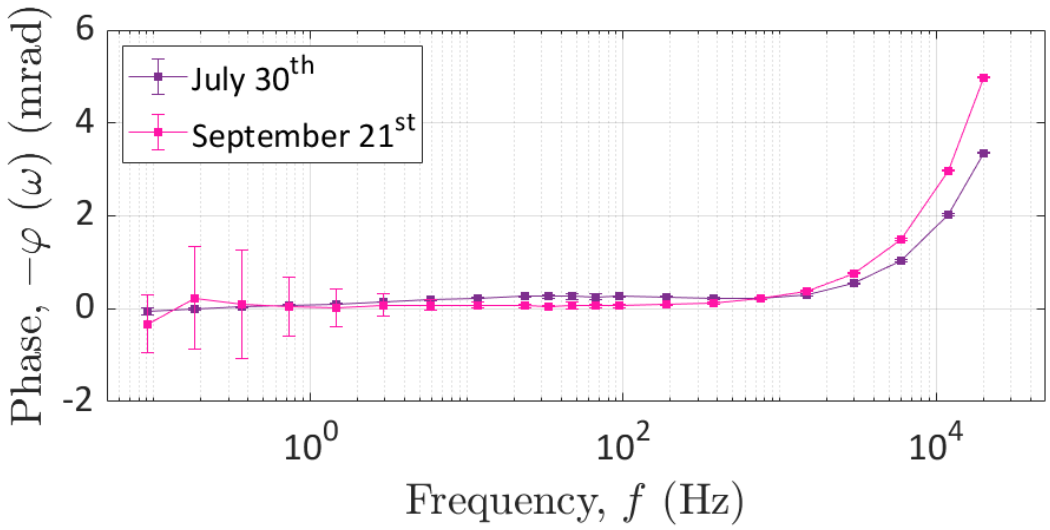

Figure 4.6: SIP phase spectra of the same pair of electrodes acquired 3 d after their conception and 8 weeks later. The error bars are calculated by the SIP Fuch III from the deviations of the values of the repeated measurements.

to be renewed.

4.4 First column design

The sample is thus made of loose grains that have to be contained in a column air and watertight. In addition of being a sample holder, the column is also equipped to enable geo-electrical measurement and the pore water circulation.

4.4.1 Description of the first column

The column is composed of a Plexiglas cylinder of 25 cm long and with an inner and an outer diameter of 9 cm and 10 cm, respectively. Thus, it has a volume of 25 cm^3.

We wanted to discretize the geo-electrical measurements along the column to get its distribution in the medium. Thus, we drilled four holes in the cylinder wall for four measuring electrodes, named P_1, P_2, P_3, and P_4. We flattened the surface to ensure a good sealing with the o-ring of the screwed cable gland holding the electrode (Figure 4.7a and b).

The current electrodes, named C_1 and C_2, are two stainless steel cylinders, whose sides facing the edges of the cylinder are carved to facilitate the distribution of water over their entire surface (Figure 4.7c). These cylinders are drilled in their center to let the water flow and on their side to plug an electrical wire (Figure 4.7c and d).

PVC cylinders are positioned on each side of the current electrodes to screw water inlet and water outlet tube connectors (Figure 4.7a). They also insulate the injection electrodes from the outside and close the measuring circuit.

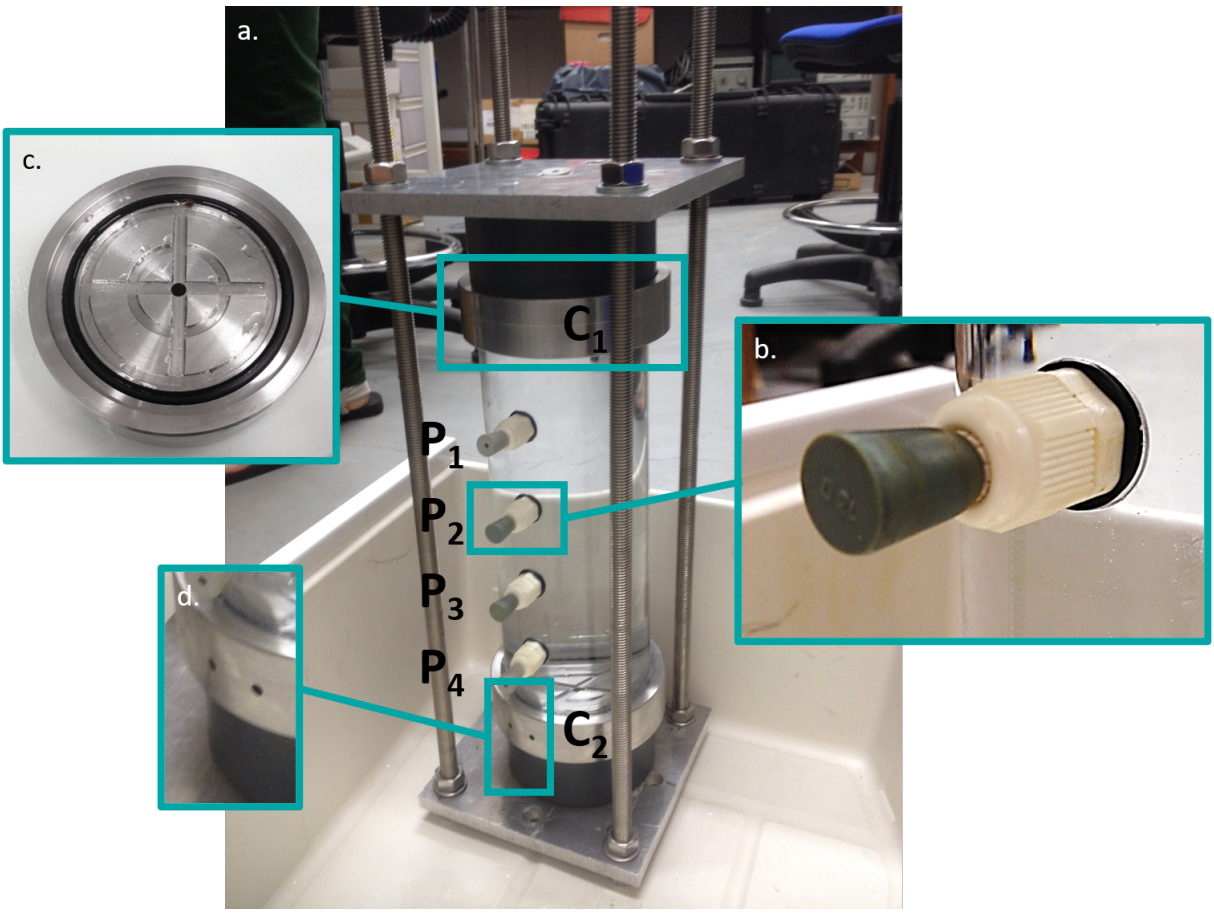

Figure 4.7: (a) photography of the column filled with water to test its waterproofness. C_1 and C_2 refer to the electric current injection electrodes. P_1, P_2, P_3, and P_4 refer to the electric potential measurement electrodes. (b) the cable gland screwed in the Plexiglas cylinder wall and plugged with a rubber stopper. (c) the stainless steel current electrode carved for a better repartition of the water on in surface while injecting. The black rubber O-ring enables to seal the cylinder hermetically. (d) two holes are drilled on the side of the steel cylinder to connect an electric cable for current injection.

4.4.2 Effect of the tightening structure composition

The Plexiglas cylinder, the current electrodes (C_1 and C_2) and the PVC cylinders are maintained with a tightening structure. First a robust metallic structure was chosen (Figure 4.8a), but tests showed that it has an influence on the SIP phase spectrum, so it was compared with a tightening structure made of nylon (Figure 4.8b). This test was realized for the column filled with a solution of sodium-chloride for two measurement electrode spacing: the small spacing corresponds to the dipole P_2-P_3 and the large spacing corresponds to dipole P_1-P_4.

Figures 4.8c and d show that for both small and large spacings, the metallic structure has an influence on the phase amplitude for frequencies below 1 kHz and is more important on the large spacing. On the contrary, the nylon structure does not seem to interfere with the phase amplitude. Therefore, the nylon structure is chosen for following experiments.

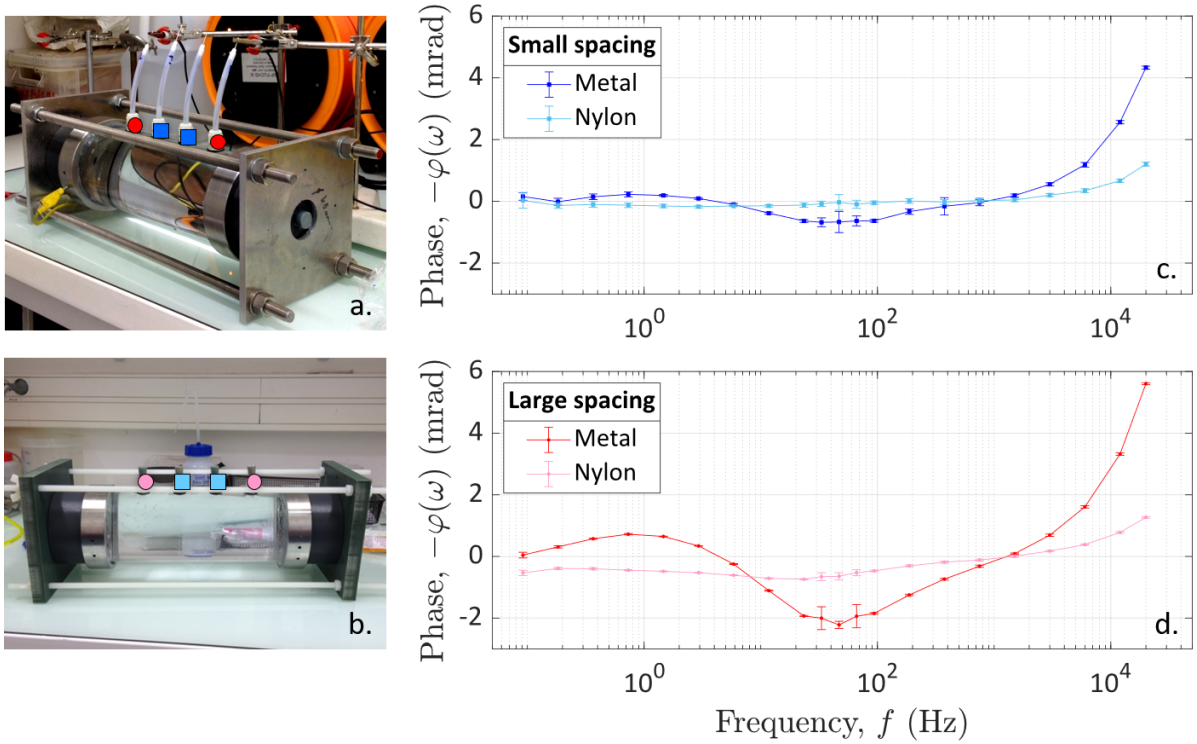

Figure 4.8: Evaluation of the effect of the tightening structure composition using SIP phase spectra measurements with the SIP Fuchs III. (a) photography of the column with the metallic tightening structure. Red discs and blue squares correspond to large and small spacing of the measurement electrodes, respectively. (b) photography of the column with the nylon tightening structure. Pink discs and light blue squares correspond to large and small spacing of the measurement electrodes, respectively. (c) SIP phase spectra of the measurement dipole small spacing (P_2-P_3). (d) SIP phase spectra of the measurement dipole large spacing (P_1-P_4).

4.4.3 Geometrical factor computation from finite-elements modeling

The electrical conductivity is computed from the measured resistance using the geometric factor k_g as presented in Eq. (2.11). Thus, its value is independent of the electrodes configuration, which is taken into account by the geometric factor value. This geometric factor can be computed using analytical derivation from the array geometry when the quadripole is implanted on the ground considered as a half-space where the conductivity variations only take place parallel to the line of electrodes. Otherwise, for complex geometries, numerical computation is required (e.g., Jougnot 2009; Jougnot et al. 2010a).

I used EIDORS (Electrical Impedance and Diffuse Optical tomography Reconstruction Software) for the image reconstruction of the electrical data in the column (Adler and Lionheart 2006). This software is mainly used in medical imaging, but is also developed for geophysical applications requiring 2D or 3D reconstruction of electrical impedance tomographic images based on finite-elements numerical models (e.g., Vaukhonen 1997).

Figure 4.9 shows the designed finite-elements model of the column. This model represents the column geometry and the electrode positions and properties. Only the electrode surface in contact with the calcite sample is taken into account for the computation. Thus, the potential electrodes (P_1, P_2, P_3, and P_4) are reduced to discs with a diameter of 0.5 cm and the current electrodes (C_1 and C_2) are represented as thick rings with an outer

diameter of 9.0 cm and an inner diameter of 1.0 cm. To ensure a good resolution of the model, we have defined a regular and sufficiently fine meshing with a maximum tetrahedral mesh height of 0.2 cm.

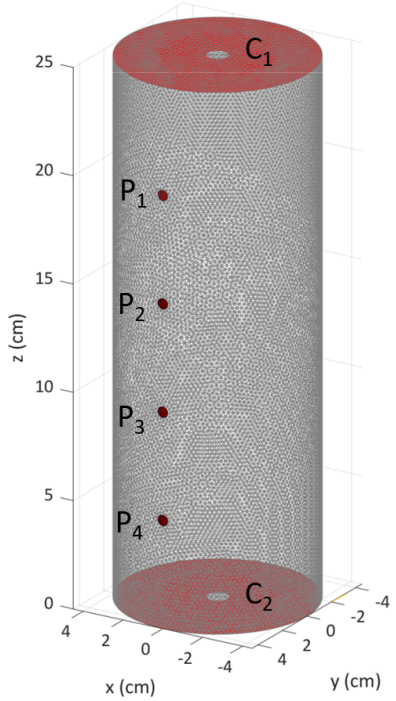

Figure 4.9: The tetrahedral mesh of the column with a maximum tetrahedral mesh height of 0.2 cm. Electrodes meshing is colored with red meshes.

To compute the geometrical factor, we set an homogeneous medium with a conductivity of 1 S m^{-1}. Thus, the geometrical factors of the different arrays are computed and presented in Table 4.1. For each computation, C_1 and C_2 are set as the current injection electrodes. It appears that for the measurement dipole P_1-P_4, the geometric factor is three times smaller than the geometric factor of dipoles P_1-P_2, P_2-P_3, and P_3-P_4, which themselves have a spacing (5 cm) equivalent to one third of the spacing between P_1 and P_4 (15 cm).

For comparison, the formation factors have also been experimentally determined by measuring the column resistance R_c (Ω) for the column filled with a NaCl solution having a conductivity σ_w =3.05 mS cm^{-1} at 20 °C. The results are presented in Table 4.1. Compared to the geometric factors determined numerically, the experimental values are of the same order of magnitude, which confirm the accuracy of the finite-elements model.

4.4.4 Design limitations

4.4.4.1 Sensitivity functions

The sensitivity function captures the changes in the electric potential due to variations of the conductivity within the sample depending on the electrodes position. It is thus defined as the Jacobian matrix of the measured electrical potential with respect to the conductivity distribution in the sample (e.g., Spitzer 1998). One

Table 4.1: Geometrical factors computed using EIDORS finite-elements numerical model and geometrical factors calculated from the column resistance measurement when filled with a NaCl solution having a conductivity σ_w =3.05 mS cm^{-1} at 20 °C. C_1 and C_2 are the current injection electrodes.

Measurement dipole	Numerical geometrical factor k_g (cm)	Measured resistance R_c (Ω)	Measured geometrical factor $\frac{1}{R_c \sigma_w}$ (cm)
P_1-P_2	12.7		
P_1-P_3	6.4		
P_1-P_4	4.2	68.7	4.8
P_2-P_3	12.7	25.7	12.8
P_2-P_4	6.4		
P_3-P_4	12.7		

method to obtain the sensitivity function is to compute the Frechet derivative (e.g., McGillivray and Oldenburg 1990) and serves to assess the depth of investigation of an array (e.g., Edwards 1977). The higher the sensitivity value, the more it will influence the measurement of the electrical potential.

The sensitivity functions of the large spacing array (P_1-P_4 for the measurement dipole) and of the small spacing array (P_1-P_2 for the measurement dipole) are presented on Figure 4.10. As expected, the sensitivity is high at the vicinity of the potential electrodes, but it rapidly decreases with the distance. It seems that the electrodes are only sensitive to a portion of the volume of the column.

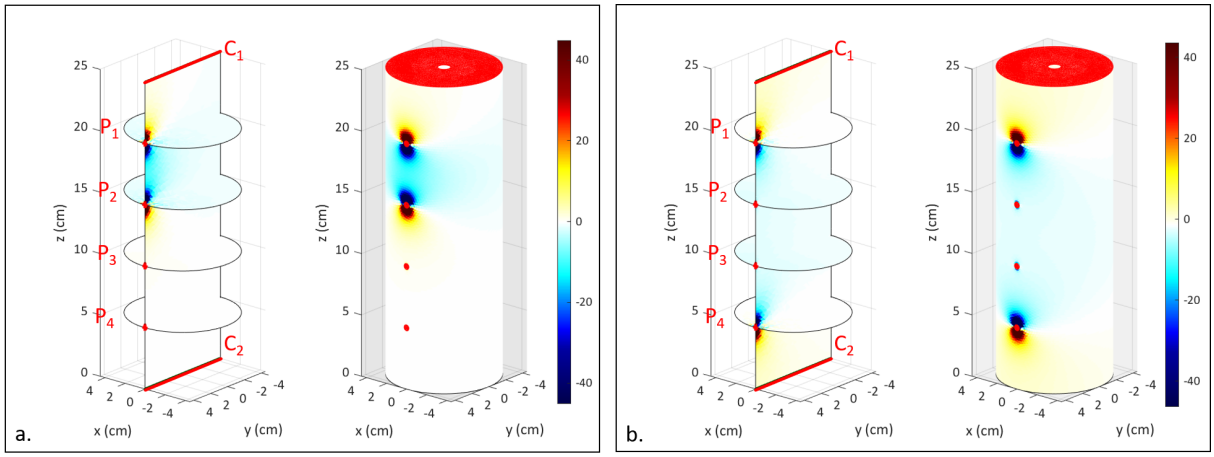

Figure 4.10: Sensitivity functions. (a) cross-sectional and external surface representations of the dipole P_1-P_2 sensitivity function. (b) cross-sectional and external surface representations of the dipole P_1-P_4 sensitivity function.

4.4.4.2 Criteria from Zimmermann et al., 2008

Zimmermann et al. (2008) developed a sample holder and identified several sources of error on phase measurement during SIP acquisitions. I, therefore, calculated the recommended ratios for designed column to verify

whether its dimensions were in agreement. The definitions of the ratios and the computed values are given in Table 4.2. It appears that the column does not respect all the criteria. It is especially true for Z_2 which, in agreement with the sensitivity analysis, shows that the column diameter is too large compared to the length of the column.

Table 4.2: Recommended criteria for the column geometry from Zimmermann et al. (2008). The values are computed for the small and large spacing arrays, corresponding to the measurement dipoles P_2-P_3 and P_1-P_4, respectively, with C_1 and C_2 as the current injection electrodes. l_{pp} is the distance between the potential electrodes, l_{cc} = 25 cm is the distance between the current electrodes C_1 and C_2, l_{cp} is the distance between the current and the potential electrode, and d_c = 9 cm is the diameter of the column.

Criteria from Zimmermann et al. (2008)	Small spacing (P_2-P_3) l_{pp} =5 cm and l_{cp} =10 cm	Large spacing (P_1-P_4) l_{pp} =15 cm and l_{cp} =5 cm
$Z_1 = \frac{l_{cp}}{d_c} \geq 2$	1.11	0.56
$Z_2 = \frac{d_c}{l_{cc}} \leq 0.17$	0.36	0.36
$Z_3 = \frac{l_{pp}}{l_{cc}} = \begin{cases} 0.33 \\ 0.66 \end{cases}$	0.2	0.6

4.4.4.3 Conclusions about the column design

The investigations of the sensitivity function and the recommendations from Zimmermann et al. (2008) point that the diameter of the column is too large and seems to be a weakness of its design. Nevertheless, we can make the hypothesis that the sample being homogeneous, the behavior measured by the electrodes on one half of the column is identical for the other half. Furthermore, the SIP measurements conducted on this column and presented in this chapter show that the column, tightened with the nylon structure, does not induce phase signal in addition to the high-frequency behavior of the Ag-AgCl electrodes (Figure 4.8). Thus, despite its somewhat large diameter, this column is still an acceptable sample holder.

This column (referred as Column 1 in the following) was used for the first experiment (Chapter 6). Since it showed some limitations, a second column was designed.

4.5 Improved design

4.5.1 A new shape to enhance the geo-electrical data quality

Column 1 was used for the first experiment, but due to its design, some important data could not be monitored. Thus, a new column geometry was designed (Figure 4.11) to overcome these limitations. This second column, referred as Column 2, is made of a Plexiglas cylinder of 31 cm in length, with an inner and an outer diameter of 4 cm and 5 cm, respectively.

As for Column 1 design, four aligned holes are drilled in the cylinder wall to screw plastic cable glands holding the potential electrodes P_1, P_2, P_3, and P_4. The potential electrodes are spaced by 5 cm between them and by

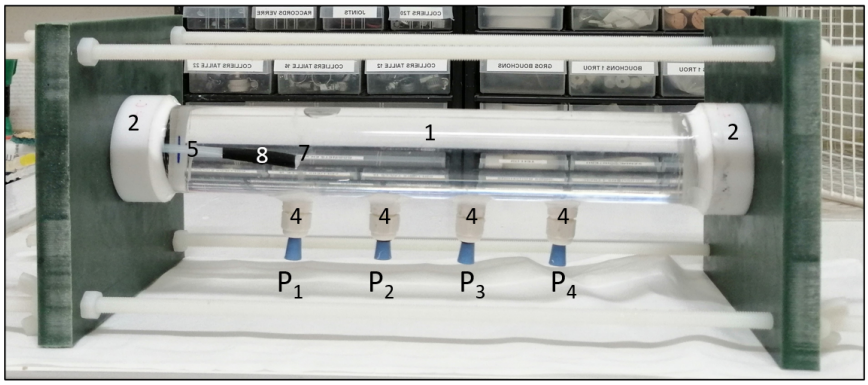

1	Plexiglas cylinder
2	Plastic cap
3a	Stainless steel disc
3b	Stainless steel wire
4	Plastic cable gland
5	Rigid plastic tubes
6	Rubber O-ring
7	Nylon filter fabrics
8	Heat-shrink sleeve

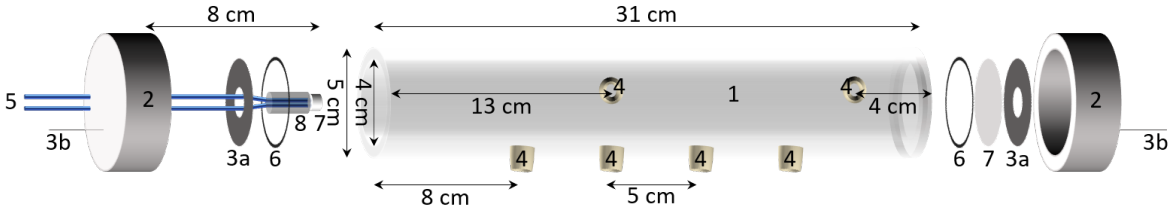

Figure 4.11: Description and dimensions of the new column.

8 cm from the edges of the cylinder. The current electrodes are two stainless steel rings attached to the plastic bases sealing the cylinder. The current electrodes are separated from the edges of the cylinder by O-rings. The elements of the column are maintained together by a nylon structure.

The SIP behavior of Column 2 was tested using the PSIP apparatus (presented further in Chapter 5). The column was filled with tap water (σ_w <800 µS cm^{-1}). The spectra were acquired on four channels corresponding to the measurements dipoles: P_1-P_2, P_2-P_3, P_3-P_4, and P_1-P_4. The results are presented on Figure 4.12, apart from the high-frequency polarization reaching the small value of 2 mrad at 10 kHz, the spectra remain flat. This high-frequency polarization can be attributed to the electrodes behavior. Thus, the shape of Column 2, as for Column 1, does not induce polarization and seems suitable for SIP acquisition.

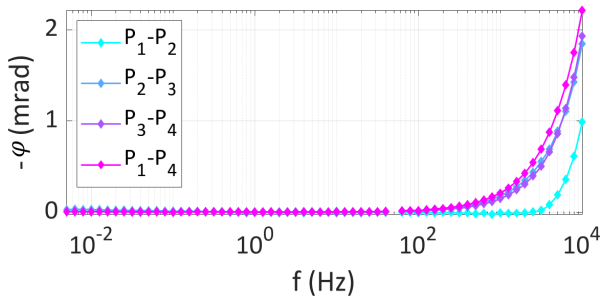

Figure 4.12: SIP phase spectra of Column 2 filled with a NaCl solution. These spectra were acquired using the PSIP, which does not provide error bars. The measurements at 50 Hz are removed due to the noise created at this utility frequency by the background radiation of the power grid.

Column 2 is thinner than Column 1. Figure 4.13 present the sensitivity maps obtained with EIDORS finite-elements modeling of Column 2 for the measurement dipoles P_2-P_3 and P_1-P_4. The color scale is identical to the one of Figure 4.10. Thus, it is clearly visible that with this new design, the electrodes are sensitive on the

conductivity changes over the entire width of the column.

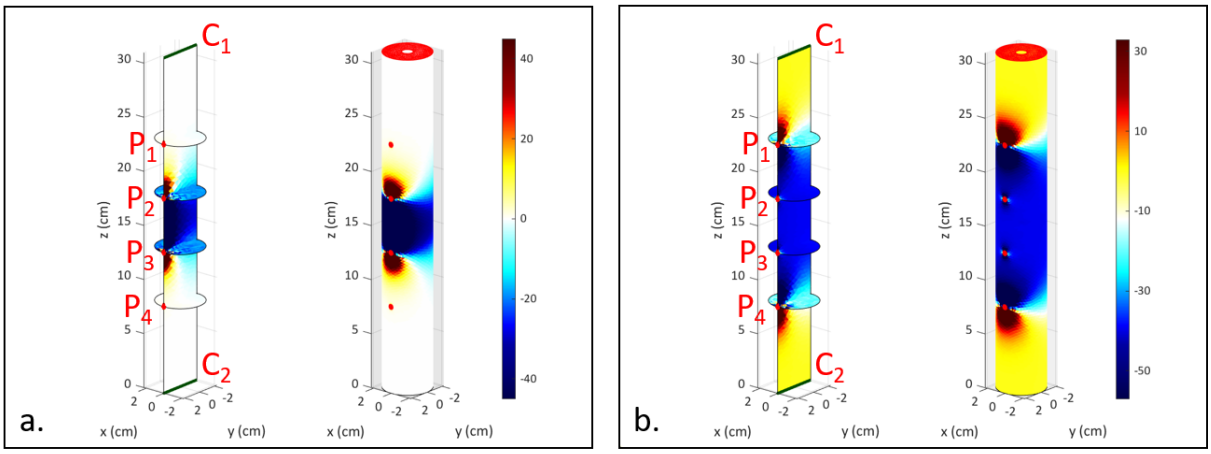

Figure 4.13: Sensitivity functions of Column 2. (a) cross-sectional and external surface representations of the dipole P_2-P_3 sensitivity function. (b) cross-sectional and external surface representations of the dipole P_1-P_4 sensitivity function.

To confirm the numerical results of the sensitivity maps, the criteria recommended by Zimmermann et al. (2008) have also been computed and are shown in Table 4.3. The results of the criteria Z_1 and Z_2 are comprised in the recommended range, showing that the diameter of Column 2 is adapted to its length. However, one can note that the values of criterion Z_3 are further from the recommended values than those of Column 1, revealing that the potential electrodes are less well distributed along the column, but more concentrated towards the middle, which participates of the better results the first criterion Z_1.

Table 4.3: Computation of the criteria recommended by Zimmermann et al. (2008) for Column 2. The values are computed for the small and large spacing arrays, corresponding to the measurement dipoles P_2-P_3 and P_1-P_4, respectively, with C_1 and C_2 as the current injection electrodes. l_{pp} is the distance between the potential electrodes, l_{cc} =31 cm is the distance between the current electrodes C_1 and C_2, l_{cp} is the distance between the current and the potential electrode, and d_c = 4 cm is the diameter of the column.

Criteria from Zimmermann et al. (2008)	Small spacing (P_2-P_3) l_{pp} =5 cm and l_{cp} =13 cm	Large spacing (P_1-P_4) l_{pp} =15 cm and l_{cp} =8 cm
$Z_1 = \frac{l_{cp}}{d_c} \geq 2$	3.25	2.0
$Z_2 = \frac{d_c}{l_{cc}} \leq 0.17$	0.13	0.13
$Z_3 = \frac{l_{pp}}{l_{cc}} = \begin{cases} 0.33 \\ 0.66 \end{cases}$	0.16	0.48

4.5.2 Shifting the injection into the column

The third criterion from Zimmermann et al. (2008) reveals that the measurement electrodes are closer to the middle of the column. Indeed, C_1 and P_1 electrodes are spaced 8 cm apart. It is therefore feared that an interesting part of the electrical signals generated by the processes of calcite dissolution and precipitation will be lost because of this spacing between the edge of the column and the position of the first measuring electrode

(this was one of the biggest limitations of Column 1, see Chapter 6 for more details). To overcome this problem, injection tubes have been inserted in Column 2 in order to align the injection with the electrode P_1.

As shown on Figure 4.11, two tubes are inserted to enable the injection of two different reactive solution (Chapter 8). The tubes are glued together and are wrapped with a filter fabric to prevent calcite grains from entering the tubes. The filter fabric is maintained on the tubes using a heat-shrink sleeve.

4.5.3 Additional pH micro-electrodes

pH is a parameter of major importance for the calcite system and for all studies involving chemical reactions. In order to relate the geo-electrical measurements to this parameter, we introduced two micro-electrodes pH_1 and pH_2 at 13 cm and 27 cm apart from the edge of the column on the side of the electrode C_1 (Figure 4.14). 2 cm of pH electrodes are inserted in the column to measure the pH variations in its middle.

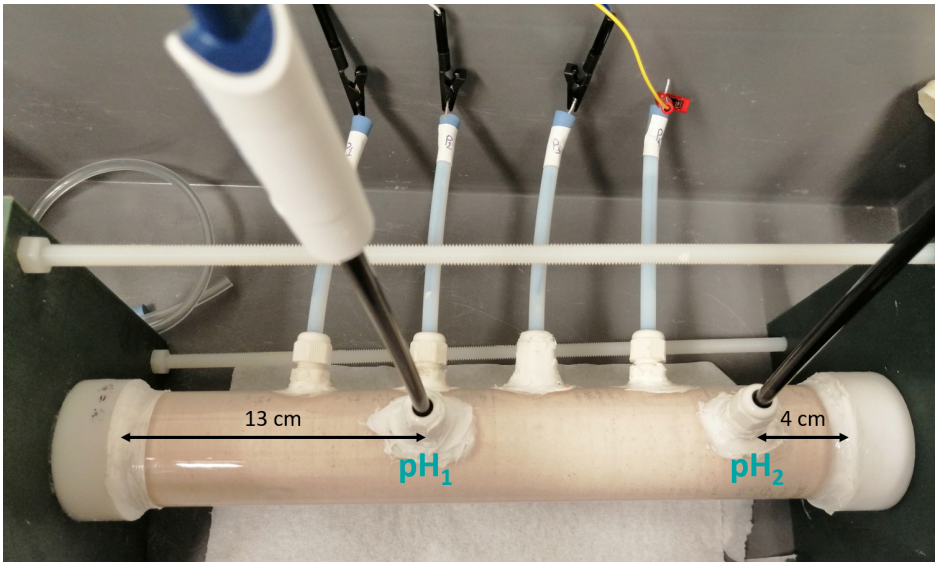

Figure 4.14: Photography of the new column filled with calcite grains and equipped with two micro-electrodes for pH measurement inside the column.

To ensure that the inserted pH electrodes do not create some polarization in the column, we measured the SIP spectra on Column 2 filled with water and equipped with the pH electrodes. We obtained similar results as presented in Figure 4.12. Thus, pH electrodes are expected to not influence the geo-electrical acquisition.

CHAPTER

5 Investigation techniques and experimental protocols

5.1 The experimental benches

The experimental benches designed for my experiments enable to monitor different electrical properties of the calcite sample during dissolution or precipitation: SIP, SP, and the pore water electrical conductivity (EC). Figure 5.1 presents the two experimental benches (referred in the following as Bench ❶ and Bench ❷). SIP and SP measurements are conducted using the electrodes of the column, while the water conductivity is measured before and after the fluid flows through the column. In addition, the outlet pore water is collected for chemical analyses. Each experimental bench is associated to one of the two columns (Column 1 with Bench ❶ and Column 2 with Bench ❷). Thus, Bench ❷ presents additional features that are the possibility to inject two reactants simultaneously and the addition of two pH meters to monitor pH in the column at two different locations (see Section 4.5.3.

The inlet solution has a defined affinity with calcite in order to dissolve or precipitate (inlet solution compositions will be summarized in section 5.2).

5.2 Experimental protocols

5.2.1 List of the experiments

I conducted several experiments for this thesis in order to tend to determinate the mechanisms which generate geo-electrical signatures and to quantify their impact of the measurements. This section outlines the experimental conditions of the performed experiments, whose results will be presented in the following chapters. Among all the experiments I performed, I present here six of them that are listed in Table 5.1.

Experiment ①, conducted with Bench ❶, lasted the longest and both SIP and SP methods were used. The purpose of Experiment ① was multiple. Firstly, it aimed at studying the feasibility of setting up a multi-method experimental bench, combining geophysical acquisitions and geochemical analyses to answer a reactive transport problem. Secondly, this experiment allowed to compare the results obtained with the two methods SIP and SP. Thirdly, Experiment ① also helped improving the column design of Column 2. Finally, this experiment helped to define what experimental strategy to adopt in order to perform shorter and more systematic tests

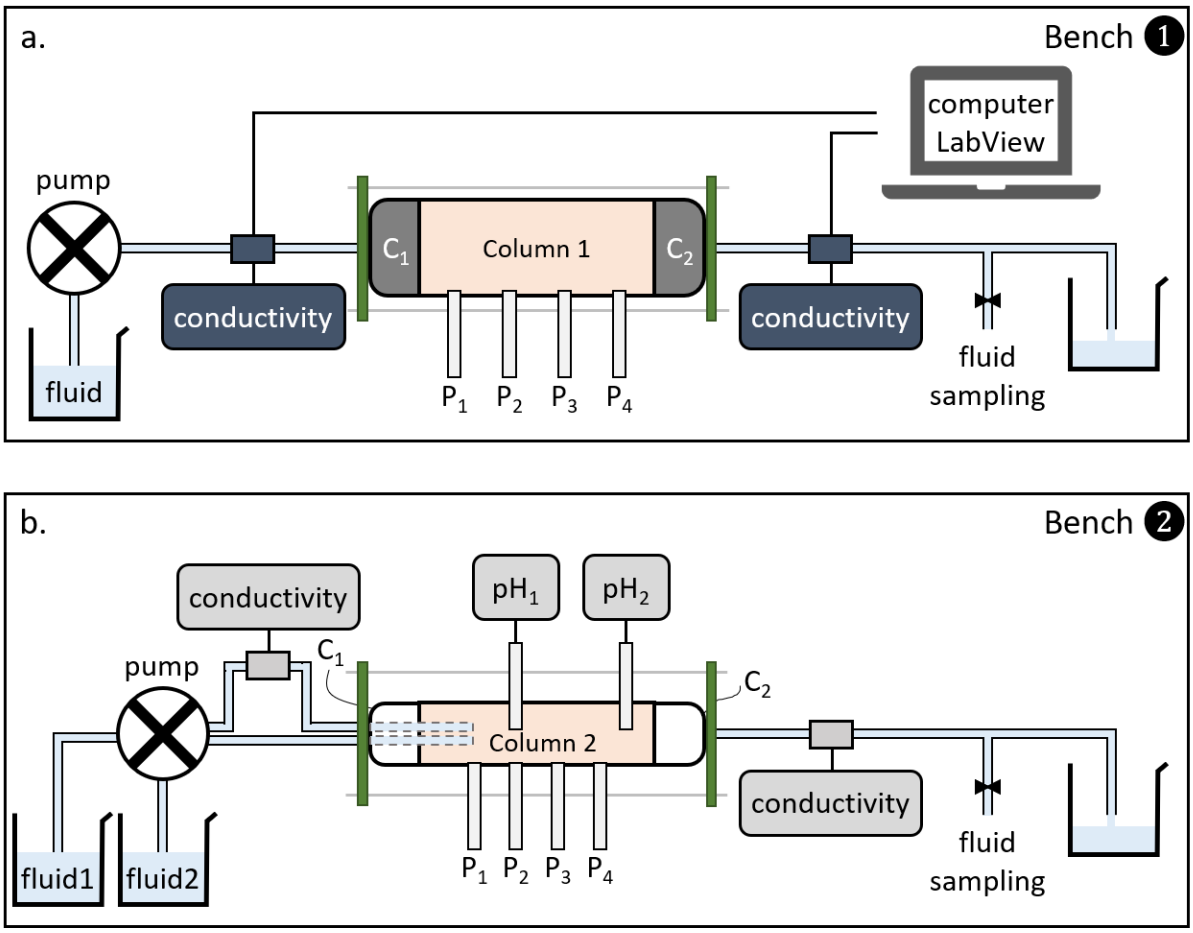

Figure 5.1: Schematic representation of (a) Bench ❶ used with Column 1 and (b) Bench ❷ used with Column 2. Two injected fluids are represented at the inlet of Column 2, but this configuration was only used for calcite precipitation induced by mixing reactants.

with Bench ❷. Experiment ① consisted of successively dissolving then precipitating calcite and measuring their signature. This experiment showed interesting results, which are the topic of a draft article presented in chapter 6.

The following experiments are more targeted tests based on the results obtained from Experiment ① and by using Column 2, which design was improved based on Experiment ① results. Experiments ②, ③, and ④ focus on the influence on the SP signal of the injected acid type at the input. Experiments ⑤ and ⑥ focus on SIP monitoring of precipitation at two different injection flow rates of the reactive species.

5.2.2 Inlet pore water chemistry

5.2.2.1 Dissolution

Dissolution of calcite is induced by the injection of an acid solution. I tested different acid solutions to characterize the effect of pH and the impact of using strong or weak acid.

Strong acid totally dissociates in water, thus pH value of the solution is directly linked to the concentration of concentration acid. This acid type was chosen since it would totally react with calcite matrix and generate fast

Table 5.1: The experimental conditions of the different experiments carried out in the laboratory.

Experiment number	①		②	③	④	⑤	⑥
Process[a]	Di	Pr	Di	Di	Di	Pr	Pr
Inlet chemistry[b]	S1	S2	S3	S4	S5	S6 and S7	S6 and S7
Duration (h)	1152	195	25	9	9	8	350
Experimental bench	❶		❷	❷	❷	❷	❷
Electrical method	SP and SIP		SP	SP	SP	SIP	SIP
Flow rate (mL h^{-1})	25.2		58.8	58.8	58.8	58.8	0.51
Room temperature (°C)	21.8±1.1		19.7±0.4	18.5±0.4	19.5±0.4	21.9±0.5	18.9±0.4
ϕ_{init} (%)	41.09		43.61	43.99	41.62	43.06	42.73
$\Delta\phi$ (%)	0.49		0.04	0.77	0.09	-0.04	-0.09

[a] Di stands for *Dissolution* and Pr stands for *Precipitation*

[b] S1 is a solution of hydrochloric acid at pH=3

S2 is a calcite over-saturated solution with $\Omega = 14$

S3 is a solution of hydrochloric acid at pH = 4.5

S4 is a buffer of acetic acid and sodium acetate at pH = 4.5 and $C_{CH_3COOH} = 1.74$ mol L^{-1}

S5 is a buffer of acetic acid and sodium acetate at pH = 4.5 and $C_{CH_3COOH} = 2.5 \times 10^{-3}$ mol L^{-1}

S6 is a solution of calcium chloride at 26.2×10^{-3} mol L^{-1}

S7 is a solution of sodium carbonate at 29.0×10^{-3} mol L^{-1}

dissolution. For Experiments ① and ②, I injected hydrochloric HCl solutions S1 and S3 at pH = 3 and pH = 4.5, respectively (Table 5.1). As Experiment ② is conducted on Column 2 with Bench ❷, this experiment informs about the impact of the injection shift at the location of P_1 (described in Section 4.5.2).

However, strong acid induces very local dissolution (e.g., Garcia-Rios et al. 2014). Thus, for Experiments ③ and ④ I injected solutions S4 and S5, respectively, which are two buffered solutions of acetic acid CH_3CO_2H and sodium acetate $NaCH_3CO_2$, both at pH = 4.5 (Table 5.1). The aim of using such different acid types is to observe the effect of local versus extended reactive area in the column on the electro-diffusive coupling of the SP signal.

Buffered solution are made of the mixing of a weak acid with its conjugate base. Since acetic acid and acetate have an acid dissociation constant $K_A = 1.74 \times 10^{-5}$, they are a good candidate to make a buffered solution with

a pH value ranging between 4 and 5. The dissociation of acetic acid in water follows

$$CH_3COOH + H_2O \leftrightarrow CH_3COO^- + H_3O^+, \tag{5.1}$$

where the double-headed arrow indicates the chemical equilibrium (i.e., dissociation and recombination occur simultaneously). Making the assumption that the activity coefficient is close to one, the acidity constant is defined by

$$K_A = \frac{C_{CH_3COO^-}\, C_{H_3O^+}}{C_{CH_3COOH}}, \tag{5.2}$$

where $C_{CH_3COO^-}$, $C_{H_3O^+}$, and C_{CH_3COOH} are the concentrations (mol L^{-1}) of acetate, oxonium, and acetic acid, respectively. Knowing that pH is related to $C_{H_3O^+}$ ($C_{H_3O^+} = 10^{-\mathrm{pH}}$), for a given pH value, one can choose the acetic acid concentration and compute the related acetate concentration from Eq. 5.2

$$C_{CH_3COO^-} = K_A\, C_{CH_3COOH}\, 10^{\mathrm{pH}}. \tag{5.3}$$

Acetic acid is available as an almost pure solution. Thus, the volume of acetic acid V_{CH_3COOH} (L) is computed with the following expression

$$V_{CH_3COOH} = \frac{C_{CH_3COOH}\, M_{CH_3COOH}\, V_{sol}}{p\, \rho_{CH_3COOH}}, \tag{5.4}$$

where M_{CH_3COOH} = 60.05 g mol^{-1} is the molar mass of acetic acid, V_{sol} (L) is the volume of the buffered solution, p (-) is the purity coefficient of the initial solution, and ρ_{CH_3COOH} (g L^{-1}) is the volumetric mass density of acetic acid ($\rho_{CH_3COOH} = 1.05 \times 10^3$ g L^{-1}).

The acetate ion can be found in the solid form of sodium acetate. In this case, the required mass of sodium acetate m_{NaCH_3COO} (g) is calculated from

$$m_{NaCH_3COO} = K_A\, 10^{\mathrm{pH}}\, C_{CH_3COOH}\, V_{sol}\, M_{NaCH_3COO}, \tag{5.5}$$

where M_{NaCH_3COO} = 82.03 g mol^{-1} is the molar mass of sodium acetate.

The concentrated buffered solution S4 has thus a concentration of acetic acid of 1.74 mol L^{-1} and the diluted buffered solution S5 has a concentration of acetic acid of 2.5 $\times 10^{-3}$ mol L^{-1}.

5.2.2.2 Precipitation

I conducted precipitation during Experiment ① on Bench ❶ by injecting solution S2 and on Bench ❷ for Experiments ⑤ and ⑥ by mixing solutions S6 and S7 (Table 5.1).

For Experiment ①, the injected solution S2 to precipitate calcite was over-saturated with a saturation index Ω = 14. This solution S2 was prepared from the mixture of calcium chloride $CaCl_2$ (1.2 mmol L^{-1}), sodium hydrogencarbonate $NaHCO_3$ (4.8 mmol L^{-1}), and sodium carbonate Na_2CO_3 (0.1 mmol L^{-1}). To avoid calcite precipitation in the inlet reservoir, the ratio of calcium over carbonate was set to 30.

For Experiments ⑤ and ⑥, calcite precipitation is chemically induced by the mixing of two injected reactants S6 and S7, which are solutions of sodium carbonate Na_2CO_3 and calcium chloride $CaCl_2$. This type of mixing to induce calcite precipitation monitored with SIP was performed by Wu et al. (2010) and Izumoto et al.

(2020a). In order to compare my results with these data from the literature, I prepared S6 and S7 with the same concentrations as chosen by Wu et al. (2010) and Izumoto et al. (2020a). Thus, for Experiments ⑤ and ⑥, the injected solutions of $CaCl_2$ (S6) and Na_2CO_3 (S7) present concentrations of 26.2 mmol L^{-1} and 29 mmol L^{-1}, respectively.

5.2.3 Experimental conditions

5.2.3.1 The flow rate

The inlet solution flows through the sample with a constant flow rate thanks to a peristaltic pump Minipuls 3 from Gilson company. The two injected fluids of Bench ❷ (Figure 5.1b) are connected to the same pump head. They thus have the same flow rate.

For Experiment ① conducted on Bench ❶, the flow rate was set to 25.2 mL h^{-1} so that the time to percolate through the column and the sampling time are reasonable (25 h to cross the column and 1 h to collect a sample of outlet pore water). Indeed, due to Column 1 dimensions (described in Section 4.4) and initial porosity (41.09 %, see Table 5.1), the pore water flows through the column in 25 h approximately and it takes 1 h to collect the necessary volume for chemical analyses. Given the size of the column used for this experiment (see Section 4.4), the Darcy velocity is $U = 1.1 \times 10^{-6}$m s^{-1} and for a diffusion coefficient $D = 3.0 \times 10^{-9}m^2$ s^{-1}, the Péclet number is $Pe = 92$.

For the experiments performed Bench ❷, the flow rate is higher (58.8 mL h^{-1}, see Table 5.1) in order to reduce the time of each experiment to a few hours for SP acquisition and to explore the effect of various flow rates on the SIP response.

The flow rate of Experiment ⑥ was chosen to be able to compare the results with the data of previous studies. Wu et al. (2010) and Izumoto et al. (2020a) used 2.16 mL h^{-1} and 1.31 to 2.93 mL h^{-1}, respectively. Thus the flow rate of Experiment ⑥ was set to 0.51 mL h^{-1} for each reactant, thus it gives a total flow rate of 1.02 mL h^{-1}.

For Experiments ② to ⑥, Column 2 was used. Thus, given the two different flow rates imposed for these experiments, the Darcy velocity is $U = 1.3 \times 10^{-5}$m s^{-1} for Experiments ② to ⑤ and $U = 1.1 \times 10^{-7}$m s^{-1} for Experiment ⑥. Thus, for the same diffusion coefficient, Péclet number is $Pe = 997$ for Experiments ② to ⑤ and $Pe = 9$ for Experiment ⑥.

5.2.3.2 Filling the column and initial porosity

For all experiments, the column is filled using the same technique designed to fill the column with packed, water saturated grains of calcite.

First, the column is placed vertically with the inlet at the bottom. For Column 1, a filter fabric with a 20 µm filter mesh is placed between the cylinder bottom edge and the O-ring of current injection electrode C_1 to prevent the grains from escaping the column. For Column 2, the injection tubes are already covered with such filter (see the descriptions of Columns 1 and 2 in Sections 4.4 and 4.5, respectively).

Then, to ensure water-tightness, I placed a silicone gasket between the bottom edge of the Plexiglas cylinder and the current injection electrode C_1. I let this gasket dry for 24 h. Once the silicone gasket is dry, water is slowly injected from the bottom while calcite grains are sprinkled from the top of the column. The amount of poured grains is limited to ensure that a thin layer of water always cover the grains. Before reaching the location of one of the potential electrodes with the pore water, I added the electrode in its cable gland and added some silicone to ensure the water-tightness. I did the same for the pH micro-electrodes inserted in Column 2.

Periodically, I tapped on the wall of the column with a stick to compact the grains. Since I did not count the exact number of strokes with the plastic rod, the grain compaction could not be accurately reproduced between each experiment (see Table 5.1). This explains the initial porosity variations of 1-2 %. Note that the porosity of the first experiment is the lowest. This may be due to the shape of the large column, whose larger diameter has facilitate the compaction of the grains.

When reaching the top of the column with water, I completed the remaining volume with grains. Since grains take a greater volume than water, some water overflowed from the column. After cleaning the column, I placed a 20 μm filter fabric, the current injection electrode C_2, and the plastic cap. Then, I clamped the column by screwing the plates on the threaded rods of the tightening structure. The column is tightened until it becomes difficult to screw more by hand without breaking the wing nuts that serve to screw the plates of the tightening structure. Some water would leak from the edge of the column due to the pressure increase when screwing the tightening structure. After cleaning, I placed another silicone gasket between the top edge of the Plexiglas cylinder and the current injection electrode C_2 and I let this gasket dry for 24 h.

Once all the silicone gaskets are dried, I laid the column horizontally because the plastic threaded rods were not strong enough to support the weight of the column filled with grains and water. Then, I placed a sheet of paper towel beneath the column to verify that there was no leakage and started the injection of water.

5.2.3.3 Initialization before each experiment

Before the beginning of dissolution or precipitation experiments, the column is flushed with a solution close to calcite saturation.

For Experiment ①, this initialization phase was carried out by circulating the same water in a closed circuit for several days until reaching a stationary state.

For the following experiments, the water used to fill the column was a mixture of deionized water and calcite grains immersed during several weeks. In spite of the long mixing time between the grains and the water before using it to fill the column, the use of this water to saturate the column systematically increased the conductivity of this water after a few hours in contact with the grains in the column. To avoid creating gradients within the column before initiating the experiment, the column was rinsed. The conductivity of the output water was recorded in order to check that the salinity of the outlet water had returned to its base value.

5.3 Monitoring and analyses

5.3.1 The temperature

For all experiments, the room temperature was monitored in case of abrupt changes. The room temperature sensor is a HOBO U14 002 from Onset company that can launched using the software HOBOware. For all experiments except Experiment ⑥, the room had air conditioning, guarantying a certain stability. Thus, room temperatures of all experiments, presented in Table 5.1, show similar values and small standard deviations, indicating that the room temperature was stable, even for Experiment ⑥ despite the absence of air conditioning.

In addition, for Bench ❷ the pore water temperature was monitored at the inlet and at the outlet of the column (see Figure 5.2). The recorded values present analogous amplitudes and similar standard deviation to the room temperature. However, due to the air conditioning regulation, the room temperature oscillates periodically. This effect of the air conditioning system is also noticeable on the curves of the inlet and outlet pore water temperature as shown on Figure 5.2.

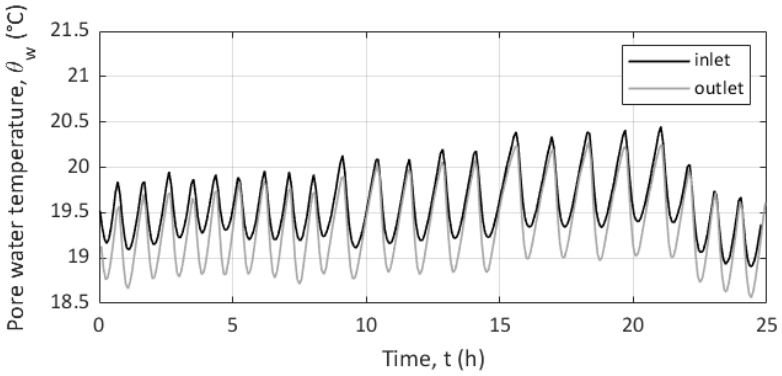

Figure 5.2: Inlet and outlet pore water temperature monitoring for Experiment ② conducted under air conditioning.

One can note, that the mean temperature of the first and the fifth experiments are a bit higher than for the rest of the experiments (see Table 5.1). This may come from changes of the air conditioning settings.

5.3.2 Chemical monitoring and measurements

5.3.2.1 Outlet pore water chemistry analyses

The outlet pore water chemistry gives important information of the chemical transformation that occurred in the column. Contrary to the geo-electrical methods, which are indirect properties affected by chemical processes, the chemical analyses provide direct information on the chemical evolution of the system. For each sample, we performed three different analyses. We measured the solution pH, alkalinity, and ionic composition. For all these analyses, at least 22 mL of solution was required. For most of the experiments, the flow rate was large enough to get this volume in 1 h. Thus, no sealing was required. On the contrary, when the flow rate was slower (the collect of 22 mL took 24 h), the sample was sealed to prevent from water evaporation. For each

sample, pH was measured right after the collecting the sample. I used a pH meter (model C931) of the Consort brand that I calibrated using three buffers at pH 4, 7, and 10.

For alkalinity and ionic concentration composition, I filtered the sample in case of the presence of non-dissolved microscopic particles of calcite which would distort the measurement. Indeed, despite the use of a filter fabric at the outlet edge of the column particles smaller than 20 µm (limit of the filter fabric) can pass through it. Moreover, the alkalinty measurement is an acid-base titration. Thus, the addition of acid into the sample would dissolve the small particles present in the sample. Thus, I used a syringe filter with a maximal pore size of 0.2 µm. The alkalinity measurement was performed using a titrator from Metrohm with an hydrochloric acid (HCl) with a concentration of 0.01 mol L^{-1} on 10.0 mL of the sampled outlet solution.

The ionic composition was measured at the end of each experiment. As anions and cations concentrations were measured separately, two separate samples were prepared separately. For anions, only 2 mL were required while 10.0 mL of the solution acidified at 3 % to 4 % were required for the cations. The anions concentrations were measured using an ion chromatography system (from Dionex), while cations concentrations were analyzed using inductively coupled plasma atomic emission spectroscopy (ICP-OES 5100 from Agilent technologies). The samples in waiting of analysis were stored in a refrigerator for better conservation.

5.3.2.2 pH monitoring inside Column 2

Two pH electrodes were inserted in Column 2 used with Bench ❷ (Figure 5.3). The pH electrodes have a diameter of 3 mm and are made of a flexible plastic material for more robustness (glass micro-electrodes had been tested, but because of their great fragility, they were not retained). The pH meters are of the same brand as the conductivity meters and the recorded data can also be downloaded to the computer via USB.

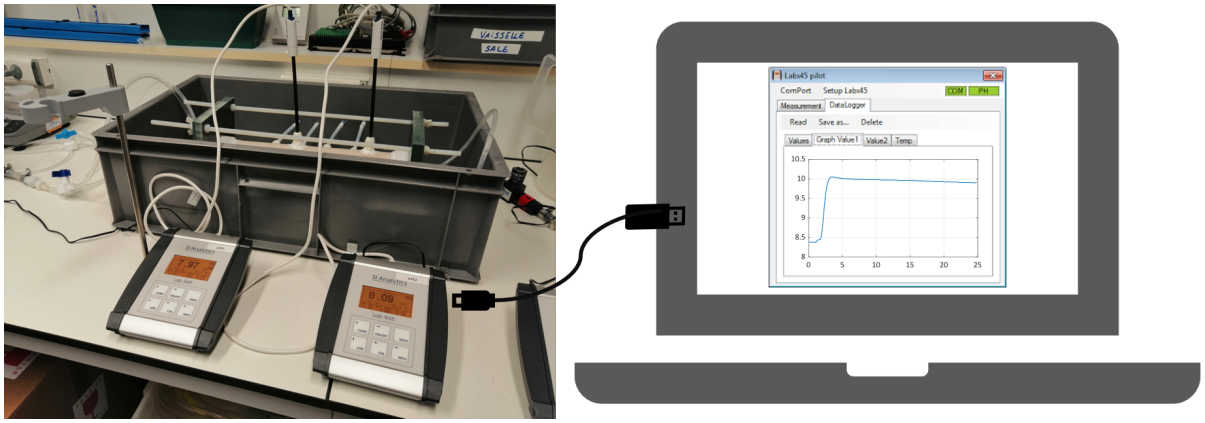

Figure 5.3: Photography of the pH micro-electrodes and associated pH meters used with the second experimental bench. The pH meters are connected to the computer with an USB wire. One example of pH curve is shown in the user interface window.

As the pH electrodes are inserted in the column, they record pH continuously. Thus, they are calibrated before each experiment using three buffers at pH 4, 7, and 10.

As shown on Figure 5.3, the monitoring of pH is of high precision. However, when SIP measurements were performed, the injection of electrical current generated noise on the pH data which have hence been filtered.

using a first order low-pass Butterworth filter with a normalized cutoff frequency of 0.06 (see Figure 5.4).

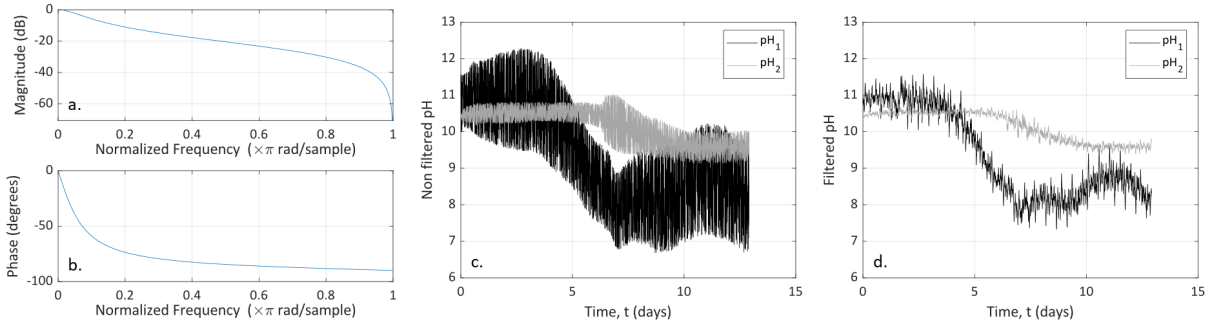

Figure 5.4: Processing of the pH measured in the column during SIP monitoring. (a) (b) magnitude and phase frequency variations of the low-path Butterworth filter used on the raw pH data. (c) raw pH data curves obtained during one experiment on the thin column during SIP monitoring. The electrical current injected for SIP acquisition is responsible for the noise on pH curves. (d) pH curves after filtration. The noise level is reduced and the curves are not shifted in time nor in amplitude.

5.3.3 Geo-electrical monitoring

5.3.3.1 Pore water EC monitoring

For Bench ❶, inlet solution and outlet pore water are monitored using two conductivity meters (Lab 730 from Inolab) which were not capable to store a sufficient number of recorded data. Thus, they were connected to a digital acquisition unit, composed of a digital multimeter (Keithley 2000) and a laptop controlling the acquisition using Labview software (Figure 5.5). The conductivity was recorded every 3 s.

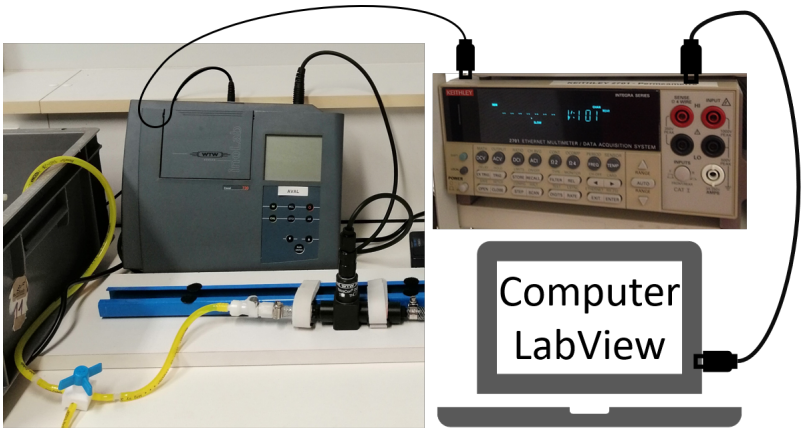

Figure 5.5: The downstream conductivity meter connected to the digital acquisition unit composed of the Keithley digital multimeter and the pilot Labview interface

For Bench ❷, other conductivity meters (Lab 945 from SI Analytics) that can store the recorded data were used for the inlet solution and outlet pore water conductivity monitoring. The advantage of these conductivity meters is that the data could directly be downloaded on the computer via USB cable using the Labx45 pilot (Figure 5.6). Given the reduced memory capacity of the conductivity meters, the conductivity was recorded every 5 min.

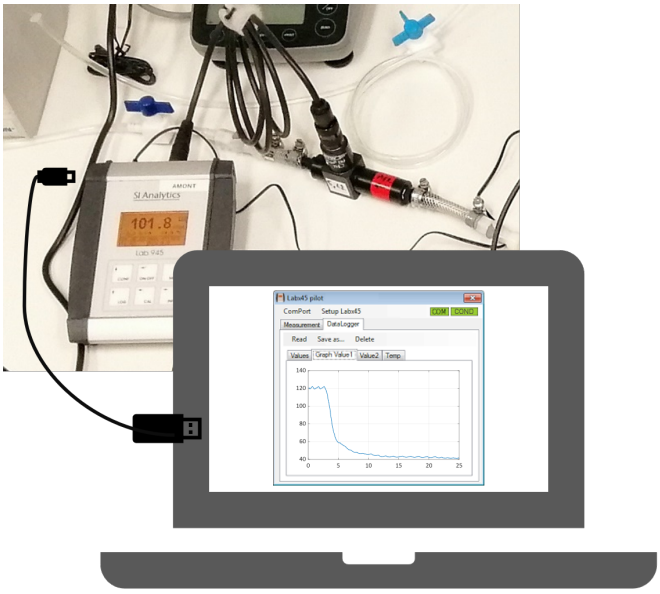

Figure 5.6: The conductivity meter used with the second experimental bench connected to the computer. One example of the outlet conductivity is shown in the user interface window.

Note that no temperature correction was applied to the raw geophysical signal, since we were not interested in apparent values, but wanted to compare the results obtained from the different methods. Thus, some small variations can be observed on the data as on the example shown on Figure 5.6. These variations correspond to the control of the air conditioning in the room.

5.3.3.2 SIP monitoring

For the tests of the electrodes and column desing presented in Chapter 4, I used both SIP Fuchs III system from Radic Research and the PSIP (Portable SIP Field/Lab Unit) device from Ontash&Ermac. However, for all the experiments performed with the experimental benches, I used the PSIP which was more convenient for a such laboratory use. Indeed, as discussed by Kaouane (2015), the SIP Fuchs III is designed for field applications, so multi-channel acquisitions require the use of several large optic fiber coils (see Figure 4.3). The advantage of the SIP Fuchs III is that it estimates error bars. Nevertheless, the PSIP gives more accurate results (Kaouane 2015).

The PSIP is designed for multi-channel acquisitions. Thus, SIP measurements were always conducted on four channels corresponding to the pairs: P_1-P_2, P_2-P_3, P_3-P_4, and P_1-P_4 (Figures 5.7a and b). These channels were chosen to monitor the complex conductivity of different slices (P_1-P_2, P_2-P_3, and P_3-P_4) of the column and to get a mean value (P_1-P_4).

The alternating electrical current injection was ensured through the stainless steel electrodes C_1 and C_2. For most of the acquisitions, the sinusoidal voltage covered a spectrum from 5 mHz to 10 kHz at 41 frequencies uniformly distributed on a logarithmic scale and with an amplitude of ±5 V. The device records amplitude and phase of the complex electrical conductivity.

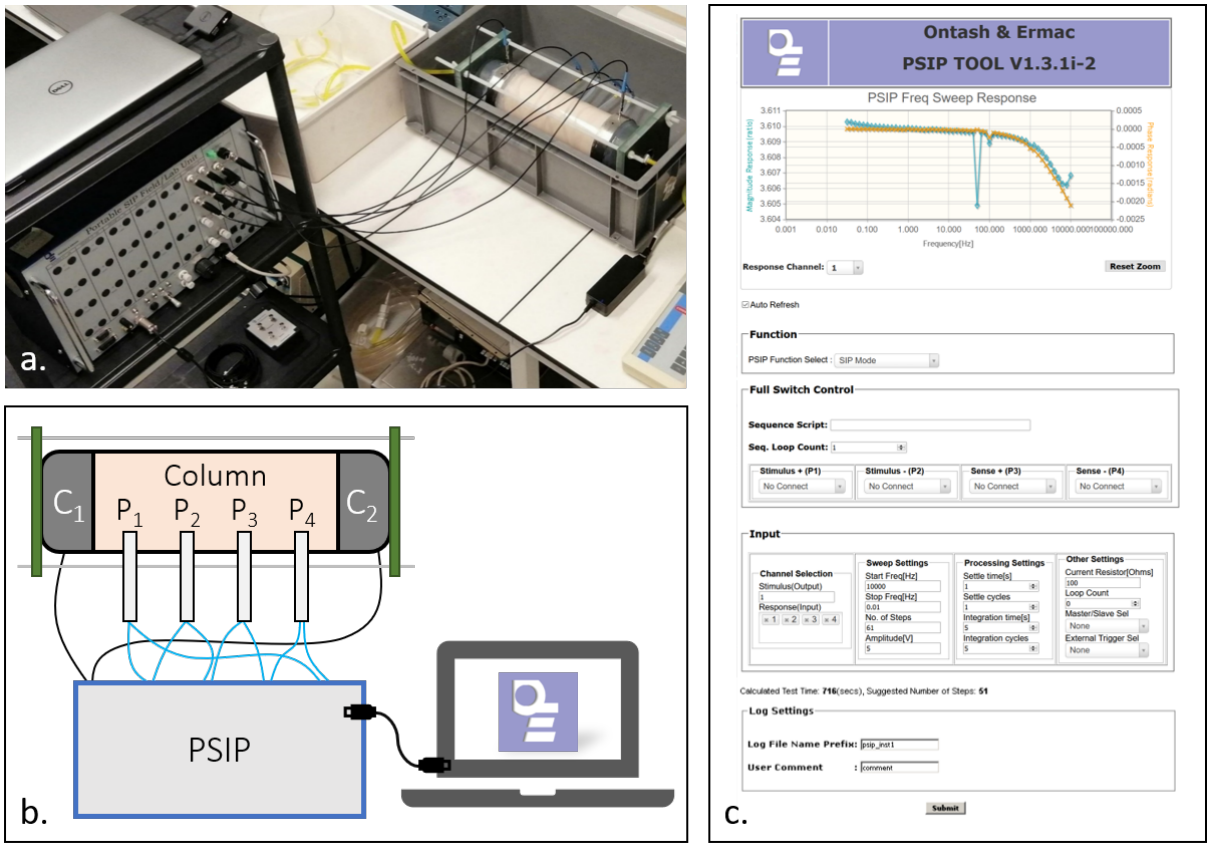

Figure 5.7: SIP monitoring. (a) photography of SIP acquisition on Bench ❶. (b) Schematic representation of the SIP four-channels acquisition. (c) the user interface.

The advantage of the PSIP is that one can continuously record the spectra by programming a loop counter via the user interface (Figure 5.7c).

5.3.3.3 SP monitoring

SP data were recorded on three channels with the total field method (Lowrie and Fichtner 2020). The fixed reference was the electrode P_4 and we measured the potential on three channels corresponding to the pairs P_1-P_4, P_2-P_4, and P_3-P_4 (Figures 5.8a and b). The data logger used for the SP monitoring is a CR1000 from Campbell Scientific.

The data logger is connected by an USB cable. The recorded data can be watched and downloaded via the Loggernet software (Figure 5.8c).

The Loggernet software serves also to program the data logger. For all the acquisition, the CR1000 was programmed to measure the voltage every 1 ms, then to compute and record a mean value every 5 s. Despite the rejection of 50 Hz frequency, the high level of noise compared to the amplitude of the SP variations (Figure 5.8c) required to filter the data. Thus, the SP signal is filtered using a moving average by sliding a one-hour window for Experiment ①, a thirty-minutes window for Experiment ②, and a ten-minutes window for Experiments ③ and ④.

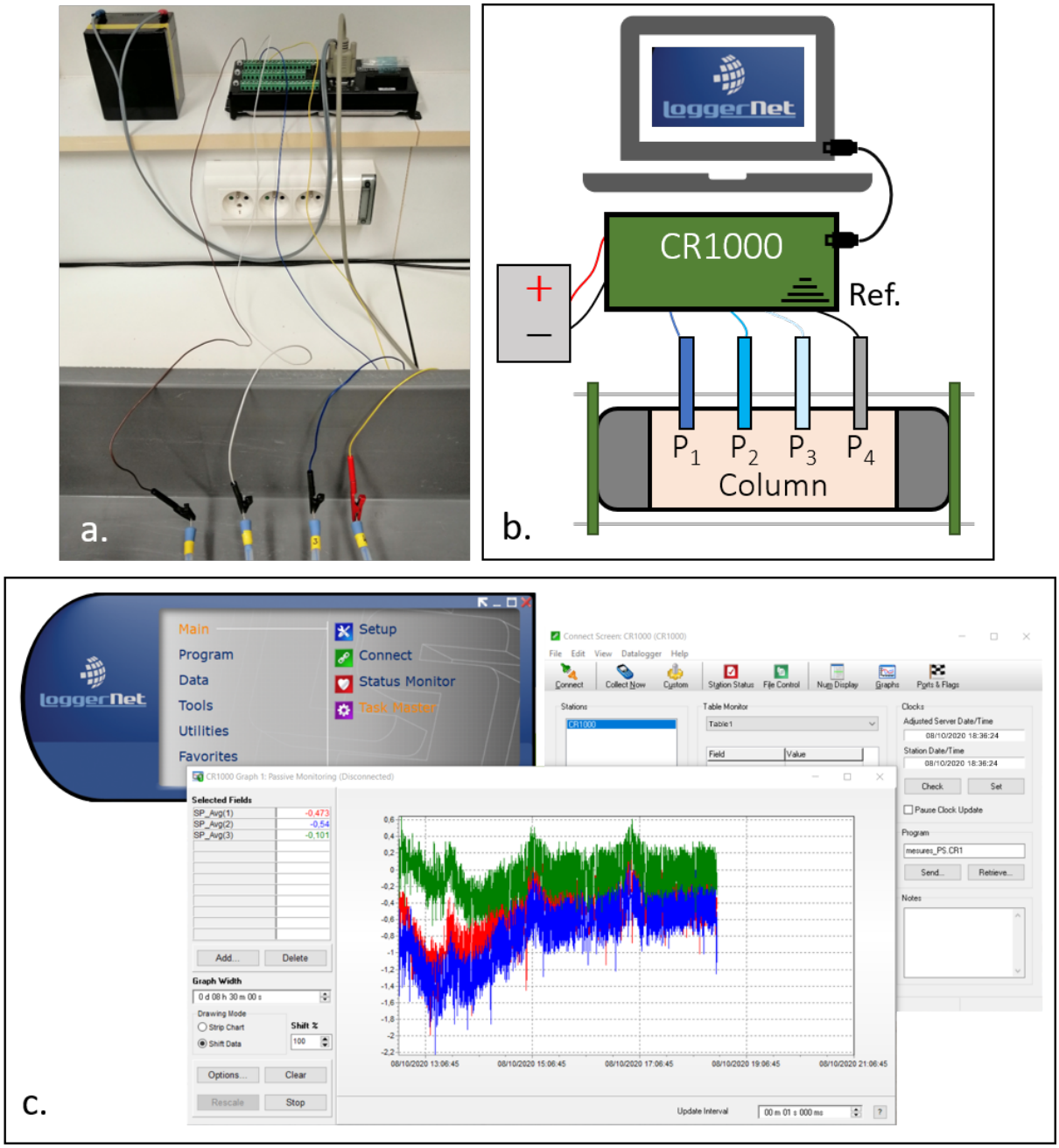

Figure 5.8: SP data acquisition unit. (a) photography of the data logger recording SP signal. P_1, P_2, and P_3 are connected with black clips, while P_4 is connected with a red clip. (b) schematic representation of the SP acquisition. The data logger CR1000 is powered by a battery and connected via USB to the computer. (c) interface of the Loggernet software used to read and download the recorded data.

Part III

Laboratory investigations and numerical modeling

CHAPTER

6 Geo-electrical characterization of calcite dissolution and precipitation: an experimental and numerical study

6.1 Introduction to the paper

This chapter presents the results obtained for Experiment ①, which experimental protocol is summarized in Section 5.2. Experiment ① was conducted on Bench ❶ (presented in Section 5.1) and using Column 1 (described in Section 4.4).

This experiment is divided into three sequential steps that are a first phase of equilibrium, followed by calcite dissolution, and the final step consists in precipitating calcite. If most of the obtained data show consistent results regarding the chemical reactivity of calcite, the interpretation of SIP phase spectrum is still questionable. On the contrary, SP method, gives remarkable variations associated to calcite dissolution and precipitation processes.

This experimental work is completed by numerical modeling, whose purpose is to assess which coupling can be the source of electric current measured with the SP method. As the study is focused on geochemical processes creating ionic concentration gradients, the source of SP signal comes from the electro-diffusive potential (presented in Section 2.3.4). Thus, a new theoretical framework is developed in this innovative study that contributes to the improvement of non-intrusive monitoring of reactive transport by coupling experimental geophysics investigation with numerical geochemical study. This new framework is also based on a petrophysical relationship describing electro-diffusion processes in a multi-species context. Furthermore, it should be pointed out that this petrophysical model is the first of its kind to be successfully tested on real data including reactive transport.

6.2 Paper

The experimental and numerical results of Experiment ① are reported in the form of an article that is intended for submission in *Water Resources Research*.

Geo-electrical signature of dissolution and precipitation processes in a synthetic carbonate sample

Flore Rembert[1⋆], *Damien Jougnot*[1], *Linda Luquot*[2], *Roger Guérin*[1]

[1] *Sorbonne Université, CNRS, EPHE, UMR 7619 METIS, 4 Place Jussieu, 75005, Paris, France*
[2] *Université de Montpellier, CNRS, Géosciences Montpellier, 22 Place Eugène Bataillon, 34090, Montpellier, France*

⋆ *Corresponding author: flore.r@wanadoo.fr*

Highlights

- Calcite precipitation and dissolution produce clear signature in self-potential and EC data
- We set-up a numerical framework to mechanistically link geo-electrical signals to reactive-transport processes
- We propose a new multi-ionic model to reproduce the self-potential signals

Abstract Dissolution and precipitation are the main chemical processes occurring in carbonate rocks, ubiquitous at the earth subsurface. Understanding and quantifying them is therefore necessary for the critical zone study. These fundamental geochemical processes can be monitored using geo-electrical methods sensitive to pore space changes, water mineralization, and mineral-solution interactions. In this study, we designed a new experimental set-up to monitor the self-potential (SP) and spectral induced polarization (SIP) signals during the dissolution and precipitation of calcite material. The column is packed with calcite grains and subjected to alternating dissolution or precipitation conditions through appropriate solution injection. We obtained clear SP response due to chemical changes provoked by dissolution and precipitation processes. Indeed, SP signals show clear signatures related to ionic concentration gradients, but no measurable electrokinetic coupling was recorded. In order to quantify the SP signal as ionic concentrations distribution in time and space, we propose a new framework based on the fluid junction potential theory for multiple ionic species coupled with 1D reactive-transport simulations. This approach reproduces well the measured geo-electrical signatures and allows us to determine and predict the precise location of the reactive area ; therefore helps the SIP spectra interpretation. The framework developed for this study opens new perspectives for SP applications to characterize key processes in the critical zone.

Keywords Calcite, Precipitation-dissolution, Laboratory experiment, Self-potential, Electrical conductivity

1 Introduction

Carbonate rocks occupy a vast area of land subsurfaces (Chen et al. 2017) and constitute reservoirs for key resources such as ground water (e.g., Kačaroğlu 1999; Bakalowicz et al. 2005), geothermal energy (e.g., Montanari et al. 2017), or fossil energies (e.g., Burchette 2012). The study of carbonate rocks is also very active because of their potential to serve for carbon dioxide (CO_2) geologic sequestration (e.g., Luquot et al. 2009; Cherubini et al. 2019). Carbonate rocks are also well known to be linked to coastal or agricultural problematic with contamination, erosion, and landsliding, to civil engineering with risks of cavity presence and collapsing, but also as a commonly exploited noble building material (e.g., Drew et al. 2017; Buckerfield et al. 2020).

However, studying carbonate reservoirs is a crucial challenge due to the multi-scale heterogeneity of rock properties and their strong chemical reactivity (e.g., Meyerhoff et al. 2014). These features are responsible for specific processes occurring in carbonate rocks over a wide size range (nm to km), such as groundwater flow and ionic transport in a reactive porous medium subjected to dissolution and precipitation. Dissolution of carbonate samples caused by CO_2 injection has already been well studied to understand the formations of wormholes and their complicate relationship with transport properties as permeability and porosity (e.g., Golfier et al. 2002; Noiriel et al. 2004; Noiriel et al. 2005; Luquot et al. 2009; Rötting et al. 2015). However, these experiments were generally based on images analysis which is an accurate technique for laboratory works but cannot be used on the field.

To comprehend carbonate reservoirs behavior during dissolution and precipitation, we need to be able to monitor their properties. On one hand, in a subsurface context, chemical analysis of the pore water can be quite intrusive, providing only restricted and spatially limited information (Goldscheider et al. 2008). On another hand, geo-electrical methods are non-intrusive and present a high sensitivity to physical and chemical properties of rocks and of pore fluids (e.g., Glover 2015), therefore being quite suitable for such monitoring (e.g., Binley et al. 2015). An increasing amount of work have shown the interest and the effectiveness of geo-electrical methods for laboratory or in situ monitoring hydrological processes and reactive transport (e.g., Revil et al. 2012). Nevertheless, geophysical methods are indirect, and thus, require appropriate models to give a quantitative interpretation (e.g., Hubbard et al. 2011; Kemna et al. 2012). In this laboratory study, we perform a geo-electrical monitoring of calcite dissolution and precipitation using three electrical methods: inline pore water electrical conductivity (EC), spectral induced polarization (SIP) and self-potential (SP).

The pore water only conducts electric current due to the presence of ionic species, behaving as electric charge carriers. Thus, the pore water EC depends on the nature of the ions in solution, as not all ions have the same mobility (e.g., hydrogen H^+ protons are much more mobile than hydrated ions such as sodium Na^+) and their concentrations. The pore water EC can hence be calculated knowing its chemical composition (McCleskey et al. 2012), but it requires temperature compensation (Sorensen et al. 1987).

The rock sample EC of a water saturated porous medium is very sensitive to the pore water EC and to geometrical rock properties, such as the porosity. The most famous law to link the rock EC to its porosity,

is an empirical relation developed by Archie (1942). Since then, many petrophysical models (i.e., based on physical couplings) have been developed and allow to use the EC measurement to describe the geometry of the pore space (e.g., Rembert et al. 2020). Furthermore, rock sample EC petrophysical modeling serves also to characterize ionic transport (e.g., Maineult et al. 2016; Jougnot et al. 2018) and reactive-transport (e.g., Ghosh et al. 2018).

The SIP method, by injecting an alternating current, measures both the rock sample EC and the ability of the porous rock to polarize. This method was originally developed to detect metallic particles (Schlumberger 1930; Kemna et al. 2012). Its use on sedimentary rocks is quite recent because the measured signal shows a much lower amplitude particularly in the case of carbonate rocks (e.g., Hupfer et al. 2017; Norbisrath et al. 2017; Johansson et al. 2020), requiring the development of high-precision acquisition instruments (e.g., Zimmermann et al. 2008).

A precursor study of Wu et al. (2010) showed that SIP method is sensitive to calcite precipitation in a matrix of glass beads by mixing calcium dichloride $CaCl_2$ with sodium carbonate Na_2CO_3. However, Wu et al. (2010) only used an empirical model to interpret their SIP results. Thus, this study, despite high-quality results, lacks of mechanistic explanation of the SIP signals. Indeed, in a first step, the SIP signal increases during the calcite precipitation experiment. Then, while the experimental conditions remain unchanged, the signal decreases day by day until the end of the experiment. Based on images of the sample at the end of the experiment, the authors hypothesize that the size of the precipitated calcite grains must play a role in the amplitude of the measured SIP signal but did not propose a physical model to explain it.

Leroy et al. (2017) proposed a physical-based model to re-interpret the SIP results of Wu et al. (2010) by polarization around the grains. In their model, the authors assume the grains to be spheres. At the beginning of the experiment, the observed polarization increase is considered to correspond to the nucleation of the calcite grains. Then, these grains nucleate as suspended solids and later homogeneously deposit at glass beads surfaces and polarize individually. Leroy et al. (2017), therefore, consider that the more grains nucleate, the more the signal of polarization is important. On the contrary, they explain the decrease of polarization occurring at the end of the experiment with the formation of aggregates of grains. This new configuration of calcite grains decreases the surface area and so does the polarization. Consequently at the end of the experiment, only small new nucleated grains polarize but there are fewer of them over time. Nevertheless, the model is based on many simplifications, such as the sphericity of grains or a homogeneous solute concentration inside the cell.

Nevertheless, the influence of calcite precipitation on SIP response remains difficult to characterize. Indeed, more recent experiments of SIP monitoring during calcite precipitation have been conducted. Izumoto et al. (2020) induced calcite precipitation in a sand matrix by mixing $CaCl_2$ with Na_2CO_3 and observed an SIP response sensitive to the concentration of the dissolved reactive species, rather than on the amount or the shape of precipitated calcite as conceptualized in the model of Leroy et al. (2017). Zhang et al. (2012) conducted an experiment of urea hydrolysis (by injecting urea in a water saturated sample, producing hydrogencarbonate HCO_3^-, hydroxide HO^- and ammonium NH_4^+ ions) followed by calcite precipitation (by injecting dissolved cal-

cium reacting with the hydrogencarbonate resulting from urea hydrolysis) in a silica gel column. They observed SIP variations, but they found that SIP was much more sensitive to pH variations (due to HO^- ions producted by urea hydrolysis) than by calcite precipitation. In light of these experimental results of Zhang et al. (2012), the results presented in Saneiyan et al. (2019) and in Saneiyan et al. (2021) must be carefully considered. In these field and laboratory studies, calcite precipitation is induced from ureolytic bacteria activity. Therefore, although pH changes are not mentioned in these studies, the bacterial activity stimulated to precipitate calcite involves the hydrolysis of urea, impacting the SIP measurement as shown by Zhang et al. (2012). Thus, the observed variations in SIP should not be attributed solely to calcite precipitation.

To the best of our knowledge, Halisch et al. (2018) is the only published reference on carbonate dissolution SIP monitoring. However, unlike for the precipitation studies, they did not observe a clear signature. Indeed, Halisch et al. (2018) conducted SIP measurements on a carbonate sample saturated with brine after several steps of dissolution with an acid activated by heating the sample (Kjoller et al. 2016). They measured a specific response but it remained constant with time, while the petrophysical measurements showed clear patterns in favor of strong dissolution. A first hypothesis to explain this absence of variations could be that, contrary to calcite precipitation, calcite dissolution does not generate variations on the SIP signal. A second hypothesis that we propose to examine in this study, is that the experimental protocol proposed by Halisch et al. (2018) does not enable to observe SIP variations, because they did not perform the measurements on a sample that is undergoing a chemical imbalance.

The SP method is based on the measurement of the perturbation in the electrical field due to currents naturally generated by different contributions. This method, simple to set up, is however complex to interpret as it involves the superposition of different possible sources of current. In case of calcite dissolution or precipitation at constant temperature, SP signal can be related to water flow and chemical reactions through electrokinetic and electrochemical couplings, respectively (e.g., Jouniaux et al. 2009; Revil et al. 2013). The electrokinetic coupling is related to separation of electrical charges at the interface between the charged mineral surfaces and the pore water solution (i.e., generating the so-called streaming potential). The electrochemical coupling, in the case of calcite dissolution or precipitation is related to the presence of ionic concentration gradients. This source of current give rise to the so-called electro-diffusive (or junction) potential. It originates from the separation of charges due to the difference of mobilities between migrating dissolved ionic species (e.g., Revil 1999; Maineult et al. 2005). The SP method therefore allows to study mixing and reaction zones between solutions such as saline intrusions (e.g., Graham et al. 2018; MacAllister et al. 2018) or water intrusion into hydrocarbon reservoir (Gulamali et al. 2011). In this study, we propose to model the SP signature of reactive transport, that is, the chemical interaction between the flowing pore water and the porous calcite matrix.

Cherubini et al. (2019) conducted SP and EC measurements on limestone samples submitted to drainage with a non-wetting phase composed of CO_2. They found that the calcite dissolution, induced by CO_2 injection, caused a change in calcium concentration in the pore water during drainage, which explains the change of pore water EC. Cherubini et al. (2019) also observed a decrease of the magnitude of the streaming potential

coupling coefficient. They conclude that the streaming potential coupling coefficient obtained from SP measurements can be a tool to estimate dissolution rates because it is sensitive to brine concentrations after a CO_2 release. However, Cherubini et al. (2019) do not take into account the contribution of ionic gradients that can be generated by calcite dissolution in their sample. To the best of our knowledge, there is no study of calcite precipitation using SP monitoring.

In light of the small number of studies using geo-electrical methods to investigate calcite dissolution and precipitation and in view of the conflicting results reported in the literature, we consider appropriate to present the results of a study jointly addressing dissolution and precipitation processes using both SP and SIP methods. Thus, we present a new experimental setting able to alternatively put the carbonate sample under precipitation or dissolution conditions and to monitor these processes with several geo-electrical signals using SP and SIP methods, while collecting samples of the outlet pore water to compare the geophysical results with physico-chemical characterization of the pore water.

2 Theoretical framework

2.1 Reactive transport in carbonaceous system

2.1.1 Carbonate material reactivity

In this work, we consider pure calcite mineral as it is a very reactive mineral when in contact with a non-equilibrated solution. This chemical reactivity can be described by the following system. Table 1 summarizes the equations of the system in equilibrium with calcite in aqueous media proposed by Plummer et al. (1982) and their associated thermodynamic constants at 25 °C.

Table 1: Equations proposed by Plummer et al. (1982) for the carbonate system in equilibrium with calcite in aqueous media.

Equations	Thermodynamic constants (25 °C)
$CO_2 + H_2O \leftrightarrow H_2CO_3$	$K_h = 10^{-1.47}$
$H_2CO_3 \leftrightarrow H^+ + HCO_3^-$	$K_{A_1} = 10^{-6.35}$
$HCO_3^- \leftrightarrow H^+ + CO_3^{2-}$	$K_{A_2} = 10^{-10.33}$
$Ca^{2+} + CO_3^{2-} \leftrightarrow CaCO_3$	$K_{sp} = 10^{-8.42}$

Dissolution or precipitation occur when the pore water is not at the chemical equilibrium with calcite. In order to quantify this equilibrium, the saturation index of calcite is defined as

$$\Omega = \frac{(Ca^{2+})(CO_3^{2-})}{K_{sp}}, \tag{1}$$

where (Ca^{2+}) and (CO_3^{2-}) (-) are the calcium and carbonate ions activities, respectively, and K_{sp} (-) is the solu-

bility product of calcite. Ion activity of ion X_i is defined as the product of the ion concentration C_{X_i} (mol m^{-3}) with the activity coefficient γ_{X_i} (-) as follows (e.g., Cohen et al. 2007)

$$(X_i) = \gamma_{X_i} \frac{C_{X_i}}{C^{\ominus}}, \tag{2}$$

where $C^{\ominus}$ is the standard concentration ($C^{\ominus}$ = 1 mol L^{-1}). Given the low ionic force IF (mol L^{-1}) of the solutions, defined by

$$IF = \frac{1}{2} \sum_{X_i} C_{X_i} z_{X_i}^2, \tag{3}$$

where z_{X_i} (-) is the valence of ion X_i, activity coefficients are determined using the Güntelberg approximation

$$\log\left(\gamma_{X_i}\right) = -0.509\, z_{X_i}^2 \left(\frac{\sqrt{IF}}{1+\sqrt{IF}}\right). \tag{4}$$

In this study, as we consider synthetic material, the only ions present in the pore water solution are the one from the carbonate system and bystander ions like sodium (Na^+) and chloride (Cl^-). In this case, for a measured pH around 8, alkalinity can be approximated by the concentration of the bicarbonate ion ($C_{HCO_3^-}$). The saturation index, defined by Equation (1), can thus be rewritten as

$$\Omega = \frac{\gamma_{Ca^{2+}}\, C_{Ca^{2+}}\, \gamma_{HCO_3^-}\, Alk\, K_{A_2}}{K_{sp}\, 10^{-pH}}, \tag{5}$$

with Alk (mol m^{-3}) the alkalinity measurement.

2.1.2 Flow and transport

When considering water flow in the pore space of a carbonate material, the reactivity presented above is influenced by the flow kinetic. Porous media and the flow within can be characterized by porosity ϕ (-) and permeability k (in m^2). Ionic transport within the pore space can be done through advection or diffusion processes (e.g., de Marsily 1986). The Péclet number describes the relative significance of advection to molecular diffusion (e.g., Bear 2013). For a non consolidated medium it is defined as

$$Pe = \frac{UL}{D}, \tag{6}$$

where L (m) is the length of the column and D (m^2 s^{-1}) is the diffusion coefficient in water. U (m s^{-1}) is the Darcy velocity of fluid particles and is defined as

$$U = \frac{Q}{S}, \tag{7}$$

where Q is the flow rate (m^3 s^{-1}) and S is the crossed surface area of the column (m^2). $Pe > 1$ means that advection dominates while transport dominated by diffusion is characterised by $Pe < 1$.

2.2 Electrical conductivity

2.2.1 Pore water electrical conductivity

The pore water EC σ_w (S m^{-1}) is an easy parameter to measure but its calculation is non-trivial and is often no more than an approximation. Multiple approaches exist, but physical-based methods are generally based on the notion of the molar conductivity Λ_m (S m^2 mol^{-1}), defined as the EC of an aqueous solution of one molar solute concentration ($C = 10^{-3}$ mol m^{-3}), measured in a conductimetry cell with electrodes spaced 1 cm apart. Thus, the molar conductivity is defined as

$$\Lambda_m = \frac{\sigma_w}{C}. \tag{8}$$

For an electrolyte composed of multiple solutes, the molar conductivity can be decomposed in the sum of ionic molar conductivity Λ_i. Hence, the pore water EC can be written as

$$\sigma_w = \sum_{X_i} \Lambda_{X_i} C_{X_i} \tag{9}$$

For a porous medium subjected to an electric field E (V m^{-1}), charged particles of the electrolyte (i.e., cations and anions) will move through the pores in response. The ability of the particle to reach certain velocity v (m s^{-1}) is called the mobility β (m^2 s^{-1} V^{-1}): $v = \beta E$. The mobility is dependent of the electrical charge and of the particle Stokes radius. Each ionic specie has hence, a specific mobility value β_{X_i}, which is proportional to the molar conductivity

$$\Lambda_{X_i} = z_{X_i} \beta_{X_i} \mathscr{F}, \tag{10}$$

where $\mathscr{F}$ is the Faraday constant ($\approx 9.649 \times 10^4$ C mol^{-1}). Thus, the pore water EC becomes

$$\sigma_w = \mathscr{F} \sum_{X_i} z_{X_i} \beta_{X_i} C_{X_i} \tag{11}$$

2.2.2 Sample complex electrical conductivity

The complex EC is a frequency dependent parameter that can be obtained from SIP measurements. For each frequency { (Hz), it can be described by its magnitude $|\sigma^*|$ (S.m^{-1}) and its phase shift φ (mrad) (e.g., Weller et al. 2013), such as

$$\sigma^*(\omega) = |\sigma^*(\omega)|\, e^{i\varphi(\omega)}. \tag{12}$$

where ω (rad) is the angular frequency ({ $= 2\pi\omega$). The phase shift φ is a negative value because polarization effects create a delay in porous media responses to the electrical excitation. As for all complex values, σ^* can also be described by its real part σ' and its imaginary part σ'' according to

$$\sigma^* = \sigma' + i\sigma''. \tag{13}$$

The real part σ' represents the ohmic conduction while the imaginary part σ'' corresponds to charge polarization mechanisms.

At low frequencies, the complex EC can be modeled based on a parallel addition of two contribution terms (e.,g., Vinegar et al. 1984; Weller et al. 2012),

$$\sigma^* = \frac{\sigma_w}{F} + \sigma^*_{surf}. \tag{14}$$

In the above expression, the first term σ_w/F corresponds to the EC of the connected pores filled with the electrolyte in which we neglect the frequency dependence and F (-) is the formation factor (e.g., Glover 2015). Archie (1942) proposes the following relationship (the so called Archie's law),

$$F = \phi^{-m}, \tag{15}$$

where m (-) is an empirical parameter called the cementation exponent. The formation factor can be related to geometrical parameters of the pore space such as the tortuosity and the constrictivity (e.g., Rembert et al. 2020).

The second term σ^*_{surf} (S m^{-1}) is a complex value which real (σ'_{surf}) and imaginary (σ''_{surf}) components correspond to the conduction and polarization effects, respectively. For a fully saturated porous medium, this leads to

$$\sigma' = \frac{\sigma_w}{F} + \sigma'_{surf} \tag{16}$$

and

$$\sigma'' = \sigma''_{surf}. \tag{17}$$

In the case of carbonate rocks, σ'_{surf} is low compared to the groundwater EC in carbonate reservoirs (e.g., Rembert et al. 2020). Thus, for the study of dissolution and precipitation of water saturated carbonate rocks at standard values of σ_w, the real part of the surface conductivity can be neglected (e.g., Cherubini et al. 2019).

Equation (17) assumes that the polarization is only associated with the surface conductivity σ''. Indeed, polarization effects occur within the so-called electrical double layer (EDL) at the interface between the electrolyte and the mineral surface and the amplitude of these polarization effects depends on the frequency of the exciting electrical field. Several laboratory studies of calcite precipitation have shown an evolution of this parameter through time in multiple contexts (Wu et al. 2010; Izumoto et al. 2020; Saneiyan et al. 2021), but never in a calcareous matrix as we propose in this study and which is more realistic for the study of karst systems. Furthermore, for now, only one mechanistical model has been proposed by Leroy et al. (2017) and tested on the dataset from Wu et al. (2010).

2.3 The self-potential method

The SP method is a passive geophysical technique based on measuring the natural electric field, generated by a physical coupling with other forces impacting the geological media. Following the framework of Sill (1983), the total electric current density J_{tot} (A m^2) follows

$$J_{tot} = -\sigma \nabla V + j_s, \tag{18}$$

where ∇V (V m^{-1}) is the gradient of the electric potential ($E = -\nabla V$) and j_s (A m^2) is the cross coupling current density also called the source current density. If no external source is imposed, then for an homogeneous medium, the total electric current density is divergenceless ($\nabla \cdot J_{tot} = 0$), leading to

$$\nabla \cdot j_s = \nabla \cdot (\sigma \nabla V). \tag{19}$$

The two main contributions to SP signal are related to electrokinetic (superscript EK) and electrochemical (superscript $diff$) couplings (e.g., Linde et al. 2011; Revil et al. 2013) and can be summed to obtain the total source current density: $j_s = j_s^{EK} + j_s^{diff}$ (e.g., Jougnot et al. 2013).

2.3.1 The electrokinetic contribution

The SP signal that originates from the electrokinetic coupling is called the streaming potential. It is induced by pore water fluxes in a porous medium composed of minerals electrically charged at their surface. This surface charge of the mineral is counterbalanced by an excess of charge located in the EDL. These counterions are distributed between the Stern Layer and the diffuse layer (e.g., Hunter 1981). Ions from the Stern layer are sorbed onto the mineral surface and can be considered fixed. While ions in the diffuse layer, as its name suggests, can diffuse more freely because they are less affected by the surface charges. Therefore, when the pore water flows, it effectively drags a volumetric excess of charge $\hat{Q}_v$ (C m^{-3}) from the diffuse layer, creating an advective flow of electrical charges (e.g., Kormiltsev et al. 1998; Jougnot et al. 2020). This net electrical charge advection creates in turns an electrokinetic source current density that can be defined by

$$j_s^{EK} = \hat{Q}_v U. \tag{20}$$

Therefore, one can note that, for very low surface charge or small water flow, the displaced excess of charge will be low, leading to a small streaming potential contribution. Jougnot et al. (2020) present an overview of the methods and models to obtain the effective excess charge density. It is worth noting that the $\hat{Q}_v$ decreases for increasing permeability and pore water EC (e.g., Guarracino et al. 2018; Jougnot et al. 2019).

Revil et al. (2004) propose an entire theoretical framework to describe coupling in porous media among which the electrokinetic coupling coefficient, that is the ratio between the water pressure gradient to the electrical field (i.e., voltage) gradient (Smoluchowski 1903). Hence, they relate the coupling coefficient C^{EK} (V Pa^{-1})

to this effective excess charge by

$$C^{EK} = -\frac{\hat{Q}_v k}{\eta_w \sigma}, \tag{21}$$

where η_w (Pa s) is the dynamic viscosity of water, σ (S m^{-1}) is the medium EC, and k (m^2) is the medium permeability. This expression shows that permeability or EC variations will directly affect the streaming potential coefficient. Thus, the pore water EC and its reactivity with the porous matrix can have strong influence on the streaming potential (Cherubini et al. 2019).

2.3.2 The electro-diffusive contribution

In the case of the carbonate system, the chemical reactions occurring during precipitation or dissolution generate ionic concentration gradients, therefore generating electrochemical couplings (e.g., Revil et al. 2006). This source of SP signal is called the electro-diffusive potential or the fluid junction potential (e.g., Jouniaux et al. 2009). It is an electrostatic field which compensates the charge separation due to differential mobility between ions (e.g., $\beta_{Na^+} < \beta_{Cl^-}$) along the concentration gradient to maintain the electroneutrality of the system. Many laboratory works have observed and successfully modeled this phenomena for simple systems (e.g., Maineult et al. 2005; Leinov et al. 2014; MacAllister et al. 2019). For example, Maineult et al. (2005) conducted laboratory experiments of NaCl diffusion in a sand matrix and succesfully modeled it using the Henderson formula (Henderson 1907; Guggenheim 1930; Revil 1999). This model, initially developed for cells with liquid-liquid junctions, have been adapted by Maineult et al. (2005) for porous media, by introducing the porosity ϕ in the electro-diffusive coupling coefficient α^*. As a result, the electrical potential difference ΔV (V) can be written as follows,

$$\Delta V = \alpha^* \frac{\nabla C}{C} = \phi \frac{\mathscr{R} T}{\mathscr{F}} \frac{\beta_{Na^+} - \beta_{Cl^-}}{\beta_{Na^+} + \beta_{Cl^-}} \frac{\nabla C}{C}, \tag{22}$$

where $\mathscr{R}$ is the molar gas constant (≈ 8.314 J mol^{-1} K^{-1}) and T (K) is the absolute temperature.

Revil et al. (2006) propose an a mechanistic framework and an expression for the electro-diffusive source current in a multi-ionic context, which can be synthesized as (Linde et al. 2011)

$$j_s^{diff} = k_B T \sum_{X_i} \frac{t_{X_i}^H \sigma}{q_{X_i}} \nabla \ln(C_{X_i}) \tag{23}$$

where X_i describes the different ions present in solution. Then, $t_{X_i}^H$ corresponds to the microscopic Hittorf number (-) of ion X_i. However, in this model the Hittorf number does not present a single definition (see, Revil et al. 2006, for details) and is expected to be used for an electrolyte in which the mobilities of the different ions do not significantly differ from each other. However, in the present experiment we have to consider different solutions with, among them, an acid solution to dissolve calcite. Injecting acid releases hydrogen protons (H^+) which present a mobility ten times greater than for other ions in the studied system. Therefore, the model proposed by Revil et al. (2006) is not suitable for our study.

2.3.3 Development of a new model for the diffusion potential in a multi-ionic system

In the context of a multi-ionic electrolyte with a concentration gradient, the cross coupling electro-diffusive source current density j_s^{diff} combines the contribution of all ions in solution. Thus, the corresponding coupling must take into account the contributions from all the ions.

In the following, the solution is assumed to be ideal, that is, the activity of a component is identical to its concentration. The diffusion anions and cations can be described by Fick's law. In one-dimension, the flux J_{X_i} (mol s^{-1} m^{-2}) of each ion specie X_i is defined as (Strathmann 2004; Revil 1999)

$$J_{X_i} = -D_{X_i}\phi\frac{dC_{X_i}}{dx}, \tag{24}$$

where D_{X_i} (m^2 s^{-1}) is the ionic diffusion coefficient and C_{X_i} (mol m^{-3}) is the molar concentration of ion X_i. The original definition of J_{X_i} coming from Strathmann (2004) is used for aqueous media, but since we consider a porous media, only the pore fraction must be considered. Thus, the porosity ϕ is introduced in the above expression as developed by Sen (1989).

As we consider a dielectric porous medium, it is assumed that only ions of the electrolyte can be electric charge carriers. Thus, the electric current density j_s^{diff} is defined by (Strathmann 2004)

$$j_s^{diff} = \mathscr{F}\sum_{X_i} J_{X_i} z_{X_i}. \tag{25}$$

Nevertheless, the electric current density is above all defined by Ohm's law and, thus, is given by

$$j_s^{diff} = \sigma\frac{dV}{dx}. \tag{26}$$

Then, combining Eqs. (24), (25), and (26) yields to

$$\frac{dV}{dx} = -\frac{\phi\mathscr{F}}{\sigma}\sum_{X_i} z_{X_i} D_{X_i}\frac{dC_{X_i}}{dx}. \tag{27}$$

Then, integrating this expression for a couple of electrodes leads to

$$\Delta V_{\mathrm{P}_j-\mathrm{P}_4} = \frac{\phi\mathscr{F}}{\sigma}\sum_{X_i} z_{X_i} D_{X_i}(C_{X_i,P_j} - C_{X_i,P_4}), \tag{28}$$

where ΔV (V) is the electrical voltage measured with SP method. P_j is one of the measurement electrodes, with index j comprised between 1 and 3. P_4 is the reference electrode. In this equation, the concentration of each dissolved ionic specie is supposed to present no lateral variation, thus it presents a single value at each electrode position along the porous medium.

3 Material and method

3.1 Experimental set-up

The experimental set-up used in this work allows to dissolve or to precipitate calcite and to monitor the sample electrical properties during these processes with several methods: SIP, SP, and the pore water EC (see Figure 1).

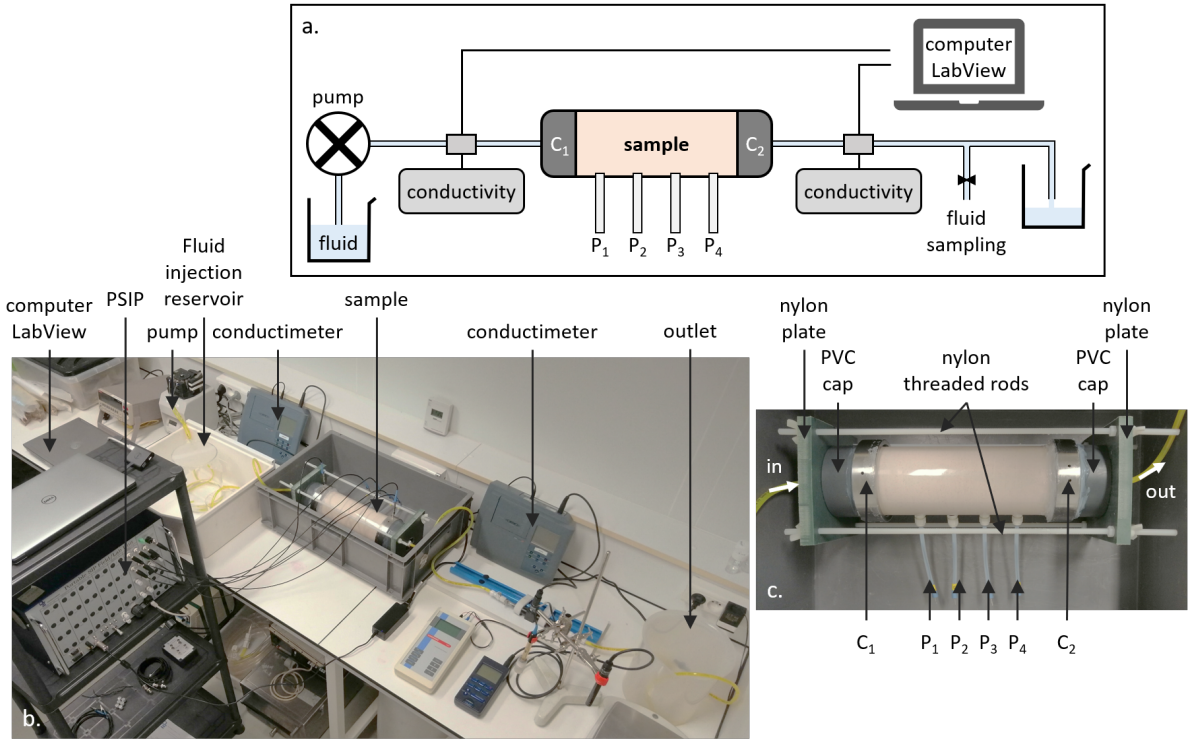

Figure 1: a, schematic drawing of the experimental set-up. C_1 and C_2 are the current electrodes made of stainless steel while P_1 to P_4 are the Ag-AgCl unpolarizable potential electrodes. b, photography of the set-up during an SIP acquisition. c, photography of the sample. The sample is a plexiglas cylinder filled with calcite grains. The tightening structure clamps the sample and the current electrodes with four threaded rods between two rigid plates.

The porous matrix is composed of compacted calcite grains. These grains come from crushed limestone made of almost pure calcite and are sieved so that their diameters are comprised between 125 and 250 µm (thus, the mean grain diameter is $< d_g >$ = 188 µm). The porosity is calculated by weighing the amount of calcite required to fill the entire column volume, we obtain an initial porosity ϕ_{init} = 41.1%.

The column is a Plexiglas cylinder with a length of 25 cm and an inner diameter of 9 cm leading to a surface area of S = 4.5 cm^2. The cylinder is drilled every 5 cm to screw 4 measurement electrodes named P_1, P_2, P_3, and P_4. Two drilled metallic cylinders, referred as C_1 and C_2 in Figure 1, are placed on both sides of the Plexiglas cylinder in order to shut the sample, let the water flow through the device, and serve for the electric current injection. PVC caps are placed on both sides of electrodes C_1 and C_2 to connect the inlet and outlet tubes (Figure 1c). All of these elements are maintained together with a tightening structure made of nylon. A plastic material was used instead of a metal structure because the latter caused interference during the SIP

measurement.

The measurement electrodes are of the silver/silver-chloride (Ag/AgCl) type, because this type of electrodes is reputed to have a steady intrinsic potential and to not polarize when subjected to an electric field (e.g., Jougnot et al. 2013). The Ag/AgCl electrodes manufactured for this study are made of a silver wire coated with AgCl salt (obtained by bleaching) and put in a tube, filled with a gelled NaCl solution and plugged by a porous ceramic.

At the inlet there is a given solution which has a defined affinity with calcite in order to dissolve or precipitate (inlet solution compositions are given in Table 2). This inlet solution flows through the sample with a constant flow rate of 25.2 mL h^{-1} thanks to a peristaltic pump. Combining Equations (6) and (7), we compute a Péclet number of 92, which means that advection is the most important mechanism of transport, but diffusion is not negligible. Given the flow rate and the dimensions of the set-up, it takes 2 h for the injected solution to reach the column entrance. Then it takes 25 h for the inlet solution to cross the column. It takes a total of 28 h for the injected solution to flow through the entire set-up.

To monitor the chemical evolution through time the outlet pore water is collected during 1 h (a volume of 20 mL of outlet solution was required to perform the entire set of analysis), filtered (< 0.2 μm), and analyzed. For each outlet pore water sample, we measured pH immediately after collecting the sample, then the sample was filtered and we measured alkalinity on the same day of the collect. Alkalinity is the amount of alkaline species present in solution and in this system there are three of them: HCO_3^-, CO_3^{2-} and HO^-. Its value is obtained with an acid/base titration. Then, we measured calcium concentration at the end of the experiment. Meanwhile, samples were stored between 2 °C and 4 °C). Calcium concentration is obtained from HPLC (High Performance Liquid Chromatography) analysis with the chromatograph ICS-3000 from Dionex©.

As water EC depends on the ionic concentrations (Equation (11)), two conductivity meters (inoLab Cond 730 from WTW) logged continuously the inlet and outlet pore water EC. The values were transferred through analog outputs to a digital multimeter (Model 2000 Multimeter from Keithley) cabled to computer with a Labview interface to record simultaneously the inlet and outlet data every 3 s.

The room temperature was controlled with an air conditioning system, but to verify the temperature stability during the entire experiment the room temperature has been recorded. It shows steady results with maximal variations of ±1.3 °C around a mean value at 21.8 °C and a standard deviation of ±1.1 °C. No temperature correction was applied to the raw geophysical signal, since we were not interested in apparent values, but wanted to compare the results obtained from the different methods. Note that the room temperature presents an anomaly during precipitation. It rose up to 27 °C, then returned to 22 °C.

For the SIP measurements, we injected an alternating electrical current through the stainless steel electrodes C_1 and C_2 and measured simultaneously on three channels between pairs of the aligned electrodes on the cylinder wall (see Figure 1). To be able to monitor the EC of different slices of the cylinder we measured on pairs P_1-P_2, P_2-P_3 and P_3-P_4. The SIP measurements were conducted with a PSIP device from Ontash et al. (2015). The sinusoidal voltage covered a spectrum from 5 mHz to 10 kHz at 40 frequencies uniformly dis-

tributed on a logarithmic scale and with an amplitude of ±5 V. The device records amplitude and phase of the complex EC.

SP data were recorded on three channels with the total field method. The fixed reference was the electrode P_4 and we measured the potential on three channels using the pairs P_1-P_4, P_2-P_4, and P_3-P_4, respectively. The measuring electrode dipoles have thus a decreasing spacing towards the reference electrode P_4. Indeed, P_1-P_4 = 15 cm., P_2-P_4 = 10 cm, and P_3-P_4= 5 cm. The data logger used for the SP monitoring is a CR1000 from Campbell Scientific. It was programmed to measure the voltage every 1 ms, then to compute and record a mean value every 5 s.

3.2 Time-line

The experiment is divided into three stages of different duration which are defined by the chemistry of the inlet solution and referred later as stage I, stage II, and stage III. As sketched on Figure 2, stars represent specific events during the experiment. Event 1: we turned-on the pump. Event 2: we connected the outlet to the inlet. Event 3: inlet and outlet compartments are disconnected and the injected solution is hydrochloric acid. Event 4: the new injected solution is over-saturated with calcite.

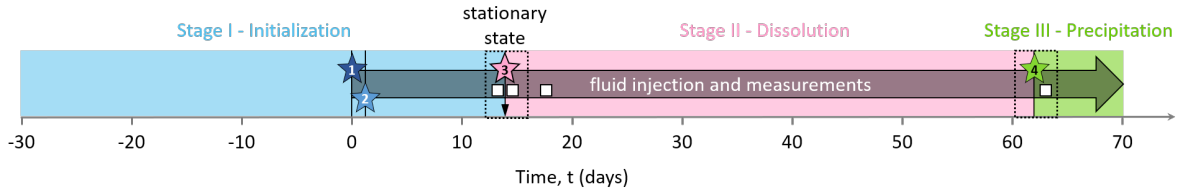

Figure 2: Time-line of the experiment successive stages and events. Blue, pink, and green rectangles indicate the different stages: stage I consists in the initialization to reach a stationary state close to the equilibrium with calcite, stage II corresponds to calcite dissolution with the constant injection of hydrochloric acid (solution S1), and stage III refers to calcite precipitation with the constant injection of a calcite over-saturated solution (S2). The four stars of the time-line are related to specific events. Event 1 refers to the turned-on of the peristaltic pump, event 2 to the connection between inlet and outlet, event 3 to the disconnection between inlet and outlet compartments and to the injection of hydrochloric acid, and event 4 to the start of injection of calcite over-saturated solution. The white squares corresponds to the four acquisition time of the phase spectra acquired with the SIP method and presented in Figure 7.

Stage I ($t \in [-30\ ;\ 13.85]$ d) played the role of the sample initialization. At the beginning the sample has been filled with grains and a saturating solution meant to be at saturation with calcite. The pump remained shut down during three weeks in order to reach a certain chemical equilibrium between the solution and the grains at the macro-scale ($t \in [-30;0]$ d). Then we turned on the pump to collect a sample of outlet pore water (star 1 on Figure 2). This first event (event 1) defines the experiment time-zero (t = 0 d). Then we closed the circuit (event 2 referred as star 2 on Figure 2) by connecting the inlet to the outlet at t = 1.09 d, to reach the system equilibration. We kept the set-up working on for a dozen days ($t \in [1.09\ ;\ 13.85]$ d).

Event 3 (presented as star 3 on Figure 2) starts stage II at t = 13.85 d. It corresponds to the disconnection between the inlet and outlet and the beginning of solution S1 injection to dissolve calcite grains. S1 is a solu-

tion of hydrochloric acid (HCl) concentrated at 10^{-3} mol L^{-1} (see S1 composition in Table 2). This step lasted approximately one month and half ($t \in [13.85 ; 61.84]$ d).

Table 2: Experimental conditions, chemical composition (from chromatography and ICP-OES analysis), experimental pH and alkalinity of the injected solutions (concentrations are given in mmol L^{-1}), and computed saturation index for calcite and activity coefficients. γ_1 corresponds to the activity coefficient of all ions with a valence of 1 (e.g., H^+ and HCO_3^-) and γ_2 corresponds to the activity coefficient of all ions with a valence of 2 (e.g., Ca^{2+}).

Experiment	**Dissolution**	**Precipitation**
Experimental conditions		
Temperature (°C)	21.8 ± 1.14	
Pressure (bar)	1	
pCO_2 (bar)	$10^{-3.5}$	
Sample	Crushed calcite with diameter ranging from 125 µmto 250 µm	
Inlet solution	Diluted hydrochloric acid (S1)	Over-saturated brine (S2)
Average concentrations of the inlet solutions in mmol L^{-1}		
$C_{Ca^{2+}}$	-	1.2
C_{Na^+}	-	4.9
C_{Cl^-}	1.0	2.4
pH	3.0	8.5
Alk (mmol L^{-1})	-	4.8
Saturation index and activity coefficients		
Ω	-	14
γ_1	0.96	0.90
γ_2	-	0.67

Event 4 (presented as star 4 on Figure 2) starts stage III at t = 61.84 d, corresponding to the change of the injected solution to precipitate calcite. The injected solution, referred as S2 (Table 2), is a calcite over-saturated solution, obtained by mixing $CaCl_2$ (1.2 mmol L^{-1}), Na_2CO_3 (0.1 mmol L^{-1}), and $NaHCO_3$ (4.8 mmol L^{-1}). It has a high saturation index (Ω = 14), while maintaining a low $C_{CO_3^{2-}}$ over $C_{Ca^{2+}}$ ratio to avoid calcite precipitation in the inlet reservoir (see S2 composition in Table 2).

3.3 1D reactive-transport simulations using CrunchFlow

CrunchFlow is a software package for simulating reactive transport to a variety of conditions in the earth and environmental sciences. Developed by Carl Steefel and co-workers (Steefel 2009), the code is based on a finite volume discretization of the governing coupled partial differential equations linking flow, solute transport, multi-component equilibrium, and kinetic reactions in porous media (e.g., Molins et al. 2014; Garcia-Rios et al. 2014).

The experiments of dissolution and precipitation were modeled using CrunchFlow code and the obtained simulation results were compared with the results from the outlet solution chemical analyses. Hence, we ob-

tained spatial and temporal ionic distributions during the entire experiment and considering the column as an effective 1D porous medium.

Table 3: Input parameters used for the CrunchFlow simulations under atmospheric conditions. Input pore water concentration values come from the outlet pore water chemical analyses and inlet solution concentration values come from S1 and S2 compositions.

Experiment	**Dissolution**	**Precipitation**
Rock composition	Calcite	
Reactive specific surface area ($m^2_{mineral}/m^3_{bulk}$)	1.5	
Discretization	60 patches: 20×0.0025 m - 40×0.005 m	
Temperature (°C)	22	from recording file
*Initial pore water (*mmol L^{-1}*)*		
pH	Charge	7.4
$C_{Ca^{2+}}$	Calcite	1.4
$C_{HCO_3^-}$	CO_2(g) 37	1.4
C_{Cl^-}	2.0	1.0
C_{Na^+}	2.0	0.0
C_{H^+}	-	-
*Inlet Solution (*mmol L^{-1}*)*		
pH	Charge	8.5
$C_{Ca^{2+}}$	0.0	1.2
$C_{HCO_3^-}$	CO_2(g) 37	4.8
C_{Cl^-}	1.0	2.4
C_{Na^+}	0.0	4.9
C_{H^+}	1.0	-
Flow and transport properties		
Effective diffusion coefficient (m^2 s^{-1})	3.0×10^{-9}	
Dispersivity (m)	0.9×10^{-2}	
Darcy velocity (m s^{-1})	0.9×10^{-6}	

3.3.1 Thermodynamic and kinetic data

Five aqueous primary species are considered in the simulations (Ca^{2+}, Cl^-, H^+, HCO_3^-, and Na^+), but CrunchFlow database has also specified thirteen secondary species (CO_2(aq), CO_3^{2-}, $CaCO_3$(aq), $CaCl^+$, $CaCl_2$(aq), $CaHCO_3^+$, $CaOH^+$, HCl(aq), $NaCO_3^-$, NaCl(aq), $NaHCO_3$(aq), NaOH(aq), OH^-). Rate laws for the reacting minerals were taken from the literature (Palandri et al. 2004).

During dissolution experiment, the monitored room temperature was steady (≈ 22 °C), but during precipitation, the room temperature rose to 27 °C, then fell and stabilized at 22 °C again. We therefore used the recorded temperature as an input of the CrunchFlow code for this simulation.

3.3.2 Rock and solution composition

The rock is considered as a pure calcite ($CaCO_3$) sample with an initial porosity of 41 %. For each simulation, only the dissolved and precipitated calcite phase is considered.

The rock sample for dissolution simulation is considered to be initially at the equilibrium with calcite (see the second column of Table 3) and the input solution is composed of HCl acid solution at pH = 3. In Tab. 3, pH = Charge means that pH is computed by the software according to the thermodynamics and not imposed by the initial conditions.

For precipitation, input solution and pore water chemistry are taken from the measurement of the chemical composition of the prepared solution S2 and from the outlet pore water sampled between day 20 and day 60 of the experiment, respectively (see the third column of Table 3). pH value for the input rock composition is low compared to the expected theoretical value. This is probably due to the fact that the dimensions of the column induce a certain isolation, shifting the calcite thermodynamic equilibrium.

3.3.3 Flow and transport properties

Darcy velocity, longitudinal dispersivity, and effective diffusion coefficient used in the simulations are shown in Table 3. Darcy velocity is computed from the constant flow rate imposed by the peristaltic pump. Dispersivity is chosen to be of the order of 10 % of the column width (Schulze-Makuch 2005; Chakraborty et al. 2018). The effective diffusion coefficient is the mean value of the diffusion coefficients of the main ionic species present in solution.

3.3.4 Discretization

The column is considered as a one-dimension domain composed of 60 aligned elements for both dissolution and precipitation simulations. The column is discretized using a two-zones domain composed of 20 shorter elements (0.0025 m) at the start of the column and 40 longer elements (0.005 m) along the rest for better resolution of changes in solution composition through time. The first centimeters of the column are finer discretized to better simulate the evolution of the system in this zone, assumed to be more reactive than the rest of the column.

3.3.5 Reactive specific surface area

The fit of the model to the experimental data (calcium concentration, alkalinity, and pH) was performed by adjusting the value of the mineral reactive surface area S_r (m^{-1}), only. This parameter is defined as the ratio of the grains surface area which will meet the reacting pore water over the total bulk volume. The reactive specific surface area was chosen to be the same for both dissolution and precipitation simulations, with a fitted value $S_r = 1.5\ m^{-1}$.

Considering the calcite grains as tightly packed and non-deformable spheres with a mean radius $< d_g >$ of 188 μm, the specific surface area S_s (m^{-1}), which represents the total surface area of the porous matrix in

contact with the pore water over the bulk volume, can be expressed as

$$S_s = \frac{6\, d_c}{< d_g >}, \tag{29}$$

where $d_c = 0.74$ is the volumetric density value for a maximum compactness. Thus, $S_s = 2.36\ 10^4$ m^{-1}for this porous medium. The fitted reactive specific surface area is lower than the specific surface area, which is in accordance with the definition of these two parameters.

3.4 A new numerical framework for multi-ionic junction potential modeling

We developed a new theoretical framework to quantitatively interpret SP measurements induced by ionic concentration gradients. First, we use CrunchFlow to simulate ionic temporal and spatial concentration evolution during calcite dissolution or calcite precipitation for each ion specie: $C_i = f_i(x,t)$ (see Figure 3). The inputs of the CrunchFlow simulations come from the experimental conditions. The only adjustable parameter is the mineral reactive surface area. Thus, the results of the CrunchFlow simulations are compared to the analyzed ionic composition of the outlet solution to set the appropriate value for the mineral reactive surface area.

Then, the distributions of C_{X_i} are used as inputs to compute the electro-diffusive potential using Equation (28). The EC term of Equation (28) comes from the interpolation of the rock sample complex EC amplitude $|\sigma^*|$ measured with SIP method. As a result, the modeled SP signal is also a function of time and space $\Delta V = f(x,t)$.

Finally, the modeled SP curves are compared to the experimental results to assess if the measured SP signal is controlled by ionic concentration gradients induced by dissolution and precipitation processes.

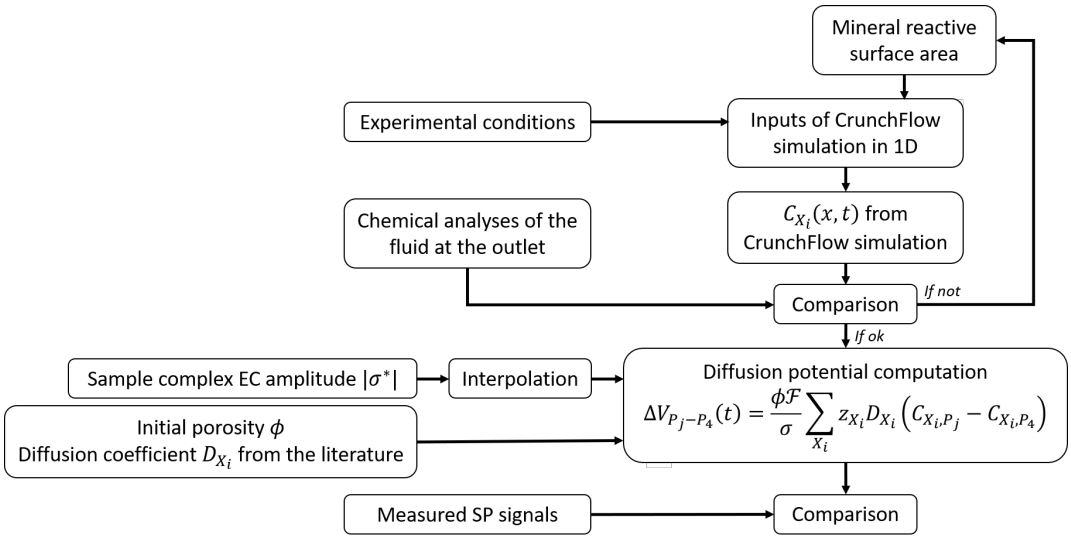

Figure 3: Numerical framework for SP signal modeling using successively experimental data, CrunchFlow simulation, and diffusion potential computation.

4 Results and discussion

As we intend to compare the data obtained from the different measurement methods, all the results are presented on the same figures. Figure 4 shows the results over the entire time-line of the experiment and Figure 5 focuses on the variations generated by dissolution (stage II which starts with event 3 at t = 13.85 d) and precipitation (stage III which starts with event 4 at t = 61.84 d).

4.1 Pore water electrical conductivity monitoring

Figure 4b presents significantly different behaviors between the stages of the experiment. The inlet pore water EC (σ_{in}) reveals that the solutions injected at events 3 and 4 present contrasting properties. However, the constant values of inlet solution EC during stages II and III (around 360 µS cm^{-1} and 710 µS cm^{-1} respectively) are the sign of steady experimental conditions over time.

Before turning on the pump (t < 0 d), the column filled with grains and the first inlet solution remained shut for a week. The goal of this time period was to let the grains and the pore water to reach a chemical equilibrium. At the beginning of stage I (t = -20.94 d), inlet and outlet solutions have two drastically different EC (σ_{in} = 210 µS cm^{-1} while σ_{out} = 460 µS cm^{-1}). This means that chemical reactions occurred in the sample before we turned-on the pump and some new ions were added in solution to increase the pore water EC. For this reason the inlet and outlet chambers have been connected (event 2, t = 1.09 d). This step ended when a certain horizontal asymptotic behavior has been reached with close values for both inlet and outlet solutions.

At the beginning of both stages II ($t \in$ [13.85 ; 61.84] d) and III ($t \in$ [61.84 ; 70] d), the water EC of the inlet solution varies drastically because of the change of injected solution with S1 (hydrochloric acid solution) at event 3 and with S2 (calcite over-saturated solution) at event 4 (see Figure 5a and b). After these abrupt jumps, the inlet water EC remains constant for the rest of each stage. The water EC curve of the outlet solution shows similar variations as the inlet solution curve with a time delay of 25 h to 30 h after each injection, corresponding to the required time to cross the column.

At stage II, the outlet water EC is expected to be higher than the inlet water EC due to the dissolution of calcite, which adds calcium and hydrogencarbonate ions in solution. However, the outlet water EC reaches 230 µS cm^{-1}, a lower value than the inlet water EC during stage II, σ_{in} = 360 µS cm^{-1}). The difference of EC between the inlet and the outlet is a clear sign of chemical reaction inside the sample, i.e., calcite dissolution. This counter-intuitive result can be explained by the difference in mobility between the hydrogen proton ($\beta_{H^+} = 3.62 \times 10^{-3}$ cm^2 s^{-1} V^{-1}) and the calcium ($\beta_{Ca^{2+}} = 0.62 \times 10^{-3}$ cm^2 s^{-1} V^{-1}) and hydrogen carbonate ($\beta_{HCO_3^-} = 0.46 \times 10^{-3}$ cm^2 s^{-1} V^{-1}) ions. Indeed, hydrogen proton mobility is much higher while the water EC value is controlled by the sum of the mobilities (Equation (11)). However, the water temperature during the experiment was closer to 21 °C than to 25 °C. We therefore need to apply a linear model of temperature

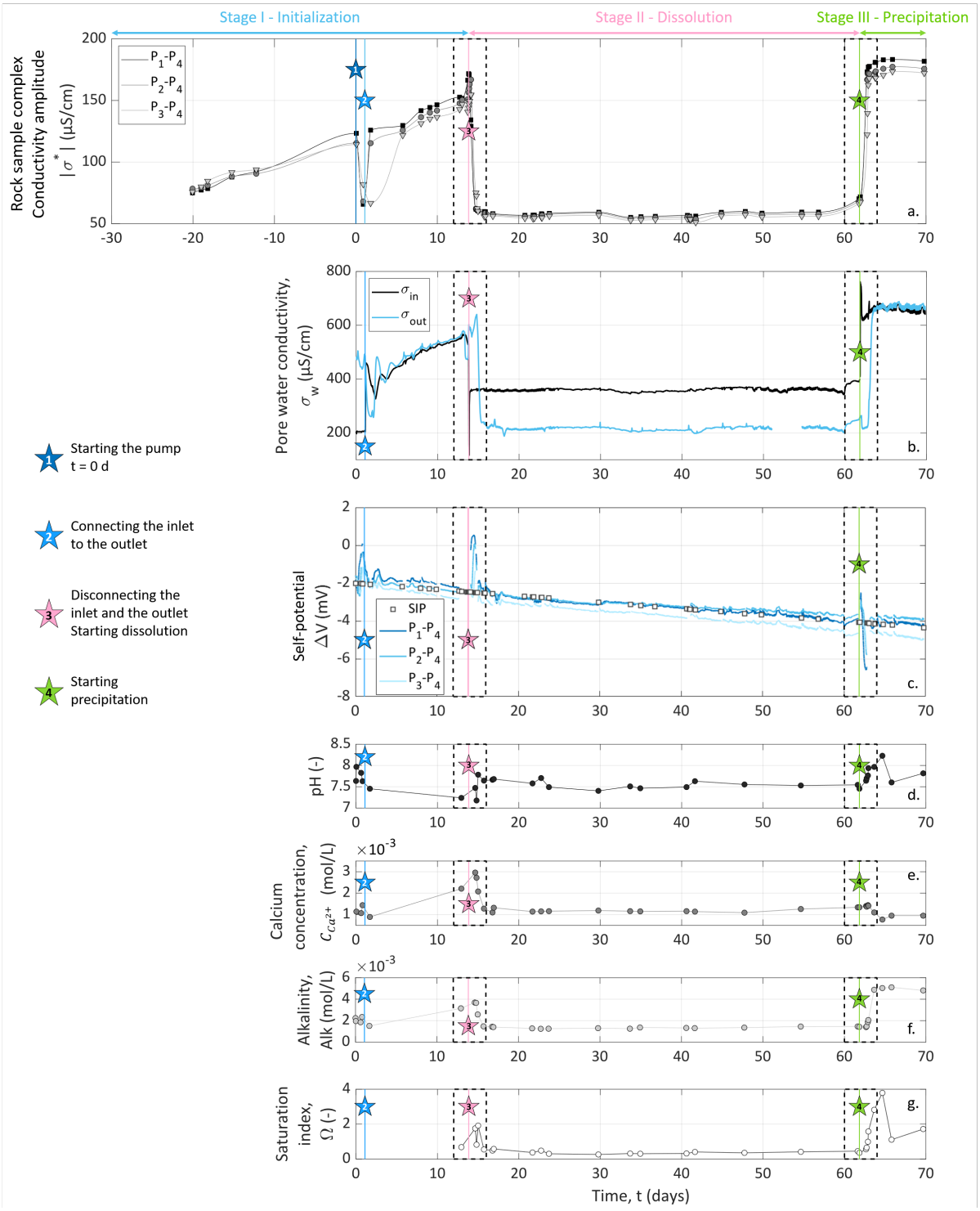

Figure 4: Measurements performed during the laboratory experiment. Stars represent the specific events defined in the time-line. Time zero is defined as the peristaltic pump turned-on moment (star 1). The dashed boxes are the delimitations of the zoom-in views presented on Figure 5. (a) rock sample complex EC amplitude measured with SIP method on three channels of acquisition corresponding to different dipoles of potential electrodes. (b) Inlet and outlet pore water EC. The data gap of the outlet water EC curve comes from an acquisition interruption due to the conductivity meter flat battery. (c) SP curves measured on three channels of acquisition corresponding to different dipoles of potential electrodes, using electrode P_4 as the reference. The white squares represent the interruption of SP acquisition to use SIP instead. (d, e, f) pH, calcium concentration $C_{Ca^{2+}}$, and alkalinity of the water sampled at the outlet of the column, respectively. (g) Saturation index for calcite computed from outlet pore water chemical analysis.

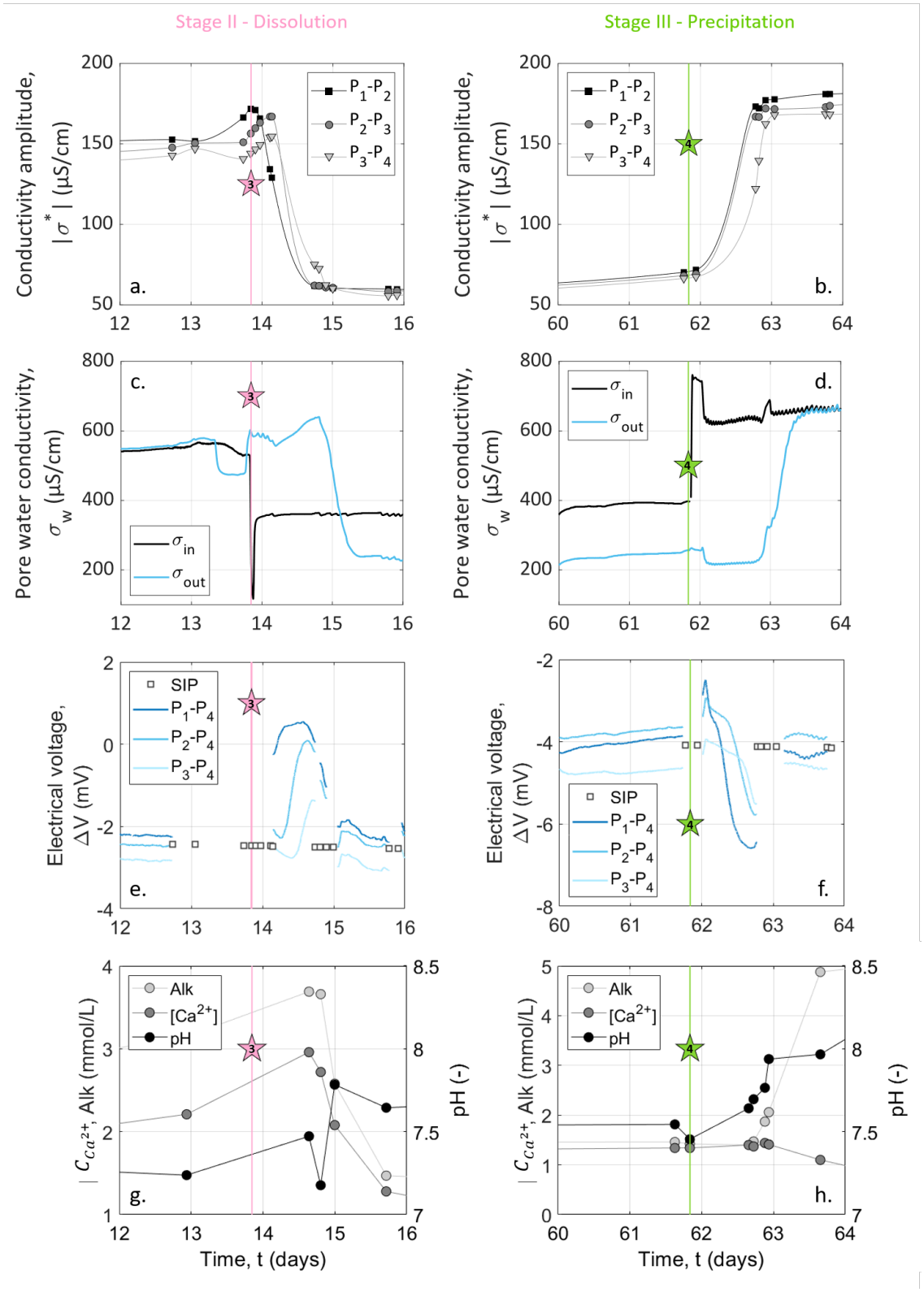

Figure 5: Zoomed views of Figure 4 centered on events 3 and 4. (a, b), rock sample complex EC amplitude measured with SIP method on three channels of acquisition corresponding to different dipoles of potential electrodes. (c, d), Inlet and outlet pore water EC. (e, f), SP curves measured on three channels of acquisition corresponding to different dipoles of potential electrodes, using electrode P_4 as the reference. The white squares represent the interruption of SP acquisition to use SIP instead. (g, h), calcium concentration, alkalinity, and pH variations.

compensation (Sorensen et al. 1987; Hayashi 2004)

$$\sigma_{w,\theta} = \sigma_{w,25}(1 + p_e(\theta - 25)), \tag{30}$$

where θ (°C) is the temperature to compensate and p_e is an empirical parameter equal to 0.03 °C^{-1} here (Smart 1992). Thus, from the chemical compositions of the inlet and outlet solutions measured during stage II, the combination of Equation (11) and Equation (30), it is possible to calculate the corresponding pore water EC in and out of the column: σ_{in} = 368 µS cm^{-1} and σ_{out} = 239 µS cm^{-1}(~ 35 % decrease). These values are a fairly similar to the measured data and reproduce well the decrease of water EC due to calcite dissolution (~ 36 % decrease), which consumes the most mobile hydrogen protons.

On the contrary during stage III, both inlet and outlet pore water EC are close to 710 µS cm^{-1}, therefore not giving a clear indication that chemical reaction occurred in the column.

4.2 Chemical analysis on outlet water samples

The chemical analysis of the outlet pore water samples are presented on Figure 4d, e, and f. pH measurements seem steady around 7.5 throughout the experiment. There is an exception during stage III ($t \in$ [61.84 ; 70] d): pH increases around 8.0 (Figure 5g and h). Variations on calcium concentration and alkalinity are clearer: they both increase during stage I ($t \in$ [0 ; 13.85] d) from 1.1 to 2.2 mmol L^{-1} for $C_{Ca^{2+}}$ and from 2.0 to 3.2 mmol L^{-1} for Alk. Then, event 3 (at t = 13.85 d) induces their decrease followed by their stabilization around 1.2 mmol L^{-1}. At event 4 (t = 61.84 d), alkalinity levels off at 5 mmol L^{-1}, while $C_{Ca^{2+}}$ decreases slightly to 1 mmol L^{-1}.

The variations of calcium concentration and alkalinity occur simultaneously with the fluctuations of the outlet pore water EC (Figure 5a, b, g, and h.). During stage I for $t \in$ [0 ; 13.85] d, we observe an increase of both pore water EC, alkalinity and calcium concentration because of calcite grains dissolution. At the beginning of stage II, outlet pore water EC, alkalinity and calcium concentration decrease and stabilize. This drop is caused by the inlet solution change from the previous inlet solution to chlorid acid which does not contain any dissolved calcite. The nonzero values of calcium and alkalinity are caused by calcite dissolution. The succeeding stabilization is the result of a constant dissolution rate. At stage III alkalinity, pH and outlet pore water EC increase while calcium concentration slightly decreases. The inlet solution calcium concentration worth 1.2 mmol L^{-1} and the alkalinity worth 4.9 mmol L^{-1}. The measurements of alkalinity and calcium concentration on the outlet solution ($C_{Ca^{2+}}$ = 1.1 mmol L^{-1} and Alk = 4.8 mmol L^{-1}) are slightly lower than in the inlet solution. This could be an indication of calcite precipitation. However, as both inlet and outlet solutions have close EC values, if precipitation occurred it must be a very few amount.

Figure 6 presents the porosity computation based on the calcium concentration measurements. The initial porosity value of 41.11 % (at t = -20.94 d), is obtained from the measurement of the mass of the calcite grains

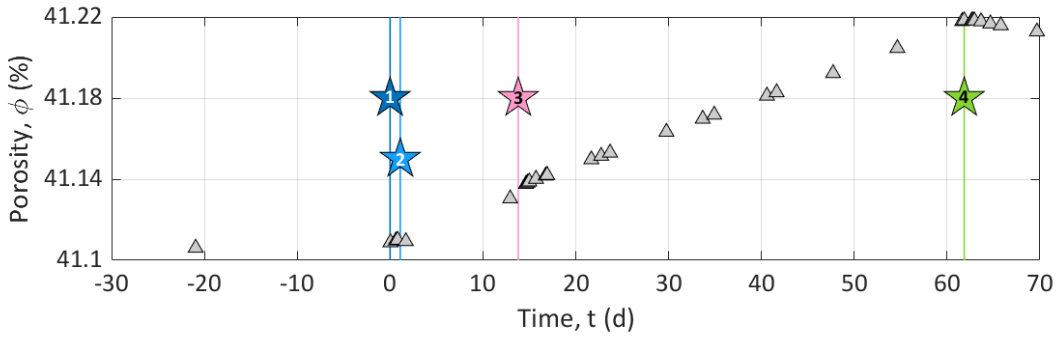

Figure 6: Porosity evolution during the experiment. The first point is obtained computing the mass of calcite filling the column. Then, the other points are estimated from the calcium concentration measurements.

m_{CaCO_3} (kg) filling the column

$$\phi(t = -20.94 \text{ d}) = \frac{V_{tot} - V_{CaCO_3}}{V_{tot}} = \frac{V_{tot} - \frac{m_{CaCO_3}}{\rho_{CaCO_3}}}{V_{tot}}, \tag{31}$$

where V_{tot} (m^3) is the volume of the column, V_{CaCO_3} (m^3) is the volume of the grains, and ρ_{CaCO_3} is the calcite volumetric mass ($\rho_{CaCO_3} = 2.7 \times 10^3$ kg m^{-3}). Then, the following points are obtained by computing (Vialle et al. 2014)

$$\phi(t_{i+1}) = \phi(t_i) + \frac{Q\, M_{CaCO_3}\, C_{Ca^{2+},t_{i+1}}}{\rho_{CaCO_3}\, V_{tot}}, \tag{32}$$

where $M_{CaCO_3} = 100.086 \times 10^{-3}$ kg mol^{-1} is the molar mass of calcite. Figure 6 shows that dissolution increased the initial porosity by 0.11 % and then precipitation decreased the porosity by 0.01 %. This implies that dissolution and precipitation occurred in the column, but they slightly affected the porous medium effective properties due to the size of the column. The final porosity ϕ_{end} was determined by weighing the grains and we obtained ϕ_{end} = 41.5 %. This value is higher than the final porosity computed from the calcium concentration measurements. We think that this final value could not be properly weighed, since several samples where collected to analyze their grain size distribution, which implied summing up multiple weighing operations.

4.3 Complex electrical conductivity measurement

SIP method measures the complex EC amplitude and phase shift frequency spectra (Equation (12)). During the entire experiment, SIP spectra were acquired on three channels corresponding to the dipoles P_1-P_2, P_2-P_3, and P_3-P_4. Figure 7 present the three channels phase shift spectra at four different time-steps. For the complex EC amplitude, we do not present this component as a frequency spectrum. We present the temporal variations for the values taken at the frequency {= 0.005 Hz. Figure 4a presents the complex EC amplitude during the entire experiment. The remarkable variations of the complex EC amplitude, close to events 3 (t = 13.85 d) and 4 (t = 61.84 d), are enlarged in Figure5c and d.

4.3.1 Monitoring of the complex electrical conductivity amplitude

Compared to inlet and outlet pore water EC curves we observe that the complex EC amplitude follows the same variations on every channels with values comprised between 50 and 200 $\mu S\ cm^{-1}$. The measurements presented on Figure 4 begin 20 days before the peristaltic pump turned on (event 1, defined as time-zero). Thus, the preceding time period is represented with negative X-axis values.

The zoomed views of Figure 5c and d allow to see the time offset between the channels. Their borders are represented on the main graph by the dashed outlines (Figure 4a).

During the initialization stage (stage I) we observe that the complex EC amplitude increases from 80 to 170 $\mu S\ cm^{-1}$ except when we turned on the pump (between events 1 and 2 on Figure 4a). This increase is due to the calcite dissolution as the initial water used to saturate the grains had to equilibrate with calcite. The drop of complex EC amplitude between day 0 and day 6 is caused by the re-introduction of this initial water which has a lower EC. Then, we connected the inlet to the outlet in order to reach an equilibrium.

When hydrochloric acid is injected (event 3), there is a sudden decrease of the complex EC amplitude because of the change of the inlet solution to a less conductive hydrochloric acid solution (see Figure 5c), reaching 60 $\mu S\ cm^{-1}$. This stagnation of the sample complex EC amplitude means that if dissolution occurred from day 14 to day 62, it was not important enough to significantly affect effective properties of the sample like porosity and permeability even after 48 days of hydrochloric acid injection.

Following event 4 (t = 61.84 d, Figure 5d), there is an abrupt increase of the complex EC amplitude and the curves reach a plateau around 170 $\mu S\ cm^{-1}$. Additionally, one can observe an increasing time delay before the change of the complex EC amplitude from pair P_1-P_2 to pair P_3-P_4 and a small decrease from the inlet to the outlet of the column ($\sigma_{P_1-P_2} > \sigma_{P_2-P_3} > \sigma_{P_3-P_4}$). These results could be due to calcite precipitation through the column.

Figure 5c, d, e, and f clearly show that the change of inlet pore water EC controls the complex EC amplitude variations. Thus, we computed the formation factor for the different dipoles (P_1-P_2, P_2-P_3, and P_3-P_4) considering the pore water EC as the mean between the inlet and the outlet water EC. The computed formation factor remains constant through time, but its value slightly increase along the column. Indeed, the formation factor mean values are $F_{P_1-P_2}$ = 4.51, $F_{P_2-P_3}$ = 4.61, and $F_{P_3-P_4}$ = 4.83. This spatial variation of the formation factor could be related to chemical processes occurring preferentially close to the column entrance, but since the pore water EC is such an approximation from the water EC measured at the inlet and outlet, this tendency may be distorted by the computation. Nevertheless, these formation factor values, related by Archie's law to the variations of porosity, calculated from the calcium concentrations measured on the outlet pore water, give a cementation exponent comprised between 1.70 and 1.77. These low values correspond well to a compacted, but non-consolidated granular medium (e.g., Friedman 2005).

Figure 5c and d also allow to show time delays and slight variations between the pairs of potential electrodes. So with a greater number of measurements, this electrodes disposition would enable to follow front of the complex EC amplitude variations along the column related to the new injected solution propagation.

4.3.2 Complex electrical conductivity phase spectra analysis

The phase spectrum shown in Figure 7 was obtained during the different stages of the experiment. They show a phase close to zero over the most frequencies and an inched up by 15 to 20 mrad at frequencies above 1 kHz. On this frequency range some noise is generated by the apparatus during acquisition and generates this phase signal amplification. At low frequencies (below 1 Hz), phases have non-zero values, but they are still very low. We, thus, consider them within the uncertainty range.

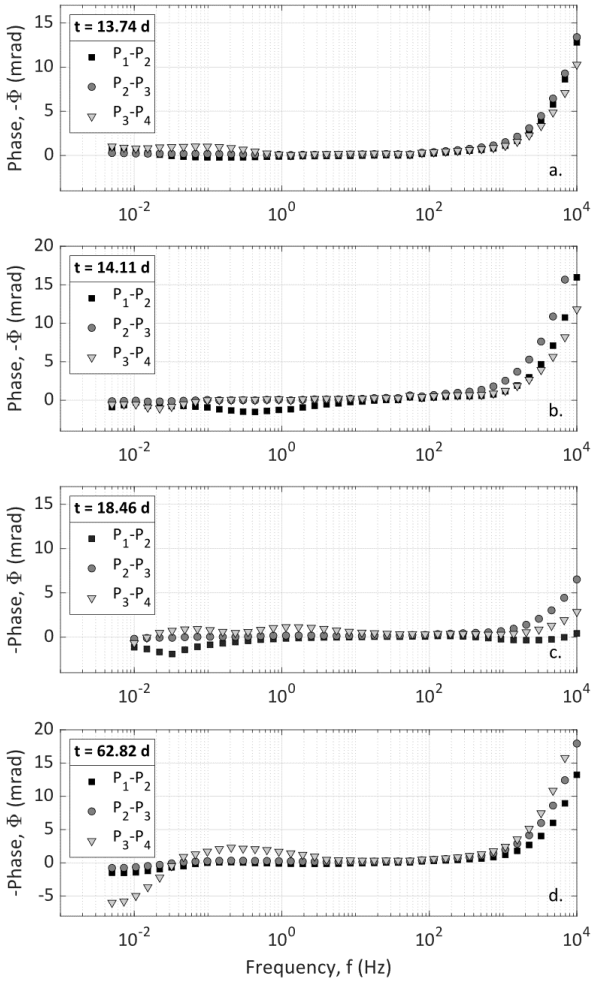

Figure 7: Four examples of phase spectra recorded during the experiment for the the measurement dipoles P_1-P_2, P_2-P_3, and P_3-P_4. The acquisition time of each subplot is reported as a white square on Figure 2. a, these spectra were acquired during stage I, at t = 13.74 d, just before hydrochloric acid injection (event 3). b, these spectra were acquired at the beginning of stage II, at t = 14.11 d, just after event 3, where complex EC amplitude is still not stabilized (Figure 5c). c, these spectra were acquired at t = 18.46 d, during stage II, after that complex EC amplitude reached a plateau. d, these spectra were acquired at the beginning of stage III, at t = 62.82 d, just after starting the injection of the calcite over-saturated solution (event 4), where complex EC amplitude is still not stabilized (Figure 5d).

The phase spectra of Figure 7a, were acquired at the end of the stabilization stage (stage I). In these conditions, the sample was in a steady state close to the equilibrium with calcite, thus inducing few interaction between the calcite matrix and the pore water. Furthermore, pH was close to 7.5, known to be close to the pH range of point of zero charge of calcite (Somasundaran et al. 1967). Therefore, the flat phase spectra of Figure 7a

can be explained due to calcite low surface charge in these conditions, resulting in a very small chargeability.

On the contrary, dissolution and precipitation processes affect the mineral reactive surface and thus, could generate phase electrical signal; i.e., see Wu et al. (2010) and Izumoto et al. (2020) for monitoring calcite precipitation on silica material. Note that no electrical signature for dissolution has been reported in the literature (Halisch et al. 2018). Stages II and III were meant to be able to dissolve or precipitate calcite, but the phase spectra recorded during both stages remained close to zero (Figure 7b, c, and d). From this experimental set-up, our monitoring do not show significant phase signal during dissolution of pure calcite nor during precipitation of calcite upon already formed calcite grains. This could be due to the calcite behavior itself or because of the location of the reactive zone, as it will be discuss in the next section.

4.4 SP monitoring

4.4.1 Experimental results

SP measurements are presented over the entire experiment on Figure 4c. SP signals are also shown focused on events 3 (t = 13.85 d) and 4 (t = 61.84 d) on Figure 5e and f, respectively. Note that the data interruptions are due to SIP acquisition conducted in alternation with SP monitoring. SP signal is filtered using a moving average by sliding a one-hour window. Otherwise, there is no additional processing.

Figure 4c shows that the SP signals measured on pairs P_1-P_4, P_2-P_4, and P_3-P_4 present similar amplitudes and variations through time. The curves have a roughly linear general trend from -2 to -4 mV. This slow decrease can be caused by the reference electrode potential variation through time (see Jougnot et al. 2013). Nevertheless, clear amplitude variations of ±3 mV can be shown at t = 13.85 d and t = 61.84 d. These timings correspond to the beginning of dissolution and precipitation stages at events 3 and 4, respectively (see on Figure 4c and the zoomed views of Figure 5e and f).

The streaming potential amplitude depends on the excess of charge displaced by the pore water advection. Thus, for measuring electrodes aligned in the direction of the water flow, the more distant the electrodes are from one another, the greater is the electrokinetic potential measured between them. Here, the distance to the reference electrode decreases from pair P_1-P_4 to pair P_3-P_4, but no clear amplitude decrease between the curves. In addition, the strong changes in the pore water EC does not seem to affect the trend nor the amplitude of the measured signals as it would be expected in the definition of the electrokinetic coupling coefficient (Equation (21)) given by Revil et al. (2004). Therefore, the SP results suggest that the electrokinetic coupling contribution seems negligible. To verify this, the pump has been shut down for 5 minutes on day 30 without any incidence on the observed SP values. Then, the flow rate has been increased until 498 mL h^{-1} during 1 min with no resulting changes. The fact that the electrokinetic contribution can be neglected in this system can be expected from the literature, since surface charge of calcite is known to be really low (e.g., Cherubini et al. 2019).

The remarkable SP variations, highlighted by the dashed outlines of Figure 4c and zoomed in on Figure 5e

and f, follow the change of inlet solution at events 3 (t = 13.85 d, beginning of stage II) and 4 (t = 61.84 d, beginning of stage III) to induce dissolution and precipitation in the column, respectively. One can observe positive SP variations after event 3 and negative SP variations after event 4. If we compare these results to the inlet water EC (Figure 5a and b), we observe that at event 3, the new inlet solution has a lower EC value than the one which was already in the column while the new inlet solution is more conductive at event 4. In view of this, it appears that ionic gradients of the different species along the column caused by the change of inlet solution could be the main contribution of the SP signal (i.e., electro-diffusive potential, see section 2.3.2).

The zoomed views of Figure 5e and f support this observation. Indeed, on each graph SP variation occur first for the pair P_1-P_4, then for the pair P_2-P_4, and finally for the pair P_3-P_4, but they all end at the same time. For the pair P_1-P_4, the duration is about 1 day. Knowing the flow rate and the column dimensions, the travel time of fluid can be computed: it takes 25 h to a drop of the inlet solution to cross the column. It appears that the SP value changes when the new inlet pore water reaches the position of electrodes P_1, P_2 and P_3 but SP signals return to their basic values when the inlet solution reaches the position of electrode P_4 (i.e., the reference electrode) because there is no more concentration gradients in the column. We also observe that the maximal amplitude of the SP variation is increasingly smaller from pair P_1-P_4 to pair P_3-P_4. This may be related to the decreasing distance between the electrodes P_1, P_2 and P_3 to the reference electrode P_4. So ionic fluxes due to ionic concentration gradients must be the main coupling phenomena with our SP signals.

However, events 3 (t = 13.85 d, beginning of stage II) and 4 (t = 61.84 d, beginning of stage III) correspond to the injection of solutions S1 and S2, that is generating dissolution and precipitation of the calcite material in the column, respectively. According to the fluid junction theory (section 2.3.2), if calcite dissolution and precipitation occur between the electrodes P_1 and P_4, it is expected to generate an ionic concentration gradient during the entire stages II and III. Thus, the SP signal would reach a plateau rather than presenting transient variation induced by the injection of a new inlet solution. Nevertheless, chemical analysis on the outlet pore water shows that inlet and outlet concentrations are different, thus chemical reactions must have occurred in the column. As SP variations are transitory, they are not related to calcite dissolution nor calcite precipitation, but only to concentration gradients caused by the change of inlet solution at events 3 and 4. Consequently, calcite dissolution and precipitation have occurred in the column, but not in the instrumented portion (i.e., between the electrode P_1 and P_4). Thus, we conclude that calcite dissolution and precipitation have occurred between the electrodes C_1 and P_1 and that the SP transient variations of events 3 and 4 result from the electro-diffusion potential generation caused by ionic concentration gradients following the change of injected solution.

As the SP measurements depend on concentration gradients, we developed a new theoretical framework (section 3.4). It combines reactive-transport simulation using CrunchFlow (section 3.3) with chemical analysis, rock sample EC measurement, and Equation (28).

4.4.2 CrunchFlow simulation results for the reactive-transport

We run two simulations with the CrunchFlow code using the input conditions described in Table 3 during 80 h and with a time-step of 1 h between each computation of the ionic concentration distributions along the column. We then compare the results to the chemical analysis of the outlet solution, the results are presented in Figure 8 for the pH, the calcium concentration, and the hydrogencarbonate concentration. This last parameter is assumed to present identical values with alkalinity measurements in this pH range. For each variable, a correlation coefficient C_{cor} (-) is determined to estimate the linear dependence between the measurements and the simulation results from CrunchFlow. Ranging from -1 to 1, these extreme values of C_{cor} represent direct negative and positive correlations, respectively, while C_{cor}=0 indicates that there is no correlation.

The simulation results from CrunchFlow present variations visually close to the experimental data except for pH values during dissolution. We think that the measured pH values are higher than expected because of some degassing at the column exit and during the sampling process since the column is long and behaves like a confined environment. Thus, we set the pH as a thermodynamic input parameter computed by CrunchFlow.

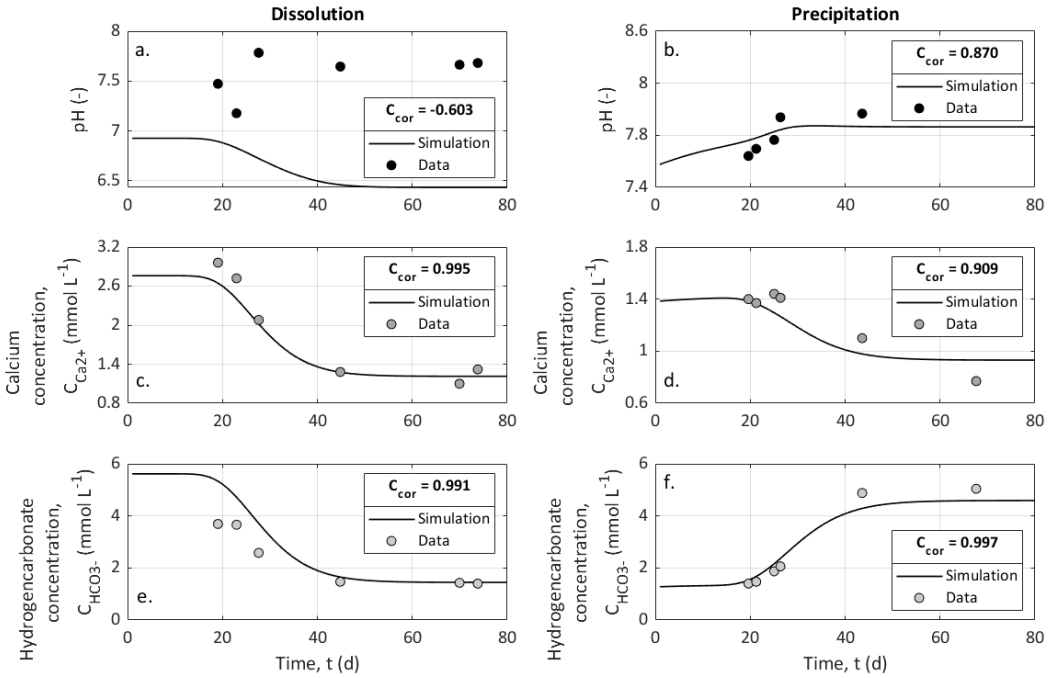

Figure 8: Measured and modeled pH, calcium concentration, and hydrogencarbonate concentration. The data points come from the chemical analyses conducted on the outlet pore water samples and the curves are obtained from CrunchFlow simulations. (a, c, e) data and simulations for dissolution with the event 3 of the time-line (Figure 2) defining time zero. (b, d, f) data and simulations for precipitation with the event 4 of the time-line (Figure 2) defining time zero.

4.4.3 Results from electro-diffusive potential modeling

Following the numerical framework showed in Figure 3, we propose to model the measured SP signals from the computation of the electrical potential based on Equation (28), as these data seem related to the diffusion

potential. Here, cations and anions concentration distributions are obtained from CrunchFlow simulations and the rock sample EC is obtained from the complex EC amplitude measured with the SIP method. We tested to compute the complex EC amplitude using the calculated formation factors (section 4.3.1) and the water EC definition based on the ionic molar conductivities (Equation (11)). The diffusion potential curves modeled from the EC computation give results close to SP measurements. Nevertheless, since we obtained results less consistent with the data than those obtained from the complex EC amplitude measurements, we prefer to present the diffusion potential curves obtained from the complex EC amplitude measurements.

Following the method presented in section 4.2, we computed the change of porosity during the experiment based on calcium concentration measurements. We obtained very low porosity variations, thus we set a fixed porosity value $\phi = 0.41$.

Table 4: Diffusion coefficient values obtained from the literature (Robinson et al. 1952; Gregory et al. 1991; Parkhurst et al. 2013) of ionic species present in solution according to CrunchFlow database. Reference values found in the literature are given at 25 °C.

Ions	Diffusion coefficient (10^{-9} m^2 s^{-1})
$CaHCO_3^-$	0.506
$NACO_3^-$	0.585
Ca^{2+}	0.793
CO_3^{2-}	0.955
$CaOH^+$	1.030
HCO_3^-	1.180
Na^+	1.330
$CaCl^+$	1.340
Cl^-	2.030
OH^-	5.270
H^+	9.310

CrunchFlow database has specified eleven ionic species from speciation computing. These species are listed in Table 4 and their diffusion coefficients are taken from the literature (Robinson et al. 1952; Gregory et al. 1991; Parkhurst et al. 2013).

SP data and modeled electro-diffusive potential are presented on Figure 9. On Figure 9a and b, the data are plot after removing the decrease assuming that it is a linear function and time zero corresponds to the start of injection of S1 and S2 to dissolve and to precipitate, respectively. The modeled electrical potential presented on Figure 9c and d, are shifted of 4 h. This delay corresponds to the amount of time required for the pore water to reach the electrode P_1.

For both dissolution and precipitation the modeled curves present variations that are fairly similar to the SP measurements, although not identical. Furthermore, we observe that modeled peaks are between two and three times larger than the measurements in the case of dissolution. We think that the model is better adjusted

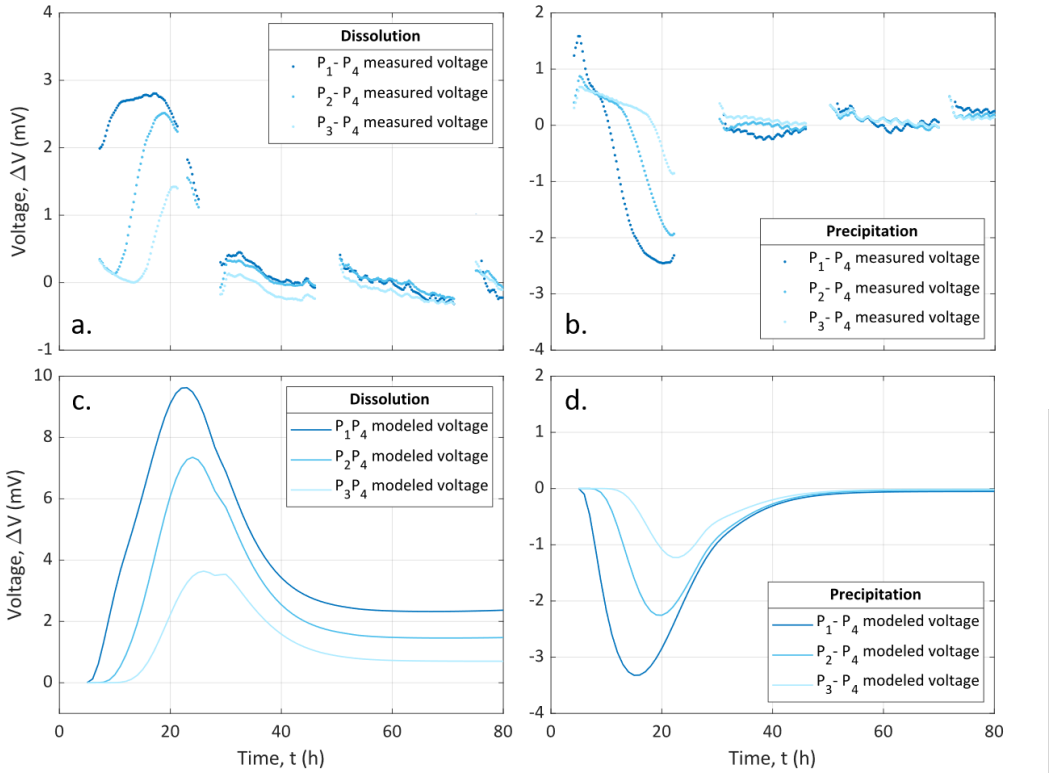

Figure 9: (a, b) SP data without the linear decrease generated by the drift of intrinsic potential electrode P_4. Time zero corresponds to the timing of events 3 (injection of solution S1) and 4 (injection of solution S2), respectively. (c, d) diffusion potential curves obtained from the developed framework using CrunchFlow simulations as inputs for the electro-diffusive potential computation. The curves are shifted with a time delay of 4 h, corresponding to the amount of time required for the pore water to reach the electrode P_1.

in case of precipitation than in case of dissolution because of CO_2 degassing that affected the system during dissolution. Moreover, hydrogen protons (H^+) have a much higher diffusion coefficient than the other ions (see Table 4), which influences a lot the electro-diffusive amplitude.

Our 1D approach contains some simplifications which also explains the differences between the measured and the modeled curves. Indeed, electrical methods are integrative but the model does not consider the column width while it is non negligible since it worth 40 % of the column length, therefore inducing potential 3D effects around the injection. Furthermore, the porous medium is considered as an effective medium, where the formation of preferential path is neglected. Nevertheless, this framework could be used for other purpose addressing multispecies reactive transport and mixing (e.g., Oliveira et al. 2020).

4.5 Location of the reactive area

CrunchFlow simulation, in addition to the ionic concentrations, resolves the porosity evolution. As each simulation lasts 80 h, Figure 10 shows the difference of porosity along the column at t_{simul} = 80 h: $\Delta\phi(x) = \phi_{80}(x) - \phi_{init}$. One can observe that the porosity changes are small with a maximal increase of 0.1 % for dissolution and a maximal decrease of -0.005 % for precipitation. Besides, only the first 2 cm at the column entrance are affected by these changes of porosity (see the gray rectangle on Figure 10). We are pretty confident in these

results since the measured Ca^{2+} concentrations are well reproduced by simulations and the porosity changes are consistent with the low porosity evolution (see Section 4.2). Thus, most of dissolution and precipitation occurred in this portion of the column and did not reach the portion equipped with the measurement electrodes. Consequently, the transient variations of SP signal and the absence of phase signal come from the fact that all dissolution and precipitation occurred at the entrance of the column and did not induce a sufficient chemical imbalance as suggested by Izumoto et al. (2020).

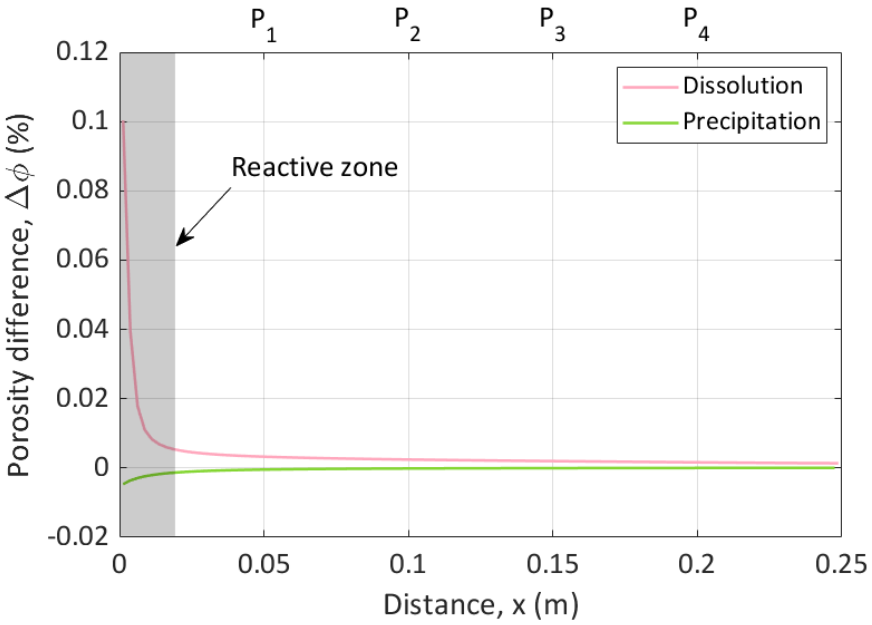

Figure 10: Porosity difference along the column for dissolution and precipitation simulations from CrunchFlow after 80 h. Positions of measurement electrodes P_1, P_2, P_3, and P_4 are indicated at the top of the graph. The reactive area is represented by the gray rectangle.

5 Conclusion

In this study we induced alternatively calcite dissolution or precipitation in a synthetic sample. This sample was made of calcite grains contained in a column. This experimental set-up is equipped to monitor the geo-electric properties with two methods: SP and SIP, together with inlet and outlet pore water EC monitoring and chemical analysis on outlet pore water samples (alkalinity, pH and major ions concentrations). The experiment has been reproduced numerically using reactive-transport CrunchFlow.

SP, pore water EC, chemical analyses, and complex EC amplitude (from SIP measurement) show clear correlated transient variations in response to new inlet solution injections in the column. These results suggest that chemical reactions with calcite grains occurred at the entrance of the column and before reaching the portion of the column equipped with the measurement electrodes. This experimental evidence is confirmed by numerical simulation of reactive-transport and explains the flat SIP phase spectra. Consequently, this experimental set-up enables the joint use of multiple geo-electrical methods, which, once compared with chemical

analyses, can be quantitatively interpreted. However, the chemical reactions with calcite grains occurred to close to the entrance to be fully-monitored. Thus, we consider this column obviously perfectible and further study, with a revised experimental set-up, are required.

The source of SP signal is attributed to ionic concentration gradients through the column. To interpret the SP results according to the fluid junction potential theory, a new multi-ionic numerical framework to reproduce the measured SP data has been developed for this study and has proven its efficiency. Therefore, we believe that studies addressing multi-species reactive transport and mixing could use this framework with SP monitoring to improve the characterization of these processes.

This work clearly shows the interest of geo-electrical methods to non-intrusively monitor these geochemical processes. Thanks to a fully coupled approach, this study allowed us to locate the reactive zone and better understand the impact of the reactivity on the porous medium petrophysical properties. Future works will help improving this approach to provide a more quantitative tool to study reactive transport in carbonate media.

6.3 Conclusion to the paper

Self-potential is a method mostly known to monitor fluid flow, through the electrokinetic coupling, but this study shows that the electro-diffusive coupling generated by ionic concentration gradients can be an important source of electric current. Furthermore, using one-dimension reactive transport modeling as an input for such model reproduces fairly well the experimental data despite the simplicity of the approach. Nevertheless, the monitored transient variations are generated by ionic concentration gradients rather than calcite dissolution and precipitation.

In this experiment, no phase shift is measured with the SIP method. Using the results from the reactive transport location, we show that the reactive area is located between the current electrode and the first potential electrode. This could explain that no SIP phase spectra variations were recorded.

CHAPTER

7 Study of the electro-diffusive coupling generated by calcite dissolution under variable conditions

7.1 Introduction of the chapter

First interesting experimental results and numerical modeling have been performed thanks to Experiment ①. During this experiment, I observed that calcite dissolution and calcite precipitation generate similar SP response related to ionic gradients. Thus I decided to study further the SP response for different inlet conditions inducing calcite dissolution since strong and weak acids influence differently the system.

This chapter intends to present and discuss the results of Experiments ②, ③, and ④. Experiment ② consists in the injection of the solution S3, a solution of hydrochloric acid at pH = 4.5. Experiments ③ and ④ consist in the injection of solutions S4 and S5, respectively. Both of solutions S4 and S5 are pH = 4.5 buffered solutions of acetic acid and sodium acetate. Solution S4 has a concentration of acetic acid of 1.74 mol L^{-1} and solution S5 has a concentration of acetic acid of 2.5×10^{-3}mol L^{-1}. Solutions S4 and S5 are thus referred as the concentrated buffer and the diluted buffer, respectively. Experiments ②, ③, and ④ are all conducted using Bench ❷ and Column 2. They were also all performed under the same imposed flow rate Q = 58.8 mL h^{-1}.

This chapter is divided into two sections. In the first section, the results of Experiment ② are presented, analyzed, and discussed regarding the findings of Experiment ①. The second section addresses jointly the results of Experiments ③ and ④ and then discusses them in light of both Experiments ① and ②. The comparison of these four experiments allows to discriminate the location and the extent of the reactive zone in the column depending on the acid solution injection location and inlet chemistry.

7.2 Influence of the reactive zone location

This section is based on the description of the results of Experiment ②, which was a calcite dissolution experiment by injecting solution S3, a solution of hydrochloric acid at pH = 4.5 (see Section 5.2), and their comparison with the results of Experiment ① during the dissolution part (stage II, corresponding to $t \in$ [13.85 ; 61.84] d), described and discussed in Chapter 6. Experiment ② was conducted on Bench ❷ (presented in Section 5.1) and using Column 2 (described in Section 4.5), for which the injection is shifted at the same location than electrode

P_1 (at x = 8 cm). The experiment lasted 25 h.

7.2.1 Results comparative presentation

As this section intends to describe the data obtained for Experiment ② from the different methods and to compare the results, it seems appropriate to represent them in a single figure. Figure 7.1 therefore shows all the results of Experiment ②. On all the graphs in Figure 7.1, time-zero corresponds to the beginning of S3 injection.

7.2.1.1 Pore water electrical conductivity

Pore water EC was monitored with two in-line conductivity meters at the inlet (σ_{in}) and at the outlet (σ_{out}) of the column (Figure 7.1a).

At the beginning of the experiment, pore water EC is constant at the inlet and at the outlet with similar values (at t = 0.25 h, σ_{in} = 103 µS cm^{-1} and σ_{out} = 120 µS cm^{-1}). The slight difference between the inlet and the outlet EC must be caused by a small increase of calcium and hydrogencarbonate concentrations due to low dissolution when the initial fluid flows through the column, despite the imposed high flow rate of 58.8 mL h^{-1}.

At t = 0.6 h, σ_{in} drops and stabilizes at 12.5 µS cm^{-1} due to the low conductivity of solution S3. σ_{out} decreases several hours later at t = 2.8 h. At the flow rate of 58.8 mL h^{-1}, given the dimensions of the column (see Chapter 4), and for an initial porosity of 43.61 % (see Section 5.2), it requires 2.1 h to cross the column. By adding the time needed to reach the column and then the conductivity meter at the outlet, consistent timings can be retrieved. However, the decrease of σ_{out} is less abrupt than for σ_{in} and it reaches a higher plateau around 41 µS cm^{-1}. This difference in value between the inlet and the outlet is a sign that calcite has dissolved in the column.

For Experiment ①, the outlet pore water EC was lower than the inlet pore water EC despite the dissolution of calcite (see Chapter 6). This result, which at first glance, seemed inconsistent, could be explained by the computation of the pore water EC from the ion concentrations and the ion mobilities (see Section 2.2.5.1). It appeared that the consumption of H^+ ions due to calcite dissolution decreased the pore water EC because H^+ ion has a higher mobility than calcium or hydrogencarbonate ions. Thus, the important concentration of H^+ ions in the inlet solution S1 (hydrochloric acid at pH = 3) boosted its EC value compared to the outlet pore water EC. Nevertheless, contrary to the results of Experiment ①, here for Experiment ②, the outlet conductivity is higher than the inlet. This can be explained by the fact that S3 (pH = 4.5) is less concentrated than S1 (pH = 3) and therefore the mobility of H^+ does not contribute as much to the conductivity.

In addition, water EC is measured on the samples of pore water collected at the outlet (Figure 7.1a). Unsurprisingly, these measurements present synchronous variations and values very close to those obtained with the time tracking of σ_{out}.

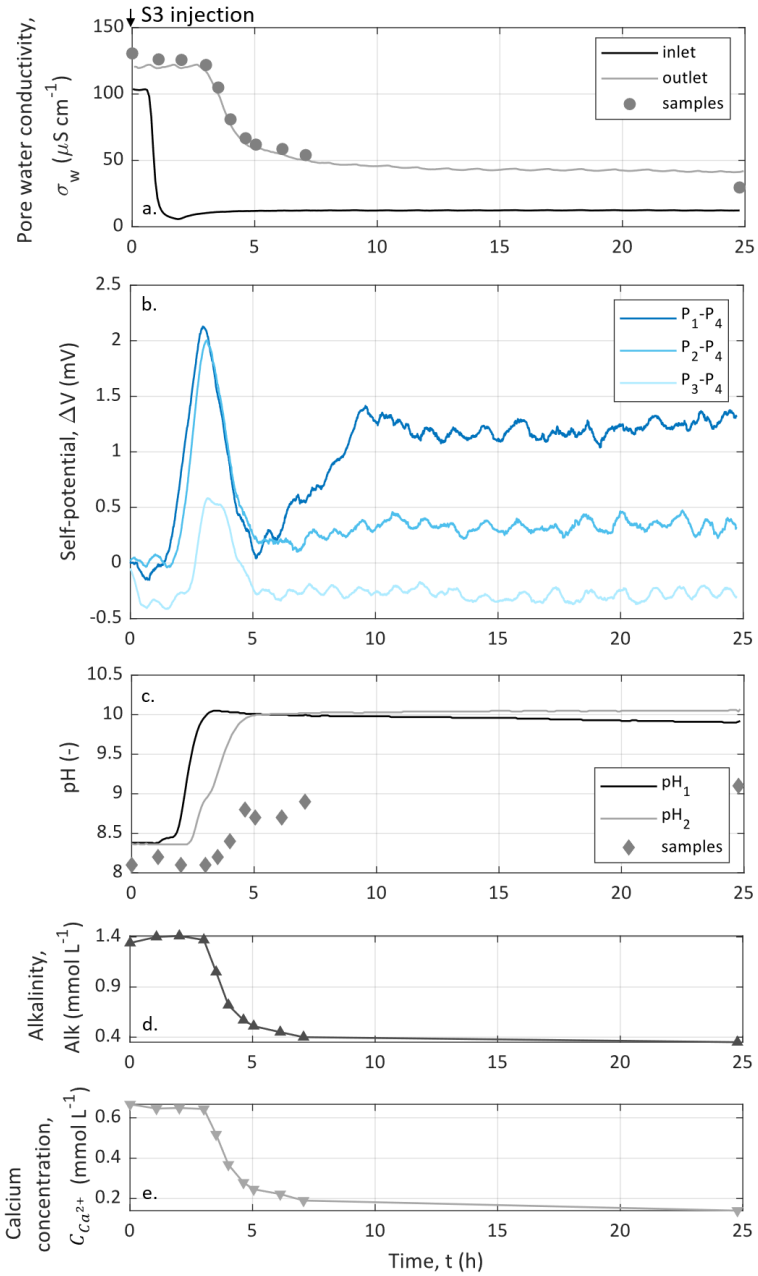

Figure 7.1: Results of Experiment ②. The injection of S3 defines time-zero. (a) the inlet and outlet pore water EC measured with the in-line conductivity meters and the pore water EC of the outlet pore water samples. (b) SP signal recorded on three channels with electrode P_4 ($x = 23$ cm) as the reference electrode. (c) curves of the pH monitored in the column at $x_{pH_1} = 13$ cm and $x_{pH_2} = 27$ cm and pH measured on the samples of outlet pore water. (d) alkalinity measured on the samples of the outlet pore water. (e) calcium concentration measured on the samples of the outlet pore water.

7.2.1.2 pH monitoring

pH was recorded at two different locations in the column (Figure 7.1c). pH_1 is located at x_{pH_1} = 13 cm and pH_2 is located at x_{pH_2} = 27 cm. As for the pore water EC monitoring, one can observe a first plateau with identical values for pH_1 and pH_2 (pH = 8.4), then abrupt variations on pH_1 followed by pH_2, approximately 2 h later, and finally both pH_1 and pH_2 reach steadier values around pH = 10.

As observed for the curves of σ_{in} and σ_{out}, the slope of pH_2, during its increase, is less abrupt than for pH_1. This must be caused by the contribution of diffusion to the transport of ionic concentrations in the pore space when the pore water flows (see Section 1.4.3). However, the Péclet number is Pe = 997 (see Section 5.2.3.1), thus, $Pe \gg 1$ and advection is dominant.

Unlike the curves of σ_{in} and σ_{out}, initial values of pH_1 and pH_2 have identical values (at t = 0 h, $pH_1 = pH_2 = 8.4$). Thus, before S3 reaches the column ($t < 1$ h), the sample seems to be close to the stationary state with really low chemical reaction.

By contrast, after pH_2 has risen to the same value than pH_1 (for $t > 5$ h), pH_2 remains stable at pH_2 = 10, but pH_1 constantly decreases until the experiment is stopped (at t = 25 h, pH_1 = 9.9). This decrease of pH_1 must be correlated to the dissolution of calcite and be located in the reactive zone of the column. Indeed, one observe changes on pH_1, while the injected pore water remains identical and showing constant σ_{in}. However, pH_2 should be located after the reactive zone because its value remains constant, as for σ_{out}.

pH is also measured on the samples of outlet pore water (Figure 7.1c). As expected, these data present synchronous variations with pH_2 curve. However, the amplitude is quite different especially for $t > 5$ h, where pH_2 = 10 while the pH measured on the samples only reaches pH = 9. This must come from CO_2 degassing (Equation (1.12) in Section 1.2.1), which is known to affect pH (e.g., Choi et al. 1998).

7.2.1.3 Outlet pore water chemical analyses

Outlet pore water alkalinity and calcium concentration are presented on Figures 7.1d and e, respectively. These curves and the outlet pore water EC curve (Figure 7.1a) present similar and synchronous variations. The initial plateau of 1.4 mmol L^{-1}, for alkalinity, and of 0.65 mmol L^{-1}, for calcium concentration, are caused by the injection of a solution rich in dissolved calcite (see Section 5.2.3.3). Then, both alkalinity and calcium concentration decrease simultaneously with the outlet pore water EC due to the injection of S3, which contains no calcium or hydrogencarbonate ions. However, alkalinity and calcium concentration do not fall to zero, but reach stable values of 0.4 mmol L^{-1} for alkalinity and around 0.2 mmol L^{-1} for calcium concentration. These amounts of dissolved calcium and hydrogencarbonate ions reveal that calcite dissolution occurred in the column even if the porosity varied of only 0.04 % (from Table 5.1 of Section 5.2).

7.2.1.4 SP measurements

SP signal was measured on three spacings using P_1, P_2, and P_3 for the measurements and P_4 as the reference electrode (see Section 5.3.3.3). The curves are presented on Figure 7.1b. They present similar patterns with a

positive bell-shaped variation for $t < 5$ h, then they reach distinct plateaus around 1.3 mV for P_1-P_4, 0.4 mV for P_2-P_4, and −0.3 mV for P_3-P_4.

The bell-shaped variation occurring at the beginning of the experiment starts first for the pair P_1-P_4, then for the pair P_2-P_4, and finally for the pair P_3-P_4, but they all decrease simultaneously. In comparison with the variations of pH monitored inside the column, the increase of SP signal on channel P_1-P_4 is synchronous with the increase of pH_1 and the SP bell-shaped variation ends when pH_2 stabilizes at 10 (for $t \approx 5$ h). Thus the SP bell-shaped variations are related to ionic concentration gradients caused by the injection of solution S3.

For $t > 5$ h, SP curve of pair P_3-P_4 returns to its base value and remains stable. Thus, this pair of electrodes is affected by a transient source of SP current which is certainly the ionic concentrations gradient caused by the injection of S3. In contrast, pairs P_1-P_4 and P_2-P_4 increase for $t \in [5\ ;\ 10]$ h before reaching stable values higher than initially. These higher values of SP measurements for pairs P_1-P_4 and P_2-P_4 for $t > 10$ h, must be correlated to the behavior of pH_1 at the same time. Indeed, pH_1 showed a decrease related to calcite dissolution and leading to the conclusion that it was located in the reactive zone. Since pH_1 is located at the same distance than electrode P_2, this electrode must also be located in the reactive zone. P_1 is located at the injection point. P_1 is thus at the beginning of the reactive area. Therefore, the reactive area must be located from P_1 and between P_2 and P_3.

However, P_2-P_4 reaches an intermediate value which is not as high than for the pair P_1-P_4 and pH_1 presents much higher values than the pH of the inlet solution S3 (pH = 4.5) due to the dissolution of calcite which increases alkalinity and the the pH. Consequently, one can conclude that most of solution S3 was consumed before reaching electrodes pH_1 and P_2, which are thus located at the end of the reactive area.

For this experiment, the flow rate was constant and no test to observe the impact of its variation on SP values was carried to determine if there was any electrokinetic contribution to SP signal. Nevertheless, at the beginning of the experiment, SP curves present very similar values for each pair of electrodes despite their different spacing with the reference electrode P_4. Furthermore, no electrokinetic contribution was observed for Experiment ① (see Chapter 6). Thus, it appears that the only contribution to SP values comes from the electro-diffusive coupling generated first by the injection of solution S3 mostly and then by calcite dissolution, explaining the different plateaus of pairs P_1-P_4 and P_2-P_4.

7.2.2 Discussion in light of the Experiment ①

Experiment ① has shown that injection of solution S1 generates diffusion potential transient anomalies due to the formation of ionic gradients between the electrodes measuring the potential (see Chapter 6). Here, SP measurements of Experiment ② present the same positive bell-shaped transient variations for $t \in [0\ ;\ 5]$ h. Thus, despite the dilution of the injected solution between S1 and S3 (see Section 5.2), the injection of S3 generates diffusion potential. One can however notice that the amplitude of the bell is more important for Experiment ①, than for Experiment ② with a maximal deviation of pair P_1-P_4 of 3 mV for Experiment ① and of 2 mV for Experiment ②. This difference must be related to the higher pH value of S3 compared to S1, which has an important effect on the pore water EC contrast between the inlet and the outlet.

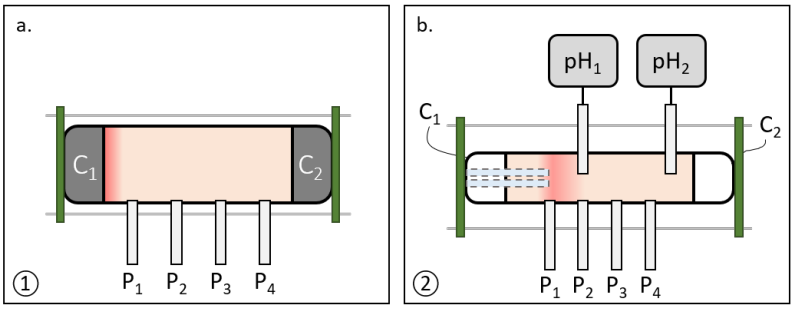

Figure 7.2: Location of the reactive zone of calcite dissolution highlighted in red for (a) Experiment ① and (b) Experiment ②.

In Chapter 6, using reactive transport modeling, I determined for Experiment ① that the reactive zone was located at the entrance of the column over 2 cm and thus did not reach electrode P_1 as illustrated on Figure 7.2a. For Experiment ②, the analysis of pH and SP curves reveals that the reactive zone begins at electrode P_1 due to the shift of the injection tubes and it reaches electrodes P_2 and pH_1, but the dissolution of calcite at the location of P_2 and pH_1 seems low due to the lower plateau of SP signal for the pair P_2-P_4 compared to the pair P_1-P_4 and because the decrease of pH_1 for $t > 5$ h is slight. Thus, as for Experiment ①, the dissolution of calcite for Experiment ② occurs in the first centimeters following the injection, with an estimated extent of 5 cm. The extent of the reactive zone for Experiment ② is therefore higher than for Experiment ①. This must be caused by the higher flow rate of Experiment ② and by the reduction of the column diameter between Column 1 and Column 2, even if this last parameter was not taken into account in the reactive transport modeling of Experiment ① presented in Chapter 6. The location of the reactive zone of Experiment ② is illustrated on Figure 7.2b.

7.3 Impact of the injected acid solution

This section is based on the description of the results of Experiments ③ and ④, and their comparison with the results of Experiment ① during the dissolution part (corresponding to stage II, for $t \in [13.85 ; 61.84]$ d), described and discussed in Chapter 6, and Experiment ②, described and discussed in Section 7.2, to compare the effect of using buffered weak acid instead of strong acid at the inlet.

Experiments ③ and ④ are experiments of calcite dissolution by injecting buffered solutions of acetic acid and sodium acetate in different concentrations, but both at pH = 4.5. The injected solutions named S4 for Experiment ③ and S5 for Experiment ④ have a concentration of acetic acid of 1.74 mol L^{-1} and 2.5×10^{-3} mol L^{-1}, respectively (see Section 5.2). Experiments ③ and ④ were conducted on Bench ❷ (presented in Section 5.1) and using Column 2 (described in Section 4.5), for which the injection is shifted at the same location than electrode P_1 (at $x = 8$ cm). These experiments lasted 9 h each, with the same constant flow rate $Q = 58.8$ mL h^{-1}.

Both Experiments ③ and ④ were conducted using the same Bench and the same techniques of acquisition than for Experiment ②. Thus, the description of the results will be lightened from the explanations of their acquisition. One can refer to the previous section and to Chapter 5 for more details.

7.3.1 Comparative presentation of the results of Experiments ③ and ④

As this section intends to describe the data recorded for Experiments ③ and ④ and to compare the results obtained from the different methods, it seems appropriate to represent all the results in a single figure. Figure 7.3 therefore shows all the results of Experiment ③ on the left with time-zero corresponding to the beginning of solution S4 injection and Experiment ④ on the right with time-zero corresponding to the beginning of solution S5 injection.

7.3.1.1 Pore water electrical conductivity

Inlet and outlet pore water EC monitoring during Experiments ③ and ④ is presented on Figures 7.3a and b, respectively.

At the beginning of both experiments, pore water EC is constant at the inlet and at the outlet with similar values. Even if it cannot be easily seen due to the vertical scale of Figures 7.3a and b, at t = 0.25 h, for both experiments, σ_{in} is comprised between 105 µS cm^{-1} and 110 µS cm^{-1} and σ_{out} is comprised between 117 µS cm^{-1} and 124 µS cm^{-1}. The slight difference between the inlet and the outlet EC must be caused by a small increase of calcium and hydrogencarbonate concentrations due to low dissolution when the initial fluid flows through the column, despite the imposed high flow rate of 58.8 mL h^{-1}. It is though interesting to be able to repeat the same initial conditions between the experiments.

For Experiment ③ (Figure 7.3a), σ_{in} starts to increase at t = 0.4 h and reaches 31.6 mS cm^{-1}, which is a really high EC plateau due to the high conductivity of solution S4 (σ_{S4} = 34.4 mS cm^{-1}). σ_{out} starts to increase 1 h later. This timing is shorter than expected for the advective regime computed from the flow rate and the size of the column. This must be related to the composition of the injected solution. However, for $t > 3$ h, σ_{out} loses stability and presents unusual oscillations. During the experiment, I noticed the formation of gas bubbles in the column and that the outlet pore water was mixed with gas. This gas must be the cause of the instability of σ_{out}. Since CO_2 is linked to carbonic acid H_2CO_3 and its dissociated ions hydrogencarbonate HCO_3^- and carbonate CO_3^{2-} (see Section 1.2.1). The gas bubbles are certainly CO_2 bubbles that form due to the dissolution of calcite.

For Experiment ④ (Figure 7.3b), σ_{in} increases sharply from t = 0.6 h and reaches a maximum value of 397 µS cm^{-1} at t = 1.5 h. Then, σ_{in} decreases slowly and reaches a plateau where σ_{in} = 134 µS cm^{-1}. This low value is consistent with the measured EC of the injected solution S5 which is σ_{S5} = 128 µS cm^{-1}). Thus, the variation of σ_{in} for $t \in [0.6\,;\,4]$ h, is most likely linked to some calcite dissolution occurring in the tubes before reaching the column. σ_{out} starts to increase at t = 2.8 h, which is consistent with the time required for the pore water to flow through the column and reach the outlet conductivity meter. Then, σ_{out} reaches an asymptotic behavior close to σ_{out} = 490 µS cm^{-1} for $t > 7$ h.

In addition, pore water EC is measured on the samples of pore water collected at the outlet (Figures 7.3a and b).

For Experiment ③ (Figure 7.3a), the values of pore water EC from the samples are higher than the values recorded on σ_{out} and reach a plateau around 42 mS cm^{-1}. This lower amplitude of σ_{out} must be due to the

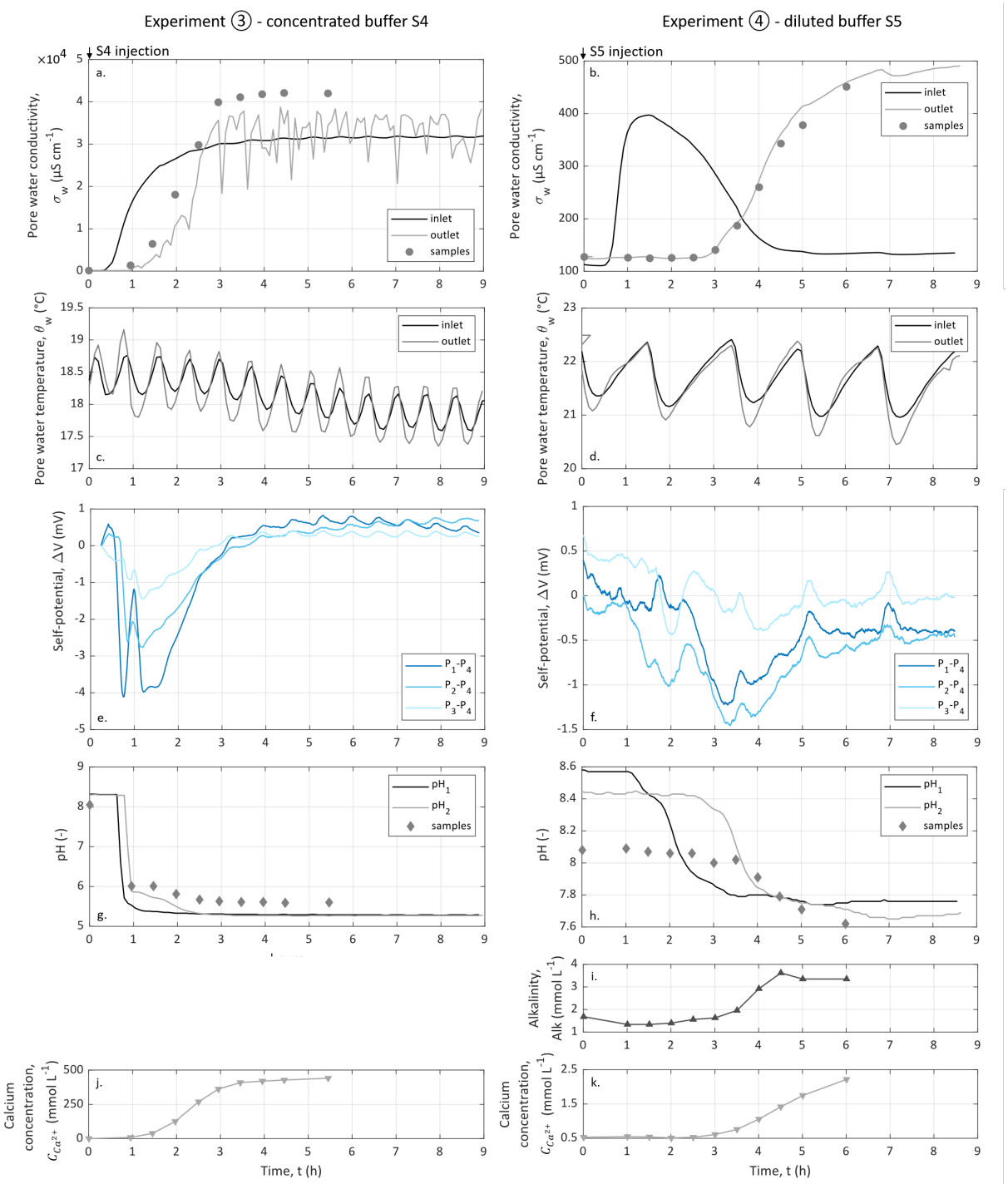

Figure 7.3: Results of experiments ③ (concentrated buffer S4) and ④ (diluted buffer S5). Injections of S4 and S5 define time-zero of each experiment. (a,b) the inlet and outlet pore water conductivity measured with the in-line conductivity meters and the pore water EC of the outlet pore water samples. (c,d) Pore water temperature monitored with the in-line conductivity meters. (e,f) SP signal recorded on three channels with electrode P_4 (x = 23 cm) as the reference electrode. (g,h) curves of the pH monitored in the column at x_{pH_1} = 13 cm and x_{pH_2} = 27 cm and pH measured on the samples of outlet pore water. (i) alkalinity measured on the sampled outlet pore water. (j,k) calcium concentration measured on the sampled outlet pore water.

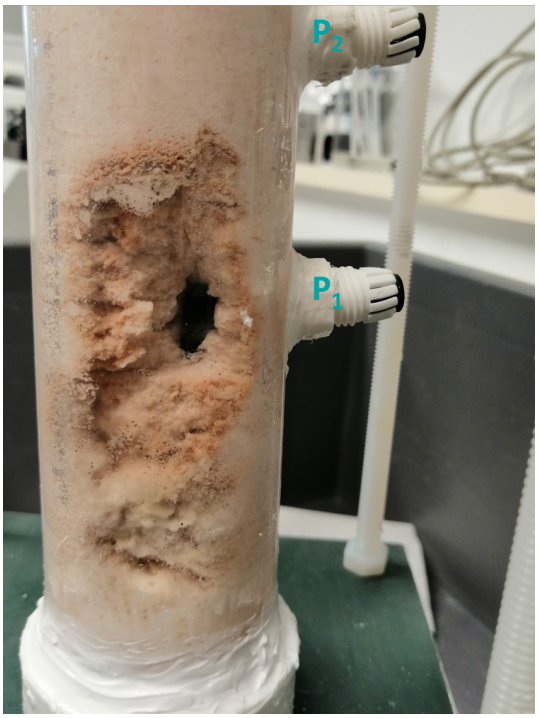

Figure 7.4: Photography of the column at the end of Experiment ③ showing that a big amount of calcite has been dissolved on the underside of the column when it is positioned horizontally.

bubbles in the tubes that have distorted the measurements. The plateau reached by the samples of outlet pore water is higher than the injected solution EC. Such a difference of conductivity between the inlet and the outlet must be linked to intense calcite dissolution rather than ionic mobility difference as discussed below. Indeed, after the experiment, I put the column vertically to disassemble the setup and I observed that a lot of calcite were dissolved on the underside of the column when put horizontally (see Figure 7.4). One can note on Figure 7.4 that the most dissolved portion is located beneath the injection. Given the concentration of the injected solution S4, I computed the density of the solution and obtained d_{S4} = 1.033. This implies that solution S4 is more dense than the initial pore water that has a the same density value than water (d = 1) since it is poorly concentrated. Saline intrusions in coastal aquifers are known to form salt wedge under the freshwater due to the contrast of density Δd >0.02 (e.g., Rattray and Mitsuda 1974). Here, solution S4 presents a density contrast Δd = 0.033. Thus, the location of the most reactive area can be explained by the fact that the injected solution S4 was more dense than the initial pore water. This led the injected acid solution to flow preferentially in the lower half of the column before replacing the initial pore water.

For Experiment ④ (Figure 7.3b), EC of the samples of outlet pore water unsurprisingly presents synchronous variations and values very close to σ_{out}.

We have seen for Experiments ① and ② that the concentration of H^+ ions has an important impact on the pore water EC contrast between the inlet and the outlet during dissolution and that even if there was not a lot of ions in solution in S1 and S3 compared to the outlet pore water due to the dissolution of calcite, the presence of H^+ ions influenced a lot the inlet pore water EC amplitude (see Chapter 6 and Section 7.2 for more details).

When using the buffered solutions, the EC of solutions S4 and S5 is more related to the concentration of the other ions than to the concentration of H^+, which is the same as for solution S3, since S3, S4, and S5 have the same pH value. However, since the other ions present in solutions S4 and S5 have similar ionic mobilities (see Table 2.1 in Section 2.2.5.1), the dissolution of calcite increases the amount of dissolved ions in solution and thus increases the pore water EC. Therefore, this explains that the outlet pore water EC is always higher than the inlet pore water EC when using the buffered solutions regardless of their concentrations.

7.3.1.2 pH monitoring

Figures 7.3g and h present pH monitoring in the column and as for the pore water EC monitoring, one can observe a first plateau with close values for pH_1 and pH_2. For Experiment ③, pH_1 and pH_2 are almost identical with values close to 8.3 and for Experiment ④, for $t < 1$ h, $pH_1 = 8.57$ and $pH_2 = 8.45$. Then, for both experiments pH_1 decreases and reaches a plateau, then pH_2 decreases similarly and reaches a plateau close to pH_1 values. However, the decrease of pH_1 and pH_2 for Experiment ③ occurs in less than 2 h, while for Experiment ④, pH_1 and pH_2 reach their asymptotic behaviors for $t > 4$ h and $t > 7$ h, respectively. Both experiments are conducted at the same flow rate, thus, this time discrepancy of pH variations between the experiments must be caused by the difference of acetic acid concentration between solutions S4 and S5. Moreover, if both experiments begin with similar pH values, the variations generated by the inlet solution injection are more important for Experiment ③ than for Experiment ④. Indeed, at $t = 5$ h, pH_1 and pH_2 reach 5.26 for Experiment ③, while pH_1 and pH_2 reach 7.75 for Experiment ④. This difference of amplitude shows that dissolution in Experiment ③ is stronger than in Experiment ④, which is consistent with the fact that solution S4 concentration is higher than solution S5 concentration. These results are also consistent with the measurements of the porosity difference (see Table 5.1 in Section 5.2), showing that more calcite has been dissolved in Experiment ③ compared to Experiment ④.

pH was also measured on the samples of outlet pore water (Figures 7.3g and h). Despite some differences in amplitude, especially for $t < 3.5$ h for Experiment ④ (Figure 7.3h), the pH measured on the samples of outlet pore water presents variations very similar to pH_2 curves for both experiments. As for Experiment ②, the misfit between pH_2 and the pH values of the samples of outlet pore water may be caused by CO_2 degassing.

For Experiment ③, since we know that the column is not saturated with water due to bubbles formation from calcite dissolution, the values of pH_1 and pH_2 could be distorted. Nevertheless, unlike σ_{out} curve, the curves of pH_1 and pH_2 do not present strong oscillations and the pH measurements of the samples of outlet pore water present close values. Thus the values of pH_1 and pH_2 seem accurate despite the presence of bubbles in the column during this experiment. Furthermore, the density of S4 is higher than the density of the initial pore water, leading to preferentially flow path in the lower half of the column. The pH electrodes in the column measure at the center of the column. Since pH_1 and pH_2 are sensitive to the variations induced by the injection of S4, it implies that S4 must flow in more than the lower half of the column section.

7.3.1.3 Outlet pore water chemical analyses

Outlet pore water calcium concentration of Experiments ③ and ④ is presented on Figures 7.3j and k, respectively. Both curves increase in time due to calcite dissolution which adds calcium ions in solution. At t = 0 h, calcium concentration is very similar for both experiments and is comprised between 0.5 and 0.7 mmol L^{-1}. However, calcium concentration reaches much stronger values for Experiment ③ than for Experiment ④. Indeed, at t = 5.5 h, $C_{Ca^{2+}}$ = 441 mmol L^{-1} for Experiment ③, while at t = 6 h, calcium concentration only reaches $C_{Ca^{2+}}$ = 2.2 mmol L^{-1} for Experiment ④. Moreover, one can seen that calcium concentration begins to increase at t = 1.5 h for Experiment ③. This increase of calcium concentration begins earlier than for Experiment ④, indeed calcium concentration only starts to increase at t = 3 h.

Outlet pore water alkalinity of Experiment ④ is presented on Figure 7.3i. As for calcium concentration, alkalinity increases due to calcite dissolution which adds hydrogen carbonate ions in solution. Alkalinity is not presented for Experiment ③ because I faced a problem with the titration of the samples.

7.3.1.4 SP measurements

SP curves of Experiments ③ and ④ are presented on Figures 7.3e and f and each of these experiments presents characteristic bell-shaped SP response. It can be seen that for both experiments, the variations in SP are negative. This is consistent with the SP results of Experiment ①, which enabled to establish that an increase of the inlet solution EC will induce negative SP variations.

For Experiment ③ (Figure 7.3e), SP curves present negative transient variation for $t \in [0\ ;\ 3]$ h, then all the curves return to their base value close to 0 mV. For $t > 3$ h, one can observe periodic oscillations of ± 0.2 mV every hour, these oscillations are generated by the variations of pore water temperature (Figure 7.3c) which are related to the air conditioning regulation as explained in Section 5.3.1. The transient negative variations occurring at the beginning of the experiment ($t < 3$ h) start first for the pair P_1-P_4, then for the pair P_2-P_4, and finally for the pair P_3-P_4, then SP curves all increase simultaneously and reach electrical potential close to 0 mV. This increase of SP negative values occurring for $t \in [1\ ;\ 3]$ h is synchronous with the increase of both outlet pore water EC and outlet pore water calcium concentration (see Figures 7.3a, d and j). Moreover, the amplitude deviation of the negative SP transient variations is more important for the pair P_1-P_4 reaching a minimal value $\Delta V_{P_1-P_4} = -4$ mV, the amplitude deviation of pair P_2-P_4 is less important reaching a minimal value $\Delta V_{P_2-P_4} = -2.7$ mV and the pair P_3-P_4 presents the smallest variation with a minimal value $\Delta V_{P_1-P_4} = -1.4$ mV. Thus, despite a positive pulse at t = 1 h, these negative transient variations of SP signal seem to correspond to a negative bell-shaped signal that can be related to diffusion potential generated by the ionic concentration gradient due to the injection of inlet solution S4. However, the presence of bubbles is certainly affecting SP signal as measured by Vieira et al. (2012) in experiments of gas injection in a sand matrix. Thus, the air in the column may be responsible for the positive pulse occurring at t = 1 h and may also distort SP curves which makes it difficult to analyze the values for $t > 3$ h, while it would have allowed to locate the extent of the reactive zone in the column. Nevertheless, as the three curves show very close values, it is likely that they all lie within the reactive zone, since the inlet buffered solution S4 is highly concentrated. Furthermore, pH_1 and pH_2 curves overlap perfectly over the same period ($t > 3$ h). It therefore seems that the reactive zone extends from the

injection (at P_1) to the exit of the column.

For Experiment ④ (Figure 7.3f), SP curves present negative variations of lower amplitude compared to the variations of Experiment ③ (Figure 7.3e). The minimal SP value is measured on pair P_1-P_4 reaching −1.5 mV. As for Experiment ③, SP are affected by oscillations caused by the pore water temperature variations shown on Figure 7.3d. These variations of temperature seem to affect more the SP values of this experiment than for Experiment ③. This can be explained by the fact that the variations of SP signal are less important than for Experiment ③. Indeed, the SP variations caused by temperature oscillations are of the same order of magnitude (± 0.3 mV) than for Experiment ③. Despite these oscillations caused by the temperature variations, SP curves seem to present a small negative bell-shaped signature that can be associated to the ionic concentration gradients induced by the injection of solution S5. The small amplitude of this electro-diffusive potential is related to the low EC difference between the initial pore water ($\sigma_{w_{init}}$ = 110 µS cm^{-1}) and the solution S5 (σ_{S5} = 128 µS cm^{-1}). The bell-shaped variation of SP curves seems to stop around t = 5.5 h and is synchronous with the stabilization of pH_2 around 7.7 and with the slowdown in growth of σ_{out} curve. For $t > 6$ h, SP signals of pairs P_1-P_4 and P_2-P_4 present similar values close to −0.5 mV, while electrical potential is close to 0 mV for pair P_3-P_4. All of these final SP values differ from the initial SP values of the three pairs. For long term measurements, the electrodes are known to present a drift of their intrinsic potential with time. However, here the experiment lasted only 9 h. Thus, the difference between the initial and the final SP values cannot be related to the drift. No electrokinetic coupling was observed for all previous experiments, therefore it is more likely that the source of these differences in SP values also comes from the electro-diffusive coupling due to the dissolution of calcite between electrodes P_1 and P_4.

7.3.2 Discussion in light of Experiments ① and ②

For Experiments ① and ②, the injection of solutions S1 and S2 that are made of hydrochloric acid generates local reactive area with an extent of a few centimeters (see Figures 7.5a and b). On the contrary, from the analysis of the results of Experiments ③ and ④, the corresponding reactive zones cover larger areas in the column as illustrated on Figures 7.5c and d. Since the inlet of the column is more reactive than the outlet, a red color reactivity gradient was used to represent it on Figure 7.5. In Figure 7.5c, the most reactive zone is even rather located towards the lower half of the column because of the density contrast between the initial pore water and solution S4, which induced calcite dissolution preferentially under the injection tubes (see Figure 7.4). This spreading of the reactive zone when injecting a buffered solution with a weak acid compared to the injection of a strong acid is in agreement with the results of the literature (e.g., Garcia-Rios et al. 2014).

The comparative use of hydrochloric acid and diluted buffered solution in Experiments ② and ④ reveals that SP variations seem not related to the intensity of the dissolution. Indeed, the change of porosity for Experiment ② corresponds to an increase of 0.04 % after 25 h, while for Experiment ④, the porosity increased by 0.09 % in 9 h only. Thus, the injection of S5 for Experiment ④ induces more dissolution of calcite than during Experiment ②, but SP signals are stronger for Experiment ② than for Experiment ④. However, the injection for S3 induced a contrast of pore water EC close to 90 µS cm^{-1}, while the injection of S5 generated a contrast of pore water EC of only 18 µS cm^{-1}. Since both conductivity and electro-diffusive potential are based on ions mobilities, a higher

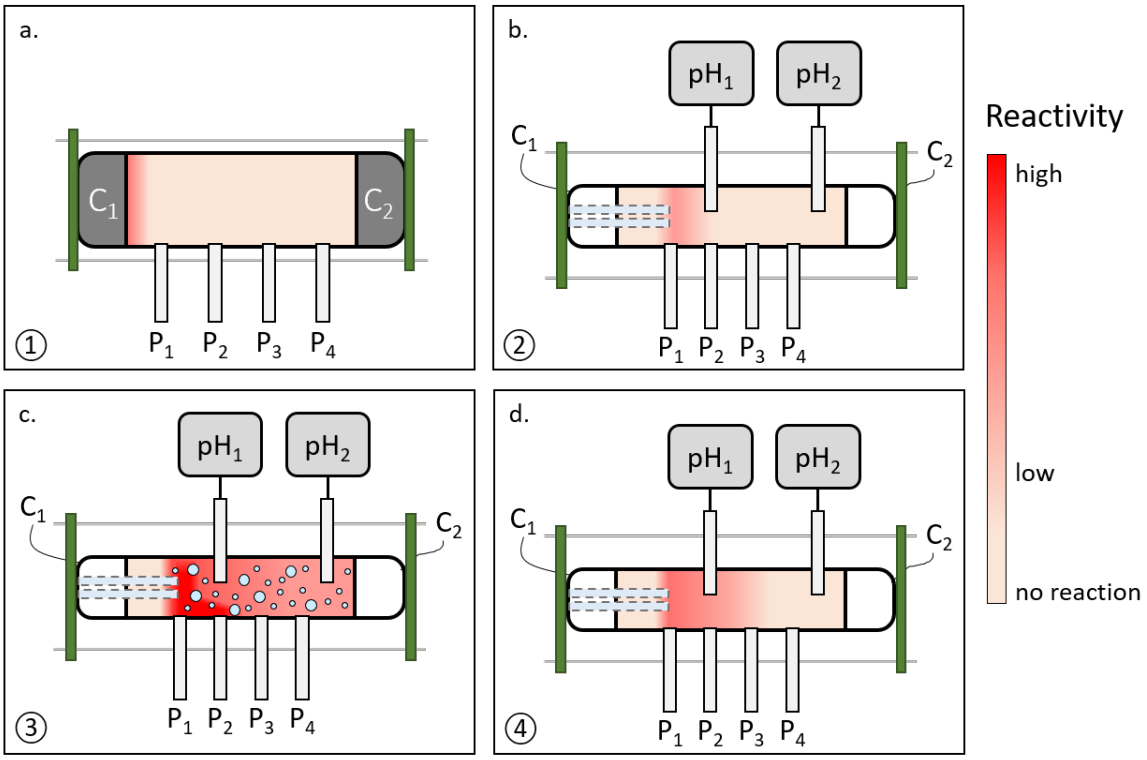

Figure 7.5: Location of the reactive zone of calcite dissolution highlighted with a reactivity gradient for (a) Experiment ①, (b) Experiment ②, (c) Experiment ③, and (d) Experiment ④. The blue circles in the column for Experiment ③ represent the bubbles.

contrast of conductivity will generate higher electro-diffusive potential differences. Therefore, the comparative use of hydrochloric acid and diluted buffered solution in Experiments ② and ④ reveals that SP variations seem more related to the contrast of pore water conductivity rather than to the intensity of the dissolution.

SP interpretation given in this chapter is only based on data observations. However, further modeling of these data using the theoretical framework developed in Chapter 6 would enable to confirm these findings and allow to quantitatively relate the SP signal to the ionic distributions in the sample. Nevertheless, as bubbles were formed in Experiment ③ due to the high concentration of the inlet solution S4, it seems difficult to be able to use the the theoretical framework as it is developed in Chapter 6, but it may be possible to adapt it for unsaturated conditions.

CHAPTER

8 Spectral induced polarization signature of calcite precipitation

8.1 Introduction of the chapter

Experiment ①, presented in Chapter 6, showed that the reactive zone was located at the entrance of Column 1, and thus was not within the portion of the column equipped with the measuring electrodes for SIP monitoring. This limitation of the column design led to the design of Column 2, whose injection tubes are shifted toward the equipped portion (see Section 4.5). Moreover, the amount of precipitated calcite was found to be low in Experiment ①, when using an over-saturated solution at the inlet (see Section 5.2 for more details about S2 chemistry). Therefore, Two experiments of SIP monitoring were conducted on Bench ❷ using Column 2. These experiments are referred as Experiments ⑤ and ⑥ in Chapter 5 and consist in calcite precipitation by injecting two reagent solutions of $CaCl_2$ (S6) and Na_2CO_3 (S7) simultaneously.

I found no experimental publication of SIP monitoring of limestone dissolution except for Halisch et al. (2018), who made measurements between different dissolution steps, but did not observe any changes in phase shift due to dissolution. Thus, since I did not observe SIP signal related to calcite dissolution while performing several experiments, not presented in this manuscript for simplicity, I decided to focus the SIP characterization on calcite precipitation process because it has already been investigated with the SIP method, hence I can compare my data with the published results from Wu et al. (2010) and Izumoto et al. (2020a).

Experiments ⑤ and ⑥ were conducted with the same injected solutions than the one used by Wu et al. (2010) and Izumoto et al. (2020a), since these previous studies could monitor SIP phase spectra variations correlated to calcite precipitation in a glass beads matrix and a sand matrix, respectively. Here, Experiments ⑤ and ⑥ intend to monitor the SIP response to calcite precipitation induced in a matrix of calcite grains at two different flow rates. The flow rate of Experiment ⑤ is $Q = 58.8\,\mathrm{mL\,h^{-1}}$. This value was chosen to make a link with other experiments conducted at the same flow rate and on the same experimental bench Bench ❷). The flow rate of Experiment ⑥ is $Q = 0.51\,\mathrm{mL\,h^{-1}}$. This low value was chosen to reproduce the experimental conditions used by Wu et al. (2010) and Izumoto et al. (2020a). The use of these two different flow rates allow to study the impact of the flow regime on the SIP signature.

This chapter is divided into three sections. First, the results of Experiments ⑤ and ⑥ are presented and analyzed in two successive sections. Then, the last section broadens the discussion of these experimental results by

comparing them with the literature.

8.2 Analysis of the results of Experiment ⑤

Experiment ⑤ lasted about 40 h. The geo-electrical and pH monitoring results are presented on Figure 8.1 in order to highlight their synchronous variations. The stars in the figure represent important events in the experiment. Event 1 (t = -16.6 h) corresponds to the start of the experiment by injecting a non-reactive solution to stabilize the system between the inlet and the outlet. Event 2 (t = 0 h) corresponds to the beginning of the simultaneous injection of solutions S6 and S7 to precipitate calcite. The outlet pore water chemical analyses are presented on the separate Figure 8.2.

8.2.1 Pore water electrical conductivity

Pore water EC is presented on Figure 8.1a. Pore water EC was monitored at the inlet and the outlet of the column with two in-line conductivity meters. During the initialization (for $t < 0$ h), one can observe that the EC of the inlet solution is steady close to 109 µS cm^{-1}, corresponding to the EC of the injected solution. After a few hours, the outlet pore water EC also stabilizes around 143 µS cm^{-1}. The slight difference between the inlet and the outlet EC must be caused by a small increase of calcium and hydrogencarbonate concentrations due to low dissolution when the initial fluid flows through the column, despite the imposed high flow rate of 58.8 mL h^{-1} as seen for previous experiments (see Chapter 7).

S6 and S7 were injected continuously from Event 2 (t = 0 h) to the end of the experiment. The solutions were injected from two separate tubes. Thus, the inlet monitored conductivity corresponds to the conductivity of one of these solutions. For this experiment, the conductivity meter was installed on the injection tube of solution S6. The inlet pore water EC starts to increase at t = 0.5 h. Then it reaches a plateau around σ_{in} = 4300 µS cm^{-1}, which is close to the EC of solution S6 (σ_{S6} = 4480 µS cm^{-1}). The oscillations of ± 50 µS cm^{-1} are due to temperature variations as explained in Section 5.3.1 and already observed and described in Chapter 7. The outlet pore water EC starts to increase at t = 2.6 h. This time delay is consistent with the computed required duration of 2.1 h to cross the column (see Section 7.2.1.1 for more details). Then the outlet pore water EC reaches a plateau around σ_{out} = 2970 µS cm^{-1}. σ_{out} also present some oscillations of ± 50 µS cm^{-1}. These oscillations seem less periodical but in absence of other physical explanation, they are also attributed to room temperature regulation. Since solution S7 is more conductive than S6, the outlet pore water EC should be higher than the inlet pore water EC, which corresponds to the EC of solution S6. As the measured pore water EC is lower at the outlet compared to the inlet, chemical reaction must have occurred in the column.

The pore water EC was also measured on the collected samples of outlet pore water. These samples unsurprisingly present close EC values and consistent time variations with the curve of σ_{out}.

8.2.2 pH monitoring

pH is monitored at two locations in the column. Electrode pH_1 is located at x_{pH_1} = 13 cm, corresponding to the position of the SIP measuring electrode P_2 and electrode pH_2 is located near the outlet of the column at

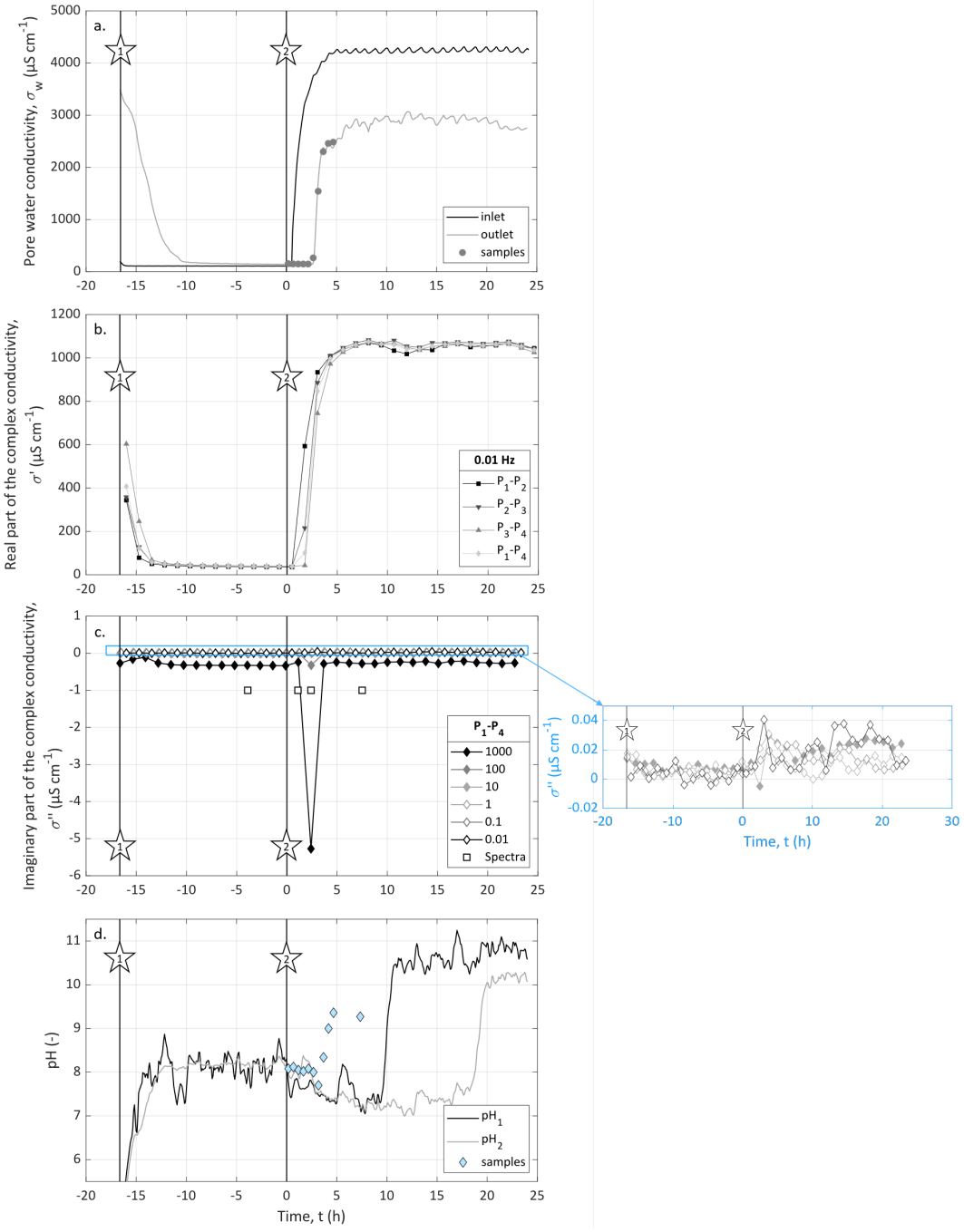

Figure 8.1: Results of Experiment ⑤. Stars 1 and 2 represent important events. Event 1 (t = -16.6 h) corresponds to the injection of a non-reactive solution. Event 2 (t = 0 h) corresponds to the beginning of the simultaneous injection of S6 and S7. (a) the inlet and outlet pore water EC measured with the in-line conductivity meters and the pore water EC of the outlet pore water samples. (b) time variations of the real conductivity signal recorded on the channel P_1-P_2, P_2-P_3, P_3-P_4, and P_1-P_4 at 0.01 Hz. (c) time variations of the imaginary conductivity signal recorded on the channel P_1-P_4 at 1000 Hz, 100 Hz, 10 Hz, 1 Hz, 0.1 Hz, and 0.01 Hz. The white squares represent the timings of the imaginary conductivity spectra presented on Figure 8.3. The blue box corresponds to the zoom view of the time variations of the imaginary conductivity at frequencies 10 Hz, 1 Hz, 0.1 Hz, and 0.01 Hz. (d) pH monitored in the column at x_{pH_1} = 13 cm and x_{pH_2} = 27 cm and pH measured on the samples of outlet pore water.

px_{pH_2} = 27 cm. pH results are presented on Figure 8.1d and one can first observe that the curves are noisy due to the electric current injection between electrodes C_1 and C_2 for the SIP monitoring and that the curves present variations that are not synchronous with all the other acquisition methods. However, pH is also measured on the samples of outlet pore water and present synchronous variations with the outlet pore water EC. These time-delayed variations in pH_1 and pH_2 must therefore be related to the complexity of the mixing of solutions S6 and S7 in the column. Indeed, the solutions S6 ($CaCl_2$) and S7 (Na_2CO_3) do not have the same pH. S6 has a pH close to 6.5 while S7 has a pH close to 9 (these data were not measured, but taken from the bottles of the pure solid compounds). In the course of the experiment, pH_1 and pH_2 values are certainly influenced by the initial pH of solutions S6 and S7, but also by the pH evolution due to the calcite precipitation in the column. It should be noted that the pH is a punctual measurement unlike electrical monitoring which integrates the volume between the measuring electrodes. The position of the pH electrodes in relation to the distribution of the injected solutions can therefore have a strong influence on the measured values. Here I have positioned the end of the pH electrodes as far as possible in the center of the column, but this does not mean that the distribution of the two input solutions S6 and S7 and the location of the mixing front are perfectly known and symmetrical.

During the initialization phase ($t < 0$ h), after some stabilization, pH_1 and pH_2 present similar steady values around 8.1. Both pH_1 and pH_2 start to decrease after the beginning of solutions S6 and S7 injection. For $t \in [0\,;\,9.4]$ h, pH_2 decreases from 8.0 to 7.2. For pH_1 it is more difficult to quantitatively analyze the variations of its curve due to a higher level of noise, but the trend seems close to the decrease of pH_2 values. Then, at t = 9.4 h, pH_1 starts to increase, reaches a first plateau around 10.5 for $t \in [10.7\,;\,18.5]$ h and a second plateau around 10.8 for $t > 18.5$ h. pH_2 slightly increases from 7.2 to 7.6 for $t \in [9.4\,;\,18.2]$ h, then at t = 18.2 h, pH_2 abruptly increases and reaches a plateau arond 10.1 for $t > 20.4$ h.

Given the pH values of the inlet solutions S6 and S7, it appears that pH_1 and pH_2 are more influenced by the pH value of solution S6 for $t \in [0\,;\,9.4]$ h, then pH_1 and pH_2 sudden increases at t = 9.4 h and t = 18.2 h, respectively, must be related to the influence of solution S7 and to the precipitation of calcite.

8.2.3 Outlet pore water chemical analyses

The samples of outlet pore water chemical analyses are presented on Figures 8.2. These analyses correspond to the measurement of pH, alkalinity, calcium concentration, sodium concentration, and chloride concentration. Unlike pH_1 and pH_2 curves, all of these analyses show synchronous temporal variations compared to σ_{in} and σ_{out} curves.

During the first 2.6 h after the beginning of solutions S6 and S7 injection, all the curves are steady. Sodium and chloride concentrations are zero since the initial pore fluid does not contain these ions since it is a solution made of dissolved calcite (see Section 5.2.3.3 for more details). While calcium and chloride concentrations begin to change at t = 2.7 h, pH, alkalinity, and sodium concentration rather start to increase at t = 3.2 h. Solution S6 is a solution of calcium chloride and solution S7 is an alkaline solution of sodium carbonate. As a result, the delay between changes in calcium and chloride concentrations on one hand and the increase in pH, alkalinity and sodium concentration on the other hand can be explained by a delay in the spread of solution S7 compared

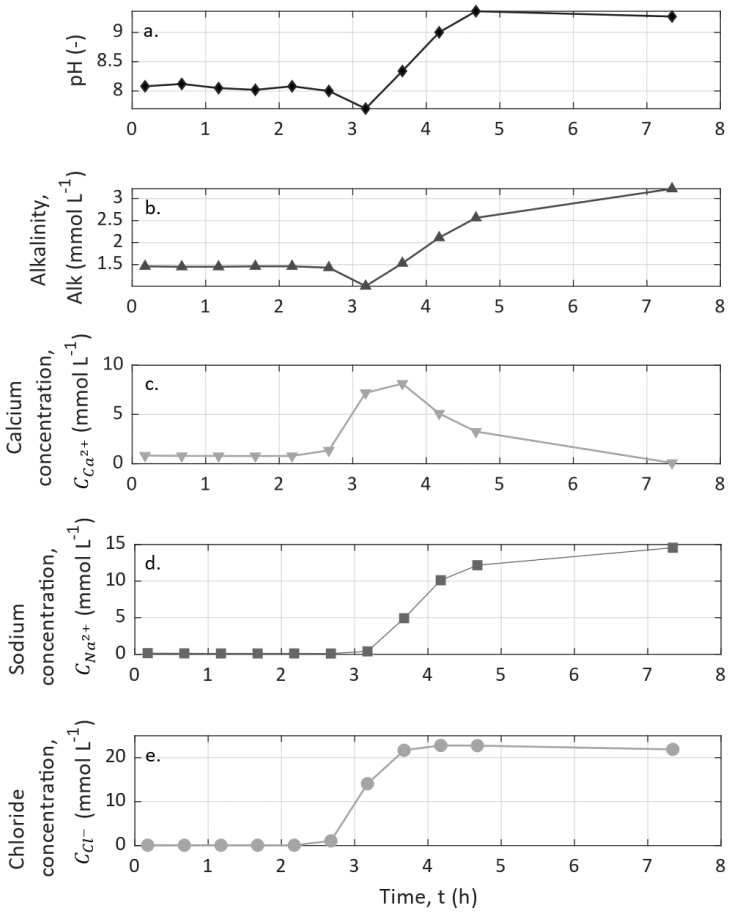

Figure 8.2: Measurements of the outlet pore water (a) pH, (b) alkalinity, (c) calcium concentration, (d) sodium concentration, and (e) chloride concentration.

to solution S6. This slight delay may be caused by a small variation in the flow rate due to a difference in the adjustment of the tightening screws of the rotating head of the pump. This time delay observation on the pore water chemical analyses is in accordance with the cause of the delay of pH_1 and pH_2 increase.

After their increase (for $t \in [3\,;5]$ h approximately) pH, alkalinity, chloride concentration, and sodium concentration become more stable until the end of the experiment. Unlike the other curves, calcium concentration does not increase and reach a plateau. From $t = 2.7$ h, calcium concentration increases up to 8.1 mmol L^{-1} and starts to decrease for $t \in [3.2\,;3.7]$ h, when pH, alkalinity, and sodium concentration start to rise, and reaches nearly zero for the last collected sample. Calcite precipitation is expected to reduce calcium concentration. Thus, the transient increase of calcium concentration can also be explained with the delay in the spread of solution S7 compared to solution S6.

Given the the comparative analyses of pH, alkalinity, and ionic concentrations variations, the time delay between solutions S6 and S7 propagation has a duration comprised between 0.5 h and 1.0 h. This duration is much shorter than the time delay of pH_1 and pH_2 to rise. Thus the time delay of pH monitoring in the column may be related to the influence of the mixing front and calcite precipitation rather than on the propagation of solution S7 through the column. However, reactive transport modeling appears necessary to confirm these findings.

8.2.4 SIP monitoring

SIP method was used continuously to monitor amplitude and phase of the complex conductivity on the four channels P_1-P_2, P_2-P_3, P_3-P_4, and P_1-P_4 from 0.005 Hz to 10^4Hz with 41 data points equally distributed over the frequency range. I choose to present time variations of the real and imaginary parts of the complex conductivity, instead of the amplitude and phase because the big change of pore water conductivity due to the injection of solutions S6 and S7 distort the phase, especially at high frequencies.

Figure 8.1b presents the time variations of the real conductivity measured at 0.01 Hz for the four channels. During the initialization phase ($t < 0$ h), after 2 h to reach the system stability, the four channels present stable and almost identical real conductivity values. Then, after the beginning of solutions S6 and S7 injection, the real conductivity increases successively for the channels P_1-P_2, P_2-P_3, and P_3-P_4. The increase of real conductivity of channel P_1-P_4 looks more like a mean behavior between the three other channels. The real conductivity increase of all these channels occurs between the increase of the inlet and the outlet pore water EC (Figure 8.1a). This implies that real conductivity amplitude is controlled by the amplitude of the pore water EC. Thus, the successive increase between the channels P_1-P_2, P_2-P_3, and P_3-P_4 is related to the propagation of the solutions S6 and S7 through the column. Then, for $t > 5.6$ h, the real conductivity of the four channels remains constant with similar values comprised between 1040 $\mu S\,cm^{-1}$ and 1070 $\mu S\,cm^{-1}$.

Figure 8.1c presents the time variations of the imaginary conductivity signal recorded on the channel P_1-P_4 at 1000 Hz, 100 Hz, 10 Hz, 1 Hz, 0.1 Hz, and 0.01 Hz. I choose to represent the variations of the channel P_1-P_4 only, since it corresponds to a mean behavior of the electrical response of the column. Over these different frequencies and during all the experiment, the imaginary conductivity is low and steady, except at $t = 2.4$h for the imaginary conductivity measured at 1000 and 100 Hz. These two data points are synchronous with the rise of the real conductivity (Figure 8.1b), induced by the increase of the pore water EC, due to the start of solutions S6 and S7 injection (Figure 8.1a).

The white squares of Figure 8.1c represent the timings of the imaginary conductivity spectra of channel P_1-P_4 presented on Figure 8.3. One can observe on Figure 8.3, that the propagation of the solutions S6 and S7 induces a strong decrease of the phase at $t = 2.4$ h, for frequencies above 100 Hz, then the imaginary spectrum returns to its shape. This evolution may come from the pore water conductivity increase, caused by the injection of S6 and S7, as measured by Lévy et al. (2019), who observed high-frequency shift toward negative values for the phase frequency spectrum when increasing the water salinity. Nevertheless, in this experiment, this imaginary conductivity decrease is only a transient variation. Thus, in this experiment of calcite precipitation, it seems, that imaginary conductivity, for frequencies above 100 Hz, is linked to the pore water chemical disequilibrium.

Calcium concentration measured on the outlet pore water samples indicates that calcite precipitates in the column. However, the low imaginary conductivity values on Figure 8.1c and the absence of imaginary conductivity increase on the spectra of Figure 8.3, except at $t = 2.4$ h, seem to indicate that calcite minerals precipitation in these experimental conditions, does not induce SIP signal similar to the spectra observed in the literature.

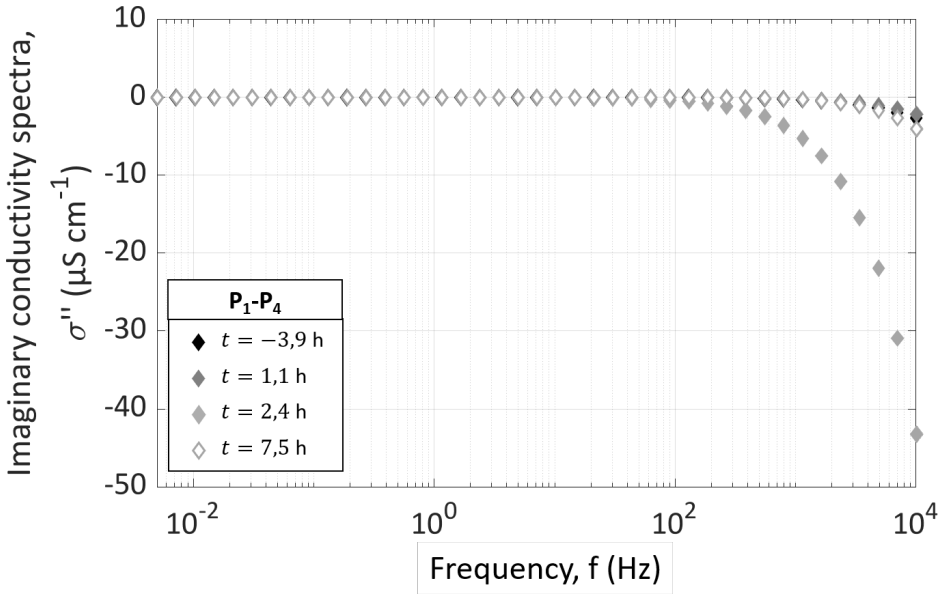

Figure 8.3: SIP phase spectra at different timings: $t = -3.3$ h, $t = 0.5$ h, $t = 1.8$ h, $t = 4.3$ h, and $t = 9.4$ h.

8.3 Analysis of the results of Experiment ⑥

Experiment ⑥ lasted about 580 h. The experimental results are presented on the unique Figure 8.4 in order to highlight their synchronous variations. The stars in the figure represent important events in the experiment. Event 1 (t = -98h) corresponds to the start of the experiment by injecting a non-reactive solution to stabilize the system between the inlet and the outlet. Event 2 (t = 0h) corresponds to the beginning of the simultaneous injection of solutions S6 and S7 to precipitate calcite.

8.3.1 Pore water electrical conductivity

Pore water EC is presented on Figure 8.4a. Pore water EC was monitored at the inlet and the outlet of the column with two in-line conductivity meters. During the initialization (for $t < 0$ h), one can observe that the EC of the inlet solution is steady close to 100 µS cm^{-1}, corresponding to the EC of the injected solution, while the EC of the outlet pore water requires nearly 100 h to stabilize. However, there is a difference of several hundreds of micro Siemens per centimeters between the inlet and the outlet. This deviation was also observed for Experiment ⑤, but thanks to the stronger flow rate, this conductivity difference was not as noticeable as for this experiment. I could have pursue the initialization by connecting the outlet to the inlet, as I did for Experiment ①, but this was too time consuming, thus I only waited for σ_{out} to reach a certain stability before injecting solutions S6 and S7.

S6 and S7 were injected continuously from Event 2 (t = 0h) to the end of the experiment and as for Experiment ⑤, the inlet conductivity meter was installed on the injection tube of solution S6. Thus, the inlet EC curves from Experiments ⑤ and ⑥ present similar amplitudes. However, due to the low flow rate of Experiment ⑥ compared to the flow rate of Experiment ⑤, inlet EC only reaches a plateau for $t > 120$ h and this value is close to the EC value of solution S6 (σ_{S6} = 4480 µS cm^{-1}). The outlet pore water is steady around its initial value (at $t = 0$ h, σ_{out} = 600 µS cm^{-1} during 145 h. Then its curve increases in slope more gently than for the

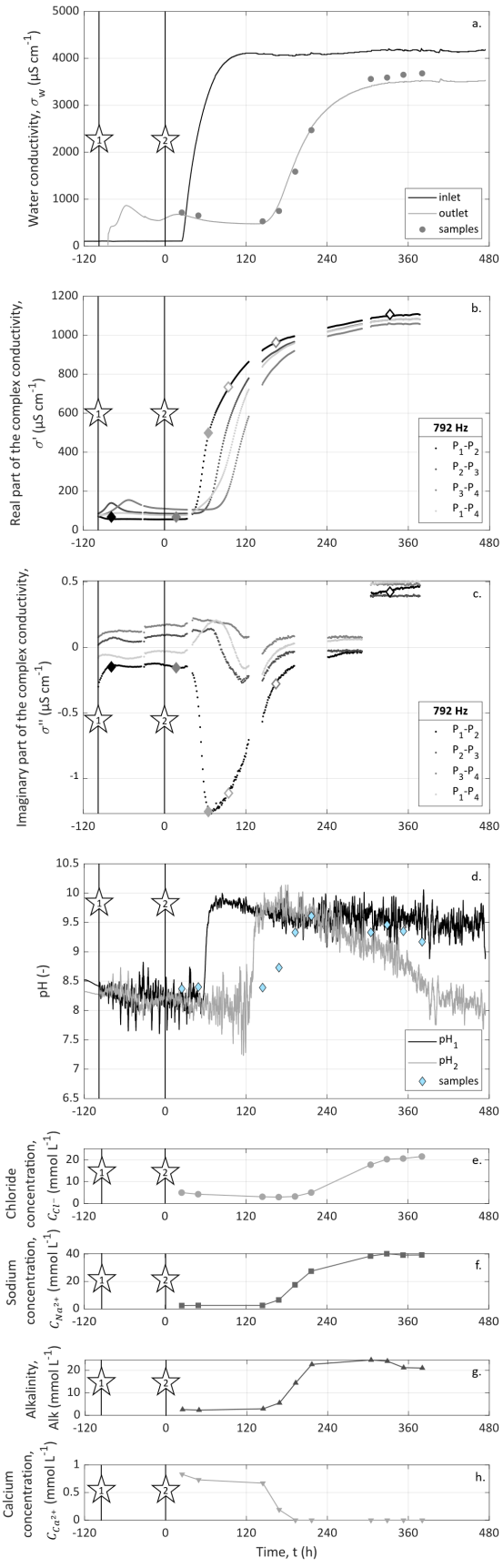

Figure 8.4: Results of Experiment ⑥. Stars 1 and 2 represent important events. Event 1 (t = -98h) corresponds to the injection of a non-reactive solution. Event 2 (t = 0h) corresponds to the beginning of the simultaneous injection of S6 and S7. (a) the inlet and outlet pore water EC measured with the in-line conductivity meters and the pore water EC of the outlet pore water samples. (b) real conductivity signal recorded on the four channels P_1-P_2, P_2-P_3, P_3-P_4, and P_1-P_4 at 972 Hz. (c) imaginary conductivity signal recorded on the four channels P_1-P_2, P_2-P_3, P_3-P_4, and P_1-P_4 at 127 Hz. (d) pH monitored in the column at x_{pH_1} = 13 cm and x_{pH_2} = 27 cm and pH measured on the samples of outlet pore water. (e,f,g,h) measurements of the outlet pore water chloride concentration, sodium concentration, alkalinity, and calcium concentration, respectively.

inlet EC curve. The delay between the start of EC increase at the inlet and the outlet of the column is about 122 h, which is consistent with the time required for the water to flow through the column according to its dimensions, the initial porosity and the imposed flow rate. For $t > 360$ h, the outlet EC curve reaches a plateau with $\sigma_{out} = 3510\ \mu S\ cm^{-1}$. As explained for Experiment ⑤, the lower pore water EC at the outlet compared to the inlet is a sign that chemical reaction occurred in the column.

The pore water EC was also measured on the collected samples of outlet pore water. These samples unsurprisingly present close EC values and consistent time variations with the curve of σ_{out}.

8.3.2 pH monitoring

pH is monitored at two locations in the column. Electrode pH_1 is located at $x_{pH_1} = 13$ cm, corresponding to the position of the SIP measuring electrode P_2 and electrode pH_2 is located near the outlet of the column at p$x_{pH_2} = 27$ cm. pH results are presented on Figure 8.4d and one can first observe that the curves are much more noisy than for the Experiments ② to ④ due to the electric current injection between electrodes C_1 and C_2 for the SIP monitoring. However, compared to the pH curves of Experiment ⑤, the curves of Experiment ⑥ present variations that seem synchronous with all the other acquisition methods.

During the initialization ($t < 0$ h), both pH_1 and pH_2 curves are superimposed and present small variations comprised between 8.1 and 8.3. 55 h after the beginning of S6 and S7 injection, pH_1 increases fast and reaches a plateau around 9.5, while pH_2 starts to increase around $t = 120$ h and after reaching a maximum pH close to 9.7 around $t = 160$ h, the curves decreases quite linearly until the end of the experiment. This constant decrease in pH_2 takes place over a much longer time period than the time required for the pore water to flow through the device. This indicates that this pH change is not related to the flow through the column by the input solutions, but to the fact that these injected solutions react chemically and change the pH conditions gradually along the column. Indeed, the solutions S6 ($CaCl_2$) and S7 (Na_2CO_3) do not have the same pH. S6 has a pH close to 6.5 while S7 has a pH close to 9 (these data were not measured, but taken from the bottles of the pure solid compounds). pH_1 therefore has a stable value influenced by the pH of solution S7, while pH_2 changes transiently from the pH value of solution S7 to a value closer to the pH value of solution S6. However, these only two observation points in the column are not sufficient to conclude on the behavior of these two reagent solutions and to locate the reacting front in the column.

pH is also measured at the outlet on collected samples of pore water. In comparison with pH_2 curve which measures the pH close to the outlet of the column, pH values from the outlet pore water samples present similar amplitudes to pH_2 for $t < 55$ h. Then pH of the samples increases with a smoother slop and with a more important time delay compared to pH_2 curve for $t \in [120\ ;\ 240]$ h. Finally, the pH values of the samples of outlet pore water show the same linear decrease than pH_2 curve for $t > 240$ h, but the values are a bit higher. This difference in amplitude may be caused by the fact that pH_2 amplitude in influenced by its vertical position in the column in relation to the position of the injection tubes, while the samples of outlet pore water are representative of the real pH solution after the mixing of S6 and S7. Note that all the samples of outlet pore water were in the form of clear water (i.e. not clouded by the precipitation of calcite micro-particles) and that they did not show any precipitated calcite grains at the bottom of the beakers, contrary to what I obtained by

directly mixing solutions S6 and S7 in a beaker.

8.3.3 Outlet pore water chemical analyses

The samples of outlet pore water chemical analyses are presented on Figures 8.4e, f, g, and h. These analyses correspond to the measurement of chloride concentration, sodium concentration, alkalinity, and calcium concentration, respectively. One can observe that all of these analyses present synchronous variations between them and with EC and pH measured on the same samples and the curve of σ_{out} (see Figures 8.4a and d).

The variations of ionic concentrations and alkalinity show that all of them increase except for calcium concentration. As the injected solutions S6 and S7 are rich in sodium and chloride, it is logical to observe the increase of their concentrations. Chloride concentration reaches a maximal value $C_{Cl^-} = 21.5\,\text{mmol}\,\text{L}^{-1}$ and sodium concentration reaches a plateau around $C_{Na^+} = 39.5\,\text{mmol}\,\text{L}^{-1}$. One can however notice that these maximal concentrations were expected to be higher given the concentrations of the inlet solutions S6 ($C_{Cl^-} = 52\,\text{mmol}\,\text{L}^{-1}$) and S7 ($C_{Na^+} = 60\,\text{mmol}\,\text{L}^{-1}$). Nevertheless, the amplitudes reached by chloride and sodium concentrations are in the same order and it is probable that these values would have continue to increase if the experiment was pursued for a longer time. Contrary to the variations of sodium and chloride concentrations, calcite concentration decreases. Since solution S6 contains a high concentration of calcium and chloride ions, calcium concentration should increase as observed for chloride concentrations. Thus, the decrease of calcium concentration is a sign that calcite has precipitated and that it consumed nearly all the available calcium ions for $t > 190\,\text{h}$ (calcium concentration measured on samples collected for $t > 192\,\text{h}$, was below the detection limit, it was thus set to $0\,\text{mmol}\,\text{L}^{-1}$). However, alkalinity increases and reach a plateau around $22\,\text{mmol}\,\text{L}^{-1}$. In the range of pH explored during this experiment, alkalinity can be approximate by the concentration of hydrogencarbonate (see Section 1.2.1 for more details). Thus, the measured alkalinity is a really high value compared to the injected hydrogen concentration of solution S7. Thus, despite this high alkalinity value, all the other chemical analyses clearly show that calcite precipitation occurred in the column.

8.3.4 SIP monitoring

SIP method was used continuously to monitor amplitude and phase of the complex conductivity on the four channels P_1-P_2, P_2-P_3, P_3-P_4, and P_1-P_4. Figures 8.4b and c present the results of the SIP monitoring on the four channels at the unique frequency 972 Hz, where clear phase shift variations were observed on the spectra. On Figures 8.4b and c, I choose to present the real and imaginary parts of the complex conductivity, respectively, instead of the amplitude and phase because the big change of pore water conductivity due to the injection of solutions S6 and S7 has a huge impact on the phase and hides the complex conductivity variations that may be related to calcite precipitation. Furthermore, Wu et al. (2010) and Izumoto et al. (2020a) also use the real and imaginary conductivity in their publications, thus it will help the comparison. Note that, one can observe some gaps in the data. These gaps are measurements that have been removed because the device showed unstable measurements. The acquisition was therefore stopped and then restarted regularly during this experiment in order to verify the quality of the measurements. This problem is discussed later when presenting the imaginary conductivity data.

The real conductivity of the four channels presents variations that seem highly related to the changes of pore water EC (Figures 8.4a and b). During the initialization (t < 0 h), the real conductivity stabilizes and reaches close steady values for the four channels. At t = 0 h, the values of $\sigma'_{P_1-P_2}$, $\sigma'_{P_2-P_3}$, $\sigma'_{P_3-P_4}$, and $\sigma'_{P_1-P_4}$, are 55.7 µS cm^{-1}, 85.0 µS cm^{-1}, 110.3 µS cm^{-1}, and 77.34 µS cm^{-1}, respectively. Real conductivity of channel P_1-P_4 appears to be a mean value of the real conductivity gradient measured between the channels P_1-P_2, P_2-P_3, and P_3-P_4. This real conductivity gradient is consistent with the difference of pore water EC between the inlet and the outlet ($\sigma_{out} > \sigma_{in}$ at t = 0 h). After the start of solutions S6 and S7 injection, the real conductivity of each channel increases one after the other for the channels P_1-P_2, P_2-P_3, and P_3-P_4 due to the fluid propagation through the column. Thanks to high sampling rate of SIP acquisition compared to the fluid velocity in the column, one can really observe the propagation of the real conductivity front, the time delay between the real conductivity increase on each of these channels is about 20 h. The channel P_1-P_4 behaves as the mean measurement and thus does not reproduce the same pattern and presents a smoother slope. Then, around t > 300 h, the real conductivity stabilizes for all the channel with values comprised between 1055 µS cm^{-1} and 1100 µS cm^{-1}. This gradient of conductivity between the channels P_1-P_2, P_2-P_3, and P_3-P_4 is consistent with the difference of pore water EC between the inlet and the outlet ($\sigma_{out} < \sigma_{in}$) and must be related to the precipitation of calcite which slightly decreases the pore water conductivity and thus the real conductivity amplitude. I do not think though that the amount of precipitated calcite is sufficient to relate this real conductivity decrease along the column to changes of the effective properties of the porous medium since the decrease of the real conductivity amplitude between the channels is low.

The imaginary conductivity presented on Figure 8.4c shows negative values whereas it is normally defined to be always positive. Nevertheless, the imaginary conductivity shows interesting time variations, with consistent patterns between the channels, suggesting that these measurements are related to the chemical changes induced by the precipitation of calcite minerals in the column. First, the reached amplitudes (between -1.3 and 0.5 µS cm^{-1}) are much lower than in the experiments conducted by Wu et al. (2010) and Izumoto et al. (2020a). Indeed, Wu et al. (2010) obtained a maximal value of 36.87 µS cm^{-1}, while Izumoto et al. (2020a) measured a maximal imaginary conductivity up to 922.8 µS cm^{-1}. Moreover, while Wu et al. (2010) associate the increase in imaginary conductivity with the growth of grain size, here the maximum variation of measured imaginary conductivity (although it is a negative value) is obtained for the P_1-P_2 channel between 30 h and 240 h, when the conductivity difference between the inlet and outlet of the column is the highest and when the real conductivity also varies strongly. This bell-shaped variation can also be observed for channels P_2-P_3, P_3-P_4, and P_1-P_4, but with smaller amplitude differences, especially for channel P_3-P_4. It is also noticeable that this transient variation presents a repeated temporal shift between channels P_1-P_2, P_2-P_3, and P_3-P_4. Channel P_1-P_4 does not follow this trend and rather represents an average value. These transient variations are more similar to SP signals, which are related to concentration gradients rather than to the growth of precipitated calcite grains. Besides, the fact that the amplitude of variation of the imaginary conductivity is the largest for the P_1-P_2 channel could indicate that the most reactive zone is located between these electrodes. However, it seems necessary to model the mixing zone to confirm this.

The diamonds of Figures 8.1b and c represent the timings of the phase spectra of channel P_1-P_2 presented on Figure 8.5. One can observe, as in Experiment ⑤, that the propagation of the solutions S6 and S7 induces

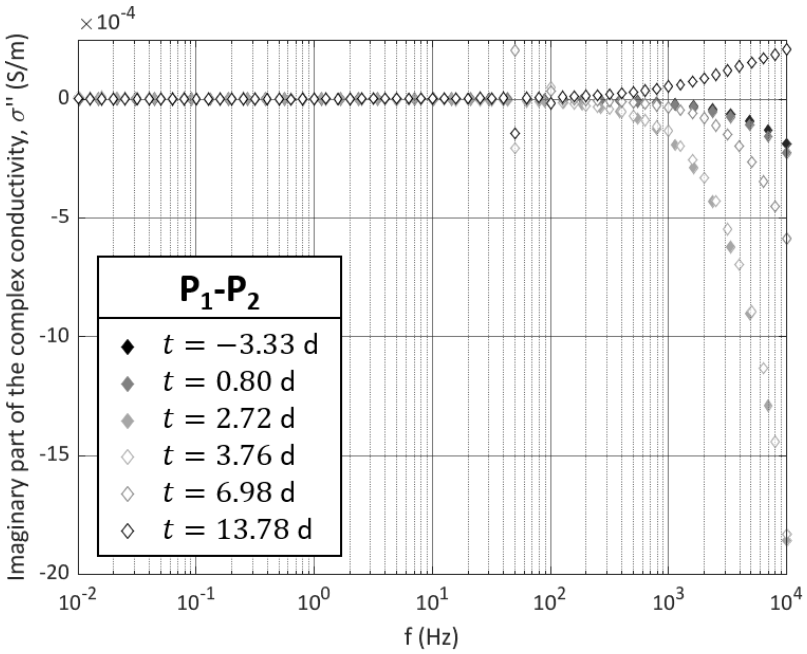

Figure 8.5: SIP phase spectra at different timings: $t = -3.33$ d, $t = 0.80$ d, $t = 2.72$ d, $t = 3.76$ d, $t = 6.98$ d, and $t = 13.78$ d.

a strong decrease of the phase for frequencies above 100 Hz, then, for $t > 3.76$ d, high-frequency imaginary conductivity values start to increase and become positive at the end of the experiment.

Izumoto et al. (2020b) performed SIP measurements during calcite precipitation in a millifluidic device on three channels along the sample (named upstream, middle, and downstream, by the authors). They obtained bell-shaped imaginary conductivity spectra associated with the formation of a horseshoe shape front of precipitated calcite minerals. In addition, on the spectra of the upstream channel, they observed negative imaginary conductivity values between 1 and 100 Hz, reaching a minimal value of $-7.6\,\mu S\,cm^{-1}$. In his doctoral thesis, Izumoto (2021) modeled these negative imaginary conductivity data using an empirical model based on a heterogeneous distribution of complex electrical conductivity, with different chargeability values. He obtains a minimal negative imaginary conductivity value of $-28\,\mu S\,cm^{-1}$ at 600 Hz. Izumoto (2021) attributes the heterogenous complex electrical conductivity distribution to the heterogeneous distribution of solute concentration, which induced faster and more abundant calcite precipitation in the part of the sample with higher concentrations. Thus, the imaginary conductivity negative variations observed in Experiment ⑥ and described in the previous paragraph are in accordance with the negative imaginary conductivity values measured by Izumoto et al. (2020b). In addition, the decrease of the imaginary conductivity spectrum of Experiment ⑤ measured at $t = 2.4$h(Figure 8.3), may be explained by the same phenomenon of heterogenous complex electrical conductivity distribution induced by heterogeneous precipitation of calcite minerals in the column.

The imaginary conductivity presented on Figure 8.4c shows some amplitude shift between the different series of acquisition without showing variations related to the experimental conditions. This shift is clearly visible between the penultimate series (acquired between 240 h and 290 h) and the last series (acquired between 300 h and 375 h). Since it may be an instrumental problem, I sent the data to the manufacturer who is currently investigating it.

8.4 Discussion in light of the data from the literature

Both Experiments ⑤ and ⑥ show interesting results that need reactive transport modeling to confirm the findings based on the analyses of the experimental results and mechanistically reproduce the propagation and the interaction between solutions S6 and S7 and the calcite matrix.

The SIP results of both Experiments ⑤ and ⑥ present imaginary conductivity data that seem not in accordance with the results of SIP monitoring of calcite precipitation already performed by Wu et al. (2010) and Izumoto et al. (2020a) that have measured important increase of imaginary conductivity related to calcite precipitation in a matrix of glass bead and a matrix of silica sand, respectively, while for Experiment ⑥ in particular, the experimental conditions (i.e., inlet concentrations and flow rate) were really close to the conditions set in these studies. The major difference is that I used a calcite grain matrix.

Literature about the dynamics of calcium carbonate formation and about the growth of calcite crystals shows that the precipitation of calcite can occur through a wide variety of pathways to form crystallized particles that will attache to the other crystals and these pathways can be very different from the commonly modeled crystallization of monomer-by-monomer addition (e.g., de Yoreo et al. 2015). The invoked precursor phases of the calcite crystal can range from amorphous phases to crystalline nanoparticles and the observation of one or another form of these precursor phases is controlled by thermodynamics and kinetics (e.g., de Yoreo et al. 2015; Lassin et al. 2018). Then, the crystal growth following the nucleation stage, can also be driven by many competing processes that can redissolve some of the solid phases and select others (e.g., Gal et al. 2013; de Yoreo et al. 2015). However, the presence of a foreign surface importantly affects the pathway of crystallization because it can lower the energy barrier to nucleation (e.g., Fernandez-Martinez et al. 2013; de Yoreo et al. 2015). In the case of calcite, it has been found that depending on the mineral surface or on the biological film that surrounds the the volume within which nucleation occurs, the mechanisms of calcite crystals formation were not universals (e.g., Hu et al. 2012). Stockmann et al. (2014) conducted an experiment of calcite crystallisation on different silica minerals and on calcite crystals for comparison. They found that calcite precipitated instantaneously and at a constant rate in the presence of calcite grains but for the silica minerals, they found slower initial precipitation rates that became independent of substrate identity over time. Noiriel et al. (2016) made also similar observation after conducting calcite precipitation in columns filled with glass beads and calcite or aragonite, with preferential precipitation on calcite and aragonite compared to glass beads and with different crystal shape, surface area, and pore roughness depending on the initial substrate between calcite and aragonite, inducing contrasted impacts on porosity-permeability evolution between the two columns.

The nature of the matrix used to generate the nucleation and growth of calcite crystals seems thus very important and may be a key parameter to explain the absence of important imaginary conductivity increase for Experiments ⑤ and ⑥. Indeed, if heterogeneous minerals help to decrease the thermodynamic barriers for the nucleation of calcium carbonate particles, this can possibly lead to the formation of amorphous forms which may influence more the imaginary conductivity than the addition of monomers, which is the mechanism mainly invoked for calcite crystals growth on calcite surface (e.g., Stockmann et al. 2014). However, none of the experiments conducted by Wu et al. (2010), Izumoto et al. (2020a) or in this thesis can give insights about

the mechanisms of calcite crystals nucleation and growth. Nevertheless, the fact that the nature of the initial matrix used to precipitate calcite may play a role in the imaginary conductivity amplitude is totally unrelated to the size of the precipitated grains as invoked by Wu et al. (2010) and modeled by Leroy et al. (2017). Thus, I believe that further investigations of the SIP signature of calcite precipitation must be conducted at smaller scale to be able to link the SIP spectra to real mechanisms of nucleation and calcite growth (e.g., Izumoto et al. 2020b).

Conclusions

Hydrogeophysics appears today as an essential discipline for the study of reactive processes since it overcomes the limits of conventional sampling and tracing techniques. Geo-electric methods in particular allow a number of advances both in the laboratory and in the field thanks to their high sensitivity to physical and chemical properties of rocks and of pore fluids. My thesis work is in the continuation of geophysical developments to study key processes that are related to mineral and pore water interactions.

This thesis focused on the development of the comprehension of the geo-electrical signal generated by calcite dissolution and precipitation processes. Some studies from the literature have already performed geo-electrical monitoring of calcite dissolution or precipitation processes, however, their number is reduced and their comparison reveals some contradictions. Besides, most of these experimental studies from the literature rely on empirical relationships rather than mechanistic interpretation of the processes involved in the geo-electrical response. Therefore, this thesis pursued two objectives. On one hand, this thesis brought new laboratory results to address the lack of experimental data with the development of an experimental device to study the coupling between fluid-rock chemical interactions, hydrodynamic properties, and geo-electrical signatures. On the other hand, this thesis proposed to improve some petrophysical relationships relating geo-electrical properties to the porous medium effective parameters, which is thus studied at the representative elementary volume (REV) scale.

The two electrical methods used for the geo-electrical monitoring were the spectral induced polarization (SIP) and the self-potential (SP). The joint use of these methods allows the characterization of both the structural properties of the porous matrix, the mineral-solution interface properties and the geochemical evolution of the porous fluid. SP is a passive technique consisting in the measurement of the natural electric field mainly generated in the context of calcite dissolution and precipitation study, by water fluxes and concentration gradients, through the electrokinetic and the electro-diffusive couplings, respectively. SIP is an active method measuring the electrical complex conductivity over a low frequency range (from mHzto kHz). The electrical complex conductivity is a geophysical property whose real and imaginary components are related to the pore water chemistry, the microstructural properties of the porous medium, and to the surface state of the minerals that form the porous matrix.

I developed a new petrophysical model in this thesis to interpret the real part of the complex conductivity when

neglecting the contribution of the surface conductivity. The electrical conductivity of the porous medium is related to microstructural parameters, such as porosity, tortuosity, and constrictivity. Taking into account the constrictivity in the description of the poral space constitutes one of the main interests of this model compared to models in the literature, that generally only consider the tortuosity to describe the complexity of the environment. This model of electrical conductivity also relates this property to the permeability of the medium which is a key hydrodynamic parameter. This model was successfully used on a variety of data of the literature from simple unconsolidated media to consolidated sedimentary rock samples presenting different types of porosity. The model was also used on digital images of calcite dissolution and precipitation simulations and showed that it can reproduce structural changes linked to dissolution and precipitation processes by only adjusting the medium constrictivity as predicted in the literature. Contrictivity monotonously decreases or increases under dissolution or precipitation conditions, respectively. Thus, constrictivity is a good witness of how dissolution and precipitation processes affect the porous medium microstructure.

Two experimental benches were developed during this thesis. They permit to follow alternatively the dissolution or precipitation of calcite using SP or SIP acquisition, with the monitoring of the electrical conductivity of the inlet and outlet pore water, and by performing chemical analyses on samples of the outlet pore water. These experimental benches were designed to ensure a constant injection of the reactive inlet solutions in the sample holder under atmospheric conditions of pressure and temperature. As my thesis focuses on the chemical reactivity of calcite, the sample chosen for the experimental work was a synthetic sample made of loose calcite crystals with sorted grains size. This development work has first led to the creation and improvement of non-polarizable Ag-AgCl electrodes, in order to provide a reliable and long-lasting acquisition. Then the development of the first experimental bench led to the design and testing of a first sample holder allowing to discretize the geo-electrical measurement. The analysis of the dimensions of the column, constituting this sample holder, according to quality criteria taken from the literature as well as from the first experimental results showed that this column was too wide compared to the spacing of the electrodes and that the injection of the input solutions was too far from the zone equipped for the geo-electric monitoring. Therefore a second column was designed to meet these limitations. This second column, thinner and with an offset injection at the level of the geo-electrical signal measurement zone, was also designed to measure the pH at two positions in the column: just after the injection and close to the exit of the column.

Among the experiments conducted for this thesis, the results of six experiments are presented in this manuscript. The first experiment, conducted on the first experimental bench, lasted the longest with a duration close to 100 d. This experiment investigated both the effects of dissolution and precipitation on the geo-electrical signatures using alternatively SP and SIP acquisition. It showed that the ionic concentration gradients induced by the injection of reactive solution in the column generated clear SP transient signal related to the electro-diffusive potential. In order to mechanistically describe and quantify this phenomenon, I developed a new theoretical framework that combines 1D reactive transport modeling and a new petrophysical relationship that I developed for multi-species reactive systems. The results of this numerical framework reproduce nicely the measured SP signals for both dissolution and precipitation. Thus, this approach is very promising for the use of SP monitoring of reactive transport. The reactive transport simulation however showed that the reactive zone was located at the entrance of the column and thus did not reach the part of the column equipped with

the measuring electrodes. This limitation of the column design could explain why SIP results did not present variations related to mineral and solution interactions.

Based on the first experiment limitations, I defined the objectives of a series of new experiments, conducted on the second experimental bench and constituting shorter and more focused tests, using a single geo-electrical acquisition method between SP and SIP and focusing on a single process between dissolution and precipitation. Thus, various experimental conditions could be tested to highlight their influence on the geo-electrical signatures. First, I investigated further the SP response to calcite dissolution by changing the location of the inlet solution injection compared to the location of the measuring electrodes in the column. By analyzing and comparing the SP signals to the results from the pH, the pore water electrical conductivity, and the chemical analyses of the samples of outlet pore water, I was able to differentiate the SP signature of the reactive zone from the one of the non-reactive zone. Then, I compared the effect of using buffered solution of weak acid instead of strong acid at the same pH but at different concentrations. I thus used one concentrated buffer and one diluted buffer. I observed contrasted results from these experiments, but the main result is that the reactive zone is larger when using a buffered solution and this can be correlated to the SP signal analysis. Since I did not find results of SIP monitoring of calcite dissolution in the literature and that I did not observe any SIP signal related to this process when I performed laboratory experiments of calcite dissolution using different inlet acid solutions, I rather focused on studying calcite precipitation monitored with SIP method in order to compare my results to the one available in the literature. While I used experimental conditions as close as possible to those presented in the literature and for which a SIP signal clearly related to calcite precipitation had been identified, I did not observe a similar SIP response. These SIP results are thus in contradiction with the common explanation which relates the amplitude of the polarization to grain size distribution. It is possible that the absence of this SIP signature is related to the different crystallization mechanisms documented in the literature and which show that the nature of the porous matrix initially present in the medium can condition the appearance of certain ephemeral phases that would be more or less capable of polarization.

In view of my thesis works, it appears first of all that the conclusions on the experimental results, which are currently only based on the qualitative analysis of laboratory measurements, must be compared with mechanistic models, in particular for the experiments of SP monitoring of calcite dissolution, in order to confirm these interpretations. Of course another perspective would be to study the impact of the variation of experimental conditions whose influence has not yet been tested. As such, the influence of the calcite matrix could give interesting results by testing for example different grain size distributions. It also seems important to validate the results of the literature by using a porous matrix similar to those used for the SIP monitoring of calcite precipitation instead of calcite grains. Nevertheless, the understanding of the source mechanisms of the SIP signal seems difficult to grasp at the REV scale. This comes first from the complexity of the medium at this scale, but it is especially due to that mineral-solution interactions involve microscopic surface processes. Therefore, the enhancement of the SIP signal understanding could be achieved through experimental development of geo-electrical monitoring at smaller scales using microfluidic devices and high-resolution imaging techniques.

Bibliography

Abdulsamad, F., N. Florsch, M. Schmutz, and C. Camerlynck (2016). "Assessing the high frequency behavior of non-polarizable electrodes for spectral induced polarization measurements". In: *Journal of Applied Geophysics* 135, pp. 449–455. DOI: 10.1016/j.jappgeo.2016.01.001.

Adler, A. and W. R. L. Lionheart (2006). "Uses and abuses of eidors: An extensible software base for eit". In: *Physiological Measurement* 27 (5), pp. 25–42. DOI: 10.1088/0967-3334/27/5/S03.

Adler, P. (1992). *Porous Media: Geometry and Transport*. Ed. by H. Brenner. 1st ed., p. 560. DOI: 10.1016/C2009-0-26183-6.

Adler, P. M. and JF. Thovert (1998). "Real porous media: Local geometry and macroscopic properties". In: *Applied Mechanics Reviews* 51 (9), pp. 537–585. DOI: 10.1115/1.3099022.

Archie, G. E. (1942). "The electrical resistivity log as an aid in determining some reservoir characteristics". In: *Transactions of the AIME* 146 (1), pp. 54–62. DOI: 10.2118/942054-G.

Arora, T., N. Linde, A. Revil, and J. Castermant (2007). "Non-intrusive characterization of the redox potential of landfill leachate plumes from self-potential data". In: *Journal of Contaminant Hydrology* 92 (3), pp. 274–292. DOI: 10.1016/j.jconhyd.2007.01.018.

Arrhenius, S. (1903). "Development of the theory of electrolytic dissociation". In: *Nobel Lecture*.

Atkins, P. W. and J. de Paula (2006). "Molecules in motion". In: *Atkins' Physical chemistry*. Ed. by W. H. Freeman and Company New York. 8th ed. Oxford University Press, pp. 747–790.

Bachmat Y., Bear J. (1987). "On the concept and size of a representative elementary volume (REV)". In: *Advances in transport phenomena in porous media*. Ed. by Corapcioglu M. Y. Bear J. Vol. 128. Springer, Dordrecht, pp. 3–20. DOI: 10.1007/978-94-009-3625-6_1.

Baek, S. H., J. W. Hong, K. Y. Kim, S. Yeom, and T. H. Kwon (2019). "X-Ray Computed Microtomography Imaging of Abiotic Carbonate Precipitation in Porous Media From a Supersaturated Solution: Insights Into Effect of CO2 Mineral Trapping on Permeability". In: *Water Resources Research* 55 (5), pp. 3835–3855. DOI: 10.1029/2018WR023578.

Bakalowicz, M. (1979). “Contribution de la géochimie des eaux à la connaissance de l’aquifère karstique et de la karstification”. Université Paris VI, p. 257.

Bakalowicz, M. and N. Dörfliger (2005). *Karst water resources: a stake for the Mediterranean basin*. Vol. 2, pp. 26–31.

Baker, R. O., H. W. Yarranton, and J. L. Jensen (2015). “7 - Conventional Core Analysis–Rock Properties”. In: *Practical Reservoir Engineering and Characterization*. Ed. by R. O. Baker, H. W. Yarranton, and J. L. Jensen. Boston: Gulf Professional Publishing, pp. 197–237. DOI: 10.1016/B978-0-12-801811-8.00007-9.

Banavar, J.R. and D.L. Johnson (1987). “Characteristic pore sizes and transport in porous media”. In: *Physical Review B* 35 (13), pp. 7283–7286. DOI: 10.1103/PhysRevB.35.7283.

Banavar, J.R. and L.M. Schwartz (1987). “Magnetic resonance as a probe of permeability in porous media”. In: *Physical Review Letters* 58 (14), pp. 1411–1414. DOI: 10.1103/PhysRevLett.58.1411.

Barker, S. (2016). “Dissolution of Deep-Sea Carbonates”. In: *Reference Module in Earth Systems and Environmental Sciences*. Elsevier. DOI: 10.1016/B978-0-12-409548-9.09717-7.

Bear, J. (2013). *Dynamics of fluids in porous media*. Courier Corporation.

Ben Clennell, M. (1997). “Tortuosity: a guide through the maze”. In: *Developments in Petrophysics, Geological Society of London Special Publication* 122, pp. 299–344. DOI: 10.1144/GSL.SP.1997.122.01.18.

Bernabé, Y. and A. Maineult (2015). *Physics of porous media: fluid flow through porous media*. 2nd ed. Oxford: Elsevier, in Schubert G., Treatise on geophysics, pp. 19–41. DOI: 10.1016/B978-0-444-53802-4.00188-3.

Bigalke, J. and E. W. Grabner (1997). “The Geobattery model: a contribution to large scale electrochemistry”. In: *Electrochimica Acta* 42 (23), pp. 3443–3452. ISSN: 0013-4686. DOI: 10.1016/S0013-4686(97)00053-4.

Binley, A., S. S. Hubbard, J. A. Huisman, A. Revil, D. A. Robinson, K. Singha, and L. D. Slater (2015). “The emergence of hydrogeophysics for improved understanding of subsurface processes over multiple scales”. In: *Water Resour. Res.* 51, pp. 3837–3866. DOI: 10.1002/2015WR017016.

Binley, A. and A. Kemna (2005a). “DC resistivity and induced polarization methods”. In: *Hydrogeophysics*. Ed. by Y. Rubin and S. S. Hubbard. Springer, pp. 129–156. DOI: 10.1016/B978-0-444-53802-4.00188-3.

— (2005b). “DC resistivity and induced polarization methods”. In: *Hydrogeophysics*. Ed. by Y. Rubin and S.S. Hubbard. Vol. 50. Water Science and Technology Library. Springer, Dordrecht, pp. 129–156. DOI: 10.1007/1-4020-3102-5_5.

Bolève, A., A. Crespy, A. Revil, F. Janod, and J. L. Mattiuzzo (2007). “Streaming potentials of granular media: influence of the Dukhin and Reynolds numbers”. In: *Journal of Geophysical Research* 112 (B8). DOI: 10.1029/2006JB004673.

Börner, F. D. and J. H. Schön (1991). “A relation between the quadrature component of electrical conductivity and the specific surface area of sedimentary rocks”. In: *The Log Analyst* 32 (5), pp. 612–613.

Bouissonnié, A., D. Daval, M. Marinoni, and P. Ackerer (2018). “From mixed flow reactor to column experiments and modeling: Upscaling of calcite dissolution rate”. In: *Chemical Geology* 487, pp. 63–75. DOI: 10.1016/j.chemgeo.2018.04.017.

Broadbent, S. R. and J. M. Hammersley (1957). “Percolation processes: I. Crystals and mazes”. In: *Mathematical Proceedings of Cambridge Philosophical Society* 53 (3), pp. 629–641. DOI: 10.1017/S0305004100032680.

Bücker, M., A. Flores Orozco, S. Undorf, and A. Kemna (2019). “On the Role of Stern- and Diffuse-Layer Polarization Mechanisms in Porous Media”. In: *Journal of Geophysical Research: Solid Earth* 124 (6), pp. 5656–5677. DOI: 10.1029/2019JB017679.

Bucker, M. and A. Hördt (2013). “Analytical modelling of membrane polarization with explicit parametrization of pore radii and the electrical double layer”. In: *Journal Geophysical Research* 194 (2), pp. 804–813. DOI: 10.1093/gji/ggt136.

Buckerfield, S. J., R. S. Quilliam, L. Bussiere, S. Waldron, L. A. Naylor, S. Li, and D. M. Oliver (2020). “Chronic urban hotspots and agricultural drainage drive microbial pollution of karst water resources in rural developing regions”. In: *Science of The Total Environment* 744, p. 140898. DOI: 10.1016/j.scitotenv.2020.140898.

Burchette, T. P. (2012). “Carbonate rocks and petroleum reservoirs: a geological perspective from the industry”. In: *Geological Society, London, Special Publications* 370 (1), pp. 17–37. DOI: 10.1144/SP370.14.

Bussian, A. E. (1983). “Electrical conductance in a porous medium”. In: *Geophysics* 48 (9), pp. 1258–1268. DOI: 10.1190/1.1441549.

Carman, P. C. (1939). “Permeability of saturated sands, soils and clays”. In: *The Journal of Agricultural Science* 29 (2), pp. 263–273. DOI: 10.1017/S0021859600051789.

Chakraborty, P. and S. D. Bhabani (2018). “Measurement and modeling of longitudinal dispersivity in undisturbed saturated soil: an experimental approach”. In: *Soil Science Society of America Journal* 83 (5), pp. 1117–1123. DOI: 10.2136/sssaj2018.05.0176.

Chalikakis, K. (2006). “Application de méthodes géophysiques pour la reconnaissance et la protection de ressources en eau dans les milieux karstiques”. Université Pierre et Marie Curie - Paris VI.

Chalikakis, K., V. Plagnes, R. Guerin, R. Valois, and F. P. Bosch (2011). "Contribution of geophysical methods to karst-system exploration: an overview". In: *Hydrogeol. J.* 19 (6), pp. 1169–1180. DOI: 10.1007/s10040-011-0746-x.

Chelidze, T. L. and Y. Gueguen (1999). "Electrical spectroscopy of porous rocks: a review-I. Theoretical models". In: *Geophysical Journal International* 137 (1), pp. 1–15. DOI: 10.1046/j.1365-246x.1999.00799.x.

Chen, Z., N. Goldscheider, A. S. Auler, and M. Bakalowicz (2017). *The World karst aquifer mapping project: concept, mapping procedure and map of Europe*. DOI: 10.1007/s10040-016-1519-3.

Cherubini, A., B. Garcia, A. Cerepi, and A. Revil (2019). "Influence of CO_2 on the electrical conductivity and streaming potential of carbonate rocks". In: *Journal of Geophysical Research: Solid Earth* 124 (10), pp. 10056–10073. DOI: 10.1029/2018JB017057.

Chhabra, R. P. and J. F. Richardson (2008). "Particulate systems". In: *Non-Newtonian Flow and Applied Rheology*. Ed. by R. P. Chhabra and J. F. Richardson. 2nd ed. Oxford: Butterworth-Heinemann. Chap. 5, pp. 249–315. DOI: 10.1016/B978-0-7506-8532-0.00005-6.

Choi, J., S. M. Hulseapple, M. H. Conklin, and J. W. Harvey (1998). "Modeling CO2 degassing and pH in a stream–aquifer system". In: *Journal of Hydrology* 209, pp. 297–310. DOI: 10.1016/S0022-1694(98)00093-6.

Clennell, M. B. (1997). "Tortuosity: a guide through the maze". In: *Geological Society* 122 (1), pp. 299–344. DOI: 10.1144/GSL.SP.1997.122.01.18.

Cohen, E. R., T. Cvitaš, J. G. Frey, B. Holmström, K. Kuchitsu, R. Marquardt, I. Mills, F. Pavese, M. Quack, J. Stohner, H. L. Strauss, M. Takami, and A. J. Thor (2007). *Quantities, units and symbols in physical chemistry*. 3rd ed. Cambridge: Royal Society of Chemistry.

Collett, L. S. (1990). "History of induced polarization method". In: *Induced polarization: Applications and Case Histories*. Ed. by J. B. Fink, B. K. Sternberg, W. G. Widuwilt, and S. H. Ward. Investigations in Geophysics. Chap. 1, pp. 5–22. DOI: 10.1190/1.9781560802594.ch1.

Comiti, J. and M. Renaud (1989). "A new model for determining mean structure parameters of fixed beds from pressure drop measurements: Application to beds packed with parallelepipedal particles". In: *Chemical Engineering Science* 44 (7), pp. 1539–1545. DOI: 10.1016/0009-2509(89)80031-4.

Connor, N. (2019). *What is Reynolds Number – Definition*. Thermal Engineering. URL: https://www.thermal-engineering.org/what-is-reynolds-number-definition/.

Currie, J. A. (1960). "Gaseous diffusion in porous media. Part 2. - Dry granular materials". In: *British Journal of Applied Physics* 11 (8), pp. 318–324. DOI: 10.1088/0508-3443/11/8/303.

Daccord, G., R. Lenormand, and O. Liétard (1993). “Chemical dissolution of a porous medium by a reactive fluid—I. Model for the “wormholing” phenomenon”. In: *Chemical Engineering Science* 48 (1), pp. 169–178. DOI: 10.1016/0009-2509(93)80293-Y.

Daily, W., A. Ramirez, D. Labrecque, and J. Nitao (1992). “Electrical resistivity tomography of vadose water movement”. In: *Water Resources Research* 28 (5), pp. 1429–1442. DOI: 10.1029/2009JG001129.

Darcy, H. (1856). *Les fontaines publiques de la ville de Dijon. Exposition et application des principes à suivre et des formules à employer dans les questions de distribution d'eau*. Victor Dalmont.

de Marsily, G. (1986). *Quantitative Hydrogeology: Groundwater Hydrology for Engineers*. 2nd ed. Paris School of Mines, Fontainebleau, p. 440.

de Yoreo, J. J., G. U. A. P A. Gilbert, N. A. J. M. Sommerdijk, R. L. Penn, S. Whitelam, D. Joester, H. Zhang, J. D. Rimer, A. Navrotsky, J. F. Banfield, A. F. Wallace, F. M. Michel, F. C. Meldrum, H. Cölfen, and P. M. Dove (2015). “Crystallization by particle attachment in synthetic, biogenic, and geologic environments”. In: *Science* 349 (6247). DOI: 10.1126/science.aaa6760.

Drew, D., P. E. Lamoreaux, C. Coxon, J. W. Wess, L. D. Slattery, A. P. Bosch, and H. Hötzl (2017). *Karst hydrogeology and human activities: impacts, consequences and implications: IAH international contributions to hydrogeology 20*. 5th ed. London: Drew, D. and Hötzl, H., p. 338. DOI: 10.1201/9780203749692.

East, G. A. and M. A. del Valle (2000). “Easy-to-Make Ag/AgCl Reference Electrode”. In: *Journal of Chemical Education* 77 (1), p. 97. DOI: 10.1021/ed077p97.

Edwards, L. S. (1977). “A modified pseudosection for resistivity and IP”. In: *Geophysics* 42 (5), pp. 1020–1036. DOI: 10.1190/1.1440762.

Ellis, M. H., M. C. Sinha, Minshull T. A., J. Sothcott, and Best A. I. (2010). “An anisotropic model for the electrical resistivity of two-phase geologic materials”. In: *Geophysics* 75 (6), E161–E170. DOI: 10.1190/1.3483875.

Fernandez-Martinez, A., Y. Hu, B. Lee, YS. Jun, and G. A. Waychunas (2013). “In Situ Determination of Interfacial Energies between Heterogeneously Nucleated CaCO3 and Quartz Substrates: Thermodynamics of CO2 Mineral Trapping”. In: *Environmental Science and Technology* 47, pp. 102–109. DOI: 10.1021/es3014826.

Fick, A. (1855). “Über Diffusion”. In: *Annalen der Physik* 170 (1), pp. 59–86. DOI: 10.1002/andp.18551700105.

Fitts, C. R. (2013). “Groundwater Contamination”. In: *Groundwater Science*. Ed. by C. R. Fitts. 2nd ed. Boston: Academic Press. Chap. 11, pp. 499–585. DOI: 10.1016/B978-0-12-384705-8.00011-X.

Foucault, A., JF. Raoult, F. Cecca, and B. Platevoet (2014). *Dictionnaire de Géologie*. Ed. by brgmédi-tions. 8th ed. Dunod.

Fox, R. W. and D. Gilbert (1830). "On the Electro-Magnetic Properties of Metalliferous Veins in the Mines of Cornwall". In: *Philosophical Transactions of the Royal Society of London* 120, pp. 399–414. DOI: 10.1098/rstl.1830.0027.

Friedman, S. P. (2005). "Soil properties influencing apparent electrical conductivity: a review". In: *Computers and Electronics in Agriculture* 46 (1-3), pp. 45–70. DOI: 10.1016/j.compag.2004.11.001.

Friedman, S.P. and D.A. Robinson (2002). "Particle shape characterization using angle of repose measurements for predicting the effective permittivity and electrical conductivity of saturated granular media". In: *Water Resources Research* 38 (11), p. 1236. DOI: 10.1029/2001WR000746.

Gal, A., W. Habraken, D. Gur, P. Fratzl, S. Weiner, and L. Addadi (2013). "Calcite Crystal Growth by a Solid-State Transformation of Stabilized Amorphous Calcium Carbonate Nanospheres in a Hydrogel**". In: *Angewandte Chemie International Edition* 52, pp. 4867–5870. DOI: 10.1002/anie.201210329.

Garcia-Rios, M., J. Cama, L. Luquot, and J. M. Soler (2014). "Interaction between CO2-rich sulfate solutions and carbonate reservoir rocks from atmospheric to supercritical CO2 conditions: Experiments and modeling". In: *Chemical Geology* 383, pp. 107–122. DOI: 10.1016/j.chemgeo.2014.06.004.

Garing, C., L. Luquot, P. A. Pezard, and P. Gouze (2014). "Electrical and flow properties of highly heterogeneous carbonate rocks". In: *AAPG Bulletin* 98 (1), pp. 49–66. DOI: 10.1306/05221312134.

Ghanbarian, B. (2020). "Applications of critical path analysis to uniform grain packings with narrow conductance distributions: I. Single-phase permeability". In: *Advances in Water Resources* 137, p. 103529. DOI: 10.1016/j.advwatres.2020.103529.

Ghanbarian, B., A.G. Hunt, R.P. Ewing, and M. Sahimi (2013). "Tortuosity in Porous Media: A Critical Review". In: *Soil Sci. Soc. Am. J.* 77, pp. 1461–1477. DOI: 10.2136/sssaj2012.0435.

Ghorbani, A. (2007). "Contribution au développement de la résistivité complexe et à ses applications en environnement".

Ghosh, U., T. Le Borgne, D. Jougnot, N. Linde, and Y. Méheust (2018). "Geoelectrical signatures of reactive mixing: a theoretical assessment". In: *Geophysical Research Letters* 45 (8), pp. 3489–3498. DOI: 10.1002/2017GL076445.

Glover, P. W. J. (2015). *Geophysical properties of the near surface earth: electrical properties*. Treatise on Geophysics, pp. 89–137. DOI: 10.1016/B978-0-444-53802-4.00189-5.

Glover, P. W. J. and N. Déry (2010). “Streaming potential coupling coefficient of quartz glass bead packs: Dependence on grain diameter, pore size, and pore throat radius”. In: *Geophysics* 75 (6), F225–F241. DOI: 10.1190/1.3509465.

Glover, P.W., I.I. Zadjali, and K.A. Frew (2006). “Permeability prediction from MICP and NMR data using an electrokinetic approach”. In: *Geophysics* 71 (4), F49–F60. DOI: 10.1190/1.2216930.

Goldscheider, N., J. Meiman, M. Pronk, and C. Smart (2008). “Tracer tests in karst hydrogeology and speleology”. In: *International Journal of speleology* 37 (1), pp. 27–40. DOI: 10.5038/1827-806X.37.1.3.

Golfier, F., C. Zarcone, B. Bazin, R. Lenormand, D. Lasseux, and M. Quintard (2002). “On the ability of a Darcy-scale model to capture wormhole formation during the dissolution of a porous medium”. In: *Journal of fluid Mechanics* 457, pp. 213–254. DOI: 10.1017/S0022112002007735.

Graham, M. T., DJ. MacAllister, J. Vinogradov, M. D. Jackson, and A. P. Butler (2018). “Self-potential as a predictor of seawater intrusion in coastal groundwater boreholes”. In: *Water Resources Research* 54 (9), pp. 6055–6071. DOI: 10.1029/2018WR022972.

Gregory, T. M., L. C. Chow, and C. M. Carey (1991). “A Mathematical Model for Dental Caries: A Coupled Dissolution-Diffusion Process”. In: *Journal of Research of the National Institute of Standards and Technology* 96 (5), pp. 593–604. DOI: 10.6028/jres.096.035.

Guarracino, L. and D. Jougnot (2018). “A physically based analytical model to describe effective excess charge for streaming potential generation in water saturated porous media”. In: *Journal of Geophysical Research* 123 (1), pp. 52–65. DOI: 10.1002/2017JB014873.

Guarracino, L., T. Rötting, and J. Carrera (2014). “A fractal model to describe the evolution of multiphase flow properties during mineral dissolution”. In: *Advances in Water Resources* 67, pp. 78–86. DOI: 10.1029/WR024i004p00566.

Guéguen, Y. and V. Palciauskas (1994). *Introduction to the Physics of Rocks*. Princeton University Press.

Guggenheim, E. A. (1930). “A study of cells with liquid-liquid junctions”. In: *Journal of the American Chemical Society* 52 (4), pp. 1315–1337. DOI: 10.1021/ja01367a004.

Guichet, X., L. Jouniaux, and N. Catel (2006). “Modification of streaming potential by precipitation of calcite in a sand–water system: laboratory measurements in the pH range from 4 to 12”. In: *Geophysical Journal International* 166 (1), pp. 445–460. DOI: 10.1111/j.1365-246X.2006.02922.x.

Gulamali, M. Y., E. Leinov, and M. D. Jackson (2011). “Self-potential anomalies induced by water injection into hydrocarbon reservoirs”. In: *Geophysics* 76 (4), F283–F292. DOI: 10.1190/1.3596010.

Halisch, M., S. Hupfer, A. Weller, R. Dlugosch, and H. P. Plumhoff (2018). “An experimental setup for the assessment of effects of carbonate rock dissolution on complex electrical conductivity

spectra". In: *Annual Symposium of the Society of Core Analysts (SCA) Proceedings, Trondheim, Norway*, SCA2018–051.

Hamamoto, S., P. Moldrup, K. Kawamoto, and T. Komatsu (2010). "Excluded-volume expansion of Archie's law for gas and solute diffusivities and electrical and thermal conductivities in variably saturated porous media". In: *Water Resources Research* 46, W06514. DOI: 10.1029/2009WR008424.

Hayashi, M. (2004). "Temperature-electrical conductivity relation of water for environmental monitoring and geophysical data inversion". In: *Environmental monitoring and assessment* 96 (1-3), pp. 119–128. DOI: 10.1023/B:EMAS.0000031719.83065.68.

Henderson, P (1907). "The thermodynamics of liquid cells". In: *Zeitschrift für Physikalische Chemie* 59, pp. 118–127.

Hoefner, M. L. and H. S. Fogler (1988). "Pore evolution and channel formation during flow and reaction in porous media". In: *AIChE Journal* 34 (1), pp. 45–54. DOI: 10.1002/aic.690340107.

Holzer, L., D. Wiedenmann, B. Münch, L. Keller, M. Prestat, Ph. Gasser, Robertson I., and B. Grobéty (2013). "The influence of constrictivity on the effective transport properties of porous layers in electrolysis and fuel cells". In: *Journal of Materials Science* 48, pp. 2934–2952. DOI: 10.1007/s10853-012-6968-z.

Hu, Q, M. H. Nielsen, C. L. Freeman, L. M. Hamm, J. Tao, J. R. I. Lee, T. YJ. Han, U. Becker, J. H. Harding, P. M. Dove, et al. (2012). "The thermodynamics of calcite nucleation at organic interfaces: Classical vs. non-classical pathways". In: *Faraday Discussions* 159 (1), pp. 509–523. DOI: 10.1039/C2FD20124K.

Hubbard, S. S. and N. Linde (2011). "Hydrogeophysics". In: *Treatise on Water Science*. Ed. by P. Wilderer. 1st ed. Vol. 2. 4 vols. Elsevier. Chap. 15.

Huisman, J. A., E. Zimmermann, O. Esser, FH. Haegel, A. Treichel, and H. Vereecken (2016). "Evaluation of a novel correction procedure to remove electrode impedance effects from broadband SIP measurements". In: *Journal of Applied Geophysics* 135, pp. 466–473. DOI: 10.1016/j.jappgeo.2015.11.008.

Hunt, A., R. Ewing, and B. Ghanbarian (2014). *Percolation theory for flow in porous media*. Springer.

Hunter, R. J. (1981). *Zeta potential in colloid science: principles and applications*. Vol. 2. Academic Press London, p. 391. DOI: 10.1016/C2013-0-07389-6.

Hupfer, S., M. Halisch, and A. Weller (2017). "Using low frequency electrical impedance spectroscopy for an enhanced pore space characterization and assessment of carbonates". In: *Proceedings of the International Symposium of the Society of Core Analysts, 27–30 August 2017* (Vienna, Austria), pp. 1–8.

Izumoto, S. (2021). “Spectral induced polarization of calcite precipitation in porous media”. PhD thesis. Fakultät Bau- und Umweltingenieurwissenschaften der Universität Stuttgart.

Izumoto, S., J. A. Huisman, Y. Wu, and H. Vereecken (2020a). “Effect of solute concentration on the spectral induced polarization response of calcite precipitation”. In: *Geophysical Journal International* 220, pp. 1187–1196. DOI: 10.1093/gji/ggz515.

Izumoto, S., J. A. Huisman, Y. Zimmermann E.and Meheust, F. Gomez, H. Tabuteau, J. Heyman, R. Laniel, H. Vereecken, and T. Le Borgne (2020b). “Spectral induced polarization of calcite precipitation: 2D experimental pore scale observation”. In: *Zenodo*. DOI: 10.5281/zenodo.4039598.

Janata, J. (2009). *Principles of Chemical Sensors*. 2nd ed. Springer US, p. 373. DOI: 10.1007/b136378.

Jardani, A., J. P. Dupont, and A. Revil (2006). “Self-potential signals associated with preferential groundwater flow pathways in sinkholes”. In: *Journal of Geophysical Research* 111 (B9), B09204. DOI: 10.1029/2005JB004231.

Jeannin, P., M. Hessenauerb, A. Malarda, and V. Chapuis (2016). “Impact of global change on karst groundwater mineralization in theJura Mountains”. In: *Science of the Total Environment* 541 (4), pp. 1208–1221. DOI: 10.1016/j.scitotenv.2015.10.008.

Johansson, S., A. Lindskog, G. Fiandaca, and T. Dahlin (2020). “Spectral induced polarization of limestones: time domain field data, frequency domain laboratory data and physicochemical rock properties”. In: *Geophysical Journal International* 220 (2), pp. 928–950. DOI: 10.1093/gji/ggz504.

Johnson, D. L. and P. N. Sen (1988). “Dependence of the conductivity of a porous medium on electrolyte conductivity”. In: *Physical Review B* 37 (7), p. 3502. DOI: 10.1103/PhysRevB.37.3502.

Johnson, D.L., J. Koplik, and L.M. Schwartz (1986). “New pore-size parameter characterizing transport in porous media”. In: *Physical Review Letters* 57 (20), pp. 2564–2567.

Jougnot, D. (2009). “Geophysical study of transfert phenomena in the Callovo-Oxfordian argillites under partial water saturation: application to the EDZ of the Bure Site”. French. Chambéry, France: University of Savoie, p. 327.

Jougnot, D., A. Ghorbani, A. Revil, P. Leroy, and P. Cosenza (2010a). “Spectral induced polarization of partially saturated clay-rocks: a mechanistic approach”. In: *Geophysical Journal International* 180 (1), pp. 210–224. DOI: 10.1111/j.1365-246X.2009.04426.x.

Jougnot, D., J. Jiménez-Martínez, R. Legendre, T. Le Borgne, Y. Méheust, and N. Linde (2018). “Impact of small-scale saline tracer heterogeneity on electrical resistivity monitoring in fully and partially saturated porous media: Insights from geoelectrical milli-fluidic experiments”. In: *Advances in Water Resources* 113, pp. 295–309. DOI: 10.1016/j.advwatres.2018.01.014.

Jougnot, D. and N. Linde (2013). “Self-Potentials in Partially Saturated Media: The Importance of Explicit Modeling of Electrode Effects”. In: *Vadose Zone Journal* 12 (2), pp. 1–21. DOI: 10.2136/vzj2012.0169.

Jougnot, D., A. Mendieta, P. Leroy, and A. Maineult (2019). “Exploring the effect of the pore size distribution on the streaming potential generation in saturated porous media, insight from pore network simulations”. In: *Journal of Geophysical Research: Solid Earth* 124 (6), pp. 5315–5335. DOI: 10.1029/2018JB017240.

Jougnot, D., A. Revil, and P. Leroy (2009). “Diffusion of ionic tracers in the Callovo-Oxfordian clayrock using the Donnan equilibrium model and the formation factor”. In: *Geochimica et Cosmochimica Acta* 73 (10), pp. 2712–2726. DOI: 10.1016/j.gca.2009.01.035.

Jougnot, D., A. Revil, N. Lu, and A. Wayllace (2010b). “Transport properties of the Callovo-Oxfordian clayrock under partially saturated conditions”. In: *Water Resources Research* 46 (8), W08514. DOI: 10.1029/2009WR008552.

Jougnot, D., D. Roubinet, L. Guarracino, and A. Maineult (2020). “Modeling streaming potential in porous and fractured media, description and benefits of the effective excess charge density approach”. In: *Advances in Modeling and Interpretation in Near Surface Geophysics*. Ed. by A. Biswas and S. P. Sharma. Springer Geophysics. Springer. Chap. 4, pp. 61–96. DOI: 10.1007/978-3-030-28909-6_4.

Jouniaux, L., A. Maineult, V. Naudet, M. Pessel, and P. Sailhac (2009). “Review of self-potential methods in hydrogeophysics”. In: *Compte Rendu Geoscience* 341 (10-11), pp. 928–936. DOI: 10.1016/j.crte.2009.08.008.

Jozja, N., P. Maget, C. Défarge, C. Mouget, A. Pidon, S. Prod’Homme, K. Rousseil, J. Munerot, and A. Dufour (2010). “Apport des traçages à la connaissance du système karstique du Val d’Orléans. Historique et nouvelles avancées.” In: *Géologues* 167, pp. 1–5.

Kačaroğlu, F. (1999). “Review of Groundwater Pollution and Protection in Karst Areas”. In: *Water, Air, and Soil Pollution* 113, pp. 337–356. DOI: 10.1016/j.earscirev.2017.04.016.

Kaouane, C. (2015). “SIP Fuchs III versus PSIP : an user review”. In: DOI: 10.13140/RG.2.1.4055.9446.

Kaufmann, O. and J. Deceuster (2014). “Detection and mapping of ghost-rock features in the Tournaisis area through geophysical methods – an overview”. In: *Geol. Belg.* 17 (1), pp. 17–26.

Kemna, A., A. Binley, G. Cassiani, E. Niederleithinger, A. Revil, L. D. Slater, K. H. Williams, A. F. Orozco, F. H. Haegel, A. Hördt, S. Kruschwitz, V. Leroux, K. Titov, and E. Zimmermann (2012). “An overview of the spectral induced polarization method for near-surface applications”. In: *Near Surface Geophysics* 6, pp. 453–468. DOI: 10.3997/1873-0604.2012027.

Kennedy, W. D. and D. C. Herrick (2012). "Conductivity models for archie rocks". In: *Geophysics* 77 (3), pp. 109–128. DOI: 10.1190/GEO2011-0297.1.

Kessouri, P., A. Furman, J. A. Huisman, T. Martin, A. Mellage, D. Ntarlagiannis, M. Bücker, S. Ehosioke, P. Fernandez, A. Flores-Orozco, A. Kemna, F. Nguyen, T. Pilawski, Saneiyan, M. S. Schmutz, N. Schwartz, M. Weigand, Y. Wu, C. Zhang, and E. Placencia-Gomez (2019). "Induced polarization applied to biogeophysics: recent advances and future prospects". In: *Near Surface Geophysics* 17 (6-Recent Developments in Induced Polarization), pp. 595–621. DOI: 10.1002/nsg.12072.

Ketterings, Q. M., S. Reid, and R. Rao (2007). "Cations and Cation Exchange Capacity". In: *Fact sheets*. Ed. by College of Agriculture, Department of Crop Life Sciences, and Soil Sciences. Cornell University. Chap. 22.

Kjoller, C., L. Sigalas, H. F. Christensen, and M. Minde (2016). "A fast method for homogeneous dissolution of chalk specimens for laboratory experiments – documentation by X-ray CTscanning and scanning electron microscopy". In: *Annual Symposium of the Society of Core Analysts (SCA) Proceedings, Snowmass, USA*, SCA2016–072.

Kormiltsev, V. V., A. N. Ratushnyak, and V. A. Shapiro (1998). "Three-dimensional modeling of electric and magnetic fields induced by the fluid flow movement in porous media". In: *Physics of the earth and planetary interiors* 105 (3), pp. 109–118. DOI: 10.1016/S0031-9201(97)00116-7.

Kyi, A.A. and B. Batchelor (1994). "An electrical conductivity method for measuring the effects of additives on effective diffusivities in Portland cement pastes". In: *Cement and Concrete Research* 24 (4), pp. 752–764. DOI: 10.1016/0008-8846(94)90201-1.

Lassin, A., L. André, N. Devau, A. Lach, T. Beuvier, A. Gibaud, S. Gaboreau, and M. Azaroual (2018). "Dynamics of calcium carbonate formation: Geochemical modeling of a two-step mechanism". In: *Geochimica et Cosmochimica Acta* 240, pp. 236–254. DOI: 10.1016/j.gca.2018.08.033.

Leinov, E. and M. D. Jackson (2014). "Experimental measurements of the SP response to concentration and temperature gradients in sandstones with application to subsurface geophysical monitoring". In: *Journal of Geophysical Research: Solid Earth* 119 (9), pp. 6855–6876. DOI: 10.1002/2014JB011249.

Leroy, P., S. Li, A. Revil, and Y. Wu (2017). "Modelling the evolution of complex conductivity during calcite precipitation on glass beads". In: *Geophysical Journal International* 209 (1), pp. 123–140. DOI: 10.1093/gji/ggx001.

Leroy, P. and A. Revil (2004). "A triple layer model of the surface electrochemical properties of clay minerals". In: *Journal of Colloid Interface Sciences* 270, pp. 371–380. DOI: 10.1016/j.jcis.2003.08.007.

Leroy, P. and A. Revil (2009). “A mechanistic model for the spectral induced polarization of clay materials”. In: *Journal of Geophysical Research: Solid Earth* 114 (B10). DOI: 10.1029/2008JB006114.

Leroy, P., A. Revil, and D. Coelho (2006). “Diffusion of ionic species in bentonite”. In: *Journal of Colloid and Interface Science* 296 (1), pp. 248–255. DOI: 10.1016/j.jcis.2005.08.034.

Lesmes, D. P. and K. M. Frye (2001). “Influence of pore fluid chemistry on the complex conductivity and induced polarization responses of Berea sandstone”. In: *Journal of Geophysical Research: Solid Earth* 106 (B3), pp. 4079–4090. DOI: 10.1029/2000JB900392.

Lesmes, D. P. and F. D. Morgan (2001). “Dielectric spectroscopy of sedimentary rocks”. In: *Journal of Geophysical Research: Solid Earth* 106 (B7), pp. 13329–13346. DOI: 10.1029/2000JB900402.

Lévy, L., B. Gibert, F. Sigmundsson, D. Deldicque, F. Parat, and G. P. Hersir (2019). “Tracking Magmatic Hydrogen Sulfur Circulations Using Electrical Impedance: Complex Electrical Properties of Core Samples at the Krafla Volcano, Iceland”. In: *Journal of Geophysical Research: Solid Earth* 124 (3), pp. 2492–2509. DOI: 10.1029/2018JB016814.

Li, S., P. Leroy, F. Heberling, N. Devau, D. Jougnot, and C. Chiaberge (2016). “Influence of surface conductivity on the apparent zeta potential of calcite”. In: *Journal of Colloid and Interface Science* 468, pp. 262–275. DOI: 10.1016/j.jcis.2016.01.075.

Liñán Baena, C., B. Andreo, J. Mudry, and F. Carrasco Cantos (2009). “Groundwater temperature and electrical conductivity as tools to characterize flow patterns in carbonate aquifers: The Sierra de las Nieves karst aquifer, southern Spain”. In: *Hydrogeology Journal* 17 (4), pp. 843–853. DOI: 10.1007/s10040-008-0395-x.

Linde, N., A. Binley, A. Tryggvason, L. B. Pedersen, and A. Revil (2006). “Improved hydrogeophysical characterization using joint inversion of cross-hole electrical resistance and ground-penetrating radar traveltime data”. In: *Water Resources Research* 42 (12), W12404. DOI: 10.1029/2006WR005131.

Linde, N., J. Doetsch, D. Jougnot, O. Genoni, Y. Dürst, B. J. Minsley, T. Vogt, N. Pasquale, and J Luster (2011). “Self-potential investigations of a gravel bar in a restored river corridor”. In: *Hydrology and Earth System Sciences* 15 (3), pp. 729–742. DOI: 10.5194/hess-15-729-2011.

Linde, N. and A. Revil (2007). “Inverting self-potential data for redox potentials of contaminant plumes”. In: *Geophysical Research Letters* 34 (14). DOI: 10.1029/2007GL030084.

Lowrie, W. and A. Fichtner (2020). *Fundamentals of Geophysics*. 3rd ed. Cambridge University Press. DOI: 10.1017/9781108685917.

Luquot, L. and P. Gouze (2009). “Experimental determination of porosity and permeability changes induced by injection of CO2 into carbonate rocks”. In: *Chemical Geology* 265 (1-2), pp. 148–159. DOI: 10.1016/j.chemgeo.2009.03.028.

MacAllister, D. J. (2016). “Monitoring Seawater Intrusion Into the Fractured UK Chalk Aquifer Using Measurements of Self-potential (SP).” Imperial College London.

MacAllister, D. J., M. T. Graham, J. Vinogradov, A. P. Butler, and M. D. Jackson (2019). “Characterizing the Self-Potential Response to Concentration Gradients in Heterogeneous Subsurface Environments”. In: *Journal of Geophysical Research: Solid Earth* 124, pp. 7918–7933. DOI: 10.1029/2019JB017829.

MacAllister, DJ., M. D. Jackson, A. P. Butler, and J. Vinogradov (2018). “Remote detection of saline intrusion in a coastal aquifer using borehole measurements of self-potential”. In: *Water Resour. Res.* 54 (3), pp. 1669–1687. DOI: 10.1002/2017WR021034.

MacInnes, D. A. (1939). “Electrolytic transference”. In: *The Principles of Electrochemistry*. Reinhold Publishing Corporation. Chap. 4, pp. 59–95. DOI: 10.1021/j150394a014.

Maineult, A., Y. Bernabé, and P. Ackerer (2004). “Electrical Response of Flow, Diffusion, and Advection in a Laboratory Sand Box”. In: *Vadose Zone Journal* 3 (4), pp. 1180–1192. DOI: 10.2136/vzj2004.1180.

— (2005). “Detection of advected concentration and pH fronts from self-potential measurements”. In: *Journal of Geophysical Research* 110, B11205. DOI: 10.1029/2005JB003824.

Maineult, A., J. B. Clavaud, and M. Zamora (2016). “On the interest of bulk conductivity measurements for hydraulic dispersivity estimation from miscible displacement experiments in rock samples”. In: *Transport in Porous Media* 115 (1), pp. 21–34. DOI: 10.1007/s11242-016-0749-0.

Maineult, A., D. Jougnot, and A. Revil (2018). “Variations of petrophysical properties and spectral induced polarization in response to drainage and imbibition: a study on a correlated random tube network”. In: *Geophysical Journal International* 212 (2), pp. 1398–1411. DOI: 10.1093/gji/ggx474.

Maineult, A., L. Jouniaux, and Y. Bernabé (2006). “Influence of the mineralogical composition on the self-potential response to advection of KCl concentration fronts through sand”. In: *Geophysical Research Letter* 33 (24). DOI: 10.1029/2006GL028048.

Mandelbrot, B. B. (2004). *Fractals and chaos: the Mandelbrot set and beyond*. Springer.

Marion, A. (2008). “Physical Transport Processes in Ecology: Advection, Diffusion, and Dispersion”. In: *Encyclopedia of Ecology*. Ed. by Brian Fath. 2nd ed. Oxford: Elsevier, pp. 359–364. DOI: 10.1016/B978-0-444-63768-0.00253-5.

Marshall, D. and T. Madden (1959). “Induced polarization, a study of its causes”. In: *Geophysics* 24 (4), pp. 790–816. DOI: 10.1190/1.1438659.

Martínez-Alvarez, V., M. J. González-Ortega, B. Martin-Gorriz, M. Soto-García, and J. F. Maestre-Valero (2018). “Seawater desalination for crop irrigation—Current status and perspectives”. In:

Emerging Technologies for Sustainable Desalination Handbook. Ed. by V. G. Gude. Chap. 14, pp. 461–492. DOI: 10.1016/B978-0-12-815818-0.00014-X.

Mary, B., L. Peruzzo, J. Boaga, N. Cenni, M. Schmutz, Y. Wu, S. S. Hubbard, and G. Cassiani (2020). "Time-lapse monitoring of root water uptake using electrical resistivity tomography and mise-à-la-masse: a vineyard infiltration experiment". In: *Soil* 6 (1), pp. 95–114. DOI: 10.5194/soil-6-95-2020.

Maxwell, J. C. (1861). "On Physical Lines of Force". In: *Philosophical Magazine* 90, pp. 11–23. DOI: 10.1080/14786431003659180.

Mboh, C. M., J. A. Huisman, E. Zimmermann, and H. Vereecken (2012). "Coupled hydrogeophysical inversion of streaming potential signals for unsaturated soil hydraulic properties". In: *Vadose Zone Journal* 11 (2), vzj2011–0115. DOI: 10.2136/vzj2011.0115.

McCleskey, R. B., D.K. Nordstrom, and J.N. Ryan (2012). "Comparison of electrical conductivity calculation methods for natural waters". In: *Limnology Oceanography Methods* 10 (11), pp. 952–967. DOI: 10.4319/lom.2012.10.952.

McGillivray, P. R and D. W. Oldenburg (1990). "Methods for calculating Fréchet derivatives and sensitivities for the non-linear inverse problem: a comparative study 1". In: *Geophysical prospecting* 38 (5), pp. 499–524. DOI: 10.1111/j.1365-2478.1990.tb01859.x.

Menke, W. (2012). "Chapter 6 - Nonuniqueness and Localized Averages". In: *Geophysical data analysis: Discrete inverse theory*. 3rd ed. Academic press, pp. 115–122. DOI: 10.1016/B978-0-12-397160-9.00006-0.

Meyerhoff, S. B., R. M. Maxwell, A. Revil, J .B. Martin, M. Karaoulis, and W. D. Graham (2014). "Characterization of groundwater and surface water mixing in a semi confined karst aquifer using time-lapse electrical resistivity tomography". In: *Water Resources Research* 50 (3), pp. 2566–2585. DOI: 10.1002/2013WR013991.

Molins, S., D. Trebotich, L. Yang, J. B. Ajo-Franklin, T. J. Ligocki, C. Shen, and C. I. Steefel (2014). "Pore-scale controls on calcite dissolution rates from flow-through laboratory and numerical experiments". In: *Environmental Science & Technology* 48 (13), pp. 7453–7460. DOI: 10.1021/es5013438.

Montanari, D., A. Minissale, M. Doveri, G. Gola, E. Trumpy, A. Santilano, and A. Manzella (2017). "Geothermal resources within carbonate reservoirs in western Sicily (Italy): A review". In: *Earth-Science Reviews* 169, pp. 180–201. DOI: 10.1016/j.earscirev.2017.04.016.

Murtaza, Y., G. E. Leinov, and M. D. Jackson (2011). "Self-potential anomalies induced by water injection into hydrocarbon reservoirs". In: *Geophysics* 76, F283–F292. DOI: 10.1190/1.3596010.

Naudet, V. and A. Revil (2005). “A sandbox experiment to investigate bacteria-mediated redox processes on self-potential signals”. In: *Geophysical Research Letters* 32 (11). DOI: 10.1029/2005GL022735.

Naudet, V., A. Revil, JY. Bottero, and P. Bégassat (2003). “Relationship between self-potential (SP) signals and redox conditions in contaminated groundwater”. In: *Geophysical research letters* 30 (21). DOI: 10.1029/2003GL018096.

Naudet, V., A. Revil, E. Rizzo, JY. Bottero, and P. Bégassat (2004). “Groundwater redox conditions and conductivity in a contaminant plume from geoelectrical investigations”. In: *Hydrology and Earth System Sciences* 8 (1), pp. 8–22. DOI: 10.5194/hess-8-8-2004.

Neumann, A Conrad (1966). “Observations on coastal erosion in Bermuda and measurements of the boring rate of the sponge, Cliona LAMPA 1, 2”. In: *Limnology and Oceanography* 11 (1), pp. 92–108. DOI: 10.4319/lo.1966.11.1.0092.

Niu, Q. and C. Zhang (2018). “Physical explanation of Archie’s porosity exponent in granular materials: A process-based, pore-scale numerical study”. In: *Geophysical Research Letter* 45, pp. 1870–1877. DOI: 10.1002/2017GL076751.

— (2019). “Permeability prediction in rocks experiencing mineral precipitation and dissolution: a numerical study”. In: *Water Resources Research* 55, pp. 3107–3121. DOI: 10.1029/2018WR024174.

Noiriel, C. (2015). “Resolving Time-dependent Evolution of Pore-Scale Structure, Permeability and Reactivity using X-ray Microtomography”. In: *Reviews in Mineralogy and Geochemistry* 80 (1), pp. 247–285. DOI: 10.2138/rmg.2015.80.08.

Noiriel, C., D. Bernard, P. Gouze, and X. Thibault (2005). “Hydraulic properties and micro-geometry evolution accompanying limestone dissolution by acidic water”. In: *Oil and Gas Science and Technology* 60 (1), pp. 177–192. DOI: 10.2516/ogst:2005011.

Noiriel, C. and H. Deng (2018). “Evolution of planar fractures in limestone: The role of flow rate, mineral heterogeneity and local transport processes”. In: *Chemical Geology* 497, pp. 100–114. DOI: 10.1016/j.chemgeo.2018.08.026.

Noiriel, C., P. Gouze, and D. Bernard (2004). “Investigation of porosity and permeability effects from microstructure changes during limestone dissolution”. In: *Geophysical Research Letters* 31 (24), p. L24603. DOI: 10.1029/2004GL021572.

Noiriel, C., L. Luquot, B. Madé, L. Raimbault, P. Gouze, and J. van der Lee (2009). “Changes in reactive surface area during limestone dissolution: An experimental and modelling study”. In: *Chemical Geology* 265 (1), pp. 160–170. DOI: 10.1016/j.chemgeo.2009.01.032.

Noiriel, C., M. Oursin, and D. Daval (2020). “Examination of crystal dissolution in 3D: A way to reconcile dissolution rates in the laboratory?” In: *Geochimica et Cosmochimica Acta* 273, pp. 1–25. DOI: 10.1016/j.gca.2020.01.003.

Noiriel, C., C. I. Steefel, L. Yang, and J. Ajo-Franklin (2012). "Upscaling calcium carbonate precipitation rates from pore to continuum scale". In: *Chemical Geology* 318-319, pp. 60–74. DOI: https://doi.org/10.1016/j.chemgeo.2012.05.014.

Noiriel, C., C. I. Steefel, L. Yang, and D. Bernard (2016). "Effects of pore-scale precipitation on permeability and flow". In: *Advances in Water Resources* 95. Pore scale modeling and experiments, pp. 125–137. DOI: j.advwatres.2015.11.013.

Norbisrath, J. H., R. J. Weger, and G. P. Eberli (2017). "Complex resistivity spectra and pore geometry for predictions of reservoir properties in carbonate rocks". In: *Journal of Petroleum Science and Engineering* 151, pp. 455–467. DOI: 10.1016/j.petrol.2016.12.033.

Nourbehecht, B. (1963). "Irreversible thermodynamic effects in inhomogenous media and their application in certain geoelectic problems". Massachusetts Institute of Technology.

Nunes, J.P.P., M.J. Blunt, and B. Bijeljic (2016). "Pore-scale simulation of carbonate dissolution in micro-CT images". In: *Journal of Geophysical Research* 121 (2), pp. 558–576. DOI: 10.1002/2015JB012117.

Okay, G., P. Leroy, A. Ghorbani, P. Cosenza, C. Camerlynck, J. Cabrera, N. Florsch, and A. Revil (2014). "Spectral induced polarization of clay-sand mixtures: Experiments and modeling". In: *Journal of Geophysical Research* 79 (6), 1ND–Z201. DOI: 10.1190/geo2013-0347.1.

Oldenburg, D. and Y. Li (2005). "5. Inversion for Applied Geophysics: A Tutorial". In: *Near-surface Geophysics*. Ed. by D. K. Butler. Society of Exploration Geophysicists, pp. 85–150. DOI: 10.1190/1.9781560801719.ch5.

Oliveira, T. D. S., M. J. Blunt, and B. Bijeljic (2020). "Multispecies reactive transport in a microporous rock: Impact of flow heterogeneity and reversibility of reaction". In: *Water Resources Research* 56 (12), e2020WR027317. DOI: 10.1029/2020WR027317.

Ontash and Ermac (2015). *Ontash & Ermac website*. URL: https://www.ontash.com/products.htm#PSIP.

Or, D., M. Tuller, and J. M. Wraith (2009). *Vadose Zone Hydrology*. Environmental Soil Physics.

Paine, J. G. (2003). "Determining salinization extent, identifying salinity sources, and estimating chloride mass using surface, borehole, and airborne electromagnetic induction methods". In: *Water Resources Research* 39 (3), p. 1059. DOI: 10.1029/2001WR000710,2003.

Palandri, J. L. and Y. K. Kharaka (2004). *A compilation of rate parameters of water–mineral interaction kinetics for application to geochemical modeling*. Tech. rep. Geological Survey Menlo Park CA.

Palciaukas, V. and P. Domenico (1976). "Solution chemistry, mass transfert, and the approach to chemical equilibrium in porous carbonate rocks and sediments". In: *Geological Society of America Bulletin* 87, pp. 207–214. DOI: 10.1130/0016-7606(1976)87<207:SCMTAT>2.0.CO;2.

Parkhurst, D. L. and C. A. J. Appelo (2013). *Description of input and examples for PHREEQC version 3: a computer program for speciation, batch-reaction, one-dimensional transport, and inverse geochemical calculations*. Tech. rep. US Geological Survey. DOI: 10.3133/tm6A43.

Pelton, W. H., W. R. Sill, and B. D. Smith (1983). "Interpretation of Complex Resistivity and Dielectric Data, Part I." In: *Geophysical Trans.* 29 (4), pp. 297–330. DOI: 10.1103/PhysRevB.50.15678.

Pelton, W. H., S. H. Ward, W. R. Hallof, W. R. Sill, and P. H. Nelson (1978). "Mineral discrimination and removal of inductive coupling with multifrequency IP". In: *Geophysics* 43 (3), pp. 1942–2156. DOI: 10.1190/1.1440839.

Petersen, E. E. (1958). "Diffusion in a pore of varying cross section". In: *American Institute of Chemical Engineers Journals* 3 (4), pp. 343–345. DOI: 10.1002/aic.690040322.

Petiau, G. and A. Dupis (1980). "Noise, temperature coefficient, and long time stability of electrodes for telluric observations". In: *Geophysical Prospecting* 28 (5), pp. 792–804. DOI: 10.1111/j.1365-2478.1980.tb01261.x.

Pfannkuch, H. O. (1972). "On the correlation of electrical conductivity properties of porous systems with viscous flow transport coefficients". In: *Developments in Soil Science* 2, pp. 42–54. DOI: 10.1016/S0166-2481(08)70527-0.

Pichot, M (1932). "«Anomalies» de viscosité des solutions de gélatine". In: *Journal de Physique et le Radium* 3 (5), pp. 205–218. DOI: 10.1051/jphysrad:0193200305020500.

Pirson, Sylvain Joseph (1983). *Geologic well log analysis*. Butterworth-Heinemann.

Plagnes, V. (1997). "Structure et Fonctionnement des aquifères karstiques. Caractérisation par la géochimie des eaux". Université Montpellier II, p. 376.

Plummer, L. N. and E. Busenberg (1982). "The solubilities of calcite, aragonite and vaterite in CO2-H2O solutions between 0 and 90°C, and an evaluation of the aqueous model for the system CaCO3-CO2-H2O". In: *Geochimica et Cosmochimica Acta* 46 (6), pp. 1011–1040. DOI: 10.1016/0016âĂŘ7037(82)90056âĂŘ4.

Pride, S. (1994). "Governing equations for the coupled electromagnetics and acoustics of porous media". In: *Physical Review B* 50 (21), pp. 678–696. DOI: 10.1103/PhysRevB.50.15678.

Quincke, G. (1859). "Ueber eine neue art elektrischer ströme". In: *Annalen der Physik* 183 (5), pp. 1–47. DOI: 10.1002/andp.18591830502.

Rattray, M. and E. Mitsuda (1974). "Theoretical analysis of conditions in a salt wedge". In: *Estuarine and Coastal Marine Science* 2 (4), pp. 375–394. DOI: 10.1016/0302-3524(74)90006-1.

Reis, J.C. and A.M. Acock (1994). "Permeability reduction models for the precipitation of inorganic solids in Berea sandstone". In: *In Situ* 18 (3), pp. 347–368.

Rembert, F., D. Jougnot, and L. Guarracino (2020). “A fractal model for the electrical conductivity of water-saturated porous media during mineral precipitation-dissolution processes”. In: *Advances in Water Resources* 145, p. 103742. DOI: 10.1016/j.advwatres.2020.103742.

Revil, A. (1999). “Ionic Diffusivity, Electrical Conductivity, Membrane and Thermoelectric Potentials in Colloids and Granular Porous Media: A Unified Model”. In: *Journal of Colloid and Interface Science* 212 (2), pp. 503–522. DOI: 10.1006/jcis.1998.6077.

— (2012a). “Spectral induced polarization of shaly sands: Influence of the electrical double layer”. In: *Water Resources Research* 48 (2), W02517. DOI: 10.1029/2011WR011260.

— (2012b). “Spectral induced polarization of shaly sands: Influence of the electrical double layer”. In: *Water Resources Research* 48 (2). DOI: 10.1029/2011WR011260.

— (2013). “Effective conductivity and permittivity of unsaturated porous materials in the frequency range 1 mHz–1GHz”. In: *Water resources research* 49 (1), pp. 306–327. DOI: 10.1029/2012WR012700.

Revil, A. and L. M. Cathles (1999). “Permeability of shaly sands”. In: *Water Resources Research* 35 (3), pp. 651–662. DOI: 10.1029/98WR02700.

Revil, A., L. M. Cathles, S. Losh, and J. A. Nunn (1998). “Electrical conductivity in shaly sands with geophysical applications”. In: *Journal of Geophysical Research* 103 (B10), pp. 23925–23936. DOI: 10.1029/98JB02125.

Revil, A. and N. Florsch (2010). “Determination of permeability from spectral induced polarization in granular media”. In: *Geophysical Journal International* 181 (3), pp. 1480–1498. DOI: 10.1111/j.1365-246X.2010.04573.x.

Revil, A. and P. W. J. Glover (1997). “Theory of ionic-surface electrical conduction in porous media”. In: *Physical Review B* 55 (3), pp. 1757–1773. DOI: 10.1103/PhysRevB.55.1757.

Revil, A. and A. Jardani (2013). *The Self-Potential Method: Theory and Applications in Environmental Geosciences*. Ed. by Cambridge University Press. DOI: 10.1017/cbo9781139094252.

Revil, A. and D. Jougnot (2008). “Diffusion of ions in unsaturated porous materials”. In: *Journal of Colloid and Interface Science* 319 (1), pp. 226–235. DOI: 10.1016/j.jcis.2007.10.041.

Revil, A., M. Karaoulis, T. Johnson, and A. Kemna (2012). “Some low-frequency electrical methods for subsurface characterization and monitoring in hydrogeology”. In: *Hydrogeology Journal* 20 (4), pp. 617–658. DOI: 10.1007/s10040-011-0819-x.

Revil, A., P. Kessouri, and C. Torres-Verdin (2014). “Electrical conductivity, induced polarization, and permeability of the fontainebleau sandstone”. In: *Geophysics* 79 (5), pp. D301–D318. DOI: 10.1190/geo2014-0036.1.

Revil, A. and P. Leroy (2004). “Constitutive equations for ionic transport in porous shales”. In: *Journal of Geophysical Research* 109 (B3), B03208. DOI: 10.1029/2003JB002755.

Revil, A. and N. Linde (2006). “Chemico-electromechanical coupling in microporous media”. In: *Journal of Colloid and Interface Science* 302 (2), pp. 682–694. DOI: 10.1016/j.jcis.2006.06.051.

Revil, A, C. A. Mendonça, E. A. Atekwana, B. Kulessa, S. S. Hubbard, and K. J. Bohlen (2010). “Understanding biogeobatteries: Where geophysics meets microbiology”. In: *Journal of Geophysical Research: Biogeosciences* 115 (G1). DOI: 10.1029/2009JG001065.

Reynolds, J. M. (2011). *An introduction to applied and environmental geophysics*. 2nd ed. John Wiley & Sons.

Robinson, R. A. and C. L. Chia (1952). “The diffusion coefficient of calcium chloride in aqueous solution at 25”. In: *Journal of the American Chemical Society* 74 (11), pp. 2776–2777. DOI: 10.1021/ja01131a021.

Rötting, T., L. Luquot, J. Carrera, and D. J. Casalinuovo (2015). “Changes in porosity, permeability, water retention curve and reactive surface area during carbonate rock dissolution”. In: *Chemical Geology* 403 (18), pp. 86–98. DOI: 10.1016/j.chemgeo.2015.03.008.

Rubenstein, D. A., W. Yin, and M. D. Frame (2015). “Mass Transport and Heat Transfer in the Microcirculation”. In: *Biofluid Mechanics*. Ed. by D. A. Rubenstein, W. Yin, and M. D. Frame. 2nd ed. Biomedical Engineering. Boston: Academic Press. Chap. 7, pp. 267–309. DOI: 10.1016/B978-0-12-800944-4.00007-X.

Rubin, Y. and S. S. Hubbard (2006). *Hydrogeophysics*. Springer Science & Business Media.

Ruffet, C, M Darot, and Y Gueguen (1995). “Surface conductivity in rocks: a review”. In: *Surveys in geophysics* 16 (1), pp. 83–105. DOI: 10.1007/BF00682714.

Rust Jr, W. M. (1938). “A historical review of electrical prospecting methods”. In: *Geophysics* 3 (1), pp. 1–6. DOI: 10.1190/1.1439461.

Saneiyan, S., D. Ntarlagiannis, and F. Colwell (2021). “Complex conductivity signatures of microbial induced calcite precipitation, field and laboratory scales”. In: *Geophysical Journal International* 224 (3), pp. 1811–1824. DOI: 10.1093/gji/ggaa510.

Saneiyan, S., D. Ntarlagiannis, J. Ohan, J. Lee, F. Colwell, and S. Burns (2019). “Induced polarization as a monitoring tool for in-situ microbial induced carbonate precipitation (MICP) processes”. In: *Ecological Engineering* 127, pp. 36–47. DOI: 10.1016/j.ecoleng.2018.11.010.

Sato, M. and H. M. Mooney (1960). “The electrochemical mechanism of sulfide self-potentials”. In: *Geophysics* 25 (1), pp. 226–249. DOI: 10.1190/1.1438689.

Schlumberger, C. (1920a). “Polarisation provoquée”. In: *Étude sur la prospection électrique du sous-sol*. Ed. by Gauthier-Villars et Cie. 2nd ed. Paris, France, pp. 72–74.

— (1920b). “Polarisation spontanée”. In: *Étude sur la prospection électrique du sous-sol*. Ed. by Gauthier-Villars et Cie. 2nd ed. Paris, France, pp. 75–89.

Schroeder, E. D. (2003). “Water Resources”. In: *Encyclopedia of Physical Science and Technology*. Ed. by R. A. Meyers. 3rd ed. New York: Academic Press, pp. 721–751. DOI: 10.1016/B0-12-227410-5/00821-8.

Schulze-Makuch, D. (2005). “Longitudinal dispersivity data and implications for scaling behavior”. In: *Ground Water* 43 (3), pp. 443–546. DOI: 10.1111/j.1745-6584.2005.0051.x.

Schwarz, G. (1962). “A theory of the low-frequency dielectric dispersion of colloidal particles in electrolyte solution”. In: *The Journal of Physical Chemistry* 66 (12), pp. 2636–2642. DOI: 10.1021/j100818a067.

Sen, P. N. (1989). “Unified model of conductivity and membrane potential of porous media”. In: *Physical Review B* 39 (13), pp. 9508–9517. DOI: 10.1103/PhysRevB.39.9508.

Shashi Menon, E. (2015). “Fluid Flow in Pipes”. In: *Transmission Pipeline Calculations and Simulations Manual*. Boston: Gulf Professional Publishing. Chap. 5, pp. 149–234. DOI: 10.1016/B978-1-85617-830-3.00005-5.

Sill, W. R. (1983). “Self-potential modeling from primary flows”. In: *Geophysics* 48 (1), pp. 76–86. DOI: 10.1190/1.1441409.

Singh, K. H. and R. M. Joshi (2020). *Petro-physics and Rock Physics of Carbonate Reservoirs. Likely Elucidations and Way Forward*. Ed. by K. H. Singh and R. M. Joshi. Singapore: Springer. DOI: 10.1007/978-981-13-1211-3.

Sisavath, S., X. Jing, and R. W. Zimmerman (2001). “Creeping flow through a pipe of varying radius”. In: *Physics of Fluids* 13 (10), p. 2762. DOI: 10.1063/1.1399289.

Smart, C. C. (1992). “Temperature compensation of electrical conductivity in glacial meltwaters”. In: *Journal of Glaciology* 38 (128), pp. 9–12. DOI: 10.3189/S0022143000009540.

Soldi, M., L. Guarracino, and D. Jougnot (2017). “A simple hysteretic constitutive model for unsaturated flow”. In: *Transport in Porous Media* 120 (2), pp. 271–285. DOI: 10.1007/s11242-017-0920-2.

— (2020). “An effective excess charge model to describe hysteresis effects on streaming potential”. In: *Journal of Hydrology* 588, p. 124949. DOI: 10.1016/j.jhydrol.2020.124949.

Somasundaran, P. and G. E. Agar (1967). “The zero point of charge of calcite”. In: *Journal of Colloid and Interface Science* 24 (4), pp. 433–440. DOI: 10.1016/0021-9797(67)90241-X.

Sorensen, J. A. and G. E Glass (1987). “Ion and temperature dependence of electrical conductance for natural waters”. In: *Analytical Chemistry* 59 (13), pp. 1594–1597. DOI: 10.1021/ac00140a003.

Soueid Ahmed, A., A. Revil, F. Abdulsamad, B. Steck, C. Vergniault, and V. Guihard (2020). “Induced polarization as a tool to non-intrusively characterize embankment hydraulic properties”. In: *Engineering Geology* 271, p. 105604. DOI: 10.1016/j.enggeo.2020.105604.

Spitzer, K. (1998). "The three-dimensional DC sensitivity for surface and subsurface sources". In: *Geophysical Journal International* 134 (3), pp. 736–746. DOI: 10.1046/j.1365-246x.1998.00592.x.

Steefel, C. I. (2009). *CrunchFlow. Software for modeling multicomponent reactive flow and transport. User's Manual*. Lawrence Berkeley National Laboratory, Berkeley, USA.

Steinwinder, J. and L. E. Beckingham (2019). "Role of pore and pore-throat distributions in controlling permeability in heterogeneous mineral dissolution and precipitation scenarios". In: *Water Resources Research* 55 (7), pp. 5502–5517. DOI: 10.1029/2019WR024793.

Stockmann, G. J., D. Wolff-Boenisch, N. Bovet, S. R. Gislason, and E. H. Oelkers (2014). "The role of silicate surfaces on calcite precipitation kinetics". In: *Geochimica et Cosmochimica Acta* 135, pp. 231–250. DOI: 10.1016/j.gca.2014.03.015.

Strathmann, H. (2004). "Electrochemical and thermodynamic fundamentals". In: *Ion-exchange membrane separation processes*. Ed. by Membrane Science and Technology. Vol. 9. Elsevier. Chap. 2, pp. 23–88. DOI: 10.1016/S0927-5193(04)80033-0.

Tallgren, P., S. Vanhatalo, K. Kaila, and J. Voipio (2005). "Evaluation of commercially available electrodes and gels for recording of slow EEG potentials". In: *Clinical Neurophysiology* 116 (4), pp. 799–806. DOI: 10.1016/j.clinph.2004.10.001.

Talman, S. J., B. Wiwchar, W. D. Gunter, and C. M. Scarge (1990). *Dissolution kinetics of calcite in the H_2O-CO_2 system along the steam saturation curve to 210° C*. In R. J. Spencer and I. M. Chou (Eds.), Fluid-Mineral Interactions: A tribute to H. P. Eugster, Geochemical Society Special Publication, 2nd edition, pp. 41–55.

Tarantola, Albert (2005). *Inverse problem theory and methods for model parameter estimation*. SIAM. DOI: 10.1137/1.9780898717921.

Teng, H. H., P. M. Dove, and J. J. De Yoreo (2000). "Kinetics of calcite growth: surface processes and relationships to macroscopic rate laws". In: *Geochimica et Cosmochimica Acta* 64 (13), pp. 2255–2266. DOI: 10.1016/S0016-7037(00)00341-0.

Thanh, L. D., D. Jougnot, V. D. Phan, and V. N .A. Nguyen (2019). "A physically based model for the electrical conductivity of water-saturated porous media". In: *Geophysical Journal International* 219, pp. 866–876. DOI: 10.1093/gji/ggz328.

Titov, K., V. Komarov, V. Tarasov, and A. Levitski (2002). "Theoretical and experimental study of time domain-induced polarization in water-saturated sands". In: *Journal of Applied Geophysics* 50 (4), pp. 417–433. DOI: 10.1016/S0926-9851(02)00168-4.

Tyler, S.W. and S.W. Wheatcraft (1990). "Fractal processes in soil-water retention". In: *Water Resources Research* 26 (10), pp. 1047–1054.

Ulrich, C. and L. D. Slater (2004). “Induced polarization measurements on unsaturated, unconsolidated sands”. In: *Geophysics* 69 (3), pp. 762–771. DOI: 10.1190/1.1759462.

van Brakel, J. and P. M. Heertjes (1974). “Analysis of diffusion in macroporous media in terms of a porosity, a tortuosity and a constrictivity factor”. In: *International Journal of Heat and Mass Transfer* 17 (9), pp. 1093–1103. DOI: 10.1016/0017-9310(74)90190-2.

Vanhala, H. (1997). “Mapping Oil-Contaminated Sand and Till with the Spectral Induced Polarization (SIP) Method”. In: *Geophysical Prospecting* 45 (2), pp. 303–326. DOI: 10.1046/j.1365-2478.1997.00338.x.

Vaquier, V., C. R. Holmes, P. R. Kintzinger, and M. Lavergne (1957). “Prospecting for groundwater by induced electrical polarization”. In: *Geophysics* 22 (3), pp. 660–687. DOI: 10.1190/1.1438402.

Varet, J. et al. (2009). *10 core challenges for geosciences. Special file International Planet Earth Year*. English. Ed. by French Geological Survey Bureau de Recherches Géologiques et Minières (BRGM), p. 128.

Vaukhonen, M. (1997). “Electrical impedance tomography and prior information”. Finland: Univesity of Kuopio. DOI: 10.1.1.208.9639.

Vereecken, H., A. Binley, G. Cassiani, A. Revil, and K. Titov (2006). “Applied hydrogeophysics”. In: *Applied Hydrogeophysics*. Vol. 71. NATO Science Series. Springer, Dordrecht, pp. 1–8. DOI: 10.1007/978-1-4020-4912-5_1.

Vialle, S., S. Contraires, B. Zinzsner, J. B. Clavaud, K. Mahiouz, P. Zuddas, and M. Zamora (2014). “Percolation of CO2-rich fluids in a limestone sample: Evolution of hydraulic, electrical, chemical, and structural properties”. In: *Journal of Geophysical Research Solid Earth* 119 (4), pp. 2828–2847. DOI: 10.1002/2013JB010656.

Vieira, C., A. Maineult, and M. Zamora (2012). “Laboratory study of self-potential signals during releasing of CO_2 and N_2 plumes”. In: *Comptes Rendus Geoscience* 344 (10), pp. 498–507. DOI: 10.1016/j.crte.2012.09.002.

Vinegar, H. J. and M. H. Waxman (1984). “Induced polarization of shaly sands”. In: *Geophysics* 49, pp. 1267–1287. DOI: 10.1190/1.1441755.

von Helmholtz, H. (1879). “Studien über electrische Grenzschichten”. In: *Annalen der Physik* 243 (7), pp. 337–382. DOI: 10.1002/andp.18792430702.

von Smoluchowski, M. (1903). “Contribution à la théorie de l’endosmose électrique et de quelques phénomènes corrélatifs”. In: *Bulletin international de l’Académie des Sciences de Cracovie* 8, pp. 182–200.

Watlet, A., O. Kaufmann, A. Triantafyllou, A. Poulain, J. E. Chambers, P. I. Meldrum, P. B. Wilkinson, V. Hallet, Y. Quinif, M. Van Ruymbeke, and M. Van Camp (2018). “Imaging groundwater in-

filtration dynamics in the karst vadose zone with long-term ERT monitoring". In: *Hydrology and Earth System Sciences* 22 (2), pp. 1563–1592. DOI: 10.5194/hess-22-1563-20181.

Waxman, M. H. and L. J. M. Smits (1968). "Electrical conductivities in oil bearing shaly sands". In: *Society of Petroleum Engineers Journal* 8 (2), pp. 107–122. DOI: 10.2118/1863-A.

Weller, A. and L. Slater (2012). "Salinity dependence of complex conductivity of unconsolidated and consolidated materials: comparisons with electrical double layer models". In: *Geophysics* 77 (5), pp. D185–D198. DOI: 10.1190/GEO2012-0030.1.

Weller, A., L. D. Slater, and S. Nordsiek (2013). "On the relationship between induced polarization and surface conductivity: Implications for petrophysical interpretation of electrical measurements". In: *Geophysics* 78 (5), pp. D315–D325. DOI: 10.1190/GEO2013-0076.1.

Wheatcraft, S.W. and S.W. Tyler (1988). "An explanation of scale-dependant diversity in heterogeneous aquifers using concepts of fractal geometry". In: *Water Resources Research* 24 (5), pp. 66–78. DOI: 10.1029/WR024i004p00566.

Wong, J. (1979). "An electrochemical model of the induced-polarization phenomenon in disseminated sulfide ores". In: *Geophysics* 44 (7), pp. 1245–1265. DOI: 10.1190/1.1441005.

Wu, Y., S. Hubbard, K. H. Williams, and J. Ajo-Franklin (2010). "On the complex conductivity signatures of calcite precipitation". In: *Journal of Geophysical Research* 115 (G2), G00G04. DOI: 10.1029/2009JG001129.

Yio, M. H. N., H. S. Wong, and N. R. Buenfeld (2017). "Representative elementary volume (REV) of cementitious materials from three-dimensional pore structure analysis". In: *Cement and Concrete Research* 102, pp. 187–202. DOI: 10.1016/j.cemconres.2017.09.012.

Yu, B. and P. Cheng (2002). "A fractal permeability model for bi-dispersed porous media". In: *International Journal of Heat Mass Transfer* 45 (14), pp. 2983–2993. DOI: 10.1016/S0017-9310(02)00014-5.

Yu, B. and J. Li (2001). "Some fractal characters of porous media". In: *Fractals* 9 (3), pp. 365–372. DOI: 10.1142/s0218348x01000804.

Yu, B., J. Li, Z. Li, and M. Zou (2003). "Permeabilities of unsaturated fractal porous media". In: *International Journal of Multiphase Flow* 29 (10), pp. 1625–1642. DOI: 10.1016/S0301-9322(03)00140-X.

Zhang, C., L. Slater, G. Redden, Y. Fujita, T. Johnson, and D. Fox (2012). "Spectral Induced Polarization Signatures of Hydroxide Adsorption and Mineral Precipitation in Porous Media". In: *Environmental Science & Technology* 46 (8), pp. 4357–4364. DOI: 10.1021/es204404e.

Zhang, S., H. Yan, J. Teng, and D. Sheng (2020). "A mathematical model of tortuosity in soil considering particle arrangement". In: *Vadose Zone Journal* 19 (1), e20004. DOI: 10.1002/vzj2.20004.

Ziarani, A. S. and R. Aguilera (2012). "Pore-throat radius and tortuosity estimation from formation resistivity data for tight-gas sandstone reservoirs". In: *Journal of Applied Geophysics* 83, pp. 65–73. DOI: 10.1016/j.jappgeo.2012.05.008.

Zimmermann, E., A. Kemna, J. Berwix, W. Glaas, H. M. Münch, and J. A. Huisman (2008). "A high-accuracy impedance spectrometer for measuring sediments with low polarizability". In: *Measurement Science and Technology* 19 (10), p. 105603. DOI: 10.1088/0957-0233/19/10/105603.